THE UNIVERSITY *of* EDINBURGH

Quantification of Wave-Current-Turbulence Interactions through Numerical Modelling and Data-Driven Method for Ocean Energy Applications

Tian Tan

THE UNIVERSITY *of* EDINBURGH

Doctor of Philosophy

2025

Lay Summary

The ocean's waves and tides offer vast, renewable energy potential, making them reliable and sustainable energy sources. Traditionally, waves and tidal currents are studied separately due to their distinct physical processes in evaluating wave or tidal energy resources. However, in regions such as the Pentland Firth and Orkney Waters (PFOW) in northern Scotland, UK, strong waves and fast tidal currents often coexist and interact. Ignoring these interactions can lead to significant errors in estimating wave or tidal energy resources and create complex, turbulent water flows that pose risks to engineering projects. This research investigates the interactions between waves and tidal currents in PFOW comprehensively, using advanced numerical modelling, wave-current decomposition method, and artificial intelligence (AI) tools.

The first part of this study focuses on simulating real-world ocean conditions using open-source numerical modelling. A North Atlantic scale wave-only model was developed to represent wave behaviour without tidal influences, alongside a regional coupled wave-current model to simulate tidal effects. Both models were validated with field data, and eight locations around PFOW were analysed to study tidal impacts on waves. Long-term simulations (of the years 2014–2023) provided extensive data on wave behaviour, offering valuable insights into wave-tidal current interactions and supporting accurate assessments of wave energy resource.

The second focus of the study investigates how wave affects turbulence levels in tidal flows. In areas with coexisting waves and currents, the combined motion creates complex turbulence patterns. To isolate and quantify the specific contributions of waves, a novel wave-current decomposition method was developed. This technique separates wave and current components from tidal flow velocity measurements in the Pentland Firth, allowing for precise calculations of turbulence intensity for wave-only, current-only, and combined wave-current scenarios. The results provide practical guidance for tidal energy site selection and risk management.

The final part of the research applies advanced AI techniques to predict wave parameters. Based on XGBoost machine learning algorithm and Informer deep learning model, the study predicted wave parameters in both open-sea and strait environments. Predictions for open-sea regions relied on wind data, while strait predictions incorporated tidal flow data to capture wave-current interaction effects. These AI models demonstrated strong predictive capabilities, significantly improving the efficiency of wave parameter estimation and offering valuable tools for energy resource assessment and ocean engineering.

Abstract

Wave-current interactions (WCI) play a critical role in shaping wave and tidal current energy resources, yet their neglect can lead to significant over- or underestimations, misrepresenting the complexities of the flow environment. Despite extensive theoretical exploration of WCI mechanisms, their application to real-world ocean settings remains limited. Long-term assessments using numerical models with two-way coupling of wave and tidal currents are rare, leaving gaps in understanding WCI under realistic conditions. Additionally, the quantification of turbulence enhanced by waves at actual sites is poorly understood. While machine learning has been widely applied to general wave predictions, it has yet to address parameters influenced by WCI.

This PhD research addresses these challenges by investigating the impact of WCI on wave and tidal parameters in the Pentland Firth and Orkney Waters (PFOW), Scotland, UK, through three complementary methodologies: numerical modelling, wave-current decomposition, and machine learning.

Numerical modelling was employed to analyse the effects of tidal currents on wave parameters and wave energy resources. Two models were developed: (1) a North Atlantic scale TOMAWAC wave-only model, which provided boundary conditions and wave parameters unaffected by tidal currents, and (2) a regional two-way coupled TOMAWAC-TELEMAC wave-current model, which simulated wave parameters accounting for WCI. Validation of both models was achieved using field measurements, including 10 years of data from Cefas WaveNet buoys (for the wave-only model) and 135 days of site measured Acoustic Wave and Current Profiler (AWAC) and Acoustic Doppler Current Profiler (ADCP) data (for the wave-current model). After that, eight representative sites across PFOW were analysed to assess tidal effects on wave parameters under Spring and Neap tides, Flood and Ebb phases. The enhanced wave breaking due to strong currents was frequently observed. Furthermore, a 10-year simulation (2014–2023) of both models produced wave maps incorporating tidal effects, revealing spatiotemporal variations in WCI phenomena across interannual, seasonal, and monthly scales.

The second focus was the use of a novel wave-current decomposition method to quantify turbulence levels enhanced by waves. A side information assisted Empirical Mode Decomposition (EMD) method was introduced to separate wave and current components from

combined velocity data. The validity of this method was demonstrated by comparing the derived wave heights and current velocity spectra with field measurements and theoretical benchmarks. The method was applied to ADCP data from three locations in PFOW, enabling the calculation of turbulence intensity (TI) for wave-only, current-only, and wave-current conditions across varying current velocities and wave heights. This analysis provided a comprehensive quantification of three-dimensional turbulence levels enhanced by waves in streamwise, transverse, and vertical directions. An empirical relationship between wave-induced, current-induced, and wave-current coupled turbulence was also proposed, offering a practical tool for estimating wave-induced turbulence levels.

The final focus of the research involved machine learning methods to predict wave parameters. For deep-water, open-sea regions around northern Scotland where tidal currents are negligible, the spatiotemporal relationship between wind and waves was modelled using the Informer deep neural networks and the XGBoost machine learning algorithm. Ten years (2012–2021) of hourly wind data from ECMWF ERA5 and wave parameters from Cefas WaveNet buoys were used for training and verification, enabling accurate wave predictions for 2022. Models for typical and extreme weather conditions were developed to enhance prediction accuracy. Additionally, at PFOW regions where WCI are significant, the Informer model was used to predict waves under tidal effects. Input features were derived from the previously mentioned North Atlantic scale wave model and the regional scale wave-current model. Training on 2016 data enabled accurate predictions of 2017 wave conditions across different sites, demonstrating the model's capability to capture wave-current interactions effectively.

Overall, this thesis integrates numerical modelling, wave-current decomposition, and machine learning to provide a multifaceted quantification of WCI in real-world settings. Their interdependence on shared datasets underscores their internal synergy. The findings offer valuable insights and tools for addressing challenges in ocean engineering, particularly for wave energy development in wave-current environments, while providing extensive and robust datasets for future research.

Acknowledgements

These four years, though short in the grand scale of life, will forever remain a golden chapter in my memories.

First and foremost, I would like to express my deepest gratitude to my PhD supervisor, Prof. Vengatesan (Venki) Venugopal. He granted me the freedom and trust to explore topics that interested me while providing expert guidance, ongoing encouragement, and unwavering support throughout the process. I truly cherished the days working with him. I am also immensely thankful for the opportunity he provided to work as a research assistant on the EPSRC WavE-Suite project. This experience allowed me to engage in experimental research beyond my PhD work, broadening my horizons and enriching my academic journey. I would also like to express my sincere gratitude to my second supervisor, Dr. Brian Seller, and my project examiner, Dr. David Forehand, for their insightful feedback and thoughtful discussions at every stage of my PhD.

My sincere thanks go to my peer and colleague, Munawir Pratama, for generously sharing his perspectives on research and life. His diligence and dedication are truly inspiring. I am also deeply grateful to other members (and former members) of the research group, Dr. Rameeza Moideen, Dr. Callum Guy, Dr. Anas Rahman, and Touhidul Islam, for their invaluable support in my research. A special thanks to Dr. Yanbin Liu, who invited me to the Scottish Green Energy Awards night, offering me the chance to connect with experts from both academia and industry in this field. To my dear friend, Doudou Huang, thank you for the countless joyful moments we shared over tea breaks. Those light-hearted times brought so much warmth to my days. To my badminton friends, Dr. Yichong Chen, Dr. Shaokang Li, and Dr. Yankai Li, thank you for helping me stay active and maintain a healthy body and mind amidst the demands of research.

I would also like to thank all my office mates in A123/4 over the past four years for creating a cheerful and supportive environment. My gratitude further extends to the broader community of the School of Engineering at the University of Edinburgh for fostering a supportive space throughout my PhD journey. Over the course of these four years, I have encountered numerous scholars and friends who have offered their help in many ways—whether through an inspiring conversation or an encouraging word before a presentation. I am incredibly grateful for their support and wish them all extraordinary success in their own lives.

Acknowledgements

I also acknowledge support from the SAE MeyGen project for providing ADCP data and am grateful for financial support from the EPSRC through CableDyn: Subsea Power Cable Dynamics Under Complex Ocean Environment (EP/W015102/1) and through WavE-Suite: New Generation Modelling Suite for the Survivability of Wave Energy Converters in Marine Environments (EP/V040235/1).

A heartfelt thanks to my lifelong friend and flatmate, Shiying Zhang. We have known each other for 10 years, ever since our undergraduate days. These four years of my PhD have been filled with challenges, and I am so lucky to have you to share the highs and lows, celebrating every milestone together. I will always treasure our friendship. Meanwhile, my gratitude goes to my beloved ragdoll cat babies, Siry and Tony, for their invaluable companionship during this long journey.

Finally, my highest appreciation goes to my dear parents. You have given me the freedom to be myself and have supported every path I've chosen with endless love and encouragement. The distance between the UK and China made traveling home especially difficult, particularly during the three years of Covid. I feel deeply guilty for not being by your side during the times when our family needed to stand together the most. Yet, you always prioritized my safety and well-being, standing by me unconditionally. Being your daughter is my greatest pride. I wish you both health and happiness, and I hope you are as proud of me as I am of you.

Table of Contents

List of Figures

List of Tables

Nomenclature

Numerical Modelling (Chapter 2, Chapter 3, Chapter 4)

$\Delta\rho$	Variation of density around the reference density
σ	Relative or intrinsic angular wave frequency
θ	Wave propagation directions in radians
ρ	Water density
υ	Kinematic viscosity
ρ_0	Reference density
η	Surface elevation
α	Wave propagation direction
δ	Tidal current flow direction
ω	Apparent or absolute angular wave frequency
β	Angle between wave direction and the normal to current direction
$B(k)$	Spectral saturation level
B_r	Threshold level
C_σ	Wave propagation velocity in frequency space
$C_{ds,cur}$	Westhuysen dissipation coefficient due to strong currents
$C_{dis,break}$	Westhuysen dissipation coefficient
$C_{dis,non-break}$	Westhuysen whitecapping dissipation coefficient
C_g	Wave group velocity
$C_{g,0}$	Wave group velocity with no ambient current
E	Directional spectrum
F	Directional spectrum of the variance density
f	Relative or intrinsic wave frequency

Nomenclature

F_x	Source terms in TELEMAC (wave driving force along x-axis)
F_y	Source terms in TELEMAC (wave driving force along y-axis)
g	Gravity acceleration
H_{m0}	Significant wave heights
h	Water depth
$H_{m0,0}$	Significant wave heights with no ambient current
k	Wave number
k_x	Wave number along x-axis directions
k_y	Wave number along y-axis directions
L	Wavelength
N	Directional spectrum of wave action density
n	Sample size
P	Wave energy flux
p	Total pressure
p_{atm}	Atmospheric pressure
p_0	Exponent variable in the Westhuysen method
Q	Sink/source terms
Q_{bf}	Bottom friction induced energy dissipation
Q_{br}	Bathymetric breaking induced energy dissipation
Q_{ds}	White capping induced interactions
$Q_{ds,cur}$	Wave blocking effects when waves meet strong adverse current
Q_{in}	Wind input for wave generation
Q_{nl}	Non-linear quadruplet interactions
$S_\eta(f)$	Power spectral density of surface elevation
T_m	Mean wave period
T_p	Peak wave period
T_z	Zero-crossing wave period

u	Streamwise velocity, velocity along x-axis
U	Tidal current velocity
U_c	Relative tidal current velocity
v	Transverse velocity, velocity along y-axis
w	Vertical velocity, velocity along z-axis
x	Horizontal coordinate variable in the Cartesian system
$\bar{x}_0$	Mean value of the measurement
$x_{0\,i}$	Number ith of the measurement data
x_{m_i}	Number ith of the model simulation results
$\bar{x}_m$	Mean value of the model simulation results
y	Vertical coordinate variable in the Cartesian system
z_s	Free surface elevation

Wave-Current Decomposition (Chapter 5)

σ	Standard deviation of velocity
$\sigma_{combined}$	Standard deviation of the wave-current combined velocity, streamwise
$\sigma_{current}$	Standard deviation of the current velocity, streamwise
σ_{wave}	Standard deviation of the wave orbital velocity, streamwise
$c_j(t)$	Time series of the j^{th} IMF from EMD method
h_i	Difference between the test data and m_i
m_i	Mean values of the data covered by the upper and lower envelope
$r(t)$	Residual from EMD method
$S_U(f)$	Power spectral density of wave orbital velocity
$TI_{combined}$	Combined wave-current turbulence intensity
$TI_{current}$	Current-induced turbulence intensity
TI_{wave}	Wave-induced turbulence intensity
$TKE_{combined}$	Combined wave-current turbulence kinetic energy

$TKE_{current}$	Current-induced turbulence kinetic energy
TKE_{wave}	Wave-induced turbulence kinetic energy
U	Tidal current flow velocity
$\overline{U}$	Mean velocity
U'	Current turbulence velocity
$\widetilde{U}$	Wave orbital velocity
U'_{clean}	Pure turbulence series (with no wave effects)
${U_i}'$	Instantaneous velocity fluctuation
${U_i}'_{temp}$	Temporary dataset (a sum of the ${U_i}'$ and U'_{clean})
$\widetilde{U}_{temp}$	Temporary wave orbital velocity (containing information from U'_{clean})
U'_{temp}	Temporary current turbulence
u'	Current turbulence for streamwise velocity
$\tilde{u}$	Wave orbital velocity for streamwise velocity
${u_i}'$	Instantaneous velocity fluctuation for streamwise velocity
$x(t)$	Target data for EMD method
z	Vertical coordinate with reference to the water surface

Machine Learning (Chapter 6)

$\Omega(f_j)$	XGBoost regularization term
α	Traveling direction of tides
θ	Traveling direction of waves (denote 0 means the absence of the tidal current)
ω	XGBoost leaf weights
λ	XGBoost a parameter controls the leaf weights
γ	XGBoost complex trees
H_s	Significant wave heights (denote 0 means the absence of the tidal current)
h	Number of heads in the multi-head attention mechanism

Nomenclature

i	XGBoost the number of the data point for a specific iteration
j	XGBoost number of the decision tree
K	Keys (attention mechanism)
$\mathcal{L}(t)$	XGBoost objective function
L	Length of the input sequence
l	XGBoost loss function
Q	Queries (attention mechanism)
T	XGBoost number of leaves
t	XGBoost iteration number
V	Values (attention mechanism)
y_i	XGBoost label (or ground truth) value
$\hat{y}_i$	XGBoost predicted results

Abbreviations

2D	Two-Dimensional
3D	Three-Dimensional
ADCP	Acoustic Doppler Current Profiler
ADV	Acoustic Doppler Velocimeter
ANN	Artificial Neural Network
AOGCMs	Atmosphere-Ocean General Circulation Models
AWAC	Acoustic Wave and Current Profiler
CNN	Convolutional Neural Network
ECMWF	European Centre for Medium-Range Weather Forecasts
EDF	Electricite De France
EEMD	Ensemble Empirical Mode Decomposition
ELM	Extreme Learning Machine
EMD	Empirical Mode Decomposition
EMEC	European Marine Energy Centre
EPSRC	Engineering and Physical Sciences Research Council, UK
ERA5	ECMWF Reanalysis v5
FBProphet	FaceBook Prophet
FFT	Fast Fourier Transform
GBDT	Gradient Boosting Decision Trees
GEBCO	General Bathymetric Chart of the Ocean
GEODAS	GEOphysical DAta System
GSHHS	Global Self-consistent, Hierarchical, High-resolution Geography Database
iFFT	inverse Fast Fourier Transform
IMF	Intrinsic Mode Function

LCoE	Levelized Cost of Energy
LSTF	Long-Sequence Time-series Forecasting
LSTM	Long Short-Term Memory
MA	Moving Average filter
MAE	Mean Absolute Error
ML	machine learning
MLP	Multi-Layer Perceptron
MSE	Mean Squared Error
NetCDF	network Common Data Form
NOAA	National Oceanic and Atmospheric Administration
PFOW	Pentland Firth and Orkney Waters
PSD	Power Spectra Density
R	Pearson's Correlation Coefficient
RNN	Recurrent Neural Network
ROMS	Regional Ocean Modeling System
RSME	Root Mean Square Error
RT	relative tolerance
SAE	SAE Renewables (formerly call SIMEC Atlantis Energy)
SB	StopBand filter
seq2seq	sequence-to-sequence
SI	Scatter Index
SVR	Support Vector Regression
SWAN	Simulating WAves Nearshore
SWT	Synchrosqueezing Wavelet Transform
TI	Turbulence Intensity
TKE	Turbulence Kinematic energy
TOMAWAC	TELEMAC-based Operational Model Addressing Wave Action Computation
TPXO9	TOPEX/Poseidon Global Inverse Solution - Version 9

UTM	Universal Transverse Mercator
WCI	Wave-Current Interaction
WEC	Wave Energy Convertor
WAM	WAve Model
WGS84	World Geodetic System 1984
XGBoost	eXtreme Gradient Boosting

Chapter 1
Introduction

The oceans cover more than 70% of the Earth's surface and brought the hope of life to our planet billions of years ago. Today, under the impact of human industrial activities, greenhouse gas concentrations have surged, and global warming has become an increasingly severe problem. At this critical juncture, the oceans may once again provide a path forward for life. Beyond their ability to absorb greenhouse gases and heat, the oceans are also a source of endless renewable energy.

1.1 Background

In 2019, the UK legislated a plan to achieve net-zero greenhouse gas emissions by 2050. Replacing traditional carbon-emitting power generation technologies with 100% zero-carbon generation—relying on all available clean energy technologies—is the most feasible and cost-effective path to realize this strategy [1]. Although wind energy (especially offshore wind) and solar energy currently provide the main sources of renewable energy in the UK, and their generation in 2050 is expected to fully cover the nation's electricity demand [2], their power generation capacities are affected by seasonal and weather variations, leading to intermittency and instability. Therefore, it remains necessary to develop other forms of renewable energy systems to achieve a diversified generation mix and maximize the balance of power supply.

As one of the world’s wealthiest nations in ocean energy resources, the UK government acknowledges that the high wave energy density and 100% predictable tidal energy can offer an important solution. Although these ocean energy technologies are still expensive and in the early stages of development (not yet fully commercialized) compared to other forms of clean energy, the UK has been at the forefront of research, innovation, development, demonstration, and deployment in this field for the past few decades. Continued investment in ocean energy by public sectors, led by the Scottish and Welsh governments [3,4], is expected to drive breakthroughs and transformative changes in current technologies, injecting new

momentum into the UK's 2050 zero-carbon plan and bringing value to other coastal countries with the potential to develop ocean energy.

1.1.1 Ocean energy

Ocean energy generation encompasses multiple forms, including wave, tidal range, tidal and ocean currents, ocean thermal energy, and salinity gradient energy [5]. Among these, wave energy and tidal current energy (also called tidal stream energy) are of greatest potential for development.

1.1.1.1 Wave energy

Wave energy is primarily driven by wind and can accumulate over long distances. Combined with the high density of seawater, this results in wave energy having the highest energy density among all renewable energy resources [6,7]. It is relatively accessible to coastal nations, whether in nearshore areas of the mainland or in remote island regions. Theoretically, the global wave energy potential (29,500 TWh/year) is sufficient to meet the world's annual electricity demand (26,700 TWh) [8].

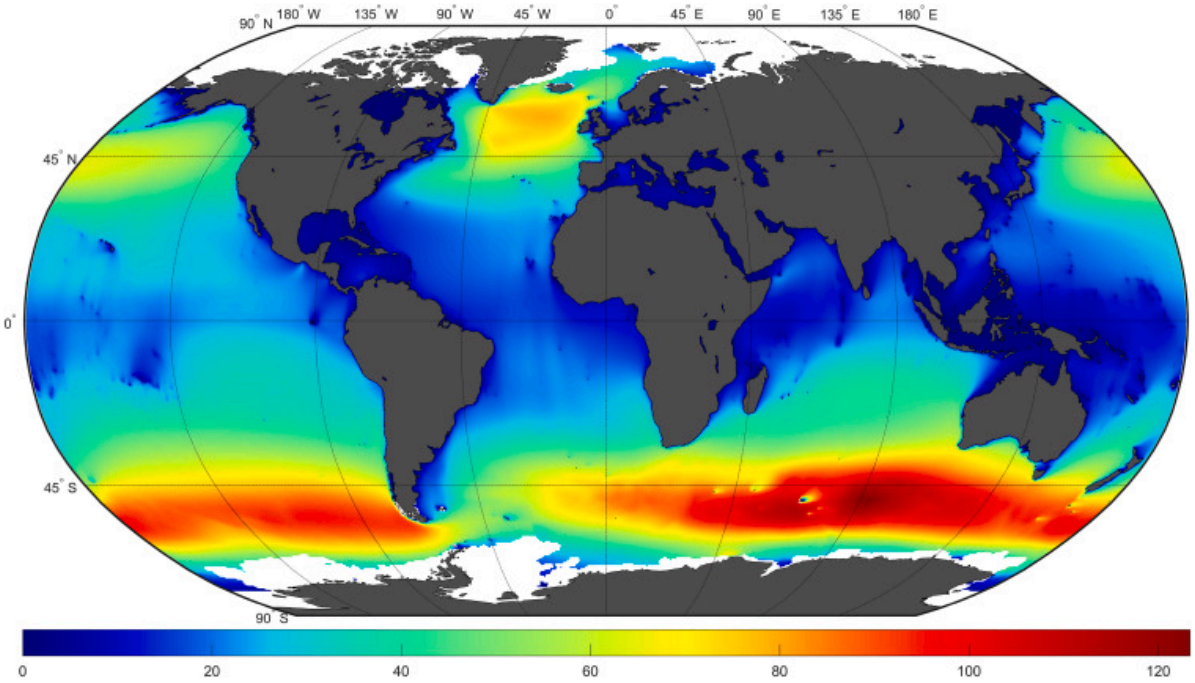

Figure 1.1 Globale mean wave power (kW/m) over the 40-year period from 1979 to 2019

The wave power is calculated using ECMWF ERA5 data, as described in [9].

The northeastern Atlantic Ocean possesses the richest wave energy resources in the Northern Hemisphere, as shown in Figure 1.1 [9]. The UK, situated in this region, accounts for 35% of

Europe's total wave energy potential [10]. If fully harnessed, these resources could supply 15% of the UK's current electricity demand [8]. Scotland, with an estimated 15 GW of wave energy capacity [11], stands out as the UK's most resource-rich area. Its western coast features an average annual wave power of up to 80 kW/m [8]. Notable regions like the North Sea, Shetland Islands, Pentland Firth and Orkney Waters, and the Hebrides Islands have been leased by The Crown Estate for wave energy development projects [8,12].

Despite its high energy density and abundant resources, wave energy development lags significantly behind other ocean energy forms, such as tidal energy. This delay stems from the high technical demands imposed by complex and dynamic wave and marine environments [13]:

1. The irregularity of wave amplitude, phase, and direction challenges the ability of devices to achieve optimal efficiency within the excitation frequency range.

2. Extreme conditions, such as storms, can impose loads on structures far exceeding their design capacity.

3. Converting the slow, irregular motion of waves into electricity requires generators capable of operating at frequencies approximately 500 times higher.

These technical challenges are compounded by the lack of a standardized mainstream technology for commercial development. Currently, various types of wave energy converters exist, such as attenuator systems, oscillating water column systems, overtopping/terminator systems, and point absorber systems, including hybrid configurations [14,15], yet no single design has emerged as dominant. This diversity led to a dispersion of research focus and slowing technological iteration.

Wave energy experienced a period of rapid development around 2010, but the industry suffered significant setbacks with the bankruptcy of prominent projects like Pelamis and Oyster around 2014/2015 due to insufficient funding [8,16]. These failures highlight the mismatch between financial and technological drivers, forcing developers to undertake costly large-scale demonstrations prematurely.

In response, Wave Energy Scotland (WES) [3], established by the Scottish Government in 2014, adopted a more structured and innovative approach. By shifting from designing complete technology pathways to developing components compatible with multiple wave energy systems, WES has helped consolidate research efforts and improve the applicability of innovations across various projects.

The wave energy industry, having learned from past failures, is now poised for greater success. Promising developers such as Scotland-based Mocean Energy [17] and AWS Ocean Energy [18] have regained investor confidence. Moreover, Sweden's CorPower Ocean [19] demonstrated commercial-scale wave energy technology in Portugal in 2023. Surviving extreme 18.5m high waves in November 2023 [20], their technology showcased resilience and efficient power generation in marine environments, offering hope for wave energy commercialization.

The UK's Engineering and Physical Sciences Research Council (EPSRC) and the 2020 Wave Energy Roadmap present an optimistic vision. They outline achieving a levelized cost of energy (LCoE) of £90/MWh by 2035 (down from £300/MWh in 2018) and installing 22 GW of wave energy capacity by 2050 [8]. This roadmap underscores the growing potential of wave energy as a critical component of the UK’s renewable energy mix.

1.1.1.2 Tidal current energy

Tidal currents are concentrated in narrow straits and inlets, around headlands, and in channels between islands. Generated by the gravitational forces exerted by the sun and the moon, tidal currents are unaffected by weather variations, making them 100% predictable and among the most reliable renewable energy sources [21]. This predictability can play a crucial role in stabilizing the electrical grid.

The primary technology for tidal current power generation is similar to wind power, where fluid flows drive horizontal-axis turbines, converting kinetic energy into mechanical energy for electricity production. The key difference lies in the medium driving the turbines—tidal currents, with a density approximately 1,000 times that of air, compared to wind. While tidal current speeds are generally lower than wind speeds, the energy density advantage of seawater results in a much higher energy output. Coupled with the continuous, year-round generation of tidal currents, this technology offers a more stable energy supply than the intermittent nature of wind power.

Scotland is widely recognized as the global leader in tidal energy development. This success stems not only from its abundant tidal current resources but also from strong governmental and financial support. Specifically, the resources around Scotland are estimated at 32 TWh annually, accounting for 25% of Europe’s tidal energy resources and capable of meeting Scotland’s entire annual electricity demand (24 TWh) [22]. Meanwhile, Scotland has fostered

numerous world-leading tidal energy projects, including the world's largest tidal current array, MeyGen [23], and the most powerful tidal turbine, the Orbital O2 [24].

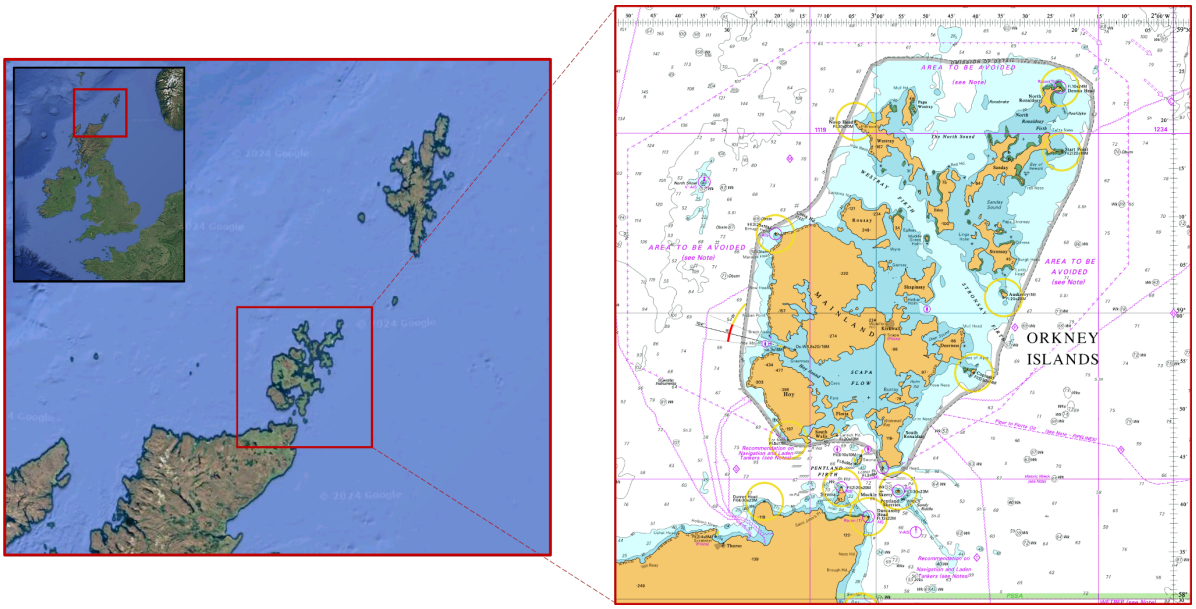

Figure 1.2 Geographical location of PFOW

Left map sources from https://www.google.com/maps; right map sources from https://digimap.edina.ac.uk/.

Despite its potential, tidal energy development is currently hindered by high installation and maintenance costs, urgently requiring a cost reduction turbine technology and a complete supply chain. However, the dominant tidal energy conversion technologies are well-established, leading to a more focused research direction in both academia and industry. Combined with the stable energy characteristics of tidal currents, this focus positions tidal energy as a likely candidate to achieve commercialization earlier than wave energy.

According to Ocean Energy Europe, the LCoE for tidal energy is expected to decrease to €90–100/MWh by around 2030 [25], comparable to the LCoE of offshore wind energy during the 2018–2019 period [26]. This projection highlights the significant potential of tidal energy as a competitive and sustainable energy source.

1.1.2 Pentland Firth and Orkney Waters (PFOW)

The preceding discussion highlighted Scotland's wealth of ocean energy resources, with one of the most promising areas being the Pentland Firth and Orkney Waters (PFOW), thanks to its exceptional geographic advantages, as shown in Figure 1.2.

1.1.2.1 PFOW wave energy resources

The west coast of the Orkney Islands faces the North Atlantic Ocean and is exposed to predominantly south-westerly winds originating from eastern Canada or southern Greenland. These conditions create significant and consistent swell waves [27], resulting in an annual mean wave power of approximately 31 kW/m along the western coast of the Orkney Islands [16]. Leveraging this abundant wave energy, the globally renowned European Marine Energy Centre (EMEC) has established two wave energy test sites in the region: Scapa Flow, south of Kirkwall, and Billia Croo, off the west coast of mainland Orkney [28,29].

As one of the world's premier at-sea test centres, EMEC provides facilities for wave energy converter developers to deploy devices, evaluate power production, and monitor device survivability under various wave conditions. Prominent wave energy developers such as LAMINARIA [30], AWS [18], Mocean [31], and CorPower [32] have recently conducted projects at these sites, advancing wave energy technology.

1.1.2.2 PFOW tidal current energy resources

Beyond its wave resources, the Orkney region is perhaps best known for its dramatic tidal energy potential, boasting some of the fastest tidal currents in the world. With over 70 islands, the region's unique geography creates ideal conditions for rapid tidal flows, often exceeding speeds of 2.5 m/s [16]. Specifically for the Pentland Firth, which is located between the Orkney Islands and the Scottish Mainland and serves as a natural channel connecting the North Atlantic and the North Sea, tidal speeds can surpass 5 m/s [33].

The Crown Estate has granted leases for nine tidal energy sites within PFOW [12,16]. EMEC has also established two tidal test sites: Shapinsay Sound, northeast of Kirkwall, and the Fall of Warness. Additionally, the world's largest tidal array, MeyGen Phase 1, has been deployed in the Inner Sound of the Pentland Firth. It consists of four 1.5 MW tidal turbines, which have successfully operated for six consecutive years and generated a cumulative 70 GWh of electricity as of November 2024 [23]. Meanwhile, the world's most powerful tidal turbine, the Orbital O2, with a 2 MW capacity, operates at Fall of Warness and is estimated to supply electricity to 2,000 households annually [24].

These achievements demonstrate the region's unparalleled potential for wave and tidal energy development, solidifying its reputation as a global leader in marine renewable energy.

1.1.3 Wave-current interactions

As discussed earlier, the PFOW region boasts abundant wave and tidal energy resources, with active waves and strong tidal currents often coexisting. This naturally gives rise to significant wave-current interaction (WCI) phenomena.

1.1.3.1 Effects of tidal currents on waves

Theoretically, WCI can profoundly impact wave parameters through both kinematic and dynamic mechanisms [34]. Kinematically, tidal currents influence waves through the dispersion relation (via Doppler shifts), which alter the intrinsic wave frequency and wavelength. These changes depend on whether the current flows in the same direction as the wave propagation (following current) or in the opposite direction (opposing current). The effects also vary under homogeneous or inhomogeneous, steady or unsteady flows. Dynamically, WCI influences wave energy and action conservation, leading to variations in wave height and average wave levels. The detailed physical mechanisms of these effects are discussed further with numerical modelling observations in Section 3.2.

One notable example of WCI affecting wave parameters is along the southeastern coast of South Africa, where the Agulhas Current creates dangerous rogue waves that pose serious threats to vessels [35]. In the Albufeira lagoon, Portugal, the currents can increase the wave height at the mouth of the tidal inlet up to 20% [36]. The WCI can also be significant in the open sea where the open-ocean tidal current is strong. For instance, studies along Norway's northern coast found tidal modulation of wave height reaching up to 90% [37]. Despite the observed and theoretical impacts of tidal currents on wave parameters, there remains a widespread lack of consideration for tidal effects in wave energy assessments.

1.1.3.2 Effects of waves on tidal currents

The WCI can also affect the tidal current flows through (1) wave radiation stress (noticeable at the very near shore region), and (2) enhanced bottom friction coefficient due to the interaction of waves with the current boundary layer [34,38]; while the second mechanism can predominantly explain the majority phenomenon of WCI in tidal currents.

To be specific, larger waves induce greater oscillatory motion of water particles, leading to near-bed turbulence and resulting in more pronounced shear stress. This interaction amplifies turbulence levels in the upper meters of water column [39,40] and reduces tidal current speeds [34,41]. Since the tidal power is proportional to the velocity cubed, such reduction may

dramatically diminish tidal energy resources. Research has shown that tidal energy resource may decrease up to 15% and 20% under mean and extreme winter wave scenario at the northwest headland of Anglesey in Wales [38], and up to 59% during peak flood tides in an idealised headland case study [41].

In some cases, steeper waves may break, injecting additional energy into the water column through air entrainment and vortex formation, further increasing turbulence of the flow [42,43]. WCI thus enhances energy transfer and shear stress alterations, particularly in shallow regions where larger waves can stir the seabed more vigorously, especially during high tide conditions [44].

Despite the critical nature of WCI, wave and tidal currents are often treated as independent phenomena in resource assessments, with limited consideration of their interactions. As previously mentioned, the high cost of ocean energy development is a major challenge. Neglecting WCI during resource assessments can result in inaccurate estimates of complex marine conditions, leading to higher equipment failure rates and increased maintenance costs. This oversight could ultimately jeopardize the fragile progress of marine energy development. Addressing WCI in resource evaluations is essential to mitigating risks and ensuring the long-term viability of ocean energy technologies.

1.2 Research objectives

The PFOW region is characterized by the coexistence of strong waves and tidal currents. An accurate assessment of WCI on both wave resources and tidal current flows in this region can significantly benefit the development of the ocean energy industry.

Hence, this research focuses on quantifying the effects of WCI on waves and tidal currents through three approaches: (1) **Numerical modelling** to investigate WCI effects on wave parameters and wave energy resources; (2) **Wave-current decomposition methods** to quantify the waves contributions on enhancing turbulence levels of tidal current flows; (3) **Machine learning techniques** to predict wave parameters in open sea and strait regions where WCI is significant.

Although these tasks address different aspects of WCI, they are inherently interconnected:

- Numerical modelling results provide a critical reference for validating wave components separated via the wave-current decomposition method.

- Numerical modelling data also serves as the training dataset for machine learning approaches to predict wave parameters.
- This integrated approach ensures a comprehensive understanding of WCI effects, bridging theoretical insights with practical applications to support marine energy development in PFOW.

The specific research objectives for each task are outlined below.

1.2.1 Numerical modelling

- Construct a large-scale wave model for the North Atlantic region using an open-source spectral wave model (e.g., TOMAWAC) to provide accurate wave boundary conditions for regional models and wave parameters unaffected by tidal currents.
- Develop a regional wave-current coupled model for PFOW region using TOMAWAC and TELEMAC flow model to simulate wave parameters by including tidal current effects.
- Quantify the impact of tidal currents on wave parameters by comparing wave conditions with and without tidal current interactions and identify the mechanisms driving these differences.
- Produce long-term, high-resolution wave maps for PFOW region, incorporating tidal currents, and compare it to maps that neglect WCI to assess the resource differences due to WCI.

1.2.2 Wave-current decomposition

- Develop an efficient wave-current decomposition method to separate wave orbital velocity and tidal current velocity from field-measured flow data in wave-current coexisting environments.
- Derive depth-wise turbulence profiles for original measurements, separated tidal current components, and wave velocities, quantifying the turbulence enhancement caused by waves.

1.2.3 Machine learning based wave prediction

- For open-sea waves (minimal WCI influence): Apply machine learning techniques, such as the Informer deep learning model, XGBoost algorithm, and their integration, to achieve accurate and fast predictions of wave parameters from wind data.

- For waves in WCI environments: Use machine learning methods, such as the Informer deep learning model, to accurately predict wave parameters by integrating wind wave data and tidal current data.

1.3 Contribution to knowledge

This research provides invaluable insights to the understanding of WCI, advancing knowledge through three primary areas: ocean numerical modelling, wave-current decomposition, and machine learning driven wave prediction.

1.3.1 Ocean numerical modelling and wave resource assessment

Pioneering the use of TOMAWAC for North Atlantic wave simulations: This study is the first to employ the TOMAWAC spectral wave model to simulate waves across a North Atlantic-scale domain. It demonstrates the effectiveness of this less commonly used numerical model in diverse environments, including oceanic, coastal, and estuarine regions.

Developing the first open-source-software-based wave-current coupled model for the Orkney region: This model eliminates licensing barriers, offering a reliable tool for studying WCI. The detailed model construction process, including parameter selection, serves as a valuable reference for future researchers using the same software.

Validating the North Atlantic wave model at a 10-year scale: The model is validated using data from four wave buoys, showcasing its robust capability to provide accurate interannual hindcast generation and wave boundary conditions for regional-scale numerical models across Scotland.

Validating the wave-current model for a 135-day period: The model's ability to accurately reproduce wave and tidal current parameters affected by WCI is confirmed through extensive comparisons with AWAC and ADCP measurements at two geographically distinct sites. These validations span both low-wave summer conditions and high-wave winter conditions.

Comprehensive analysis of WCI at diverse locations: By analysing eight sites with varying tidal and wave conditions, the study bridges theoretical WCI concepts and real-world observations, offering a detailed understanding of tidal current effects on wave parameters.

Producing a high-resolution, long-term wave resource map: This is the first long-term map for PFOW that incorporates tidal effects, quantifying the spatial differences in wave resources caused by WCI.

Creating a 10-year wave and tidal current dataset: This extensive database supports future WCI studies, provides a robust foundation for coastal hazard research, and serves as a training dataset for AI-driven predictions of high-resolution wave parameters in complex geometric environments.

1.3.2 Wave-current decomposition and turbulence analysis

Introducing a novel side-information-assisted EMD method: This innovative approach incorporates turbulence data into original input signals, improving the separation of wave and current components from tidal flow velocity.

Deriving vertical turbulence profiles: For the first time, turbulence intensity profiles for wave-only, current-only, and combined wave-current velocities are quantified, providing specific values for turbulence enhancement due to wave presence.

Turbulence analysis for three-dimensional (3D) velocities: This study provides the first 3D turbulence intensity profiles, revealing the effects of WCI on streamwise, transverse, and vertical velocities.

Comprehensive analysis methods: The research combines time-series and histogram analyses to provide a robust quantification of WCI effects on turbulence.

1.3.3 Machine learning-based wave prediction

Demonstrating the effectiveness of advanced AI models: The study highlights the efficiency of the Informer deep learning model and XGBoost machine learning algorithm in accurately predicting wave parameters in open-sea regions using spatiotemporal wind inputs.

Developing novel fusion strategies for AI models: The research proposes innovative methods to integrate Informer's temporal analysis capabilities with XGBoost's feature regression strengths. Strategies include:

- Using XGBoost prediction results as additional input features for the Informer model.
- Combining XGBoost predictions with Informer’s encoder outputs via attention mechanisms.

- Combining XGBoost predictions with Informer's decoder outputs via attention mechanisms.

High-quality predictions for WCI environments: For the first time, the Informer model achieves accurate wave parameter predictions in regions with significant WCI effects.

Unified and reliable training data: The training dataset is derived from validated numerical models developed by the author, ensuring consistency and reliability of the results.

Overall, this research contributes to advancing the scientific understanding and practical applications of WCI. It bridges gaps between theory, observation, and prediction, offering valuable tools and methodologies for the sustainable development of ocean energy.

1.3.4 Broader significance and influence

These contributions not only support the advancement of ocean renewable energy but also have broader implications for coastal hazard assessment and the improvement of atmosphere–ocean general circulation models (AOGCMs).

1.3.4.1 Contribution to coastal hazard modelling

While previous studies [45,46] have highlighted the importance of wave–current interaction (WCI) in modulating nearshore wave heights and flood risk, such analyses are typically limited to short-term events or specific regional contexts. In contrast, through a decadal-scale simulation, this work demonstrates that strong tidal currents can systematically amplify extreme wave conditions, particularly when wave propagation aligns with tidal flow. This finding shows that the influence of WCI on extreme sea states is not merely episodic but can be persistent and climatologically significant.

This insight improves the current understanding of hazard exposure in tidally energetic regions and has several practical implications: (1) For coastal and offshore infrastructure design, this work supports the need to account for coupled wave–current effects when estimating extreme wave loading conditions. (2) For operational forecasting and early warning systems, the results provide evidence that incorporating wave–tide interactions can improve the accuracy of hazard predictions during compound events.

1.3.4.2 Contribution to AOGCMs

AOGCMs are fundamental tools for global climate projections, yet they often simplify or entirely omit WCI, especially in coastal and shelf regions. This simplification contributes to persistent model biases in variables such as sea surface temperature, wind stress, and upper-ocean turbulence [47]. Through high-resolution simulation and detailed characterisation of wave–current coupling, this work offers physically based insights that can support the parameterisation of wave–tide processes in global models.

For instance, this study complements the findings [48], who demonstrated that wind bias correction alone is insufficient to improve wave modelling accuracy in regions like southeast Australia. This work advances further by showing how WCI dynamically reshape wave energy spectra and turbulence characteristics, providing a mechanism-based justification for refining surface boundary layer processes in AOGCMs. By quantifying the role of tidal currents in modulating wave breaking, energy dissipation, and directional spreading, the results presented here can inform the development of improved coastal coupling schemes, ultimately enhancing the realism of air–sea fluxes and climate feedback in global ocean–atmosphere systems.

1.4 Thesis outline

The thesis consists of seven chapters and three appendices. **Chapter 2, 3** and **4** are about the numerical modelling; **Chapter 5** is about wave-current decomposition; **Chapter 6** is about the machine learning-based wave predictions; **Chapter 7** provides an overall summary and suggestions for future work. The detailed structure is as follows:

Chapter 1 provides the research background and outlines the research objectives and contributions to knowledge, providing an overview of the thesis structure.

Chapter 2 introduces the fundamental principles of the numerical models used in this research, including the TOMAWAC spectral wave model and the TELEMAC flow model. It details the construction of the North Atlantic scale wave-only model and the regional scale wave-current coupled model. Validation against field measurements from wave buoys, Acoustic Wave Current Profilers (AWAC), and Acoustic Doppler Current Profilers (ADCP) is presented.

Chapter 3 presents a detailed comparison of wave simulation results from wave-only and wave-current coupled models. Parameters such as significant wave heights, mean and peak

wave periods, mean wave directions, directional and unidirectional wave spectra are analysed. Eight representative locations across PFOW with varying wave and tidal conditions are selected for case studies to assess tidal current effects.

Chapter 4 provides a long-term wave map (of the years 2014–2023) for the Orkney Waters, derived from the wave-only and wave-current coupled models. It includes annual, seasonal, and monthly mean values of significant wave heights and wave power, as well as maps of extreme conditions over the decade. The impact of tidal currents on wave energy resources is illustrated through maps showing numerical and ratio differences between the two models.

Chapter 5 introduces a novel wave-current decomposition strategy based on the Empirical Mode Decomposition (EMD) method, applied to field measurements to investigate turbulence levels. It begins with an overview of the field data, explains the decomposition method using side turbulence information, and outlines validation approaches. Turbulence statistics for wave-only, current-only, and wave-current combined data are presented for streamwise, transverse, and vertical flows across three sites in the Pentland Firth.

Chapter 6 explores machine learning methods for wave prediction. It introduces the principles of the XGBoost algorithm and the Informer deep neural network. These methods are applied to predict wave parameters at four open-sea sites using wind inputs, with attempts to integrate both models for improved accuracy. Additionally, modifications to the Informer model for predicting wave parameters in wave-current environments are discussed.

Chapter 7 summarizes the research findings for the three main tasks: numerical modelling, wave-current decomposition, and AI-based wave prediction. Recommendations for future research directions are provided for each area.

Appendix A provides detailed input and output information for the wave and wave-current models, including model construction processes and potential reasons for simulation failures (supporting Chapter 3).

Appendix B contains supplemental figures and tables, including the hindcast validation of the wave-only model across ten years (supporting Chapter 3 and 5) and monthly wave maps of significant wave heights and wave power from 2014 to 2023 (supporting Chapter 5).

Appendix C gives a list of conference and journal publications resulting from this research.

Chapter 2
Numerical Modelling of Ocean Waves and Tidal Currents

This chapter details the construction of the North Atlantic-scale wave model using TOMAWAC and the regional-scale wave-current model utilizing TOMAWAC and TELEMAC 3D. A step-by-step guide to the model construction process is provided in Appendix A.

The models developed in this chapter are validated against reliable field measurements, including data from wave buoys, AWAC, and ADCP. These validated models form the foundation for the research presented in Chapter 3 and Chapter 4.

2.1 Introduction

2.1.1 Wave modelling for PFOW

The most popular and accurate approach of wave resource assessment remains numerical simulation using the third-generation spectral wave models, in which WAM [49], WAVEWATCH III [50], and MIKE21-SM [51] are commonly used for ocean-scale modelling, while SWAN [52] is preferred for wave simulation in coastal or estuarine areas.

For applications specifically focused on Scotland or the waters around the Orkney Islands, Bertotti and Cavaleri [53] developed a WAM wave model with a resolution of 1/50° (approximately 2 km). Their research highlighted the importance of using a two-dimensional input wave spectrum at the model grid boundaries. Similarly, Gleizon and Woolf [54], as well as Gleizon and Murray [55], constructed wave models with SWAN, applying the two-dimensional wave spectrum from the large-scale WaveWatch III model as boundary conditions. They demonstrated that swell can propagate over long distances, affecting wave energy levels in the central area of the model. Neill al et. [17] developed a regional-scale SWAN wave model for the Orkney waters, with a two-dimensional wave boundary derived from a coarser North Atlantic

SWAN model. This study highlighted interannual and seasonal variability in wave resources over a ten-year period (2003-2012), providing valuable high-resolution wave statistics for the region. Venugopal al et. [56,57] utilized the MIKE21 to create a North Atlantic scale model with finer subgrids for Scottish and Orkney waters. They achieved a significant correlation (over 0.94) for significant wave heights at five validation points across one year. Their model incorporates a WEC array to assess the impact of large-scale energy extraction on sea state distribution around the farm. Additionally, Lavidas et al. [58] applied the SWAN model to generate an 11-year (2004-2014) wave dataset, refining previous wave charts and resource estimates.

2.1.2 Wave simulation with tidal current effects

While numerical modelling of waves in the Orkney region is well-researched, studies considering the tidal effects are relatively limited, as wave and tidal current phenomena are often simulated independently using different software. This simplification overlooks the intricate coupling between waves and currents, which can significantly affect wave parameters.

Nevertheless, insightful studies have explored it in the past decade. Saruwatari et al. [33] used tidal data obtained from the MOHID Water Modelling System as input for the SWAN model to study the impact of tidal currents around Orkney Waters. They found that when waves and tidal currents move in opposite directions, wave heights can increase by 150-200%, with wave power rising by over 100 kW/m. In the Adriatic Sea, a two-way coupled ROMS and SWAN model was developed, revealing that neglecting the tidal currents could lead to wave power estimation errors of up to 30% [59,60]. Similarly, Venugopal et al. [56,61] developed a two-way coupled wave-current model using MIKE 21 and MIKE 3 for Orkney region, incorporating wave boundary conditions from a North Atlantic wave model. Their results showed significant modulation of wave height, period, and direction by tidal currents compared to a wave-only model [62,63]. Hopkins et al. [64] developed a coupled SWAN-Delft3D model for the southern shore of Martha's Vineyard, US, and found that tidal currents modulated wave direction by ±35°, primarily due to tidal refraction rather than water level changes. Guillou [65] used TELEMAC 2D results in the SWAN model. It is observed that significant wave height at the northern entrance of Fromveur Strait in France varied by up to 30% with tidal effects, with wave power increasing by more than 100%.

Despite these advancements, gaps persist. Most wave models undergo extensive calibration, often exceeding a month or even a year at multiple locations. In contrast, wave-current coupled models rarely receive such thorough validation, often limited to brief weekly calibrations.

Furthermore, wave-current coupled models are typically applied over short timeframes, lacking long-term statistics to reveal monthly or seasonal tidal effects. This limitation is likely due to the significant computational resources required for such models. One unique example of long-term tidal influence simulation is made by Webb et al. [66], who conducted a 21-year WAVEWATCH III simulation for Japan, incorporating tidal currents from JCOPE2. While their research provided valuable insights into long-term wave-current interactions, it lacked wave calibration under tidal effects, affecting the reliability of the results. Additionally, their simulation required 35 days of supercomputer time, making replication in other regions challenging.

2.1.3 Solution from TOMAWAC and TELEMAC

This study addresses these gaps by developing a two-way coupled wave-current model, validated with field measurements over a cumulative 135 days across two geographically distinct sites in the Orkney Waters, showcasing its strong generalization capabilities. By applying open-source software with efficient computational requirements, this approach ensures replicability in other places. Specifically, the feasibility of this research relies on using the TOMAWAC wave model and the TELEMAC tidal flow model within the open-source Telemac system. TOMAWAC [67] is a reliable third-generation spectral wave model, capable of handling wave simulations for oceans, inland seas, and coastal areas. While less popular comparing to the previously mentioned wave models, partly due to its command-line interface and its common use as a submodule of the TELEMAC flow mode rather than a standalone solution, TOMAWAC has actually demonstrated strong predictive accuracy. For instance, in the Iroise Sea, France, it outperformed SWAN in estimating wave power due to its direct calculation of total energy flux, avoiding the approximations inherent in SWAN's default methods that can underestimate wave power by up to 15% [68]. Regarding the TELEMAC flow model, it has been widely applied in the Orkney Waters and is proved to be able to accurately simulate the tidal flows in this region [69,70].

The coupling between TOMAWAC and TELEMAC shares a common unstructured mesh, which offers several advantages for regional scale modelling. The unstructured mesh provides flexible multiresolution capability, allowing finer mesh refinement in areas of interests or regions with complex geometric features. Although this refinement may incur higher computational cost per node compared to structured meshes, the unstructured approach can reduce the overall number of nodes by applying coarser resolution in deep-water or open-sea regions, thereby effectively balancing computational demand [71,72]. The unstructured mesh also additionally enables improved representation of bathymetry, which can change rapidly in nearshore regions [71]. Furthermore, the use of a shared mesh between both models eliminates

the need for interpolation during dynamic interactions between wave and tidal current simulations, thereby furtherly enhancing consistency and computational efficiency. The TOMAWAC-TELEMAC coupled model was successfully applied in the northwestern headland of Anglesey, Wales, UK, to assess the wave effects on tidal currents [38].

2.2 Model overview

2.2.1 TOMAWAC spectra wave model

TOMAWAC simulates wave propagation by solving the time-dependent wave action balance equation in Cartesian coordinates system (x, y) [73],

$$\frac{\partial N}{\partial t} + \frac{\partial(\dot{x}N)}{\partial x} + \frac{\partial(\dot{y}N)}{\partial y} + \frac{\partial(\dot{k_x}N)}{\partial k_x} + \frac{\partial(\dot{k_y}N)}{\partial k_y} = Q(k_x, k_y, x, y, t) \tag{2.1}$$

where the (k_x, k_y) in the balance equation represent the wave number k vector along the x and y directions; N is the directional spectrum of wave action density and is usually used to describe the waves in unsteady or inhomogeneous medium. The definition equation of N is

$$N(\sigma, \theta) = \frac{F(\sigma, \theta)}{\sigma} \tag{2.2}$$

in which F is the directional spectrum of the variance density; σ and θ represent relative or intrinsic angular frequency and the wave propagation directions in radians, respectively. F is furtherly defined by $F(\sigma, \theta) = E(\sigma, \theta)/\rho g$, with E is the directional spectrum, ρ is the water density, and g is the acceleration due to gravity.

Equation (2.1) demonstrates that the wave action is preserved to within the source and sink terms Q, which in this study is described by

$$Q = Q_{in} + Q_{ds} + Q_{nl} + Q_{bf} + Q_{br} + Q_{ds,cur} \tag{2.3}$$

where Q_{in} is wind input for wave generation, Q_{ds} is white capping induced interactions, Q_{nl} is non-linear quadruplet interactions, Q_{bf} is bottom friction induced energy dissipation, Q_{br} is bathymetric breaking induced energy dissipation and $Q_{ds,cur}$ represents the wave blocking effects when waves meet strong adverse currents, which in this study is only enabled when coupling with the TELEMAC tidal flow model.

Specifically, the way to simulate this enhanced breaking dissipation by strong current relies on the Westhuysen method [74]

$$Q_{ds,cur} = -C_{ds,cur}\max\left[\frac{C_\sigma(\sigma,\theta)}{\sigma}, 0\right]\left(\frac{B(k)}{B_r}\right)^{p_0/2} F(\sigma,\theta) \tag{2.4}$$

in which the spectral saturation level $B(k)$ as a ratio of the threshold level B_r determines the dissipation level and can be enhanced by the factor C_σ/σ where C_σ is the wave propagation velocity. When $B(k) > B_r$ wave breaks and the function to determine the exponent of p_0 can be found in [73,75]; while when $B(k) < B_r$ there is no breaking by having $p_0 = 0$. In this study, the most critical parameter for determining enhanced breaking is $C_{ds,cur}$ and is set as 5.2 after a detailed sensitivity analysis. Notably, this value is far larger than the default value of 0.65 which would result in overestimated wave heights. A similar finding of using a value of 5 was reported in [36]. Other parameters are kept at their default settings.

The wave parameters, such as the significant wave heights (H_{m0}), zero-crossing wave periods (T_z), and the peak wave periods (T_p) are directly output from the model through the spectra moment methods. The detailed definition equation of them can be found in the TOMAWAC manual [73]. It is worthy to highlight the unit wave power rate or the wave energy flux (P), which is also a direct output of the model, is computed from the total energy transport [68]

$$P = \rho g \int_0^{2\pi}\int_0^{\infty} C_g F \, d\sigma \, d\theta \tag{2.5}$$

where C_g is the relative or intrinsic wave group velocity. Notably, though the numerical resolution of equations (from Equation (2.1) to (2.5) when frequency is involved) used the relative or intrinsic frequency (i.e., the frequency being observed in a coordinate system moving at the velocity of the current, for which linear wave theory applies), the final output of the model is transferred to the absolute frequency (i.e., the frequency observed from a fixed coordinate system) and can be directly used in the real world.

2.2.2 TELEMAC flow model

TELEMAC 2D and 3D are designed for the simulation of the flow velocity field. This study utilized the TELEMAC 3D module with two layers only (i.e., bottom and surface layers) with no intermediate layers, for the purpose of accelerating the simulations for longer-term. While this simplified two-layer configuration does not affect the accuracy of free surface elevation or water depth, it restricts the output to surface, bottom, and depth-averaged horizontal velocity components, thereby reducing the resolution of the three-dimensional velocity field. However, given that the focus of this research is on surface wave dynamics, the associated loss in 3D velocity detail is not expected to significantly impact the wave-related results. The accuracy of the wave simulation is ensured through thorough model calibration and validation. The TELEMAC 3D solves the 3D Navier-Stokes equations with a free surface, expressed by [76]

$$\frac{\partial u}{\partial x}+\frac{\partial v}{\partial y}+\frac{\partial w}{\partial z}=0 \tag{2.6}$$

$$\frac{\partial u}{\partial t}+u\frac{\partial u}{\partial x}+v\frac{\partial u}{\partial y}+w\frac{\partial u}{\partial z}=-g\frac{\partial u}{\partial x}+\upsilon\Delta(u)+F_x \tag{2.7}$$

$$\frac{\partial v}{\partial t}+u\frac{\partial v}{\partial x}+v\frac{\partial v}{\partial y}+w\frac{\partial v}{\partial z}=-g\frac{\partial v}{\partial x}+\upsilon\Delta(v)+F_y \tag{2.8}$$

$$p=p_{atm}+\rho_0 g(z_s-z)+\rho_0 g\int_z^{z_s}\frac{\Delta\rho}{\rho_0}dz' \tag{2.9}$$

in which, u, v, and w are the three-dimensional components of velocity; x, y and z are the 3D coordinates, υ is the kinematic viscosity, F_x and F_y are the source terms (which in this research are the wave driving force), p and p_{atm} are the total pressure and atmospheric pressure respectively, z_s is the free surface elevation, ρ_0 and $\Delta\rho$ are the reference density and the variation of density around it respectively.

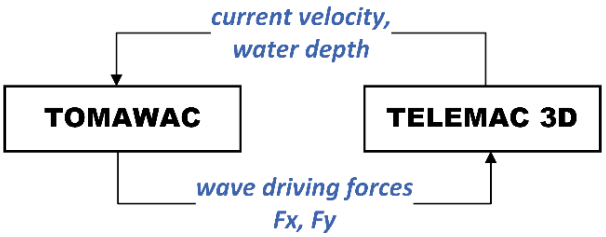

Figure 2.1 Bi-directional simulation between TOMAWAC and TELEMAC 3D

The capability to conduct interactive simulations between TOMAWAC and TELEMAC is provided by their integration within the same software, which is achieved through the definition of a set of parameters outlined in their manuals [73,76]. During the bi-directional coupling between TOMAWAC and TELEMAC, updated values of current velocity and water depth (or surface elevation, which includes the effects of tidal elevation) are transmitted from TELEMAC to TOMAWAC, while the updated values of wave driving forces F_x and F_y acting on the current are transferred from TOMAWAC to TELEMAC [73], as demonstrated in Figure 2.1

2.2.3 Metrics of performance

In order to show the match quality between the hindcast produced by the numerical modelling and the real measurement, Pearson's Correlation coefficient (R), Bias, Normalized Bias, Root Mean Square Error (RMSE), and Scatter Index (SI) are utilized in this study. The definition equations of them are given as below:

$$\bar{x}_0 = \frac{1}{n}\sum_{i=1}^{n} x_{0_i} \tag{2.10}$$

$$\bar{x}_m = \frac{1}{n}\sum_{i=1}^{n} x_{m_i} \tag{2.11}$$

$$R = \frac{\sum_{i=1}^{n}\left[(x_{0_i} - \bar{x}_0)(x_{m_i} - \bar{x}_m)\right]}{\sqrt{\sum_{i=1}^{n}\left[(x_{0_i} - \bar{x}_0)^2 (x_{m_i} - \bar{x}_m)^2\right]}} \tag{2.12}$$

$$Bias = \frac{1}{n}\sum_{i=1}^{n}(x_{0_i} - x_{m_i}) \tag{2.13}$$

$$Normalized\ Bias = \frac{Bias}{\bar{x}_0} \tag{2.14}$$

$$RMSE = \sqrt{\frac{1}{n}\sum_{i=1}^{n}(x_{0_i} - x_{m_i})^2} \tag{2.15}$$

$$SI = \frac{RMSE}{\bar{x}_0} \tag{2.16}$$

in which x_{0_i} is the number ith of the measurement data, x_{m_i} is the number ith of the model simulation results, n is the sample size, $\bar{x}_0$ is the mean value of the measurement, and the $\bar{x}_m$ is the mean value of the model simulation results.

It is noted that the R values indicate correlation in trends between the model and measurements, while the Normalized Bias and SI demonstrate the match in absolute values.

2.3 Field measurements

2.3.1 Wave buoys measurements

The calibration and validation of the North Atlantic scale wave model utilized four buoys from the Cefas WaveNet wave monitoring network [77], located in Scotland's waters, as reference points. Table 2.1 presents detailed information regarding these buoys, while Figure 2.3 (b) shows their locations. Notably, the West of Hebrides and Blackstone observation points, situated directly facing the Atlantic Ocean, contrast with the Moray Firth and Firth of Forth points, which face the North Sea in shallower channels. Collectively, these observation points offer a comprehensive representation of open sea conditions around Scotland.

These buoys were chosen because wave-current interactions were negligible due to the low tidal current speeds in the open sea. Therefore, the buoys serve as an optimal data source for validating the North Atlantic-scale TOMAWAC wave models in the absence of currents. The wave buoys measurements are recorded every 30 min unless there is missing data.

Table 2.1 Details of Cefas WaveNet buoys

Site	Latitude	Longitude	Water depth
West of Hebrides	57°17'.53 N	7°54'.85 W	100 m
Blackstone	56°03'.73 N	7°03'.41 W	97 m
Moray Firth	57°57'.99 N	3°19'.99 W	54 m
Firth of Forth	56°11'.27 N	2°30'.24 W	65 m

2.3.2 Acoustic Doppler wave and tidal current field measurements

The flow model and wave-current coupled model are calibrated and validated using field measurements obtained from the Westray Firth and Pentland Firth, as depicted in Figure 2.2. These locations are characterized by natural channels that facilitate the acceleration of waters and winds from the Atlantic Ocean and are notable for strong coexistence of waves and currents.

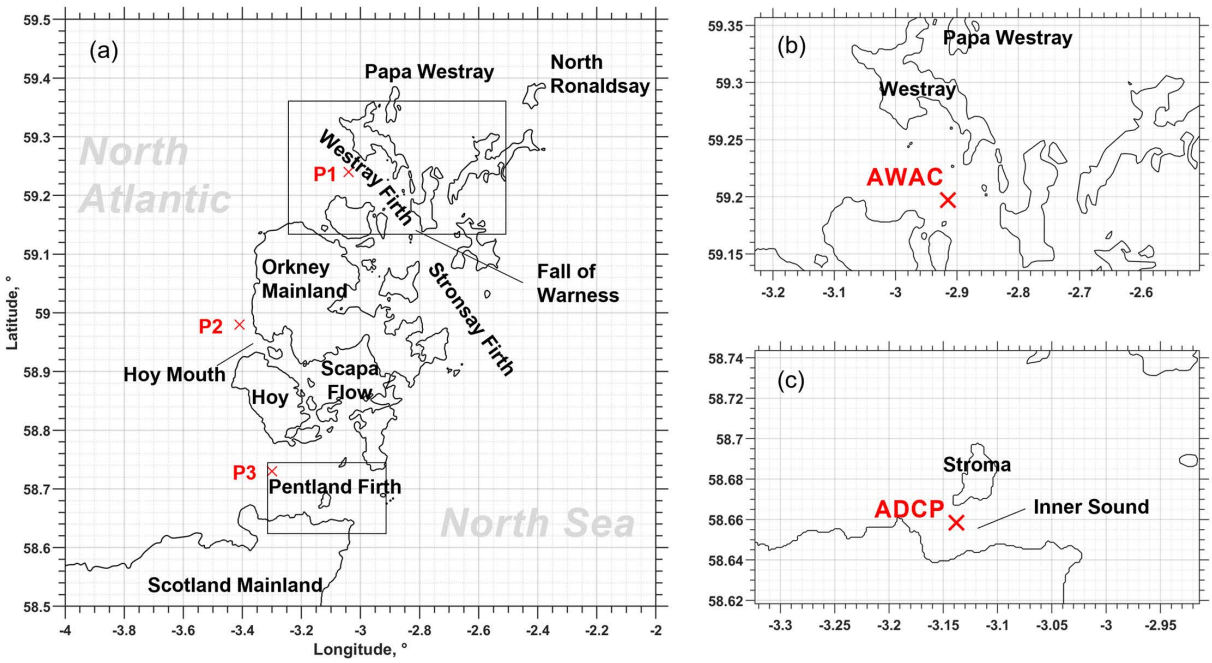

Figure 2.2 Geographic position of AWAC and ADCP deployed in PFOW

2.3.2.1 AWAC measurements at Westray Firth

The field measurements collected at the Westray Firth are recorded by a 600 kHz Nortek AWAC unit with 3 slanted and 1 vertical beam to facilitate both wave and current measurements [63]. This instrument is mounted at the sea bottom and the mean water level at this site is around 52 m. The data available to this study are the tidal current speeds and directions at specific depths, H_{m0}, and T_z, recorded during the period of 19 July to 4 October 2016 (77 days) with 30-min intervals unless there is missing data.

2.3.2.2 ADCP measurements at Pentland Firth

The field measurements at Pentland Firth were recorded using the Teledyne Sentinel V50, a bed-mounted 5-beam ADCP, which was one of the ADCPs used in the MeyGen Phase 1a project [78], with details provided in publication [79]. The mean water depth of this location is around 37 m. The ADCP data spanned 58 days, from 15 October to 12 December 2017, with sampling frequency of 2 Hz. For comparison with the model, the ADCP data were averaged to match the model's 10-minute timestep.

Notably, the tidal parameters were directly recorded by the instrument while wave parameters were indirectly derived from the recorded surface elevation using the spectral moment method, as reported in publication [79]. To ensure the same definition as the TOMAWAC wave model, the H_{m0}, T_m and T_p are derived by the same equation as the TOMAWAC,

$$H_{m0} = 4\sqrt{\int_0^\infty S_\eta(f)\,df} \tag{2.17}$$

$$T_m = \frac{\int_0^\infty S_\eta(f)\,df}{\int_0^\infty f\,S_\eta(f)\,df} \tag{2.18}$$

$$T_p = \frac{\int_0^\infty {S_\eta}^5(f)\,df}{\int_0^\infty f\,{S_\eta}^5(f)\,df} \tag{2.19}$$

where, $S_\eta(f)$ in the above equations is the power spectral density of every 10-minute-long surface elevation η, and f is the frequency. For ADCP recordings, the data were made

available by SAE MeyGen project who have deployed an array of tidal energy converters at the Inner Sound region of the Pentland Firth [23,79].

2.4 Numerical modelling of the North Atlantic Ocean

This section introduces the North Atlantic scale wave model, detailing the mesh design, model settings, and validation using reliable wave buoy measurements. Additional information on model construction and hindcast validation is provided in Appendices Appendix A and B.1.

2.4.1 Model set-up

2.4.1.1 Bathymetry and mesh generation

As the North Atlantic wave model spans more than ten UTM zones and is unsuitable to be simulated under the Cartesian coordinates, the simulation therefore operates in a spherical spatial coordinate system (i.e., by latitude and longitude). The simulation domain spans from 10°E to 75°W in longitude and from 9°N to 70°N in latitude, covering the North Atlantic and the British Isles, as shown in Figure 2.3 (a). To conserve computational resources, the model employs a lower resolution in the North Atlantic, with a maximum grid size of 1° (approximately 100 km). As the model approaches the Irish and British Isles, the mesh becomes finer, with a transitional region (continental shelf) at a maximum mesh length of 0.5° (around 50 km), further refining to within 0.2° (around 2 km) near coastlines. For model validation sites, which are the four sites recorded by the Cefas WaveNet system described in Section 2.3.1, grid spacing is controlled to within 50 m.

For the coupled wave-current model, which covers the entire Pentland Firth and Orkney Waters as well as the Hebrides Islands, high resolution meshes are necessary; hence the domain for the coupled model forms a sub-mesh of the North Atlantic model (further details about this sub-mesh is shown in Section 2.5.1.1). The boundary coordinates of the coupled model are placed within the North Atlantic model as specific nodal points, which makes it easier to directly package the directional wave spectrum at these nodes as an output file and later as input to the coupled model. Another purpose of having the sub-mesh domain is that the simulation results can be directly served for the wave-only simulation results as well, used for the comparison with the wave-current coupled model to investigate the WCIs effects.

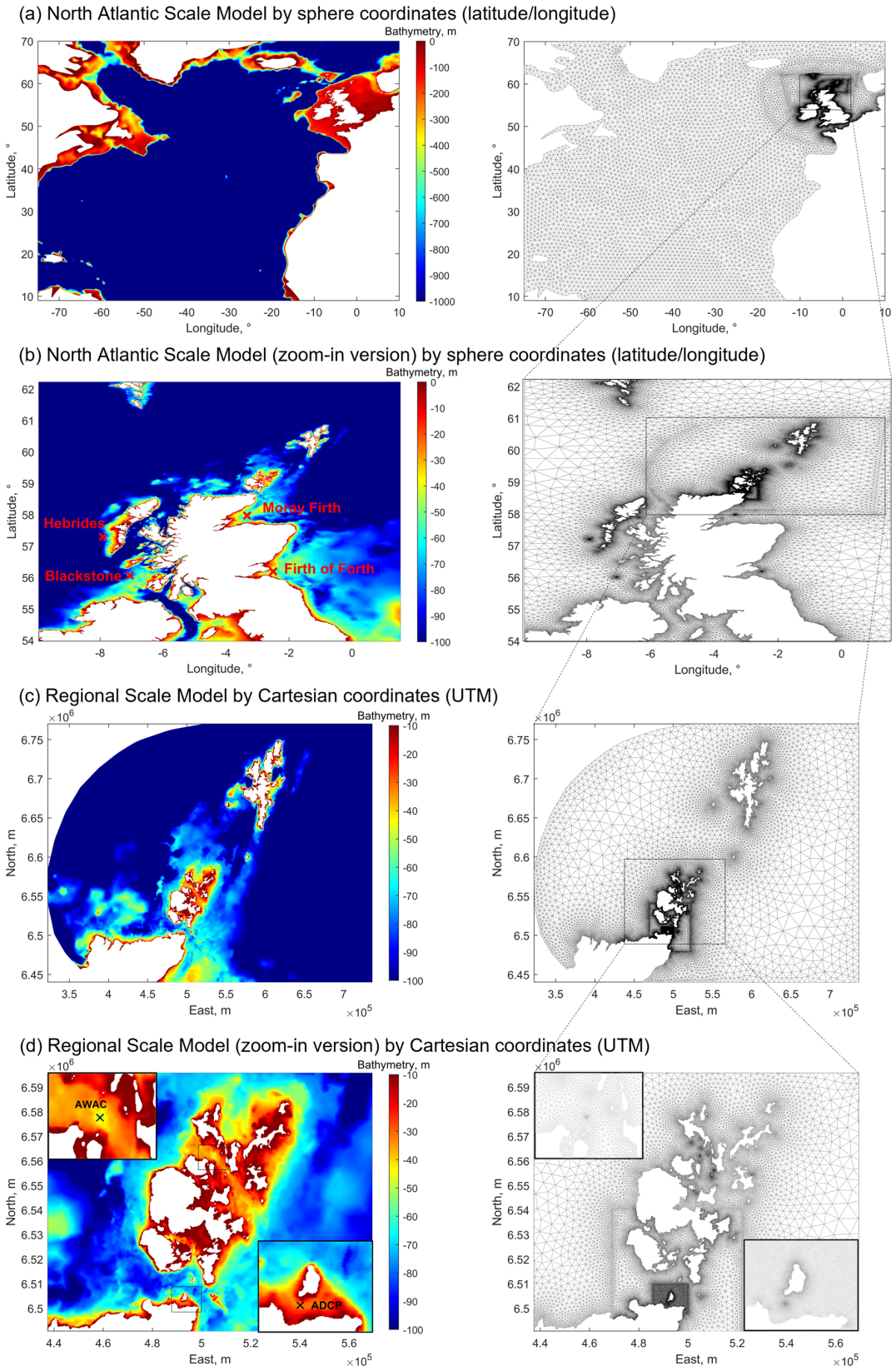

Figure 2.3 Bathymetry and mesh of the North Atlantic scale model and region scale model

2.4.1.2 Wind input from ECMWF ERA5 database

The wind data that drives the wave model is obtained from the fifth-generation reanalysis (ERA5) database provided by the ECMWF (https://cds.climate.copernicus.eu/datasets/reanalysis-era5-single-levels). The specific inputs are the eastward U and northward V components of the wind, measured at 10 m above the ground. The temporal and spatial resolutions are 1 hour and 0.25° × 0.25° in latitude–longitude coordinates, respectively. Notably, the rectangular grid is interpolated to match the model mesh.

2.4.1.3 Parameter set-up

In the numerical simulation, each node calculates waves from 36 directions (at 10° intervals), with each direction containing 36 frequency components. The minimum wave frequency is 0.04 Hz, with an increment ratio of 1.08, covering a frequency range of 0.04 - 0.6 Hz (i.e., period range: 25 - 1.67 s). The timestep of this large-scale model is set to 600 s. During the wave-only simulation, currents are not considered, while the energy dissipation due to the bottom friction Q_{bf}, depth-induced wave breaking Q_{br}, and white capping Q_{ds} are taken into account, with details shown in Table 2.2. Of particular note are two key parameters related to the Westhuysen whitecapping method [75], which were adjusted based on a sensitivity study conducted during model calibration: (1) The Westhuysen dissipation coefficient $C_{dis,break}$. It controls how rapidly energy is removed once waves exceed the breaking threshold, thus representing the intensity of whitecapping. In this study, a smaller value than the default was applied, resulting in milder dissipation of steep, breaking waves. (2) The Westhuysen white capping dissipation $C_{dis,non-break}$ governs the background energy dissipation for non-breaking waves. A reduced value means less energy loss for low-steepness waves, such as swell.

Table 2.2 Source and sink terms applied in the North Atlantic TOMAWAC model

Source and sink terms	Method/Value	Note
Bottom friction dissipation Q_{bf}	Hasselmann [80]	The only model implemented for the bottom friction-induced dissipations. The default setting applied.
Depth-induced breaking dissipation Q_{br}	Battjes and Janssen's model [81]	Parametric spectral models developed for studying random waves. The default setting applied.
White capping dissipation Q_{ds}	Westhuysen model [75]	This model is implemented in TOMAWAC in its most recent version. Values are modified.
Westhuysen dissipation coefficient $C_{dis,break}$	0.00002	The default value is 0.00005.
Westhuysen white capping dissipation $C_{dis,non-break}$	1.5	The default value is 3.29

2.4.2 Model validation – 10 years comparison

Figure 2.4**,** Figure 2.5 and Figure 2.6 present a 10-year time series comparison of H_{m0}, T_m and T_p between the North Atlantic TOMAWAC wave model and wave buoy measurements across four sites, covering the period from January 2014 to December 2023. Table 2.3 provides the detailed performance metrics. Additionally, the hindcast data for each year are presented in Appendix B.1 for further reference.

The simulation results of the H_{m0} and T_m align very well with the measurements, with the highest R values reaching 0.98 and 0.93, respectively, at the West of Hebrides site. Across all sites, R value exceeds 0.93 for H_{m0} and 0.83 for T_m, demonstrating the model's strong accuracy. For T_p, which is typically harder to match than other wave parameters, the time series closely follow the measurements, accurately capturing annual cycles. At two deep water sites, the R values for T_p are a respectable 0.85, and the SI values are even within 0.15.

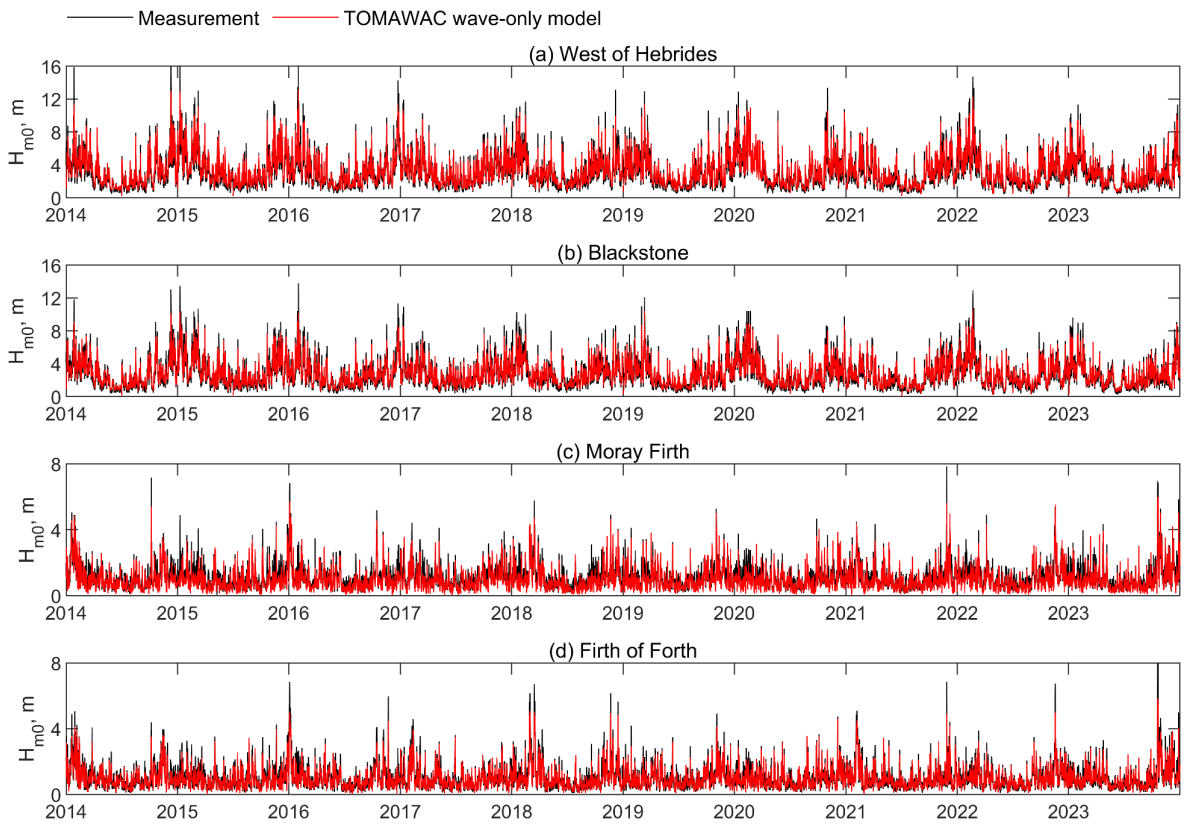

Figure 2.4 H_{m0} comparison between North Atlantic scale wave model and wave buoys' measurement, from Jan. 2014 to Dec. 2023

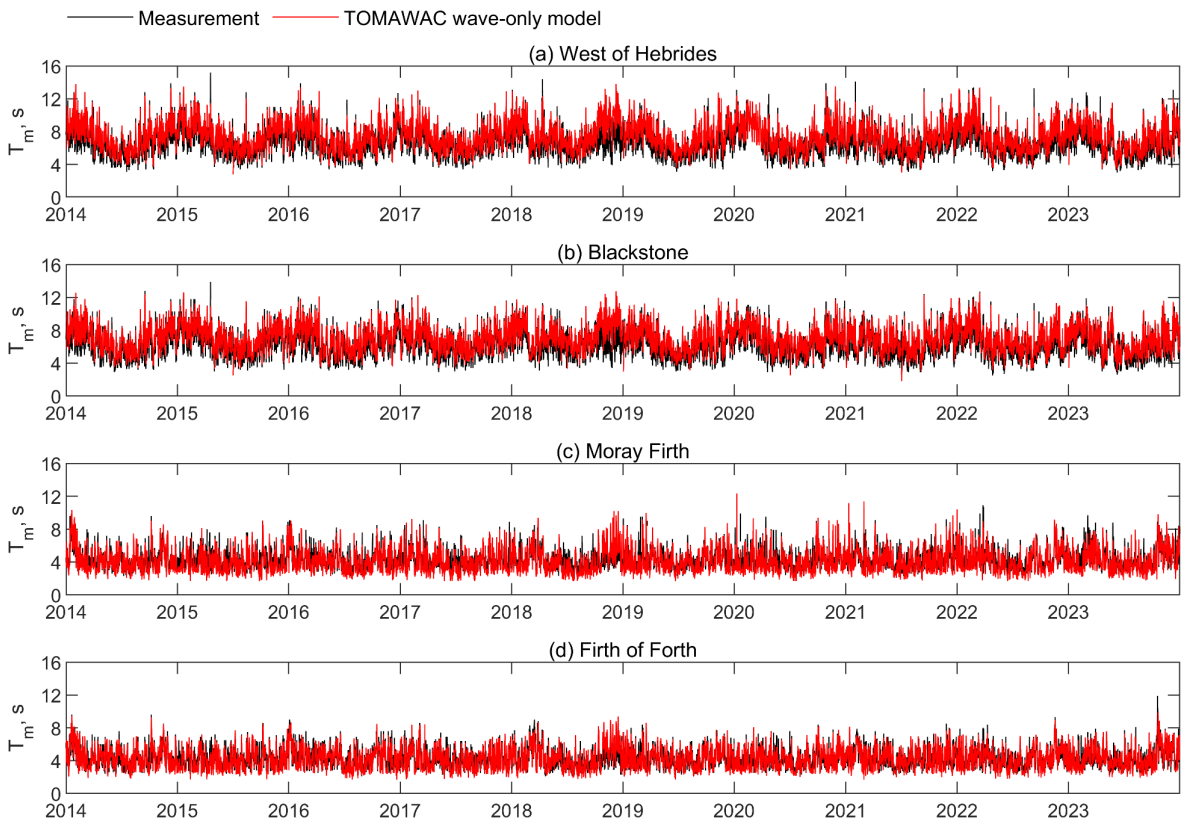

Figure 2.5 T_m comparison between North Atlantic scale wave model and wave buoys' measurement, from Jan. 2014 to Dec. 2023

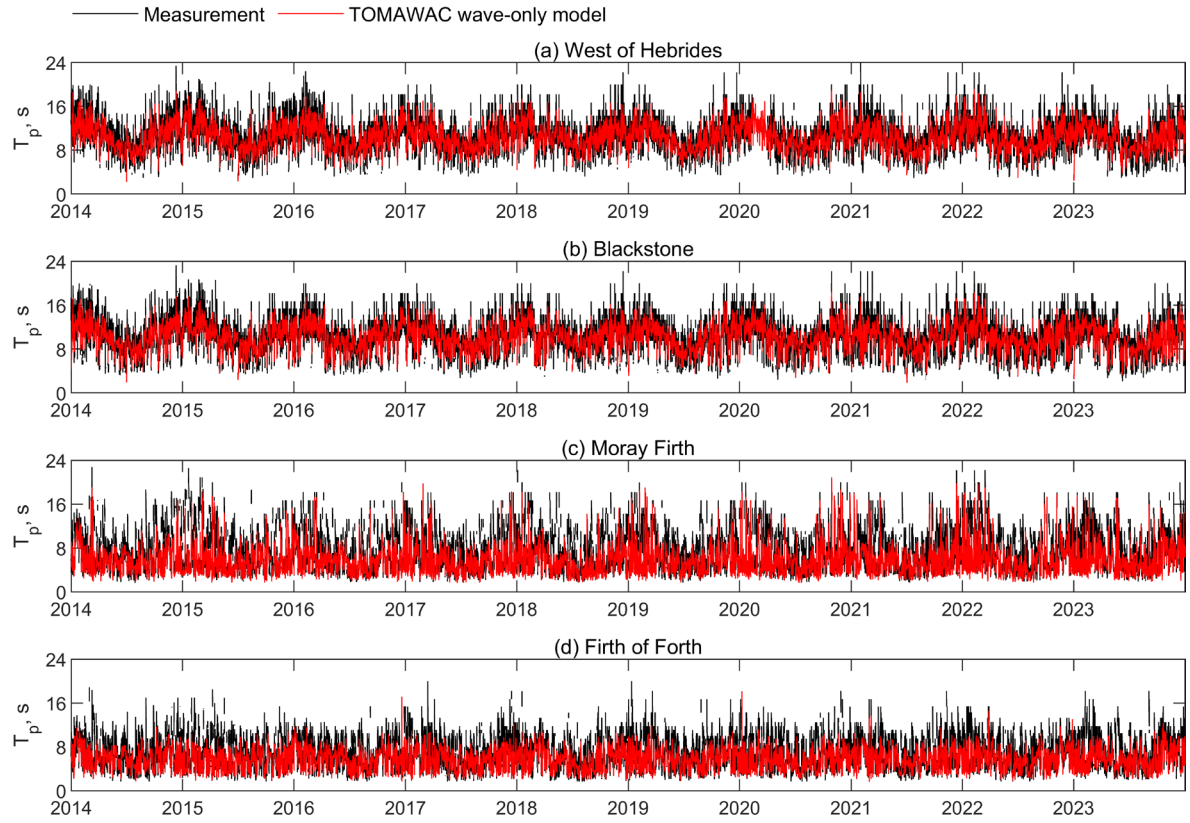

Figure 2.6 T_p comparison between North Atlantic scale wave model and wave buoys' measurement, from Jan. 2014 to Dec. 2023

Table 2.3 Metrics of the North Atlantic scale wave model, from Jan. 2014 to Dec. 2023.

Location	Parameter	Mean model (real value)	Bias	Normalized Bias	RMSE	SI	R
West of Hebrides	H_{m0}, m	3.03 (3.23)	-0.20	-0.06	0.44	0.14	0.98
	T_m, s	6.79 (7.43)	-0.65	-0.09	0.90	0.12	0.93
	T_p, s	10.97 (10.58)	0.38	0.04	1.42	0.13	0.85
Blackstone	H_{m0}, m	2.66 (2.74)	-0.08	-0.03	0.41	0.15	0.97
	T_m, s	6.43 (7.02)	-0.60	-0.08	0.89	0.13	0.91
	T_p, s	10.62 (10.31)	0.31	0.03	1.51	0.15	0.85
Moray Firth	H_{m0}, m	1.07 (0.98)	0.09	0.10	0.27	0.27	0.93
	T_m, s	4.16 (4.10)	0.07	0.02	0.75	0.18	0.83
	T_p, s	7.12 (5.80)	1.32	0.23	3.11	0.54	0.57
Forth of Firth	H_{m0}, m	1.00 (0.99)	0.02	0.02	0.20	0.20	0.96
	T_m, s	4.20 (4.28)	-0.07	-0.02	0.64	0.15	0.87
	T_p, s	6.74 (5.90)	0.84	0.14	2.08	0.35	0.64

However, at two sites facing the North Sea with shallower waters and weaker winds, particularly the Moray Firth, the model shows lower performance for T_p, as suggested by the metrics. This could be attributed to geographic factors that complicate simulation and, more importantly, frequent data gaps in measurements at these locations, making precise matching more challenging. Despite these limitations, the model demonstrates strong performance for H_{m0} and T_m at Moray Firth, further supporting its overall effectiveness. Notably, similar challenges in simulating T_p at Moray Firth have been observed in other models, such as MIKE 21-SM [56], where the R value was as low as 0.39 in 2010. In comparison, the performance of the TOMAWAC model in this study is relatively better.

2.5 Numerical modelling of the PFOW

This section introduced the PFOW regional scale two-way coupled wave-current model including the mesh design, parameter settings, and the model validation.

2.5.1 Model set-up

2.5.1.1 Mesh generation

The focused geometry domain of the wave-current coupled model covers the entire Pentland Firth and Orkney Waters as well as the Shetland Islands to ensure sufficient fetch for wave

propagation, which is defined by the UTM coordinates of zone 30, ranging from 322595 to 736421 m in the east direction and from 6440094 to 6770000 m in the north direction, as Figure 2.3 (c) shows. The TOMAWAC wave model and TELEMAC flow model share the same unstructured triangular geometric mesh when they are coupled together, of which the bathymetry database and processing software are the same as aforementioned. The mesh resolution near the Westray Firth AWAC validation sites is within 50 m, with a much finer resolution in the Pentland Firth to capture high-speed tidal flows, with the finest resolution of 30 m being applied at the inner sound of Pentland Firth, the site of the ADCP.

2.5.1.2 Parameter set-up

The boundary conditions of the regional TELEMAC flow model are set as open boundaries with prescribed water levels, utilizing the TPXO9 tidal model as the tidal database [82]. The bottom friction is modelled using the Chézy formulation, with a constant value of 66 applied across the entire computational domain. The mixing vertical length model is chosen for turbulence. The tidal flats (areas that become intermittently dry and wet) are included from the active computations. The flow model operates with a timestep of 5 s.

The regional TOMAWAC wave model settings are largely consistent with those of the North Atlantic wave model, with two key differences: (1) the Westhuysen method [74] is applied to account for the sink term $Q_{ds,cur}$ of wave blocking effects when waves meet strong adverse current, with a dissipation coefficient $C_{ds,cur}$ of 5.2; (2) the timestep is reduced to 300 s to ensure stable coupling between the wave and flow models. The coupling period between the wave and flow model is set at every 300 s.

2.5.2 Model validation – 135 days comparison

The numerical model results are presented as time series in Figure 2.7 and Figure 2.8 for Westray Firth and Pentland Firth, respectively, with a summary of the model's performance metrics provided in Table 2.4.

2.5.2.1 Tidal parameters comparison

The depth-averaged tidal current velocities produced by the numerical model were validated against field measurements at 0.4 times the total depth from the seabed. This depth is considered a reliable approximation for the averaged velocity in TELEMAC, assuming a vertical tidal profile that follows the 1/7 power law [83]. With this assumption, the model demonstrated

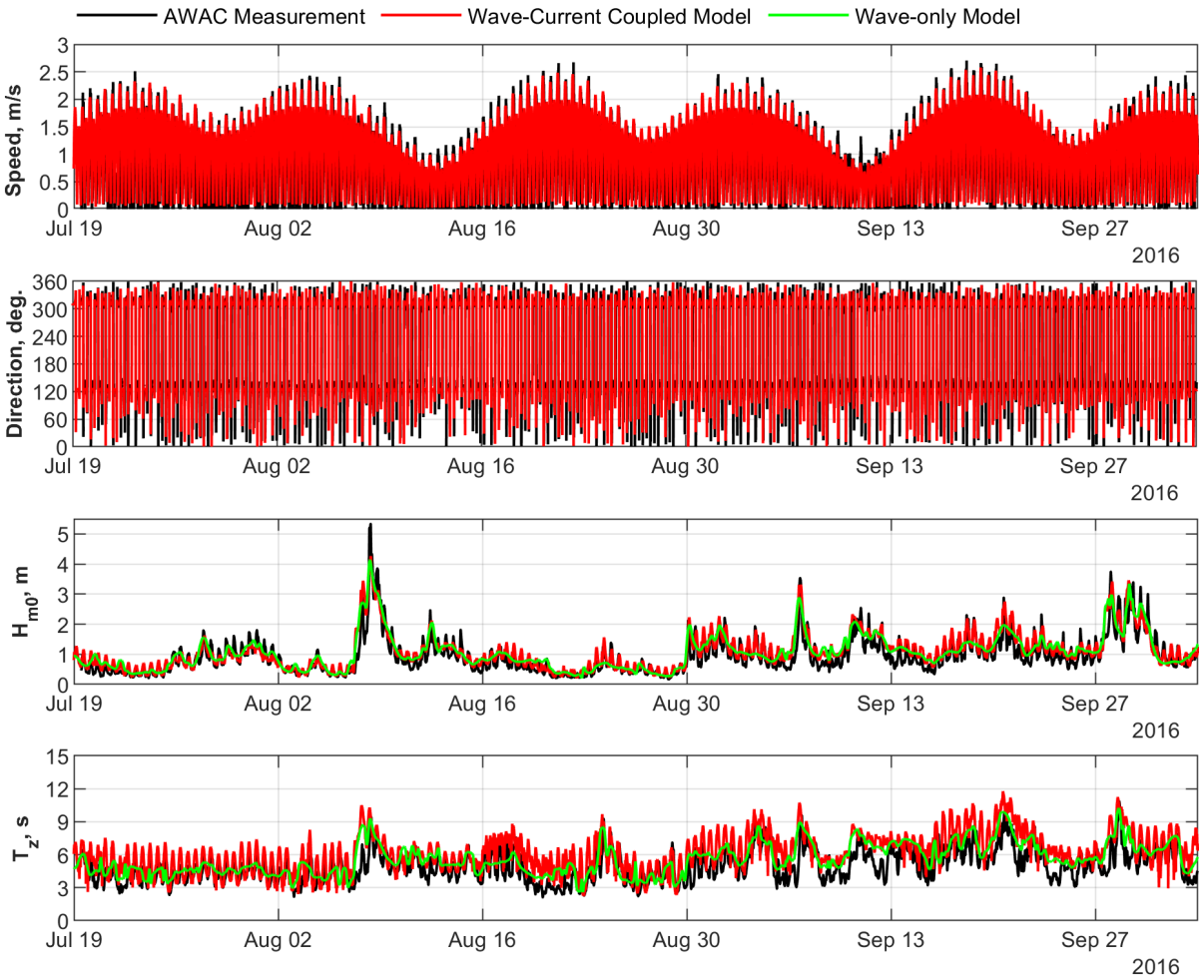

Figure 2.7 Wave-current coupled model validation with AWAC data at the Westray Firth

an excellent match with the depth-averaged tidal flow speeds at Westray Firth and Pentland Firth, achieving R values of 0.94 and 0.93, respectively. Notably, the maximum tidal speeds observed during the validation period exceeded 2.5 m/s at Westray Firth and reached up to 5 m/s at Pentland Firth, further confirming the energetic tidal flows in these regions.

To provide a broader understanding of the tidal current conditions in Pentland Firth and Orkney Waters, a map showing the maximum depth-averaged tidal speeds for the year 2017 was generated and is presented in Figure 2.9. The fastest tidal currents are concentrated in the Pentland Firth, particularly in the northern and southern regions around Stroma Island, where speeds exceed 5 m/s across a wide area. Other areas with significant tidal currents include Westray Firth, Stronsay Firth, and the northern edges of the Orkney Islands (around Papa Westray and North Ronaldsay), where speeds surpass 3 m/s. Additionally, Figure 2.9 includes maps of tidal conditions during two phases of a Spring Tide on November 5, 2017: Flood flow (20:00): Showing currents flowing from the North Atlantic into the Pentland Firth, and Ebb flow (14:20): Showing currents flowing toward the North Atlantic. It is observed that during the ebb phase, the area with tidal speeds over

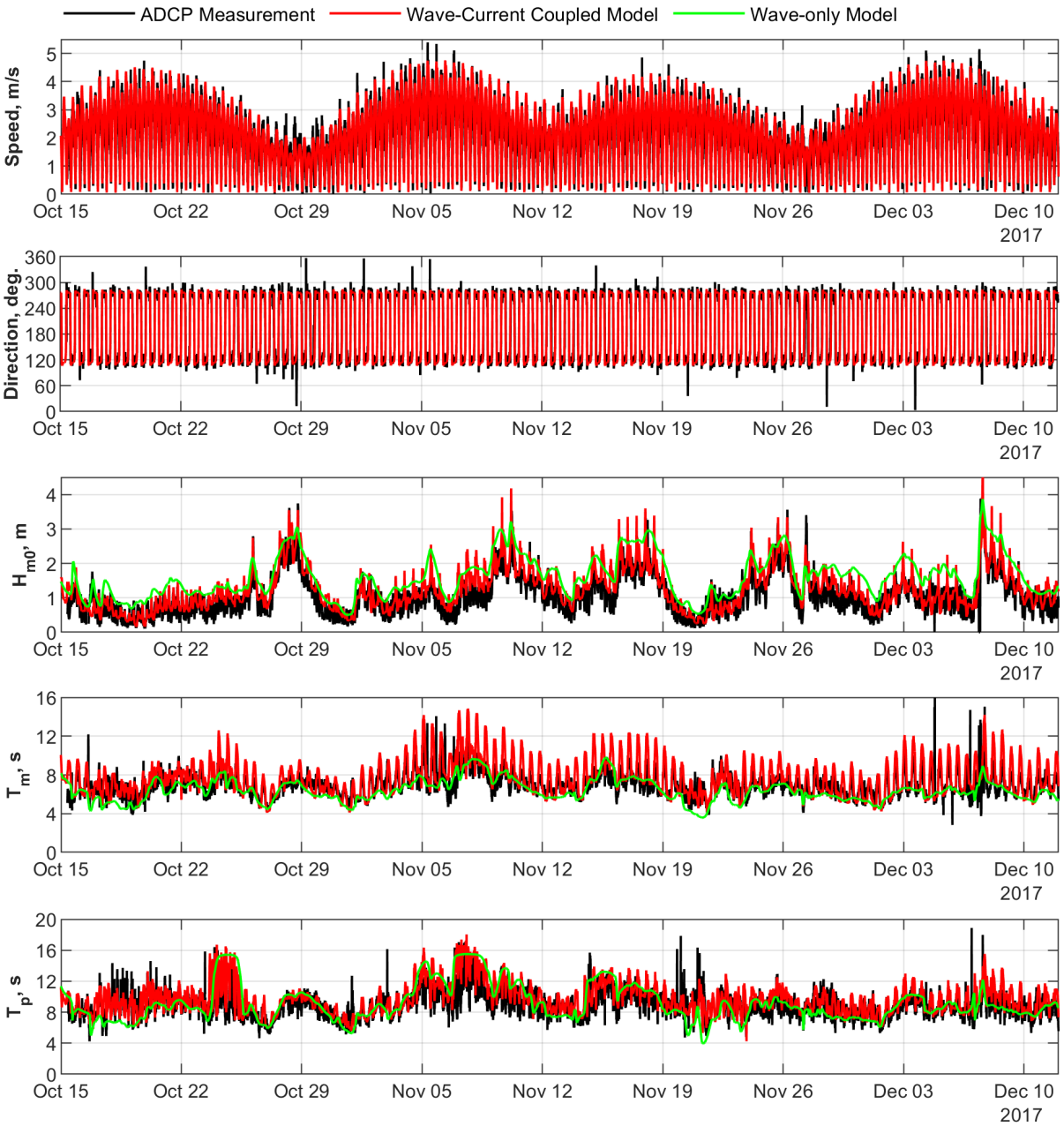

Figure 2.8 Wave-current coupled model validation with ADCP data at the Pentland Firth

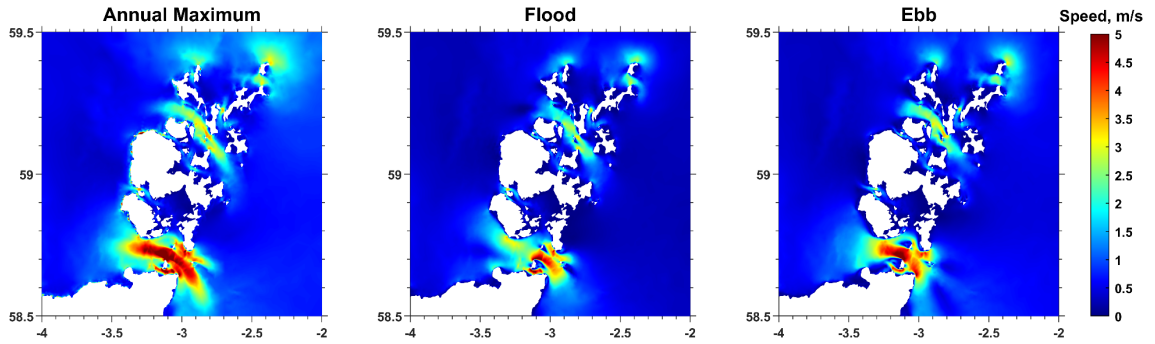

Figure 2.9 Tidal speed map of Pentland Firth and Orkney Waters

Left: annual maximum speed of the year 2017. Middle: speed during the flood phase (November 5, 2017, 20:00:00). Right: speed during the ebb phase (Novermber 5, 2017, 14:30:00).

4 m/s in the Pentland Firth is larger compared to the flood phase, confirming the phenomenon of tidal asymmetry in this region [84].

Table 2.4 Metrics of the regional scale wave-current coupled model

Location	Parameter	Mean model (real value)	Bias	Normalized Bias	RMSE	SI	R
Westray Firth AWAC	*Speed,* m/s	1.13 (1.10)	0.03	0.03	0.22	0.25	0.94
	H_{m0}, m	1.09 (0.95)	0.14	0.14	0.30	0.31	0.91
	T_z, s	6.20 (4.95)	1.26	0.25	1.73	0.35	0.72
Pentland Firth ADCP	*Speed,* m/s	2.25 (2.07)	0.17	0.08	0.46	0.22	0.93
	H_{m0}, m	1.24 (1.08)	0.16	0.14	0.37	0.34	0.85
	T_m, s	7.66 (6.94)	0.73	0.10	1.42	0.20	0.76
	T_p, s	9.67 (8.90)	0.78	0.09	1.76	0.20	0.63

2.5.2.1 Wave parameters comparison

With the tidal currents accurately simulated, the wave parameters can now be analysed. Figure 2.7 and Figure 2.8 compare the results of the North Atlantic wave-only model with the wave-current coupled model and field measurements. The wave-current coupled model and field data both exhibit clear periodic fluctuations corresponding to the tidal cycle. In contrast, the wave-only results show a relatively flat curve, providing compelling evidence of tidal modulation effects. At Westray Firth, the wave-current coupled model closely tracks the measured data, achieving an R value of over 0.92 for H_{m0}, demonstrating excellent agreement. At the Pentland Firth, the R value for H_{m0} is slightly lower at 0.85. This is expected, as the Pentland Firth data exhibit high-frequency fluctuations, which may be attributed to several factors: (1) shallower water depth but with much faster tidal currents compared to Westray Firth, leading to increased wave-breaking events, and (2) wave parameters are not directly measured but calculated from surface elevation data using spectral methods. This process can incorporate turbulence or environmental noise, amplifying fluctuations in the final wave parameters. Despite these challenges, both H_{m0} and T_m closely follow the modulations. Even the T_p shows good alignment with an R value of 0.63 and SI of 0.2.

These results indicate the wave-current coupled model's robustness in simulating wave parameters under the influence of tidal currents, even in complex environments like the Pentland Firth.

2.6 Discussion

The coupled wave-current numerical model applied in this study uses constant parameters across the entire simulation domain of the regional model, such as the bottom friction coefficient in the flow model and the dissipation coefficient for strong currents in the wave model. While these parameters are effective on a broad scale, they may not be optimal for specific areas within the domain, potentially leading to inaccuracies in tidal current or wave predictions at certain locations. This limitation is particularly relevant given the large area of the regional model, as shown in the bathymetry in Figure 2.3, where shallow regions with depths under 20m may exhibit greater variability in representation.

Such concerns are not unique to this study and are common in numerical modelling. It is impractical to ensure that all areas are perfectly simulated, especially in large domains. To address this, validation over extended periods is critical. In this study, the model was validated over a total of 135 days, covering both summer and winter, at two locations situated in dynamic wave-current environments: Westray Firth and Pentland Firth. These locations are geographically distant and present significant tidal complexities, yet the model achieved robust validation results, demonstrating its reliability in this region with water depth deeper than 30 m.

Chapter 3

Effects of wave-current interactions on wave parameters

This chapter utilizes the numerical models described in the previous chapter to analyse the effects of tidal currents on wave parameters. The analysis focuses on the time series of significant wave height (H_{m0}), mean wave period (T_m), and mean wave direction, as well as the scatter relationship between Hm0 and peak wave period (T_p). Additionally, the chapter examines unidirectional and directional wave spectra to provide a comprehensive understanding of WCI.

3.1 Wave simulation accuracy in reduced domain

Before proceeding with model comparison, it is important to clarify the comparison. The North Atlantic scale model serves as the wave-only model for direct comparison with the regional wave-current coupled model. The wave model settings are nearly identical; the primary distinction lies in whether tidal currents are considered. However, the simulation domains differ between the two models, raising concerns about the validity of direct comparisons.

This concern is technically addressed through two steps: (1) nesting the regional model within the North Atlantic model and (2) using the two-dimensional directional spectra from the North Atlantic model as wave boundary conditions of the regional model. To validate this approach, Figure 3.1 provides a three-month comparison of wave-only simulations from the North Atlantic and regional models at Westray Firth, covering July to October 2016. The results show nearly overlapping time series outputs, with negligible fluctuations in regions of small wave periods. This alignment confirms that the North Atlantic scale model produces outputs consistent with the regional scale model when tidal currents are excluded, validating the comparison between the North Atlantic wave-only model and the regional wave-current coupled model.

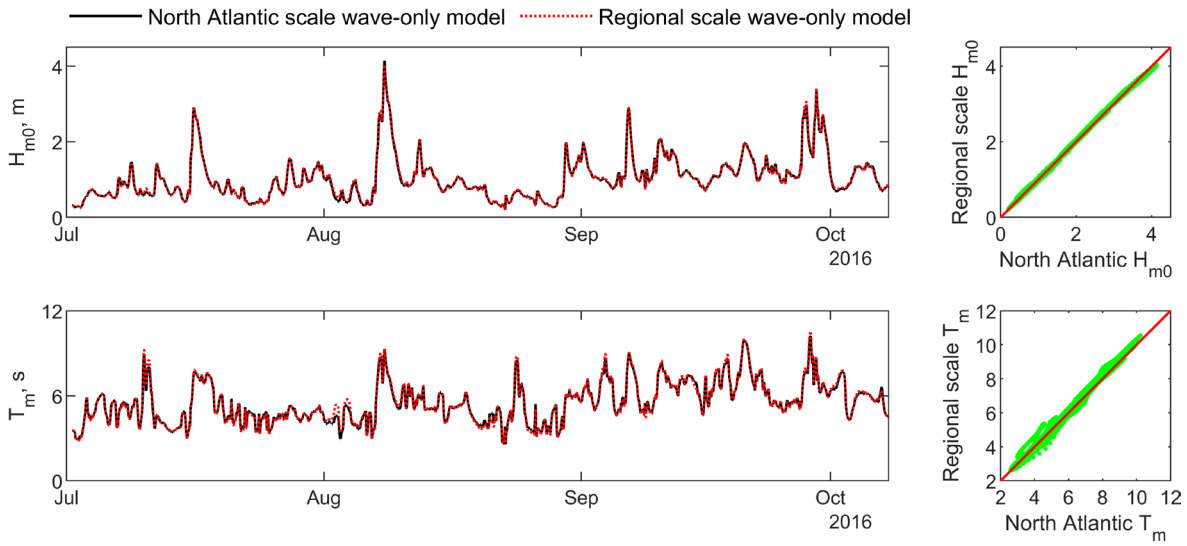

Figure 3.1 Comparison of H_{m0} and T_m between the North Atlantic scale wave model and the regional scale wave model

Left: Time series comparison. Right: Scatter plots (green dots) comparing the simulation results from the two models; the red reference indicates where both models produce identical results, i.e., R=1. Data recorded from July 2 to October 18, 2017.

3.2 Time series analysis

To gain an enhanced understanding of wave-current interactions around Orkney Waters, hindcast data for the year 2016 (January 1 to December 31) was generated using the North Atlantic scale wave-only model and the regional wave-current coupled model. This enabled detailed analysis across various seasons and locations.

Eight locations around the Orkney Waters, as shown in Figure 3.2, were selected for the case study. Locations 1, 2, 6, and 7, situated in the North Atlantic region, were chosen for their high wave activity, making them strong candidates for wave energy development. Locations 3, 4, and 8 are located in the middle of the fast-moving water channels where the strong wave-current interactions are anticipated. Location 5, positioned on the eastern side of Orkney and facing the North Sea, offers insights into WCI in that region. This selection reflects the geographical diversity of the Orkney waters. Notably, Locations 3 at Westray Firth and Location 8 at Pentland Firth were used for model validation, as discussed earlier.

Time series analyses were conducted for a Neap Tide week (September 7–14, 206) and a Spring Tide week (November 12–19, 2016), with 10-min data intervals, to demonstrate the effects of wave-current interactions under varying tidal conditions.

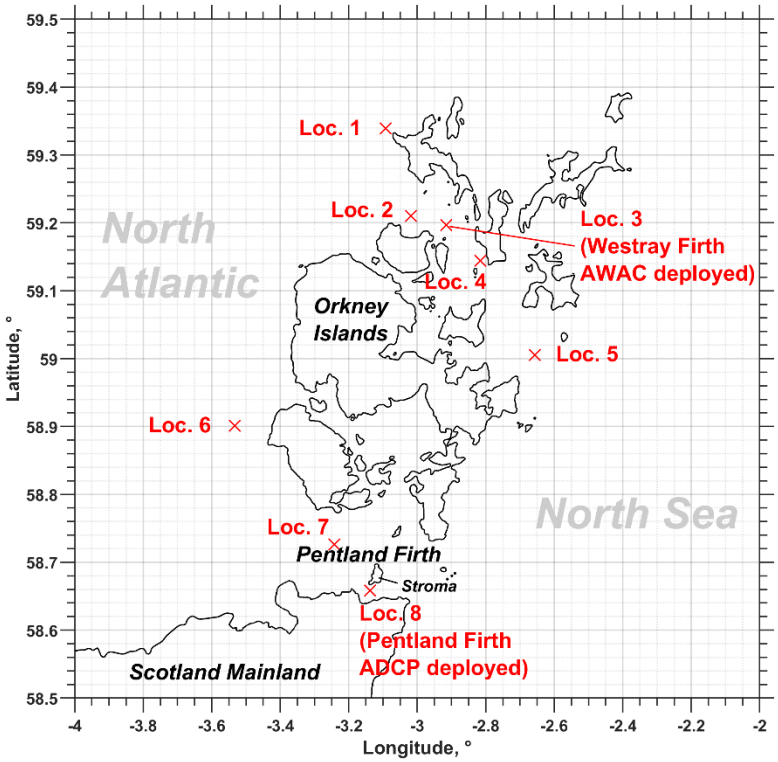

Figure 3.2 Geographical positions of the Location 1 to 8 for the case study in PFOW

3.2.1 Significant wave heights H_{m0}

The analysis of H_{m0} begins with amplitudes comparison. Figure 3.3 and Figure 3.4 illustrate the H_{m0} time series during the Neap Tide and Spring Tide weeks, respectively. The ΔH_{m0} in the plots refers to the difference in wave height between the coupled model and the wave-only model. Locations 1, 2, 6, and 7 on the west side of the islands unsurprisingly exhibit higher wave heights than other locations, though their responses to tidal currents vary. During the Neap Tide week, tidal currents show negligible effects on Locations 1 and 6. However, during the Spring Tide, a general decrease in wave heights ($\Delta H_{m0} < 0$) is observed, with a maximum of nearly 0.5 m decrease on November 15 for both locations. For Locations 2 and 7, located at the tidal inlet of the water channel, the effects of WCI are more evident due to faster flows, with increase in wave heights is up to 1 m during Spring Tides. The influence of tidal current at Location 2 primarily results in increased wave heights (i.e., $\Delta H_{m0} > 0$).

At Location 5, wave heights are more influenced by the North Sea wind conditions than by those from the North Atlantic. Due to its position in the open sea, smaller tidal velocities are expected, and tidal effects at this location are mostly noticeable only during the Spring Tide. In contrast, Locations 3, 4, and 8, situated in fast tidal channels, experience significant

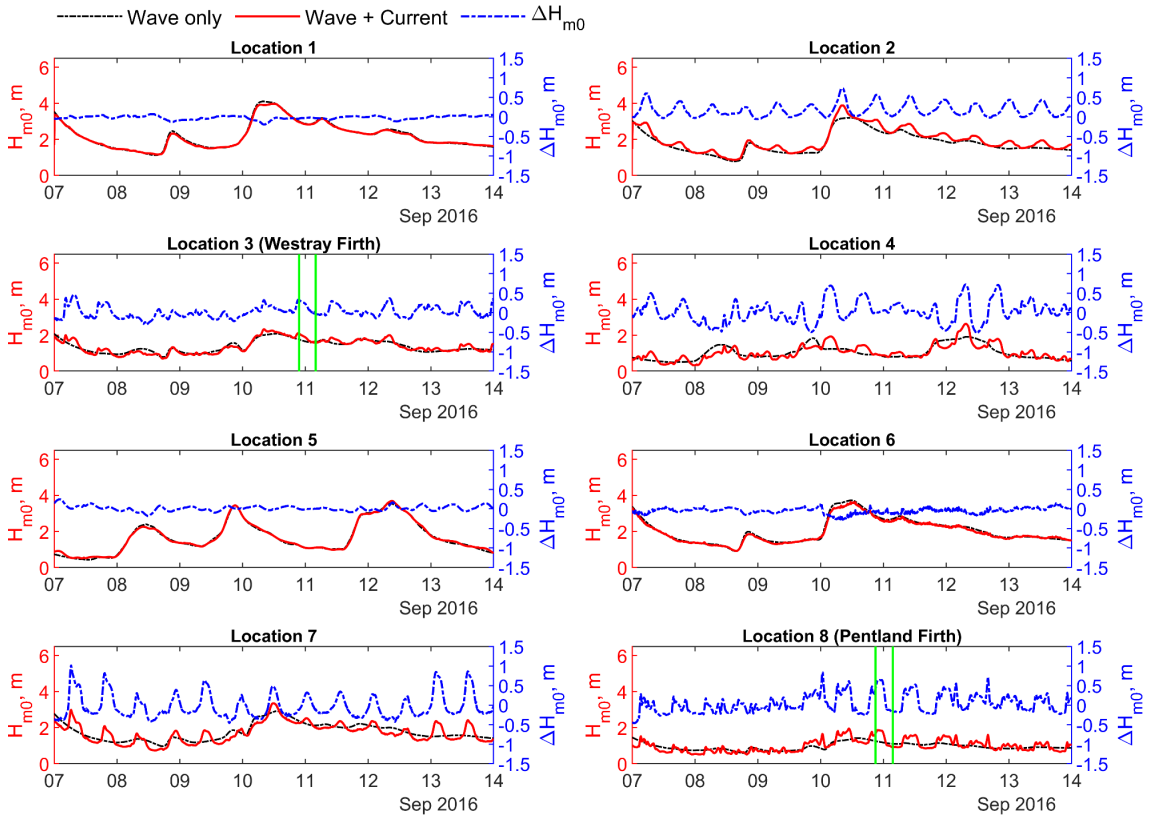

Figure 3.3 H_{m0} timeseries during a Neap Tide week.

Green lines indicate the time points selected for subsequent spectral analysis in Section 3.4.

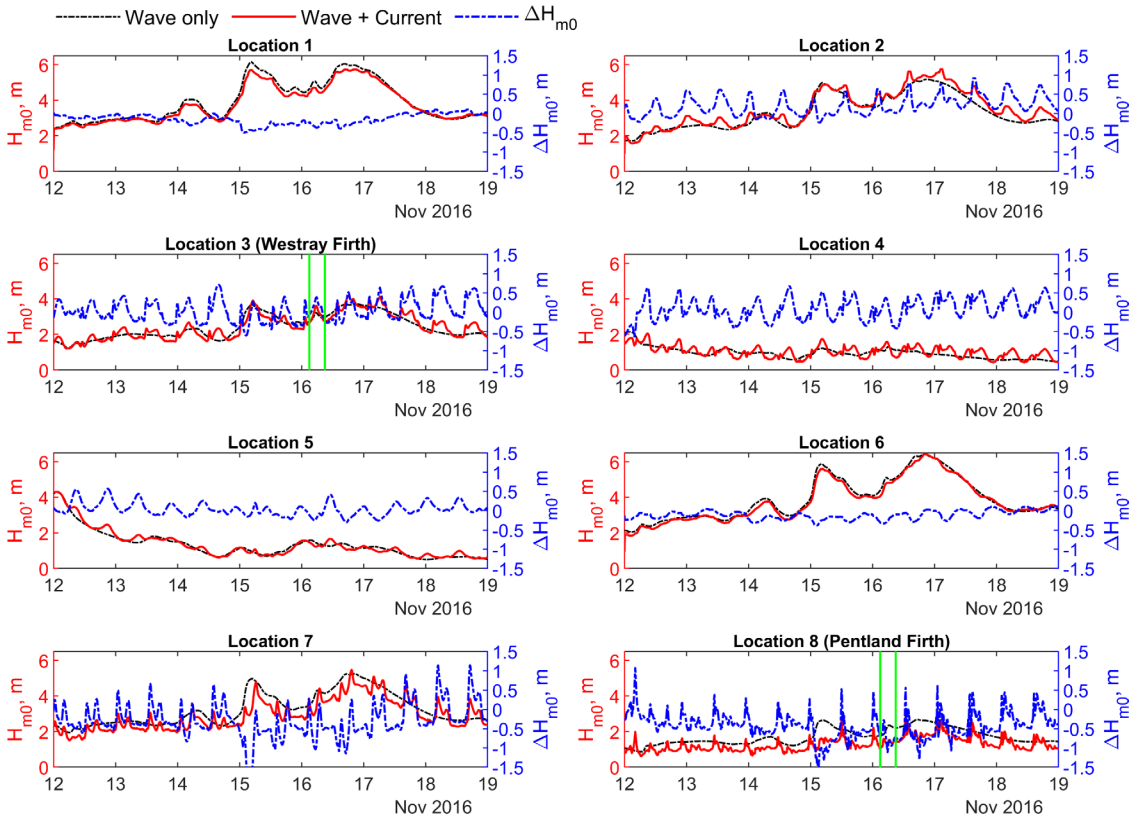

Figure 3.4 H_{m0} timeseries during a Spring Tide week

Green lines indicate the time points selected for subsequent spectral analysis in Section 3.4.

modulation in wave heights during both Neap and Spring Tides with wave heights varying up to ±1 m.

To better illustrate the impact of tidal currents, the ratio between the wave heights in the presence of currents (denote by H_{m0}) and the wave heights without currents (denote by $H_{m0,0}$) is calculated, and this ratio $H_{m0}/H_{m0,0}$ is shown in Figure 3.5 and Figure 3.6 for the Neap and Spring Tides respectively. The relative current velocity, U_c, is plotted alongside the wave heights ratio for reference, which is defined as the projection of the tidal current velocity U in the direction of wave propagation:

$$U_c = U \cdot \cos(\delta - \alpha) \tag{3.1}$$

where, δ is the tidal current flow direction, and α is the wave propagation direction. Positive U_c means tidal currents following the wave direction, while negative values indicate opposing directions.

The ratio $H_{m0}/H_{m0,0}$ at Location 1 and 6 remains nearly 1 during both Neap and Spring Tides, indicating negligible effects by currents (note that $|U_c|_{max}$ is smaller than 1 m/s even during the Spring Tide). This ratio at other sites is clearly periodically modulated by the tidal currents, following the general pattern where opposing currents (negative U_c) lead to increased wave heights (i.e., $H_{m0}/H_{m0,0} > 1$). This phenomenon can be explained by the following equation, assuming no wave breaking [85]:

$$\frac{H_{m0}}{H_{m0,0}} = \frac{c_{g,0}}{\sqrt{C_g(C_g + 2U_c)}} \tag{3.2}$$

where C_g and $C_{g,0}$ represent the wave group velocities with and without tidal current respectively.

In general, a positive U_c results in a decreased H_{m0} as predicted by the equation. However, higher negative relative velocities do not necessarily indicate that wave heights will continue to increase. For instance, at Location 4, during the Spring Tide period ($|U_c|_{max}$) reach to 3.3 m/s), a dramatic decrease in the wave height ratio is seen in the time series, forming a trough (marked by a cyan coloured dotted line in Figure 3.6 at Location 4) with two sharp peaks surrounding it. This suggests an enhanced wave breaking induced by strong currents: in the negative current gradient, wave heights increase alongside wave steepness, potentially leading to wave breaking. This process is captured by the dissipation

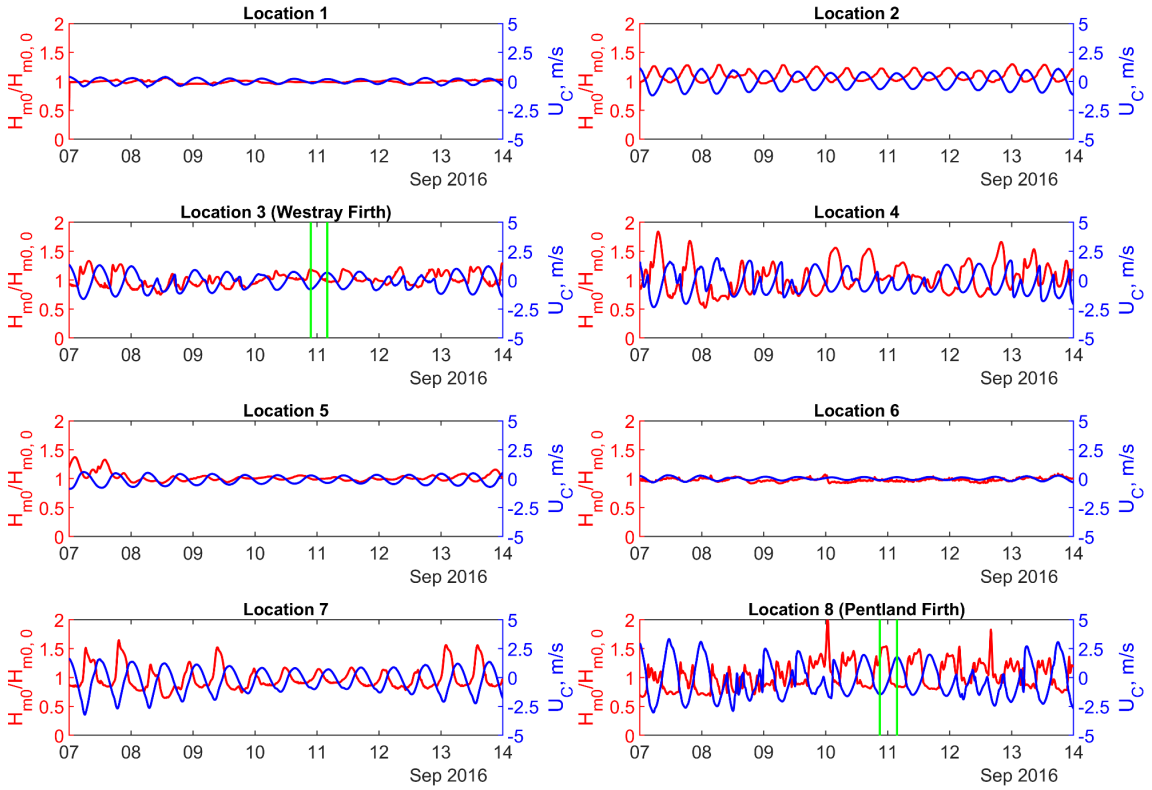

Figure 3.5 $H_{m0}/H_{m0,0}$ and the relative current velocity U_c during a Neap Tide week

Green lines indicate the time points selected for subsequent spectral analysis in Section 3.4.

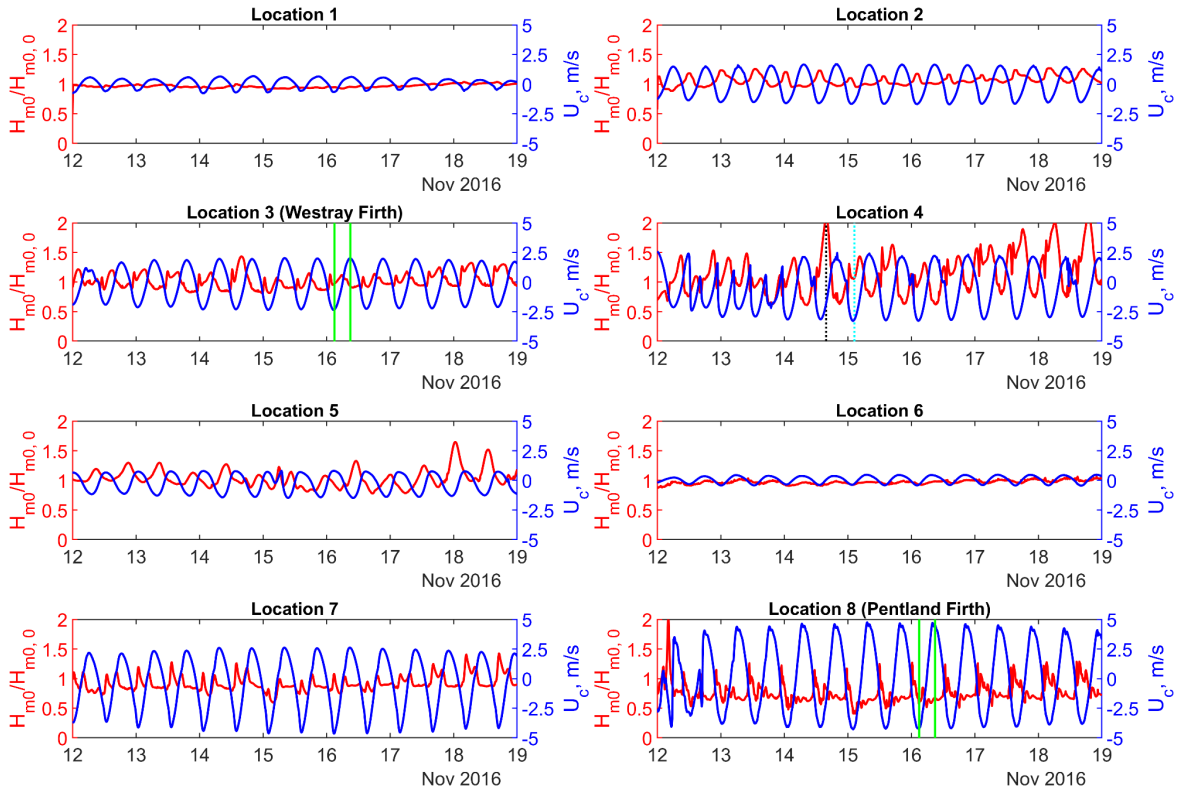

Figure 3.6 $H_{m0}/H_{m0,0}$ and the relative current velocity U_c during a Spring Tide week

Green lines indicate the time points selected for subsequent spectral analysis in Section 3.4.

method [73,74] in the wave-current coupled model, rather than solely relying on the white-capping process.

Notably, at a nearby point with a comparable level of opposing tides (marked by a black colour dot line in Figure 3.6), waves do not break, with the amplitude ratio reaching 2. This occurs because the base wave-only height is smaller (as shown in Figure 3.4), so the wave steepness may not reach the threshold for breaking.

Based on the above analysis, the time periods at which wave breaking occurred can be easily identified by examining the $H_{m0}/H_{m0,0}$ time series if discontinuous spikes appear. With this method, Location 3, 7, and 8 are found to have pronounced wave breaking. At Location 8, the amplitude ratios are primarily distributed below 1 when the ambient current velocity exceeds 4 m/s. This indicates enhanced wave breaking, and the wave-current coupled model consistently produced smaller wave heights compared to the wave-only model.

3.2.2 Mean wave periods T_m

Tidal currents seem to have a greater effect on wave periods as well, as seen in Figure 3.7 (Neap Tide) and Figure 3.8 (Spring Tide). For instance, at Locations 1 and 6, wave periods show clear modulation even during the Neap Tide (note that their wave heights remain unchanged). Interestingly, this study observed a phenomenon contrary to the common sense, that is, when the tide flows in the opposite direction to the wave (negative U_c), the wave period becomes longer. As noted in the validation at Westray Firth in the previous section, this outcome is also supported by observations from the AWAC measurements. It is worth bearing in mind that these wave periods are not calculated as individual wave by wave cycles, instead they are an average of a number of wave cycles.

To analyse this phenomenon, it is crucial to recognize that both the observations and numerical model outputs represent apparent (absolute) periods (i.e., the period observed at a fixed point), rather than intrinsic (relative) wave periods (i.e., the period observed in a coordinate system moving with the current, where the linear wave theory applies). To better apply the theory, the concept of frequency will be temporarily used instead of period. The intrinsic (relative) angular wave frequency (denoted by σ) is related to the wave number, k, by the dispersion relation [85]:

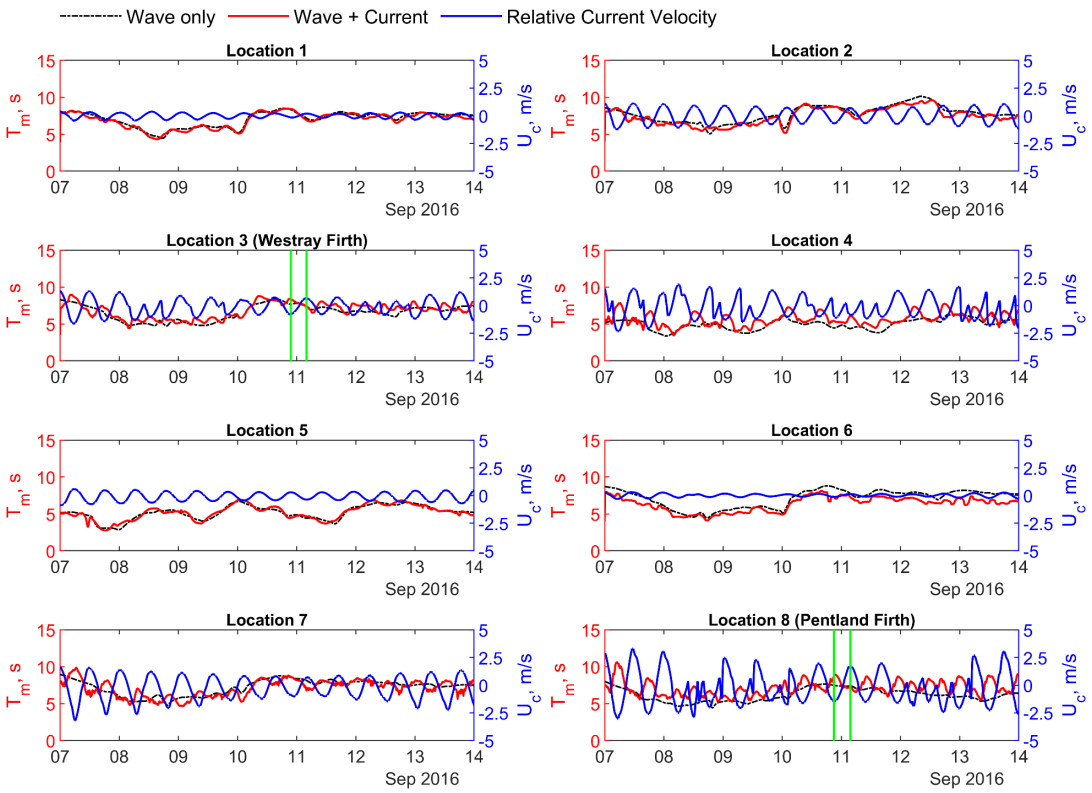

Figure 3.7 T_m timeseries against the relative current velocity U_c during a Neap Tide week

Green lines indicate the time points selected for subsequent spectral analysis in Section 3.4.

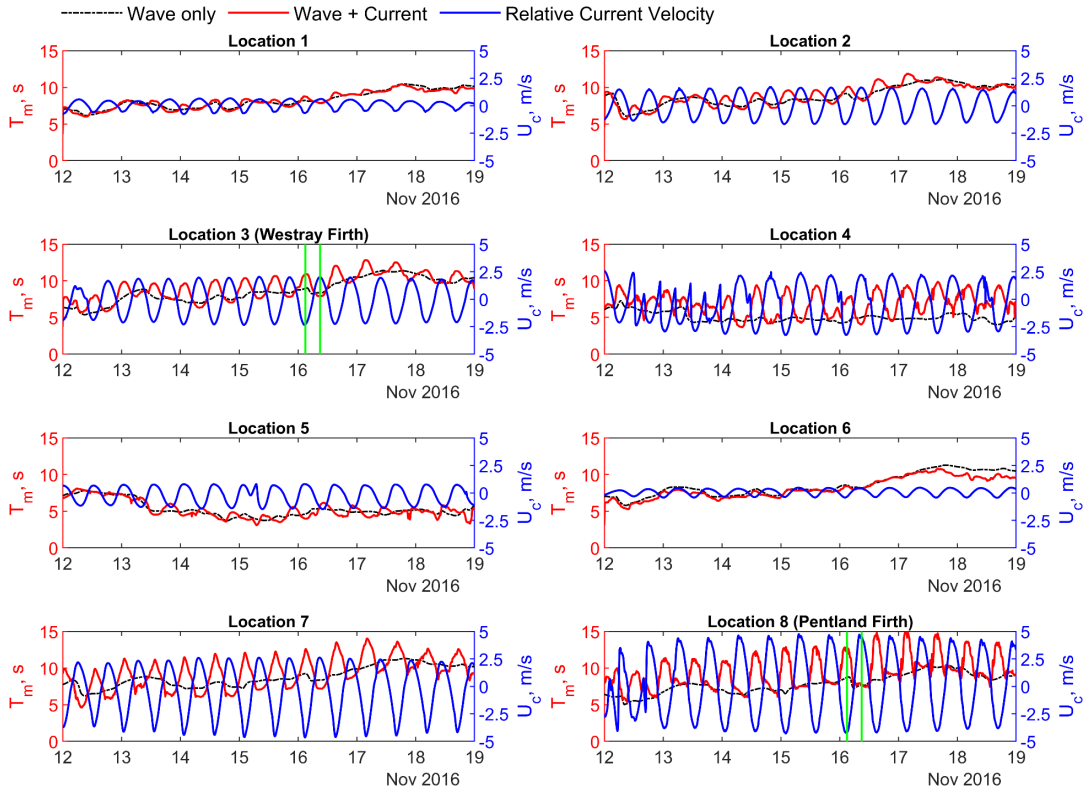

Figure 3.8 T_m timeseries against the relative current velocity U_c during a Spring Tide week

Green lines indicate the time points selected for subsequent spectral analysis in Section 3.4.

$$\sigma = \sqrt{gk \tanh kh} \tag{3.3}$$

where, the water depth is h. The Doppler shift explains the relationship between intrinsic frequency, σ, and apparent frequency ω is

$$\omega = \sigma + kU_c \tag{3.4}$$

Therefore, waves with the same apparent period ($2\pi/\omega$) exhibit longer intrinsic periods ($2\pi/\sigma$) in following currents ($U_c > 0$) and shorter intrinsic periods in opposing currents ($U_c < 0$). However, given that ambient currents vary spatially and temporally in this study, both apparent and intrinsic period will also vary and it is unrealistic to assume that either the apparent or the intrinsic periods remain the same. Derived by Jonsson [34,86], in the non-homogeneous and unsteady medium, the time derivative of the apparent frequency of current is given by

$$\frac{d\omega}{dt} = \frac{\sigma}{\sinh 2kh} \cdot k \cdot \frac{\partial h}{\partial t} + k \cdot \frac{\partial U_c}{\partial t} = k\left(\frac{\sqrt{gk \tanh kh}}{\sinh 2kh} \cdot \frac{\partial h}{\partial t} + \frac{\partial U_c}{\partial t}\right) \tag{3.5}$$

In deep water, the depth-related term disappears, and the rate of change of the apparent frequency depends on the wavelength k and the rate of change of the relative velocity U_c. In other words, any change in sign of the apparent frequency ω aligns with the sign of the rate of change of relative velocity U_c. Consequently, when converted to apparent period by $2\pi/\omega$, the rate of change in period is trends oppositely to the relative velocity U_c. That is, a positive gradient of U_c (i.e., when U_c increases) corresponds to a negative gradient in the periods (i.e., the T_m values decrease), which corroborates the simulation results.

3.2.3 Mean wave directions

Before proceeding to the detailed analysis, it should be borne in mind that both wave and tidal directions represent the direction of ‘travel-towards’. The angle 0 degrees points to the north, with positive values indicating clockwise rotation. Figure 3.13 and Figure 3.14 present the wave and tidal directions at each site during the Neap and Spring Tides, respectively. The range of angles at Location 3, 4, and 5 is adjusted to [-60°, 300°] (axis is marked by red colour) rather than [0°, 360°] used at other sites. This adjustment ensures that the plots appear continuous, as frequent directional changes occur at these locations during the analysis period.

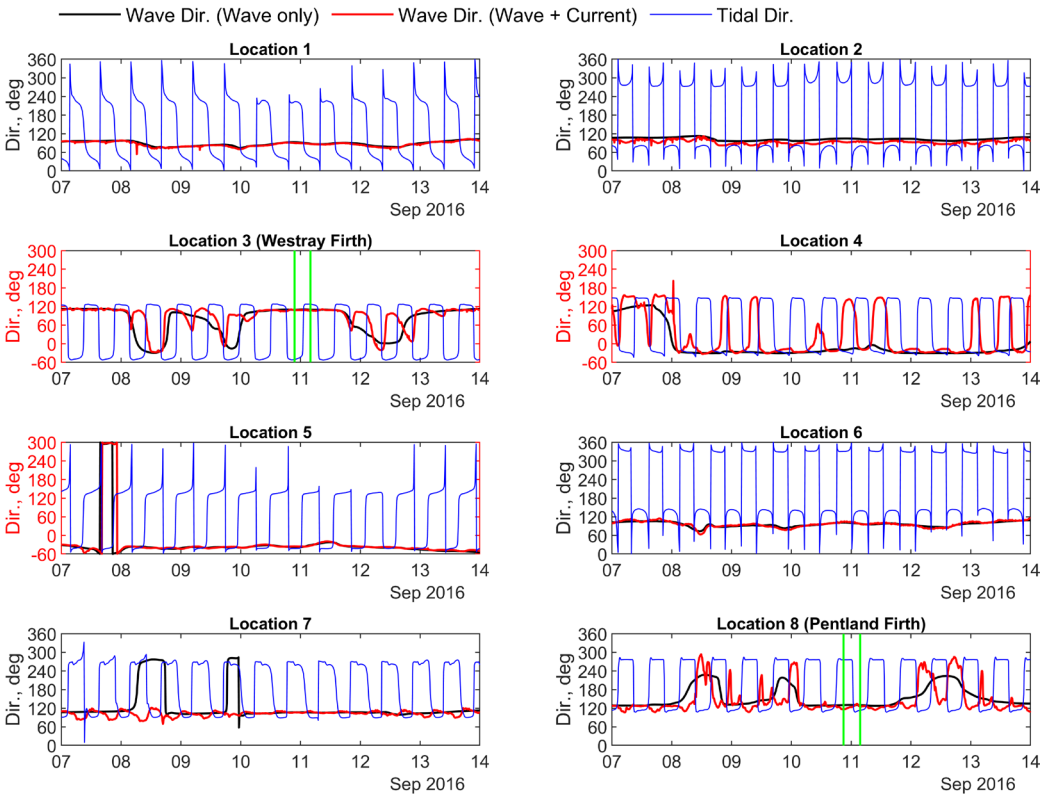

Figure 3.9 Mean wave direction time series during a Neap Tide week

Green lines indicate the time points selected for subsequent spectral analysis in Section 3.4.

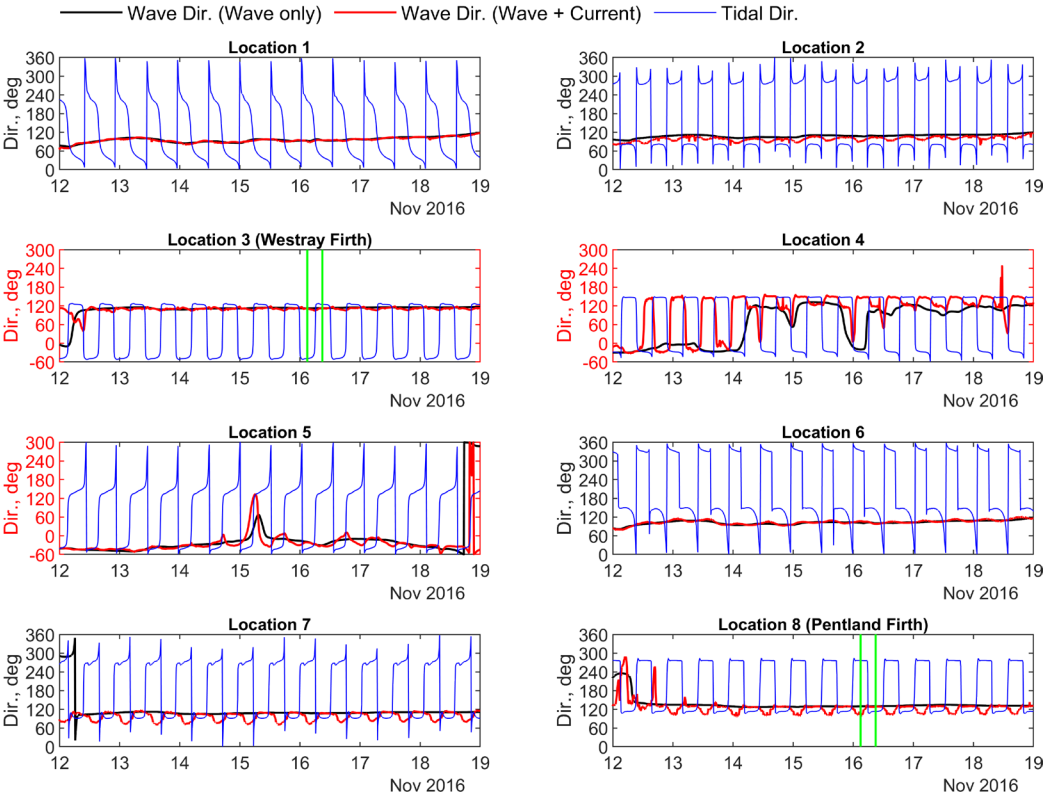

Figure 3.10 Mean wave direction time series during a Spring Tide week

Green lines indicate the time points selected for subsequent spectral analysis in Section 3.4.

In general, Locations 1, 2, and 6 are primarily influenced by winds from the North Atlantic, resulting in a straightforward, eastward wave direction. Location 5 is shaped by winds from the North Sea, causing waves to move westward. The remaining locations (3, 4, 7, and 8) experience alternating wave directions, driven by the shifting dominance between the North Atlantic and the North Sea winds.

In comparison to the tidal current propagation directions, the wave directions at all the eight target sites vary quite a lot. Locations 1 and 6 show minimal modulation in directions for the combined wave and current case, regardless of whether it is Neap or Spring Tide. Conversely, Locations 2 and 7, located at the water channel inlet, exhibit noticeable modulation during the Spring Tide compared to the Neap Tide. Specifically, wave directions remain unchanged in following currents but move toward the direction of tidal currents when wave is opposing. This observation aligns with the concept of current-induced refraction, where waves shift toward areas with lower absolute wave propagation speeds. This can be explained by the Snell's law [34]:

$$\frac{\sin(\beta_2)}{\sin(\beta_1)} = \frac{L_2}{L_1} \tag{3.6}$$

where β is the angle between wave direction and the normal to current direction. In the following currents, the wavelength L is expected to be stretched, a larger L leads to a larger $\sin(\beta)$ value, meaning the waves move towards the current. This supports the idea that the waves are refracted by the currents.

At Location 4, however, an opposite phenomenon occurs; when the waves and tidal current directions are aligned, the wave is refracted in the exact opposite direction of the current. Ignoring the depth-induced refraction, this behaviour can still be explained by [87,88],

$$\frac{d\alpha}{dt} = -\frac{\partial U_c}{\partial x} \tag{3.7}$$

where ∂x means change in the distance (x) along the wave crest between two points. This equation accounts for the negative spatial gradient of the current. Based on the map, Location 4 is positioned between two islands, a region expected to experience the area's maximum tidal speeds. As the ebb tide decelerates, the high negative spatial gradient $(-\partial U_c/\partial x)$ causes a rapid angular change in wave direction (α), making the waves propagate opposite to the tide. This refraction is less evident during the flood tide, as the tidal speed is smaller during the flood compare to the ebb (as shown in Figure 3.6 and Figure 3.8, the magnitude of

the negative U_c is larger than the positive U_c). Further analysis could provide more insights if a spatial gradient map of the tidal current were available.

It is important to note that not all negative spatial gradients at Location 4 result in a complete reversal of wave direction. For instance, during the period from September 12–13, 2016, when wave heights were unusually high, only a slight angular shift occurred in the direction opposite to the current, rather than a complete reversal. This suggests that wave refraction is actually influenced by complex factors, not solely by negative spatial gradients, but also by the magnitude of waves.

A mixed refraction pattern is observed at Locations 3 and 8, where wave heights are significantly higher than at Location 4, and tidal currents are strong. When Atlantic winds dominate, directing waves eastward, refraction towards the tidal current is predominant. Conversely, when North Sea winds prevail, causing a westward shift in wave direction, the waves are generally less affected by negative gradient effects due to their lower heights, resulting in refraction opposite to the tidal current.

3.3 H_{m0} - T_p analysis

Scatter plots of significant wave heights versus peak wave periods at eight sites during neap (Figure 3.11) and spring (Figure 3.12) tides reveal varying levels of wave-current interaction, with more dispersed points during spring tides at all locations.

Location 1 and 6, characterized by long wave heights and periods, show the least variation due to their slow tidal currents (less than 0.68 m/s during neap and 1.11 m/s during spring tides). Tidal currents mainly reduce wave heights at these locations, reflected by a lower distribution of red points. Location 2 experiences faster tidal currents (1.22 m/s during neap and 1.78 m/s during spring tides), leading to an overall increase in wave height but still showing stable wave height-period relationships. These three sites consistently exhibit mature waves with low steepness, maintaining tightly clustered scatter points, regardless of WCI.

Location 5, with short waves and high periods, shows low wave energy, driven by local winds, with minimal tidal impact because of a slowing moving ambient current (smaller than 0.88 m/s during Neap and 1.5 m/s during the Spring Tide). In contrast, Location 4, which also had short waves and high periods, experiences much faster currents (up to 3.29 m/s), nearly doubling the range of peak periods due to stronger tidal influence.

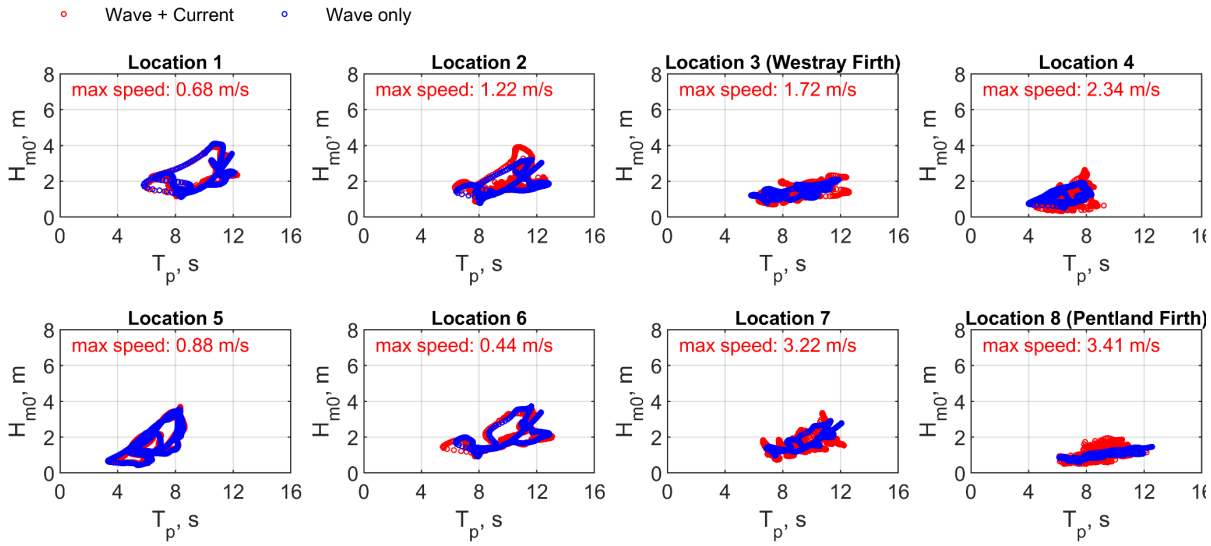

Figure 3.11 Scatter plots of T_p and H_{m0} during a Neap Tide week

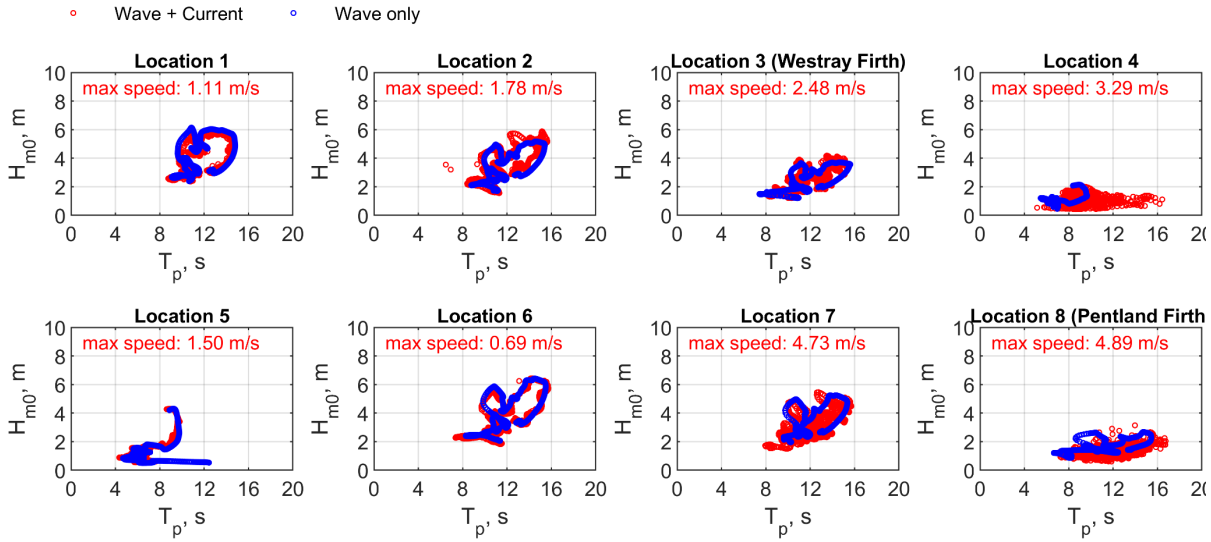

Figure 3.12 Scatter plots of T_p and H_{m0} during a Spring Tide week

Locations 3, 7, and 8, facing the North Atlantic, show a broader range of periods due to the swell component and fast currents, causing more scattered points. During neap tides, wave heights fluctuate, but during spring tides, locations 7 and 8 experience a marked drop in wave heights due to wave breaking in the Pentland Firth.

3.4 Directional wave spectra analysis

This section provides a detailed analysis of WCI using high-resolution wave spectrum through 36 directional bins (10° increments) and 36 frequency bins (in which 27 are located within 0.3

Hz) for Locations 3 and 8 in Westray Firth and Pentland Firth, respectively (Figure 3.13 and Figure 3.14). The left-hand subplot shows the unidirectional wave spectrum corresponding to the mean wave direction, and the right-hand plots are for directional spectrum of the wave-only (second column) and wave-current coupled cases (third column), and their differences (wave-current coupled model minus wave-only model, in the fourth column)). Four examples of the ebb and flood phases at both Neap and Spring tide periods are presented for each location. These selected intervals are also highlighted by solid green lines in the previous timeseries from Figure 3.3 to Figure 3.10. Notably, during the flood tide, currents flow from the North Atlantic into the channel, aligning with the primary wave directions in this region. In contrast, the ebb tide always represents opposing current flow relative to the waves.

Assuming ideal conditions—namely, no wave breaking, steady tidal currents, and the applicability of linear wave theory—the wave energy spectrum is expected to exhibit a more concentrated energy density distribution (i.e., narrower unidirectional spectra) with higher peak values during ebb flow (opposing directions), and a more dispersed distribution (broader spectra) with lower peak values during flood flow (following directions). These effects arise primarily due to Doppler shift mechanisms, as explained in Section 373.2.

In the higher-frequency band (i.e., >0.15 Hz), the spectral tail should be often suppressed by dissipative processes induced by tidal currents, leading to a net reduction in energy at these frequencies. This reduction is expected to occur regardless of current direction but should be typically more pronounced under opposing currents. In some cases, a portion of the suppressed high-frequency energy may cascade back toward lower frequencies.

Notably, when wave breaking is considered, the spectral behaviour during ebb flow can become more complex. In such scenarios, the peak energy may decrease due to enhanced energy dissipation, counteracting the sharpening effect predicted under idealised, non-breaking conditions.

3.4.1 Ebb Tide

At Location 3, during the ebb phases (opposing flows, Figure 3.13 (a) and (c)), the unidirectional spectrum (left) exhibits an increase in peak energy density when current effects are included, resulting in higher wave heights. This increase is much more evident from the right-hand side ‘difference’ spectrum, which shows that the energy increase occurs dramatically in directions skewed toward the tidal current (depicted in red colour), while the energy peak of the previous wave-only model is reduced. This redistribution of wave energy causes

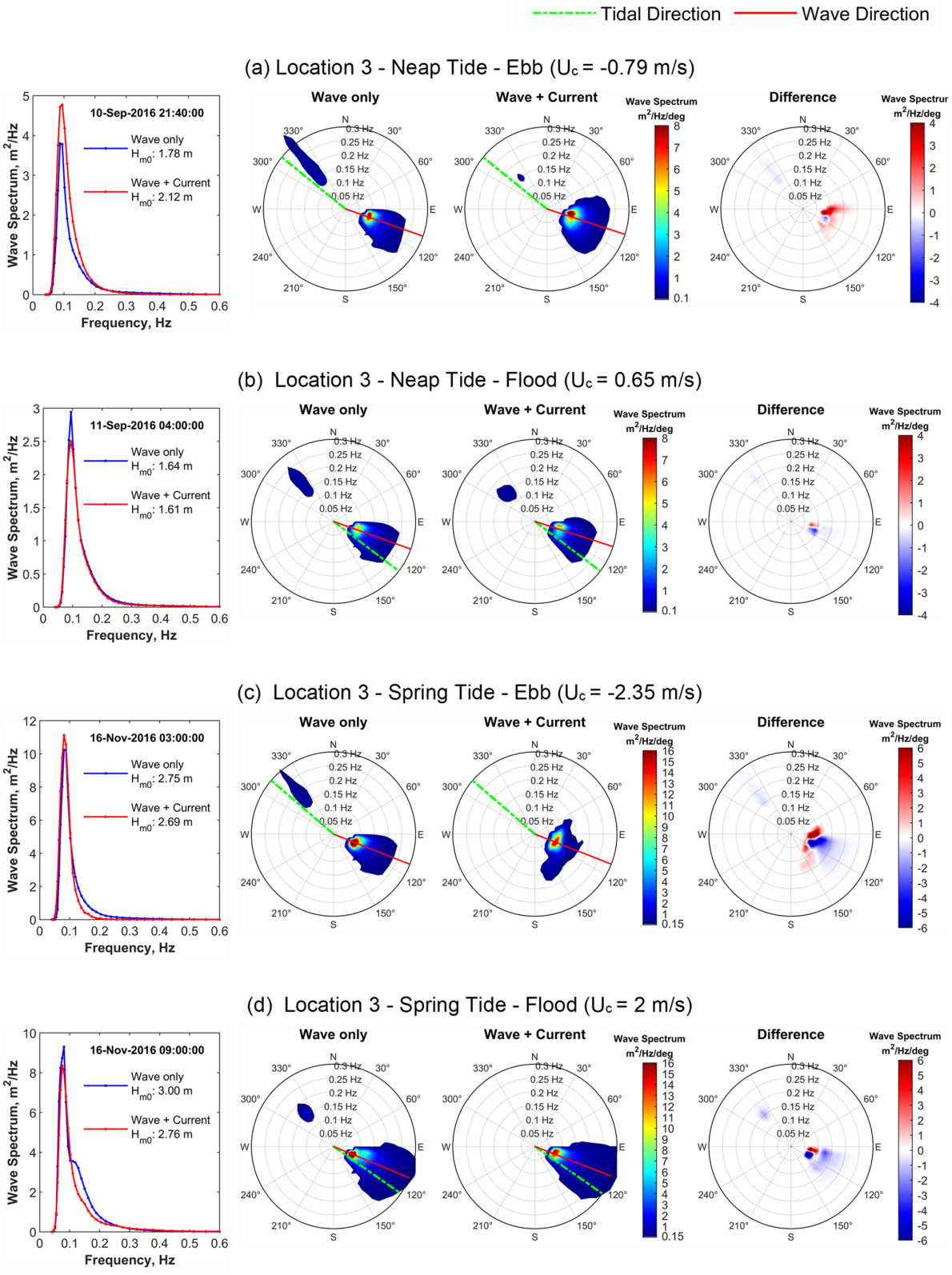

Figure 3.13 Unidirectional and directional wave spectra at Location 3 in Westray Firth

Panels (a) and (b) depict the Ebb and Flood phases during the Neap Tide period, while panels (c) and (d) illustrate the Ebb and Flood phases during the Spring Tide period. Ebb flow (opposing direction) shows an overall energy increase, mainly around the peak wave frequency (~0.1 Hz, or wave periods ~10 s) when tidal currents are present. Flood flow (following direction) shows an overall energy decrease. For both ebb and flood flows, the energy in the higher-frequency band (>0.15 Hz) is generally reduced.

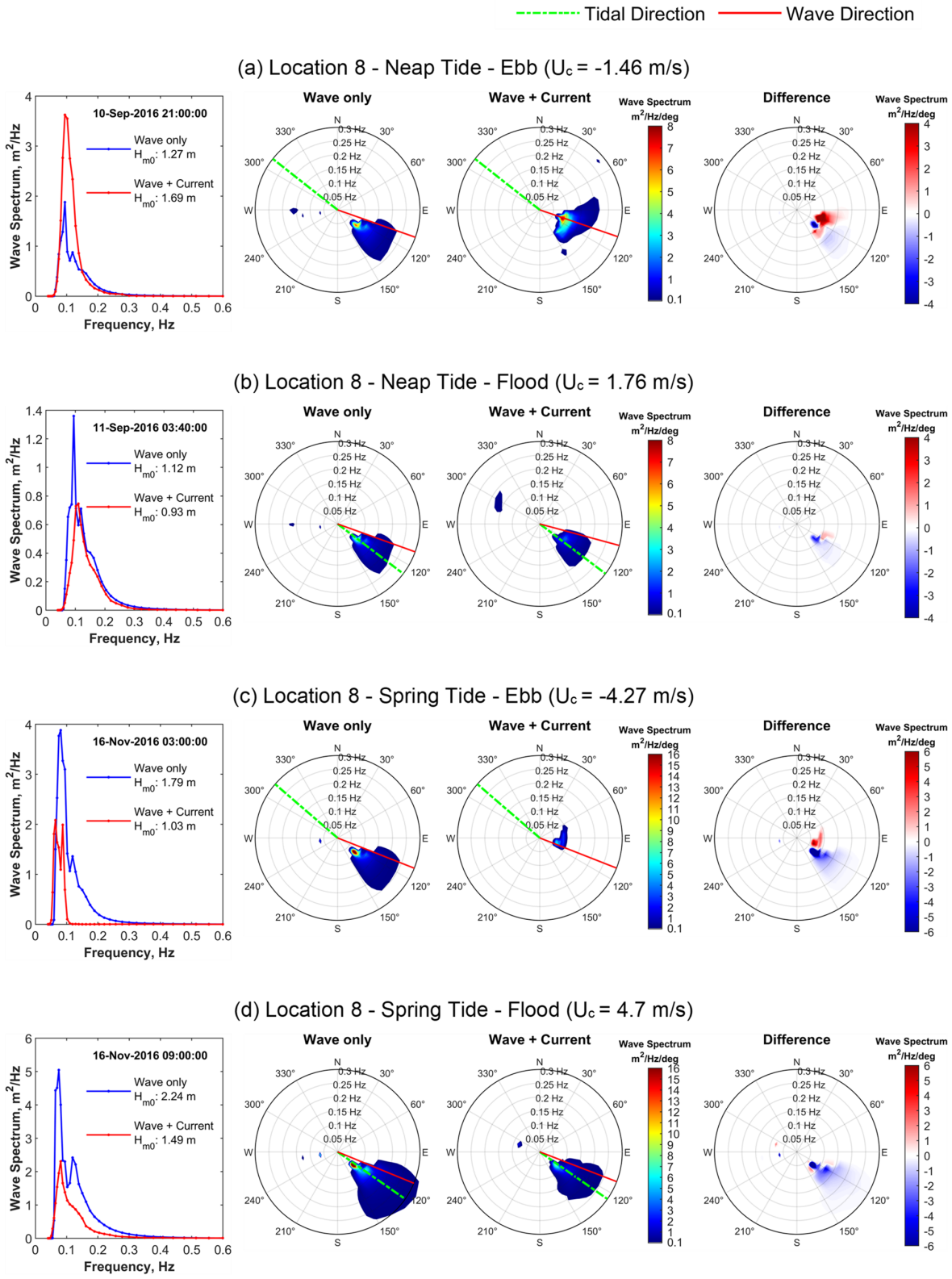

Figure 3.14 Unidirectional and directional wave spectra at Location 8 in Pentland Firth

Panels (a) and (b) depict the Ebb and Flood phases during the Neap Tide period, while panels (c) and (d) illustrate the Ebb and Flood phases during the Spring Tide period. The ebb and flood flows exhibit similar patterns to those shown in Figure 3.13, with the main difference observed in panel (c), where there is a more pronounced decrease in energy. This is primarily attributed to wave breaking under strong tidal currents.

an overall bending of the wave direction toward the tidal current, consistent with tidal-induced wave refraction under opposing flows.

In the Pentland Firth, at Location 8, the redistribution of wave energy in opposing flows follows a similar pattern but is more pronounced. During the Neap tide in Figure 3.14 (a), the energy increase in unidirectional spectrum is still much more significant. However, during the Spring Tide in Figure 3.14 (c) with faster tidal currents (-4.27 m/s relative tidal current speed), wave energy in the direction opposite to the tidal current is significantly dissipated, with the energy at frequencies above 0.1 Hz nearly vanishing. This results in an overall decrease in the values of the unidirectional spectrum, leading to wave breaking and smaller waves (H_{m0} = 1.03 m) than those predicted by the wave-only model (H_{m0} = 1.79 m).

3.4.2 Flood Tide

At Location 3, during flood phases (following directions, Figure 3.13 (b) and (d)), the unidirec-tional spectrum shows a decrease in peak energy density when current effects are included, leading to reduced wave heights. The ‘difference’ spectrum shows noticeable decrease in wave energy at the direction of the tidal currents (blue colour), while an increase in energy is observed at the original wave direction. These changes result in an overall minimal shift in wave direction, which explains the limited directional shifts observed during following flows. A similar phenomenon but more severe reduction is observed at Location 8, where tidal speeds are much faster, as demonstrated by Figure 3.14 (b) and (d).

Interestingly, at Location 3, the directional spectrum for the wave-only case consistently shows wave energy components traveling opposite to the primary wave direction, particularly at higher frequencies (above 0.12 Hz, sometimes exceeding 0.3 Hz during flood tides), possibly representing wind-driven waves from the North Sea. Tidal influence significantly reduces these high-frequency opposing wave components, regardless of whether in the ebb or flood flows. It is also noteworthy that the ‘difference’ spectrum may be specific to cases with strong tides. The results may differ in regions where currents are weaker. For example, in the Zhoushan Sea area in China, where tidal speeds are mainly under 1 m/s [89], studies have found that the peak value of the directional wave spectrum from the wave-current coupled model is consistently lower than that of the wave-only model, for both maximum flood and maximum ebb tides. However, our case demonstrates that this is not always the case, as shown in Figure 3.13 (a) and Figure 3.14 (a).

3.5 Advancement over previous research

Wave-current interactions have been widely studied in the past [34,89]. However, most of that research focused on scenarios with moderate conditions (i.e., wave heights below 2 m and tidal current speeds under 1.5 m/s), rarely leading to wave-breaking events and often explained by Doppler effects. In contrast, the unique geography of the Pentland Firth and Orkney Waters results in a more extreme combination of fast tides (exceeding 4 m/s) and high waves (over 2 m), leading to frequent wave-breaking events, as shown by high-frequency spikes in field data recordings.

Using the wave-current coupled model, this study, as presented in the above sections, reveals more pronounced WCI effects at various locations. As demonstrated in the timeseries plots, for the region around the Stroma Island of the Pentland Firth, wave heights in the presence of WCI are generally lower than in the absence of currents, even in opposing tidal conditions on seasonal and annual timescales. This study also suggests that the method proposed by [90], which applies a frequency filter to data recordings to generate current-free wave parameters, may significantly overestimate wave heights and underestimate WCI effects in regions like the Pentland Firth.

3.6 Summary

This study further analysed the effects of wave-current interactions using the wave-only and wave-current coupled numerical models with specific focuses on eight locations around PFOW. These locations represent a range of sea conditions and may also serve as a reference for similar studies in other areas. By analysing the timeseries, scatter plots, and wave spectrum, key findings are obtained:

- Tidal currents opposing wave propagation increased wave heights; however, in strong tidal conditions, this led to wave steepening and enhanced breaking, ultimately reducing overall wave heights.

- Opposing currents to waves resulted in an increase in apparent wave periods.

Current-induced refraction might have caused waves to bend in the current's direction; however, in areas with high negative spatial gradients in the current, waves might have been bent in the opposite direction.

Chapter 4

Ten-Year (2014-2023) Wave Resource Map with Tidal Effects for PFOW

This chapter employs the numerical models described in Chapter 2 to conduct a 10-year simulation for both the North Atlantic region, generating wave parameters unaffected by tidal currents, and the PFOW region, regenerating wave parameters influenced by tidal currents.

The chapter presents interannual, seasonal, monthly, and 10-year extreme condition wave maps and accompanying analyses. Monthly mean results for each year from 2014 to 2023 are included in Appendix B.2 as supplementary material.

4.1 Inter-annual analysis

The analysis focuses on the PFOW region, with the maps zoomed in on the area between 58.5°N - 59.5°N latitude and 2°W - 4°W longitude. Three locations (Figure 4.1) with potential for wave energy development, situated on the west side of the Orkney Islands and within the Pentland Firth, are selected for detailed analysis. These locations differ from the eight sites analysed in the previous chapter.

- P1: Located at the tidal inlet of the Westray Firth, where the maximum tidal speed is around 1.5 m/s.
- P2: Positioned 700 m westward of the EMEC Billia Croo wave test site on the west side of the Orkney Mainland, with a maximum tidal speed of around 0.4 m/s.
- P3: Situated at the mouth of the tidal inlet of the Pentland Firth, where the maximum tidal speed is around 2.2 m/s.

The inter-annual analysis examines annual mean wave heights and wave power from 2014 to 2023, offering insights into common characteristics and variability over a 10-year scale. This section first describes the spatial characteristics of wave resource distribution and then

compares results between the wave-current coupled model and the wave-only model to assess the impact of tidal currents.

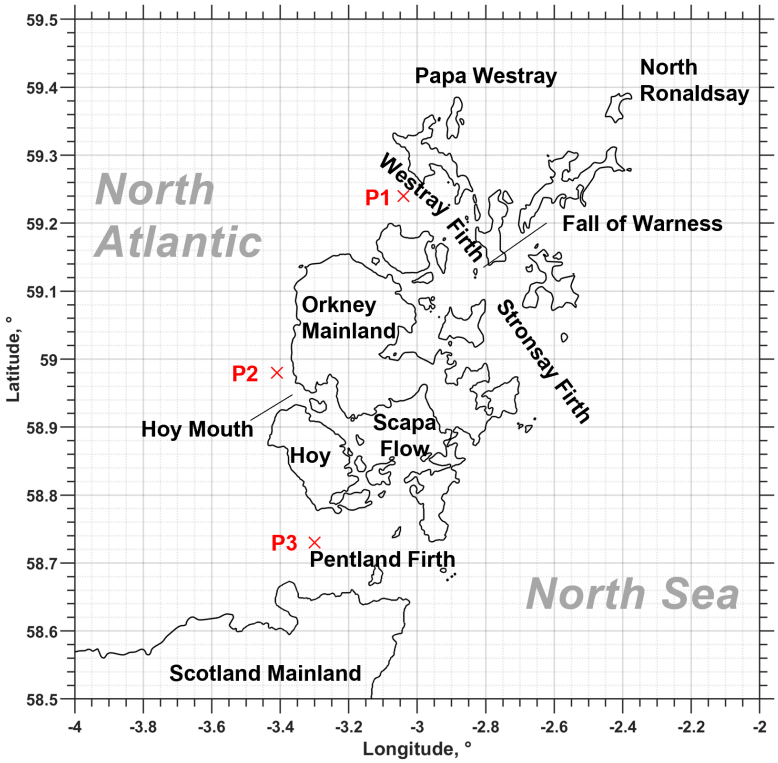

Figure 4.1 Geographical positions of P1, P2, and P3 for the case study in PFOW

4.1.1 Wave resources distribution

The annual mean H_{m0} and wave power generated by the wave-current coupled model are presented in Figure 4.2 (a) and Figure 4.3 (a). Over the ten-year period, the wave parameters display a consistent distribution pattern: values on the western side of the Orkney Islands are always higher than the eastern side, due to the North Atlantic serving as the primary source of wave energy for this region. This west-east geographic variation is most evident in the Pentland Firth. The annual mean H_{m0} and wave power at its western entrance, such as P3, reach over 2 m and 25 kW/m, while dropping to less than 1.25 m and 10 kW/m near Stroma Island.

Distinct inter-annual variations were observed throughout the decade. Wave levels on the North Atlantic side were significantly higher in 2015, 2020, and 2022 compared to other years, while 2021 exhibited the lowest levels. At P2, for instance, the maximum inter-annual difference in H_{m0} was 0.5 m, dropping from 2.6 m in 2015 to 2.1 m in 2021. The variability in wave power was even greater, as summarized in Table 4.1. For P2, wave power ranged from a high of 47.6 kW/m in 2015 to a low of 30.4 kW/m in 2021, a maximum inter-annual difference of

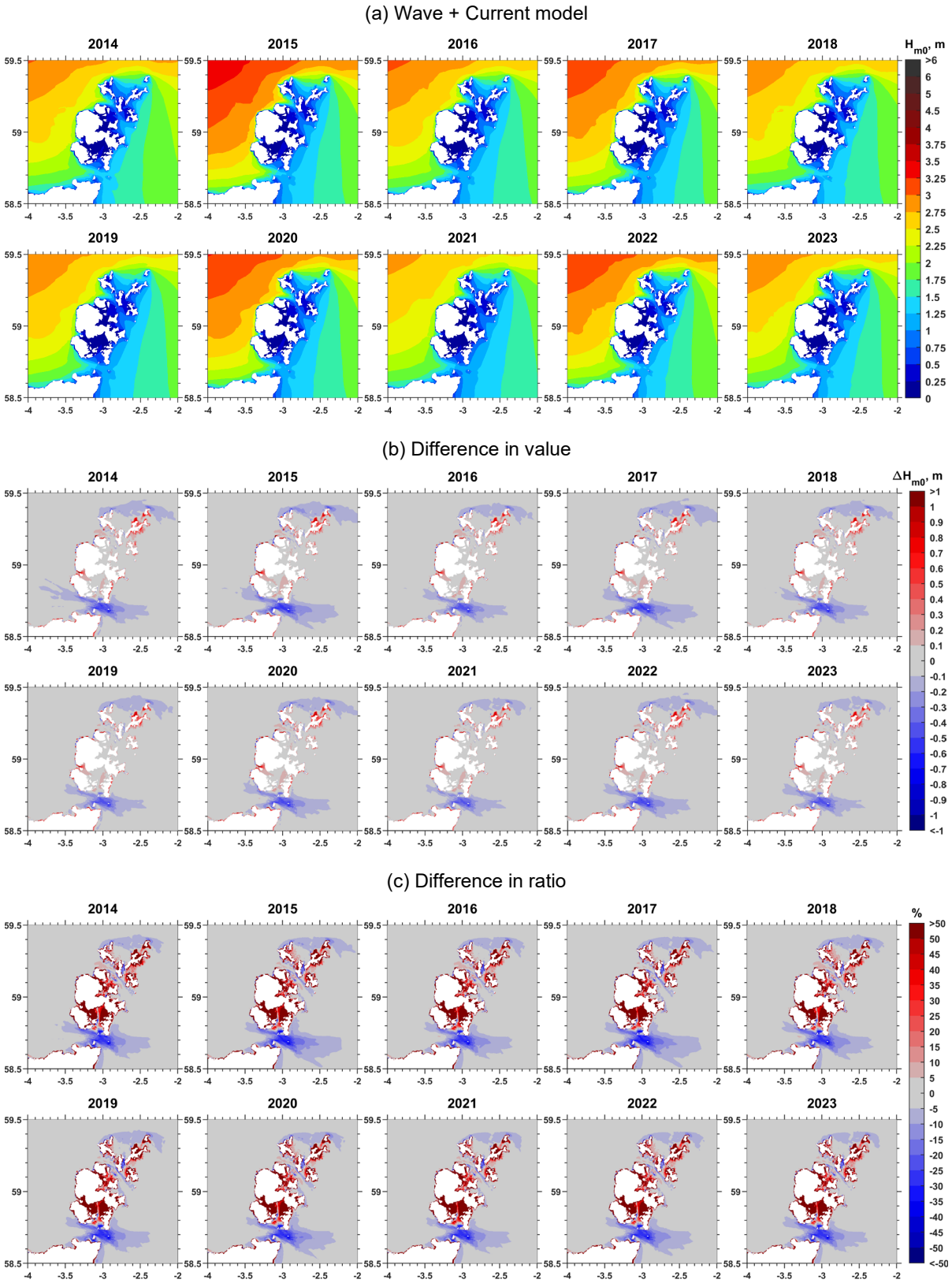

Figure 4.2 Annual mean H_{m0} map from 2013 to 2024

(a): Hm0 produced by the wave-current coupled model. (b): Numerical difference of wave-current model to wave-only model. (c): Ratio difference of the wave-current coupled model to wave-only model.

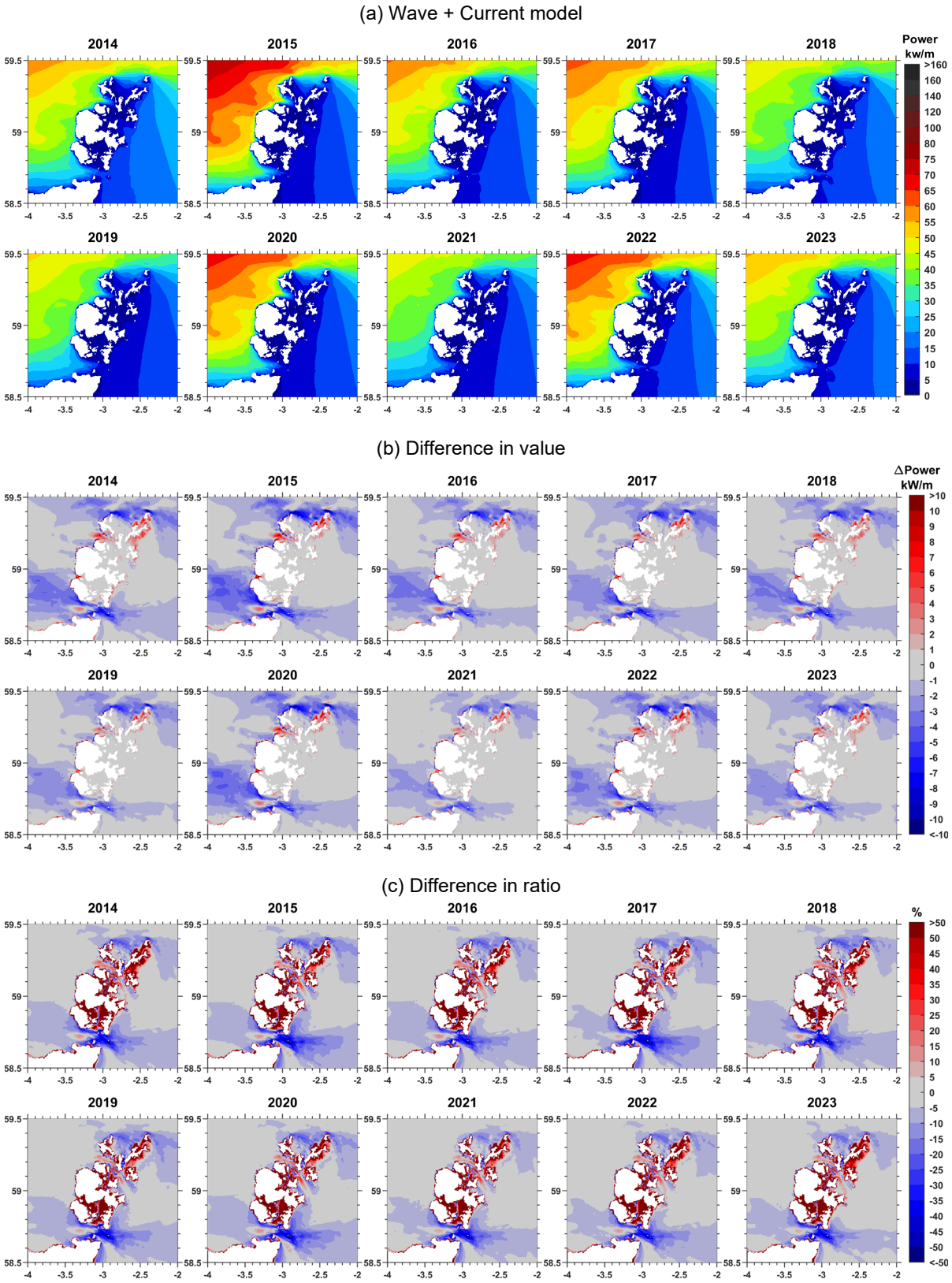

Figure 4.3 Annual mean wave power map from 2013 to 2024

(a): Wave power produced by the wave-current coupled model. (b): Numerical difference of wave-current model to wave-only model. (c): Ratio difference of the wave-current coupled model to wave-only model.

17.2 kW/m. Relative to the 10-year mean of 37.2 kW/m, this variability spanned from +28% in 2015 to -54% in 2021.

Similar patterns were observed at other locations. At P1, wave power variability ranged from +30% to -20%, and at P3, the range was +32% to -25%. These findings underscore the importance of long-term assessments in accurately evaluating resource potential. Reliance on data from only one or two years could lead to substantial over- or underestimation of wave energy resources.

Table 4.1 Annual mean wave power (kW/m)

Table includes highest wave year (2015) and lowest wave year (2021), and the 10-year mean for site P1 (Westray Firth inlet), P2 (the west Orkney), and P3 (Pentland Firth inlet). “W” represents the wave-only model; ““W+TC” represents the wave-current model.

Year	P1		P2		P3	
	W	W + TC	W	W + TC	W	W + TC
2015	44.3	55.0	49.8	47.6	33.4	37.6
2021	28.9	33.9	31.6	30.4	19.3	21.4
10 years mean	34.5	42.2	38.7	37.2	25.3	28.5

4.1.2 Tidal current effects

The impact of tidal currents on the wave resource is assessed by comparing simulation results from the wave-current coupled model with those from the wave-only model. Figure 4.2 (b) (c) and Figure 4.3 (b) (c) illustrate these effects, presenting differences in wave parameters as numerical values (i.e., coupled model – wave model) and as ratios (i.e., (coupled model – wave model) / wave model).

4.1.2.1 Numerical value difference

Minimal numerical differences (indicated in grey) are observed in open sea areas, such as the northwest and eastern of the Orkney Islands, and in sheltered waters enclosed by islands. These regions experience weaker tidal currents, leading to negligible impacts on wave parameters. Conversely, significant differences appear in straits, tidal inlets, and along the northern and southern edges of the Orkney Islands. Here, topographic constraints accelerate tidal currents, resulting in faster flows, as shown in Figure 2.9.

The reductions in wave height and wave power due to tidal currents are evident at the northern and southern edges of the Orkney Islands, including areas north of the Papa Westray, North Ronaldsay, and south of the Hoy Island. However, these reductions are less severe compared

to those observed around the northern and southern sides of the Stroma Island in the Pentland Firth, where tidal speeds exceed 4 m/s. Here, annual wave height reduction exceeds 0.5 m, and wave power reductions surpass 6 kW/m. These overall decreases are likely driven by enhanced wave breaking of the strong tidal currents. Supporting evidence comes from time series data (Figure 2.8) at the ADCP site in the Inner Sound (south of Stroma Island), which show high-frequency, discontinuous spikes characteristic of wave-breaking events.

Conversely, tidal inlets, such as Westray Firth, Hoy Mouth and Pentland Firth, show a noticeable increase in wave power (red areas in the map). For instance, P1 and P3 exhibit annual increases of up to 9 kW/m and 4 kW/m during high-wave years (e.g., 2015, 2020, and 2022). Over the decade, the mean increase is 7.7 kW/m for P1 and 3.2 kW/m for P3, and the detailed 10 years mean annual wave power can be found in Table 4.1. However, changes in wave height at these regions remain minimal.

4.1.2.2 Ratio difference

The ratio difference map mitigates the effects of varying wave baselines, providing a clearer representation of tidal influences. For instance, while the value difference map shows stronger tidal effects in 2015 compared to 2021, the ratio difference map shows nearly identical results for both years. This consistency highlights that the influence of tidal currents remains stable over the decade, largely independent of fluctuations in wave activity. A similar pattern is evident in spatial variations: although numerical differences in wave power are greater in the North Atlantic compared to the North Sea, the ratio differences indicate a comparable extent of tidal influence, remaining within 10% across both regions.

Tidal currents have their most significant influence near Stroma Island, where annual wave height changes exceed 25% and wave power changes surpass 50%, far exceeding the effects seen elsewhere in the Orkney Waters. The northern and southern edges of the Orkney Islands also see the reductions, similar to the previous finding in the numerical difference map, with the reduced percentage in H_{m0} and wave power being over 5% and 15%, respectively.

In tidal inlets, wave power increases are still notable. The ratio differences of the 10 years mean wave power reach to 22% in P1 at Westray Firth and 13% in P3 at Pentland Firth. A comparable increase is also observed in Stronsay Firth, although this effect is subtle in the numerical difference map due to the region's low wave activity (i.e., annual mean $H_{m0} < 1.25$ m, mean power < 10 kW/m). However, ratio differences reveal the tidal effects in this tidal-active region, where maximum speeds exceed 2 m/s.

Caution is needed when interpreting changes in regions with very low wave levels (i.e., H_{m0} close to 0). Specifically, in enclosed waters such as Scapa Flow and coastal zones, even minor variations in wave heights can yield high percentage changes, appearing as dark red areas on the ratio map. However, the corresponding grey areas on the numerical difference map indicate that tidal influence in these regions is negligible and unlikely to impact wave-current interactions meaningfully.

4.2 Seasonal analysis of 10-Year Averages

4.2.1 Map analysis

From the 10-year average wave hights and power for spring (March, April, May), summer (June, July, August), autumn (September, October, November), and winter (December, January, February) are presented in Figure 4.4 and Figure 4.5. These maps reveal significant

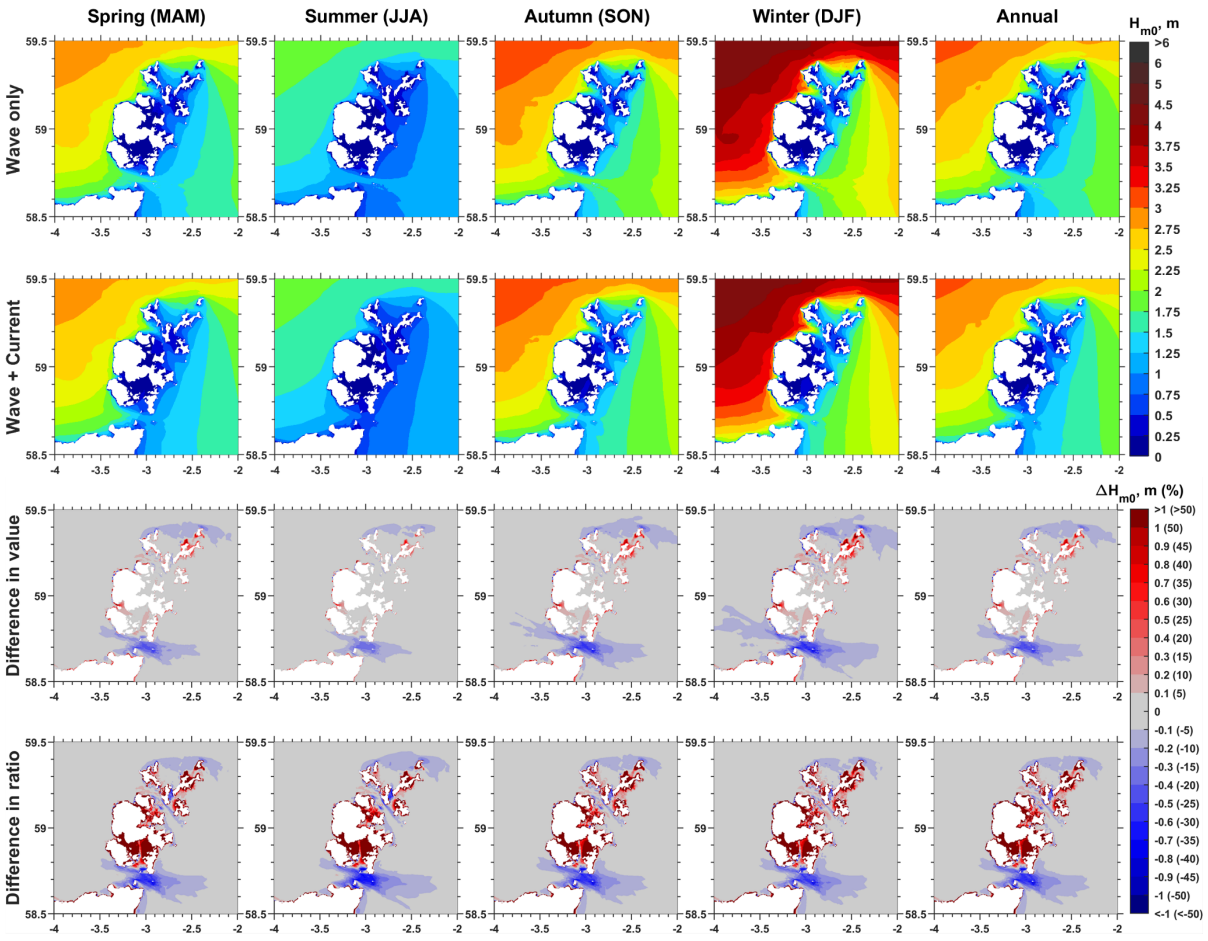

Figure 4.4 Seasonal mean H_{m0} over 10 years

seasonal variations in this region. In summer, the H_{m0} at the west Orkney nearshore areas are within 1.5 m, while it is above 3 m during the winter, with double of it in summer. This inter-season variability is more pronounced in the wave power, as summarized in Table 4.2. The wave-current coupled model shows that at P1, P2, and P3, winter wave power is approximately seven times greater than in summer. Relative to the annual mean over the decade, inter-seasonal variability ranges from -72% in summer to +91% in winter across these sites. Interestingly, the autumn seasonal mean values at these locations are very close to the annual mean, regardless of whether tidal currents are considered. This suggests that autumn results can serve as reasonable approximations of the annual mean.

While the maps of H_{m0} and wave power do not clearly differentiate between the wave-current coupled and the wave-only models, the difference maps (by numerical values and ratios) provide further insights. Numerically, differences are smallest in summer and greatest in wave-active winters, aligning with the overall wave levels. At P1, P2, and P3, the differences in wave power during summer are 1.5 kW/m, -0.7 kW/m, and 1.1 kW/m, respectively, compared to 16.7 kW/m, -2.3 kW/m, and 5.9 kW/m in winter. Similar to the wave maps, differences in

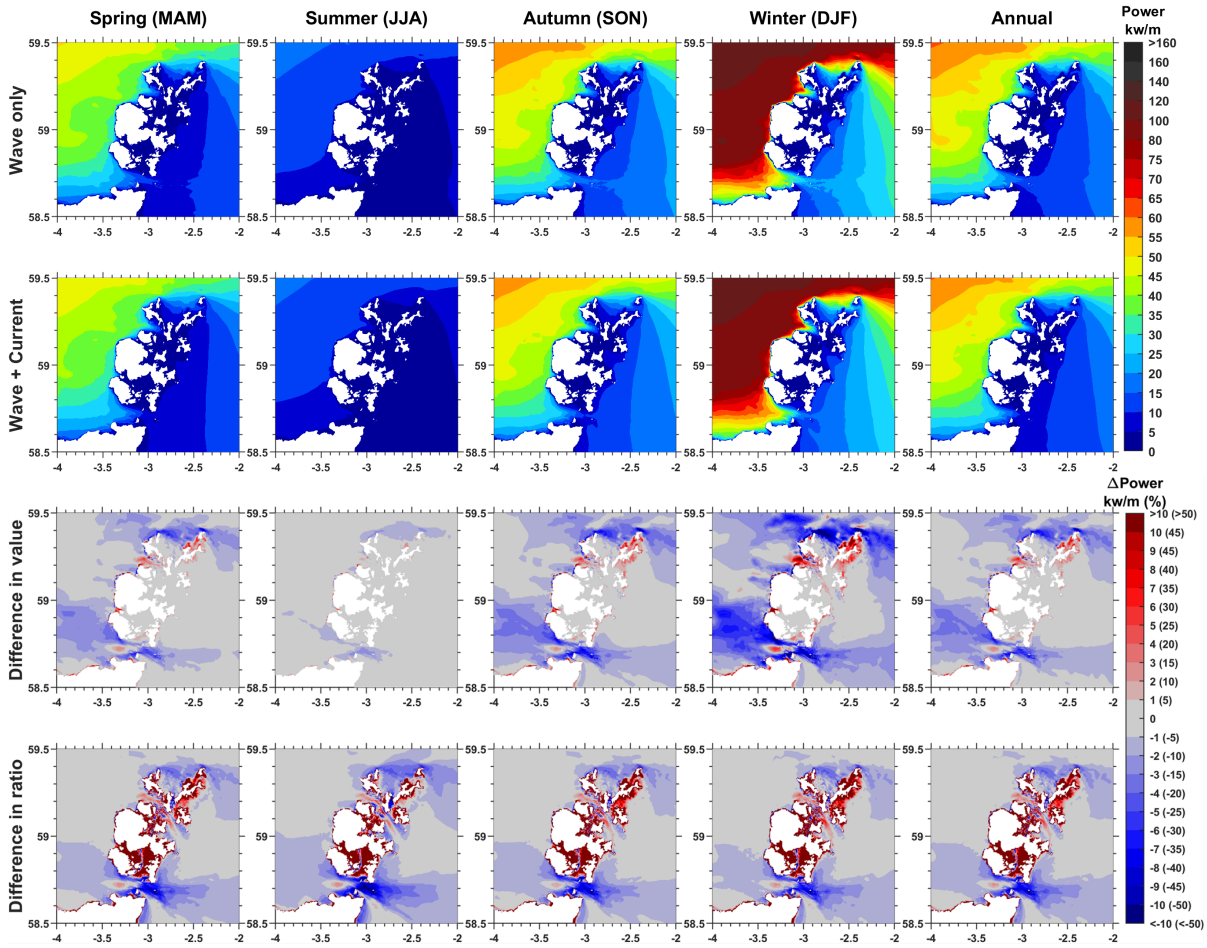

Figure 4.5 Seasonal mean wave power over 10 years

autumn closely resemble the annual differences. In contrast, ratio differences exhibit no significant seasonal variation. The regions and extents affected by tidal currents appear even slightly broader and more pronounced in summer compared to winter, highlighting the consistent nature of tidal effects irrespective of wave energy levels.

4.2.2 Rose plot of wave power

To further illustrate the seasonal variability under tidal current effects, wave power and mean wave direction are combined and presented as rose plots at P1, P2, and P3 throughout the season over the 10 years, and is shown in Figure 4.6 and Figure 4.7, Figure 4.8. Notably, the wave directions represent the direction of 'travel-from'; angle 0° in the rose plot points to the north, with positive values indicating clockwise rotation and bin size being 10°.

Across all sites, the primary directions contributing to wave power remain consistent across seasons, with the primary directions are around 280° for P1 and P2, while 290° for P3. As expected, winter consistently shows the highest wave power. Along the primary wave directions at P1, P2, and P3, wave power exceeds 80 kW/m approximately 20%, 15%, and 10% of the time during winter when tidal currents are considered.

The inclusion of tidal currents has varying effects on wave power distribution across the sites:

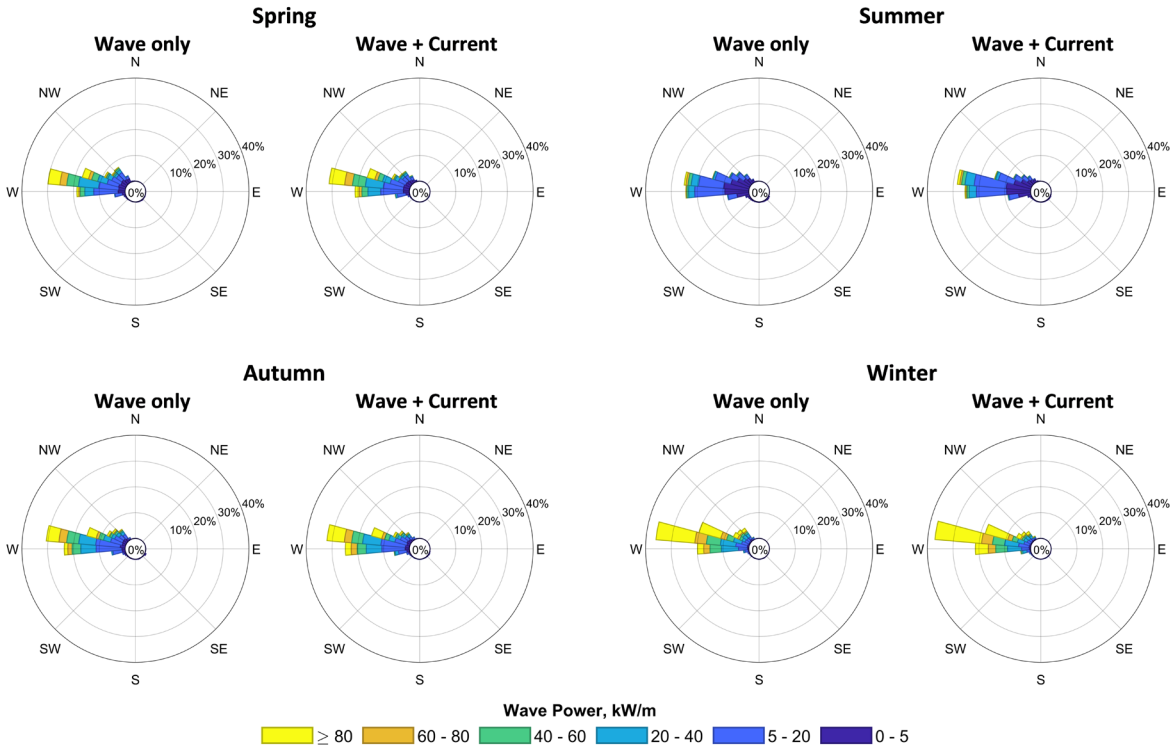

Figure 4.6 Seasonal wave power rose plots over a 10-year period at P1 (the West Orkney)

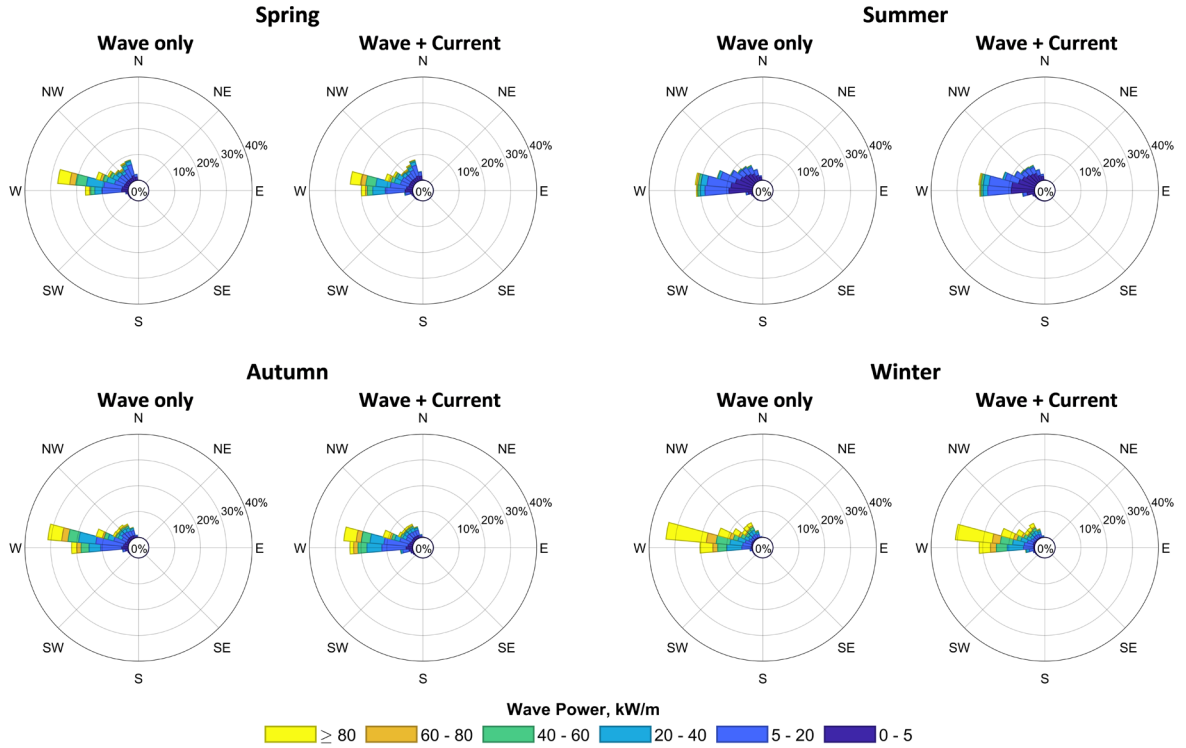

Figure 4.7 Seasonal wave power rose plots over a 10-year period at P2 (Westray Firth inlet)

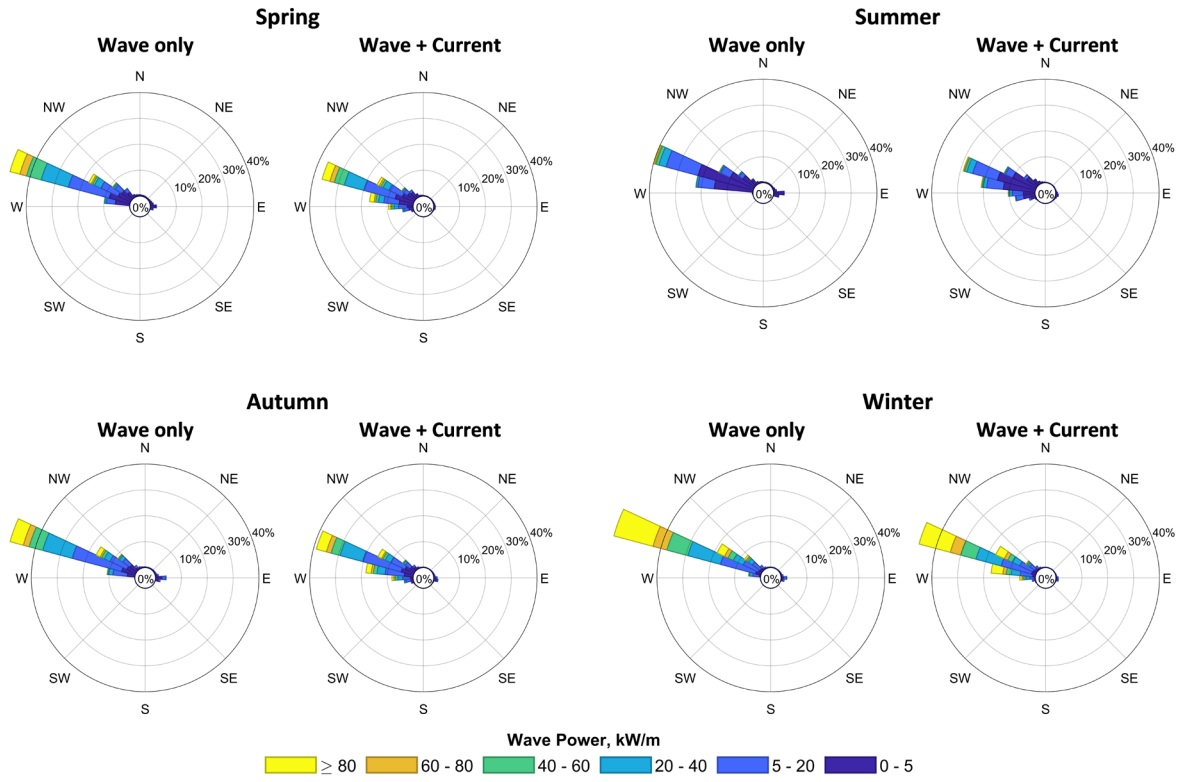

Figure 4.8 Seasonal wave power rose plots over a 10-year period at P3 (Pentland Firth)

- P1: The distribution of wave power along the primary direction (280°) intensifies, while wave power from northern directions diminishes (i.e., angle > 280°). This suggests a more focused distribution of wave power from the west.
- P2: The main wave direction (280°) sees reduced power, but there is an increase in wave power from the west (270°), resulting in a more dispersed distribution.
- P3: Despite an overall increase in wave power, the main wave direction (290°) experiences a reduction in power, with increased contributions from westward directions (280°), which also leads to a more dispersed distribution.

For these sites, tidal currents do not drastically alter the overall distribution structure, they provide valuable insights into the potential tidal effects on wave energy resources, which could concentrate (P1) or disperse the power distribution (P2 and P3).

Table 4.2 Seasonal mean wave power (kW/m) across 10 years

Table includes results for site P1 (Westray Firth inlet), P2 (the west Orkney), and P3 (Pentland Firth inlet). "W" represents the wave-only model; ""W+TC" represents the wave-current model.

Season	P1		P2		P3	
	W	W + TC	W	W + TC	W	W + TC
Spring	29.7	35.7	32.4	31	20.8	23.8
Summer	10.3	11.8	10.6	9.9	6.7	7.8
Autumn	34.9	41.7	38.5	36.6	25.4	28.2
Winter	63.8	80.5	74.2	71.9	48.8	54.7

4.3 Monthly analysis of 10-Year Averages

4.3.1 Map analysis

The monthly maps (Figure 4.9) reveal that wave power is highest during the winter months, with January exhibiting the most intense wave activity. Wave power distribution in November and March is comparable, reaching up to the level of 50 kW/m at the west Orkney nearshore regions. During the transition months between high and low wave activity, such as April and September, the monthly average wave energy power in these areas still reaches 25 kW/m. From May through August, however, the average monthly power in this area is less than 15 kW/m. This monthly pattern suggests that wave energy converters deployed here

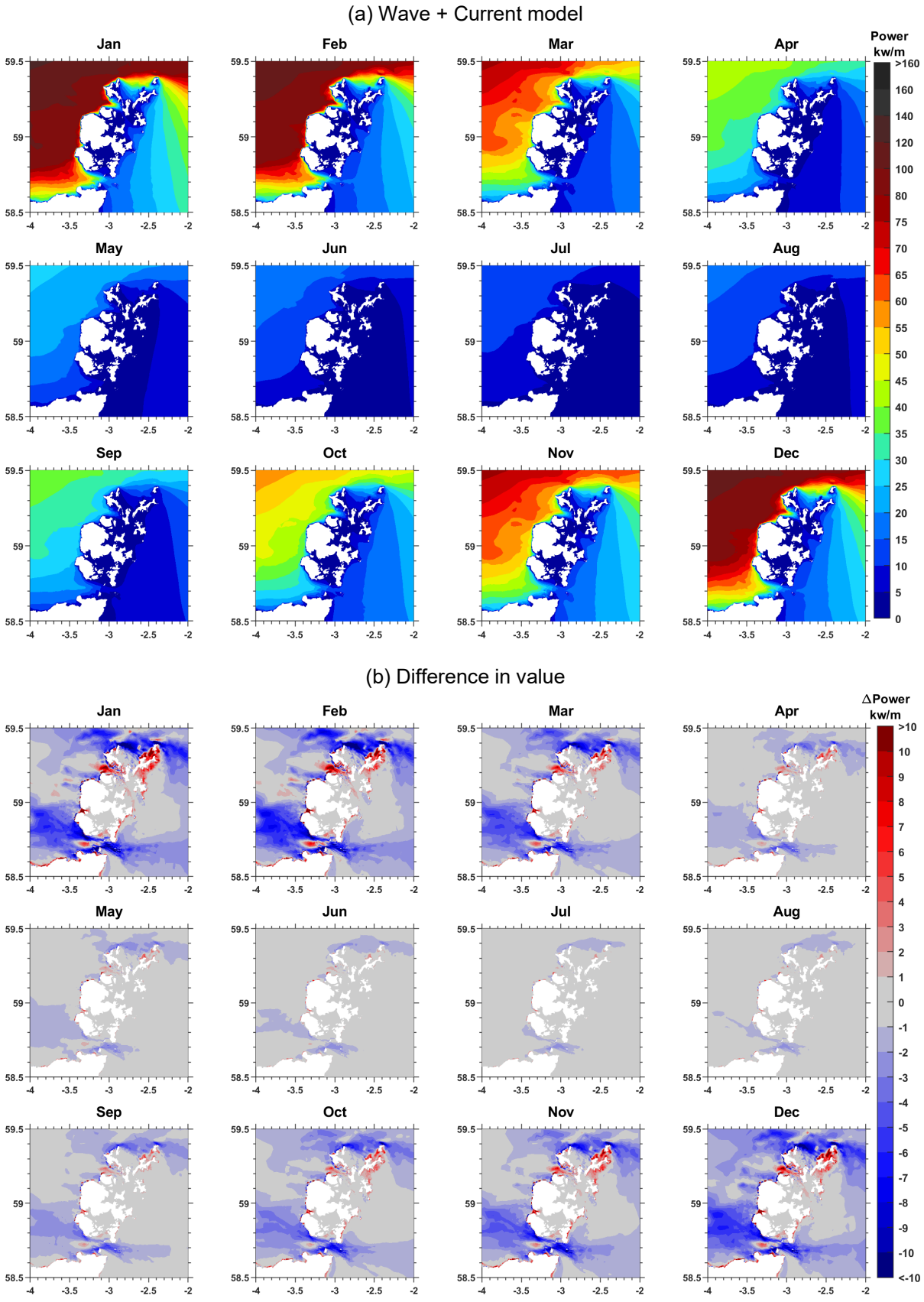

Figure 4.9 Monthly mean wave power over 10 years

could continuously generate energy from September to the following April, while the period from May to August could be reserved for maintenance and servicing.

According to the numerical difference maps, the influence of tidal currents on wave energy power is most pronounced during the peak wave resource months of winter. For example, in January, a reduction in wave energy exceeding 10 kW/m was observed around Stroma Island, as well as in the southern and northern edges of Orkney Islands (i.e., south of the Hoy Island, north of the Papa Westray and North Rondalsay). In contrast, an increase in wave power, with values rising above 10 kW/m and 7 kW/m, was observed at the tidal entrances of Westray Firth and Pentland Firth, respectively.

4.3.2 Box plot analysis

Figure 4.10 presents the 10-year annual cycle of wave power for each month at P1, P2, and P3 using box plots, where the median (middle marker) is used as a representative value. The box's upper and lower edges represent the 75th and 25th percentiles, respectively. Every box covers 50% of the data range around their median and providing a clear depiction of typical monthly wave power variations.

The box plots confirm that January has the strongest wave power overall, including the highest maximum values (upper edge), widest data range, and largest median values. In contrast, July shows the weakest wave power. As summarized in Table 4.3, the median wave power across these three sites in July is less than 10% of the January value.

Including tidal currents in the simulations has varying effects at these locations:

- For P1 and P3, tidal currents increase overall wave power levels by resulting in higher maximum and median values and causing greater data variability each month. For example, in January, median values increase by 12% (from 54.5 to 62 kW/m at P1 and 31.4 to 35.3 kW/m at P3). The data range (25th to 75th percentiles) widens by 23% at P1 and 10% at P3.

- For P2, tidal currents result in a more concentrated power distribution, with slightly reduced maximum values and narrower variability. The median decreases by 6%, and the interquartile range narrows by 3%.

While the increased median values at P1 and P3 highlight greater potential for wave energy development, the accompanying increase in power variability may pose challenges for stable

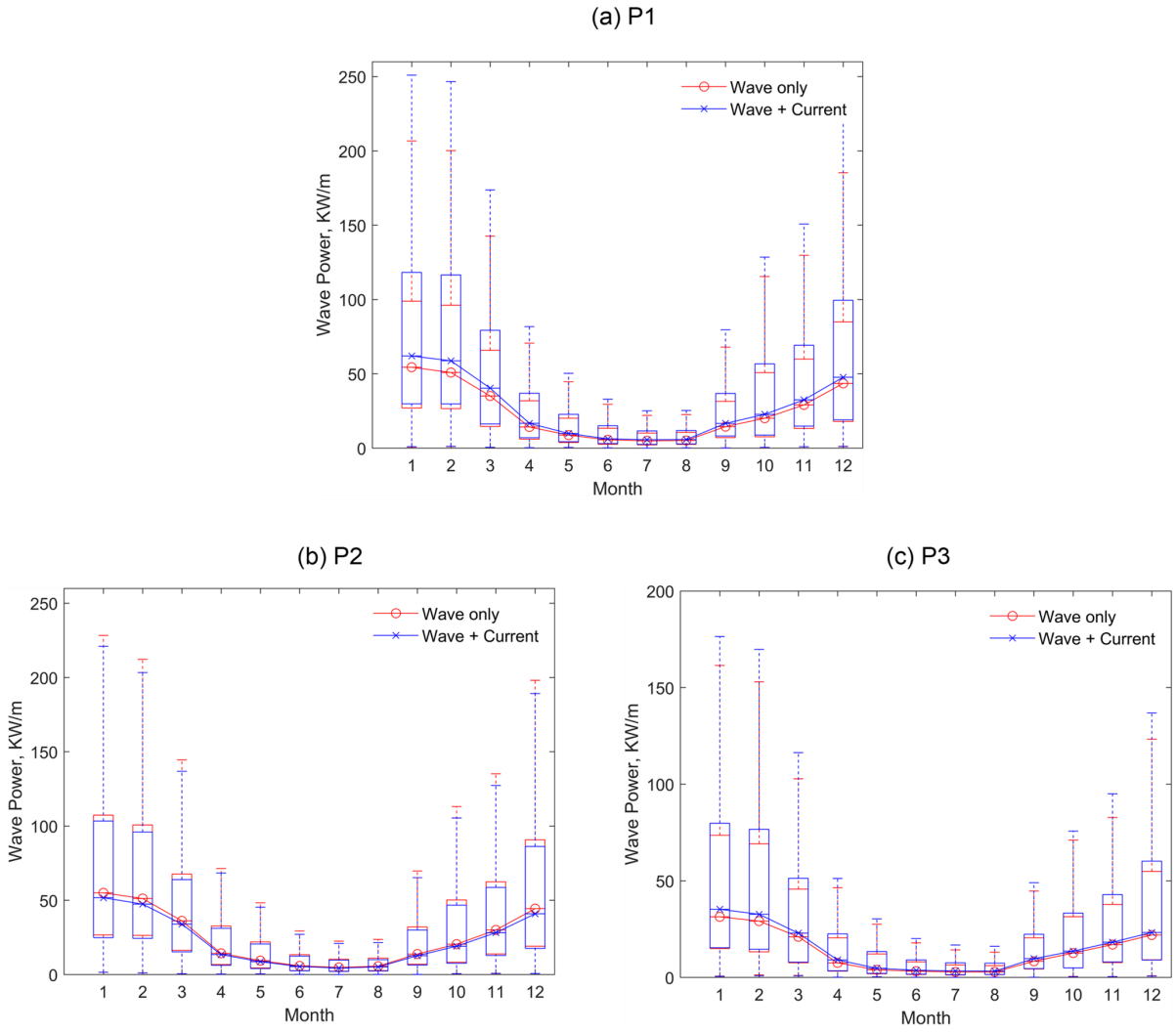

Figure 4.10 Boxplots of the annual cycles of the wave power of every month over 10 years

Table 4.3 Data features of the wave power (kW/m) for January and July across 10 years

Table includes results for site P1 (Westray Firth inlet), P2 (the west Orkney), and P3 (Pentland Firth inlet). "W" represents the wave-only model; ""W+TC" represents the wave-current model.

Month	Season	P1		P2		P3	
		W	W + TC	W	W + TC	W	W + TC
January	Median	54.5	62.0	55.0	51.7	31.4	35.3
	75% - 25%	71.9	88.5	80.7	78.5	58.2	64.4
July	Median	4.9	5.7	4.8	4.4	2.8	3.4
	75% - 25%	7.6	9.0	8.3	7.6	5.1	6.2

power output and device survivability. Conversely, the concentration of power variability at P2 reduces overall power output, making it less favourable. An ideal WEC site would exhibit minimal tidal effects, stable power variability, and consistent energy output.

It is important to note that the maximum values in the box plots exclude outliers and may not represent the 10-year extreme values discussed in subsequent sections.

4.4 Extreme conditions over 10 years

This section examines the extreme wave height and wave power in the Orkney waters over a decade, as predicted by the wave-only model, the wave-current coupled model, and their differences, as shown in Figure 4.11. These maps are critical for informing the design of WECs to ensure stability and survivability under extreme conditions.

Unlike the predominantly blue colour of the previous difference maps, the extreme value difference maps are dominated by red colour, indicating that tidal currents amplify extreme sea states. For instance, at P2, where mean and median wave parameters previously showed a decrease due to tidal currents, the inclusion of tidal effects raises extreme wave heights from 9.2 m to 9.4 m and extreme wave power from 551.6 kW/m to 577.4 kW/m.

This increase is unsurprisingly most significant at the tidal inlets. At P1, extreme wave height rises from 5.7 m to 7.8 m (over a 2 m increase), and wave power increases from 242 kW/m to 469 kW/m (a net increase of 227 kW/m). At P3, extreme wave height increases from 8.7 m to 10.1 m (1.4 m increase), and wave power rises from 460.2 kW/m to 687.4 kW/m (a net increase of 227.2 kW/m).

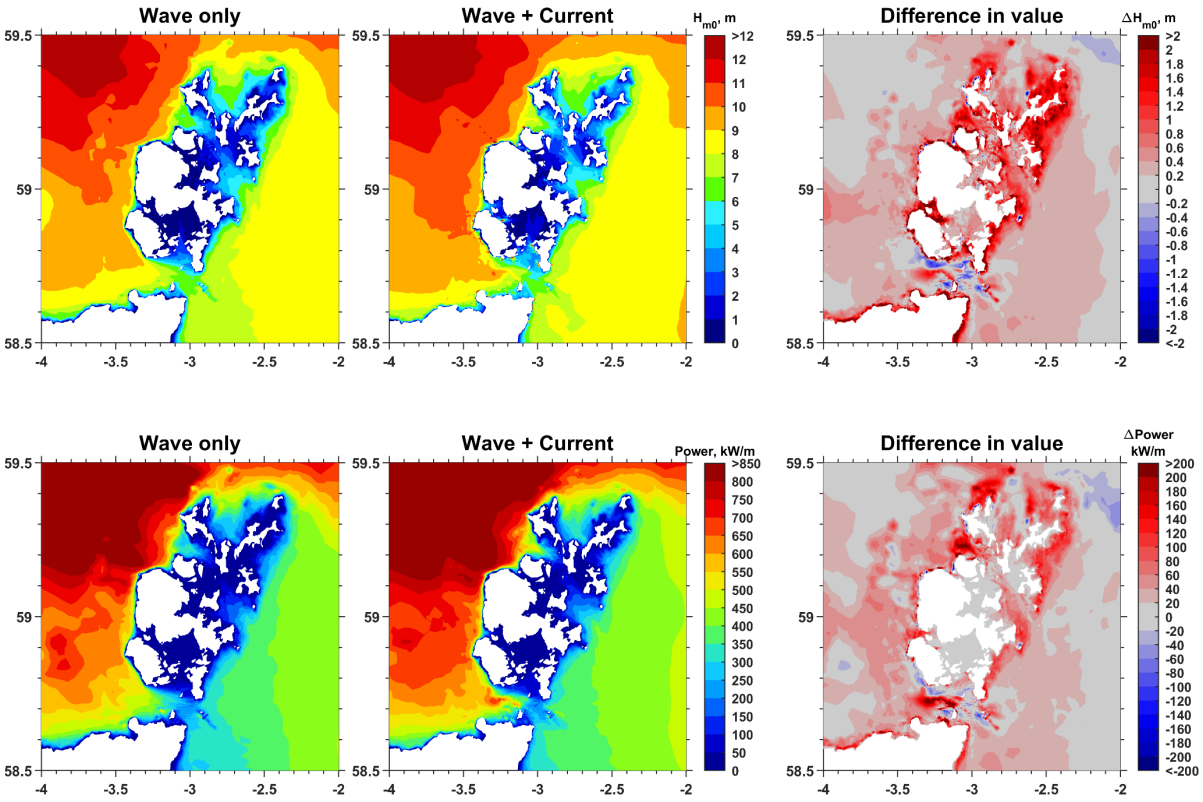

Figure 4.11 Maximum H_{m0} and wave power over 10 years

Upper: H_{m0}. Lower: wave power.

It is important to note that numerical models tend to underestimate extreme values, as observed in the model validation, where peak values were consistently underpredicted. Therefore, the actual extreme wave conditions in reality are likely to exceed the values reported in this study. These findings underscore the significant role of tidal currents in intensifying extreme sea states and highlight the importance of accounting for wave-current interactions in the design and operation of marine energy infrastructure.

4.5 Discussion

4.5.1 Limitations

Inaccuracies in the coastal regions of the coupled model are acknowledged, such as the west Orkney coastlines shown in the difference map by numerical values. This is particularly relevant in areas where water levels may intermittently drop to zero or below, forcing the model to simulate unrealistic coupling processes. For research focused on specific coastal zones, higher-resolution models would be necessary.

Additionally, the 10-year simulation was conducted by running 20 6-month simulations and combining the results. For each simulation, the initial two days were excluded from analysis due to potential spin-up effects. Given the long-term statistical nature of this study, the exclusion of these brief periods does not significantly impact the overall results.

Furthermore, the high density of contours on the maps may create a visual impression of elevated values in certain regions, making them appear more intense than they actually are. For accurate analysis, results should be interpreted based on the actual data values rather than relying solely on visual intensity.

4.5.2 Comparison to previous long-term study for Orkney Waters

When comparing the annual mean wave power map of the wave-only model in this study with the 11-year mean wave power map of Scotland produced by Lavidas et al. [58], a good match is observed as show in Figure 4.12, validating the reliability of the wave power estimation conducted in this study.

While the wave-only model has been extensively researched in the Pentland Firth and Orkney Waters, studies specifically on wave-current interactions—and especially on a wave map for

this region—are limited. The research by Saruwatari et al [33] provides valuable insights, presenting a wave map showing differences in the mean wave height with and without tidal currents. Their findings on wave power variations (i.e., regions of increase or decrease) align with those of this study; however, their model overestimated the wave power at the Pentland Firth inlet and nearshore regions on the northern side, possibly due to an inadequate representation of wave-breaking under strong currents.

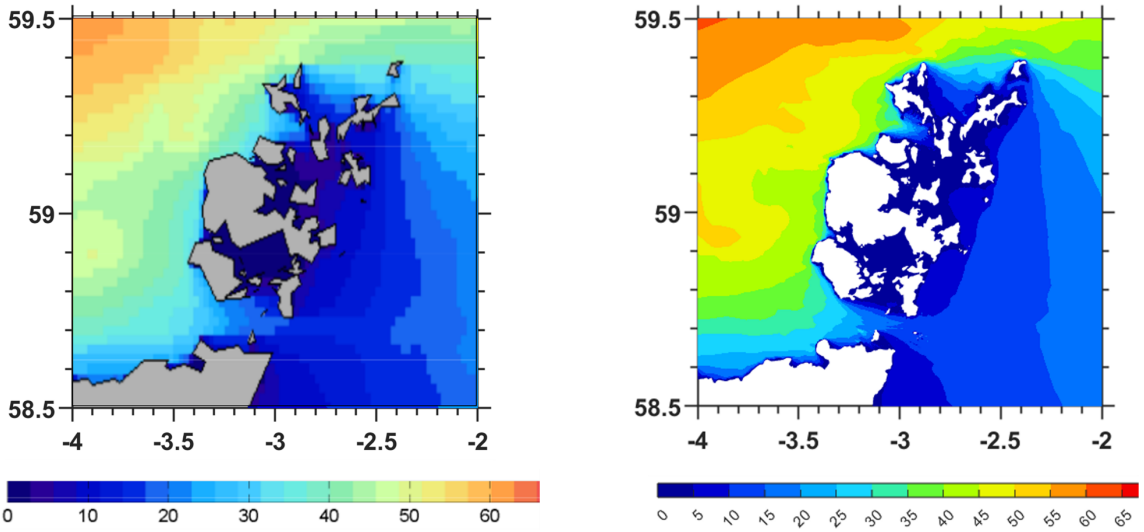

Figure 4.12 Long-term mean wave power comparison (kW/m)

Left: mean wave power over 11 years (2004-2014) at PFOW, croped from Figure 7 of the paper [58]. Right: mean wave power over 10 years (2014-2023s) of this research.

This study extends the work of Neill et.al in 2014 [91], who used the SWAN spectral wave model to produce a 10-year wave parameter dataset for the Orkney Waters, spanning 2005–2014. Their research provided a valuable foundation for assessing long-term inter-annual and inter-seasonal wave energy resources in the region. However, their results appear to underestimate wave power compared to those presented here.

Evidence to support this is that, the annual mean wave power estimated by the MIKE21 in 2012 [56] is significantly higher than the mean wave power calculated by Neill et.al during the extended winter season (December–March) in the same year, which is unrealistic. The inter-annual validation of the SWAN model is mainly proved by the Pearson correlation coefficient R with the North Atlantic Oscillation (NAO) index. It is acknowledged that the NAO index serves as an important reference for the long-term ocean modelling [92], while it mainly focused on the trend rather than the value. High correlation with the NAO index does not necessarily ensure accurate value predictions. A potential reason for the underestimation of wave power in the SWAN model lies in its default wave power calculation method, which can lead

to underestimations of up to 15%, as observed in the Sea of Iroise when compared to TOMAWAC [68].

In contrast, this study conducted continuous validation using 10 years of wave buoy measurements across four different locations. The consistent agreement between the model results and field data provides confidence not only in the trend (e.g., R) but also in the accuracy of the absolute values of the simulation results (e.g., Bias, RMSE, and SI). This robustness strengthens the case for using the TOMAWAC-TELEMAC coupled model for long-term wave energy resource assessments in regions with significant wave-current interactions.

4.6 Summary

This study employed a North Atlantic scale wave-only model and a regional scale coupled wave-current model to conduct a 10-year (2014–2023) simulation. This approach provided accurate interannual, seasonal, and monthly wave data for Orkney Waters and Pentland Firth, including tidal effects, thus revealing the long-term influence of wave-current interactions. The feasibility of this research relies on the TOMAWAC spectral wave model and TELEMAC flow model, both sub-modules of the open-source Telemac system, which enable a straightforward two-way coupling process between waves and tidal currents. With these validated techniques, key findings from this study include:

1. **Wave boundary conditions:** Using the two-dimensional wave spectra from the North Atlantic model as boundary conditions for the regional model (without tidal currents) produced results equivalent to directly applying the North Atlantic model. This validates the comparison between the North Atlantic scale wave-only model and the regional scale wave-current coupled model.

2. **Wave Resource Variability:** Significant interannual, seasonal, and monthly variability was observed in the wave resources around Orkney. For example, at P2, a site located at the west of Orkney Mainland, the wave power at a wave-active year (2015) is 47.6 kW/m and a wave-weak year (2021) is 30.4 kW/m. Comparing to its 10 years mean result, this variability ranged from +28% to -25%. Seasonal variability in wave power ranges from -72% in summer to +91% in winter across the sites of P1, P2, and P3, comparing to their annual mean results. The inter-monthly variability is more significant, with the median power production in July is just 10% of it in January across all sites.

3. **Tidal Effects on Wave Reduction:** When tidal effects are considered, wave height and power significantly decrease along the northern and southern edge of the Orkney Islands, and along the northern and southern edge of the Stroma Island in the Pentland Firth. The decrease is most substantial at the latter one, with an annual decrease in H_{m0} and wave power over 0.5 m (change by over 25%) and 6 kW/m (change by over 50%).

4. **Tidal Effects on Wave Power Increase:** At the central mouths of tidal inlets (Westray Firth, Hoy Mouth, and Pentland Firth), wave power generally rises when tidal effects are included. For instance, the annual mean wave power at P1 in Westray Firth inlet and P3 in Pentland Firth inlet reaches up to 7.7 kW/m (22% increase) and 3.2 kW/m (13% increase) over the decade. The increase phenomenon is always more obvious in wave power than in wave heights.

5. **Wave-Current Interactions Variability:** The numerical difference between the wave-only and wave-current coupled models varies significantly by year, season, and month, following a general concept that the period of higher wave levels leading to a higher value difference. In contrast, the ratio difference map remains relatively steady across different times, highlighting the consistent nature of tidal effects relatively irrespective of wave levels.

6. **Extreme Wave Values with Tidal Effects:** Tidal currents always amplify the extreme conditions of the sea states. At the P1 and P3, the tidal currents amplify the wave heights 2 m and 1.4 m higher to become 7.8 m and 10.1 m, and wave power around 227 kW/m higher than before to be 469 and 687.4 kW/m, respectively.

The results presented in this research provide a high level of confidence for wave hindcasting in the Pentland Firth and Orkney Waters, with natural tidal current effects inherently incorporated. The high-resolution, 10-year dataset, featuring 10-minute time intervals, offers a robust foundation for future machine learning applications in ocean science and engineering.

Chapter 5

Wave-Current Decomposition and Characterisation of Turbulence

This chapter introduces a novel side information-assisted EMD method for wave-current decomposition. The effectiveness of the separated results is validated through multiple approaches. Using this technique, turbulence profiles for wave-only, current-only, and combined wave-current velocities are derived, providing valuable insights into turbulence characteristics under different flow conditions.

5.1 Introduction

Despite the theory in which [34] has extensively explored the mechanism by which waves influence turbulence levels, the ability to quantify the exact contribution of wave activities in a wave-current environment to turbulence remains not fully understood. Therefore, a quantitative analysis of turbulence levels (in terms of turbulence intensity), considering the interactions between waves and currents, is essential. Numerical flow models often neglect waves in model construction, or they often use relatively large coupling time steps with wave models when developing wave-current coupled models, which tends to diminish the impact of waves on current flows, possibly leading to an underrepresentation of this significant interaction in the models [62,63,93]. Therefore, a more accurate and direct approach involves laboratory data or field measurements. Comparisons between combined wave-current flow and current-only flow in laboratory environments offer insights into wave effects [94–97], though these conditions are restrictive and may not represent real-world scenarios fully.

For practical applications like tidal energy projects, analysing turbulence in wave-current interaction scenarios is crucial. Unlike laboratory-created flows, in reality, it is difficult to distinguish between current-only and wave-current combined flows, as even small waves can generate significant turbulence in slow-moving flows. Consequently, direct handling of wave-

current separation in complex, nonlinear field measurements is more practical and meaningful for engineering projects.

At sites where waves interact with currents, the ADCPs can measure particle velocities at a given depth, which is a combination of wave orbital velocity and current velocity. Separating these two components with a suitable processing method will more accurately show their individual impacts on turbulence levels. This separation cannot rely on a simple frequency band-pass filter due to overlapping frequency ranges between wave and current components. As solutions, recent research has explored techniques such as the Coherence, Co-spectra, Stop-Band filter (SB), Moving Average filter (MA), and Synchrosqueezing Wavelet Transform (SWT) etc, with SWT showing better performance [98–101]. The phase method [102,103] that interpolates the velocity spectra to match the Kolmogorov slope [104–107] and applies the inverse Fourier Transform with the original phase to rebuild the velocity signals, is also reported to be effective in the wave-current separation for the Acoustic Doppler Velocimeter (ADV) field measurement [108].

Meanwhile, the Empirical Mode Decomposition (EMD) method, a time-domain signal processing method for non-linear and non-stationary data [109], is widely used in ocean engineering areas, including turbulence analysis [110–112] as well as wave-turbulence decomposition [113]. It breaks down time series into orthogonal sub-components to reconstruct wave orbital velocity and current velocity. However, EMD can lead to mode-mixing issues [114], potentially causing overestimation or underestimation when reconstructing signals. To address this, a 'double-EMD' method was proposed [115], applying EMD twice to extract more information. While this improves results, the process may seem inefficient and poses the question: will there be further or even endless applications of EMD if the results do not meet expectations? An alternative, the Ensemble Empirical Mode Decomposition (EEMD) [116], adds random white noise to the dataset to reduce mode mixing and has shown promising results, comparable to SWT [100,117].

Furtherly, Chávez-Dorado et al. (2024) have recently advanced this field with dynamic mode decomposition (DMD), which requires less tuning and performs well in both field and laboratory data. While these methods offer solutions, wave orbital velocity overestimation remains unsolved, or the methods are tested only during periods of typical wave activity, leaving their separation ability for subtle wave-current interactions unclear. Therefore, a method that can accurately isolate wave and current components under various wave conditions is required.

This chapter proposes a new method that enhances the EMD process by incorporating a pure turbulence series into the original target data. This addition aims to strengthen the turbulence

information, reducing mode mixing in the decomposition. The added signal is later cleaned out to maintain data integrity. Validation of this reconstructed current velocity and wave orbital velocity confirms their accuracy, and, the turbulence analysis results further prove its accuracy by showing their integration under both low and high wave conditions. To the authors' knowledge, this is the first study to add side turbulence information to the original series to assist wave-turbulence decomposition, marking an innovation in this field.

5.2 Data collection in wave-current environment

The case study in this study relies on three ADCPs [79] deployed in the inner sound of the Pentland Firth, which is a firth connecting the North Atlantic Ocean and the North Sea, and located between the mainland UK and the Orkney Islands. This region is a natural narrow water channel formed by the Stroma Island and the Scotland Mainland and is well known for its high current speed. Influenced by the winds travelling from the North Atlantic, the waves are generally active, particularly during the autumn and winter months, making it an ideal area for wave-current interaction research. Notably, those ADCP measurements applied to this study span both the low-wave conditions of the summer month (e.g., August) and high-wave

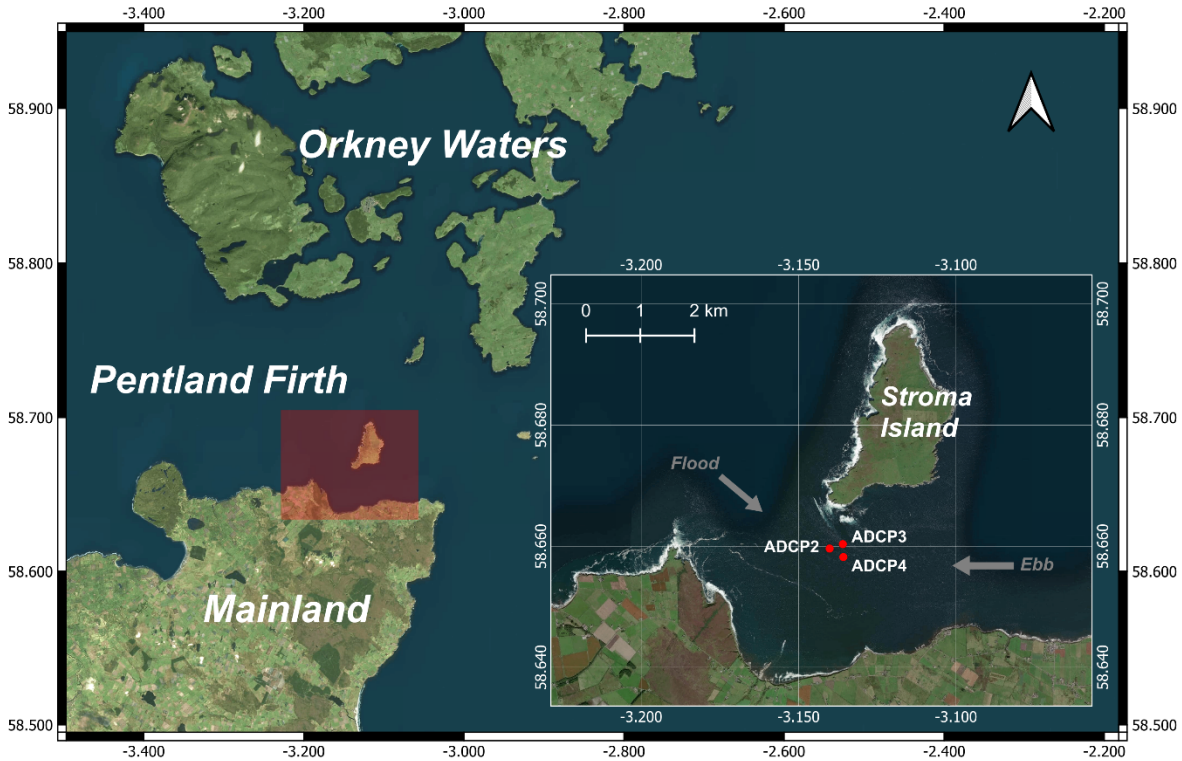

Figure 5.1 Locations of three ADCPs at the Pentland Firth

Big map source from: https://www.bing.com/maps, and small map source from: https://wego.here.com/?map.

conditions of autumn and winter months (i.e., October to December). The breadth of data under various wave conditions underscores the flexibility and robustness of the wave-turbulence decomposition method proposed in this study, as well as providing a comprehensive understanding of the turbulence statistics at different wave scenarios.

The objective of this research is to propose an efficient and straightforward wave-current decomposition method and apply it to analyse turbulence statistics to quantify the impact of waves on turbulence levels. The goal is to provide engineers and researchers with a comprehensive investigation to quantify the effects of waves on three-dimensional flows under different wave conditions.

The ADCPs (refer to Figure 5.1) discussed in this study were initially deployed to observe the flow dynamics around the four tidal turbines of the SAE MeyGen Phase 1A tidal energy project in the Pentland Firth, Scotland, UK [23]. This study accesses data from three of these instruments: ADCP2, ADCP3, and ADCP4. Specifically, ADCP2 was positioned on the Ebb tide side of the T2 turbine, while ADCP3 and ADCP4 were placed on the Flood side of the T3 and T4 turbines, respectively. These three ADCPs, deployed within a 200 m radius, represent a similar geography characteristic. These seabed-mounted ADCPs record flow velocities from the bottom to the surface at a 2 Hz sampling rate and a 1 m vertical bin size, with data captured at five 25° beam angles. This study focuses on the analysis of corrected data that were processed by the MeyGen project and provided to the authors, with the transition from raw to processed data detailed in reference [79]. Key information of the ADCPs is listed in Table 5.1.

Table 5.1 Information on three ADCPs [79,118]

Site	Water Depth	ADCP Type	Data Period for Analysis	Wave Height (m)	
				Mean	Max.
ADCP2	35.3 m	Teledyne RDI V50	6 - 28 Aug 2017 (22 days)	0.43	1.45
ADCP3	36.3 m	Nortek Signature 500	6 - 28 Aug 2017 (22 days)	0.58	2.18
ADCP4	36.5 m	Teledyne RDI V50	15 Oct – 12 Dec 2017 (58 days)	1.06	4.48

The analysis period spans 22 days in August 2017 for ADCP2 and ADCP3, and 58 days from October to December 2017 for ADCP4, providing a comprehensive dataset from summer to winter. Examining the flow speed time series at 15 m above the seabed, which corresponds to the hub-height of the MeyGen turbines, ADCP2, ADCP3, and ADCP4 all recorded maximum speeds over 4 m/s, with median speeds for the analysis periods being 2.54 m/s, 2.73 m/s, and 2.07 m/s, respectively, as shown in Figure 5.2. Wave data measurements are available in ADCP4 locations, which show maximum wave heights exceeding 4 m, highlighting events of

large waves during the autumn and winter months. Unfortunately, wave data are unavailable for ADCP2 and ADCP3, but maximum heights are reported [79] at 1.45 m and 2.18 m, respectively, typically below 1 m, indicating a limited representation of typical wave-current interactions.

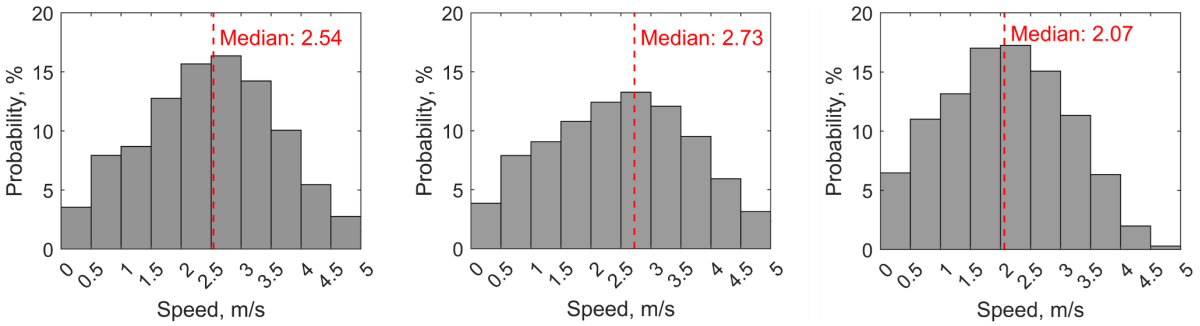

Figure 5.2 Probability histograms of occurrences of flow speeds at tidal turbine hub-height
Left: ADCP2; middle: ADCP3; right: ADCP4. Tidal turbine hub-height is 15 m above seabed. Median value of each plot is marked by the red dot line.

To address the lack of wave data for ADCP2 and ADCP3, this study utilized the numerical simulation generated by a wave-current coupled model, incorporating the spectral wave model TOMAWAC and the flow model TELEMAC 3D [67,93,119]. Covering the entirety of the Pentland Firth and Orkney Waters in Scotland, this model utilized the TPXO9 tidal database [82], ECMWF ERA5 hourly wind data [120], and wave boundary conditions from a North-Atlantic scale model developed with TOMAWAC, calibrated, and validated against field measurements from four UK sites. Further details on the database and parameters of this coupled model can be found in Section 2.5. Validation was performed using ADCP field data from the Pentland Firth, specifically, wave data collected by ADCP4 in November 2017, resulting in an R value of 0.813. Given the model's verification across various wave scenarios and locations, the wave simulation results for the site locations of ADCP2 and ADCP3 are anticipated to be reliable. The outcomes are presented in Section 5.4.4 below.

The 1.5 MW turbine from the MeyGen Phase 1A project [23,121] installed in the Pentland Firth is chosen as a reference to examine the turbulence levels at both the tip-height and hub-height. The rotor diameter measures 18 m, and the distance from the blade tip to the seabed is 24 m, with the hub centre positioned 15 m above the seabed. Prior to analysing wave-turbulence decomposition, it is essential to understand the nature of pure turbulence velocity and the impact of waves on it. Examples from ADCP4 measurements at 24 m (tip-height) and 15 m (hub-height) above the seabed demonstrate this. Figure 3 displays the Power Spectra Density (PSD) profiles at water depths of tip-height and hub-height, respectively, each plotted using more than 40 instances of 30-minute streamwise velocity time series for two cases of

significant wave heights: one with high waves above 2 m (Figure 3(a)) and another with low waves below 0.3 m (Figure 3(b)). It is clear that in high wave scenarios, the spectra show high energy densities in the wave frequency band (0.04 Hz to 0.25 Hz), with the peak wave frequency centred around 0.1 Hz. This wave frequency range closely resembles that observed in Banks Strait, Tasmania, where a consistent wave influence on turbulence levels throughout the water column has been reported [40]. These energy peaks are less pronounced for smaller waves, as seen in the left panel of Figure 5.3. Notably, the spectra for the low wave case meet the Kolmogorov −5/3 power law, confirming that the trend in 'wave-free' velocity signals typically follows this model [97,104–107]. This relationship will also be used to validate the separated current component in the later part of this study.

The difference in spectra of velocity under wave-active and wave-less conditions is clear. The main objective of this work is to isolate wave data and wave-free current data from the original combined wave-current data. The data separated in this way will then be used to determine their individual contributions to the turbulence intensity. To facilitate this, we applied the side information assisted EMD technique.

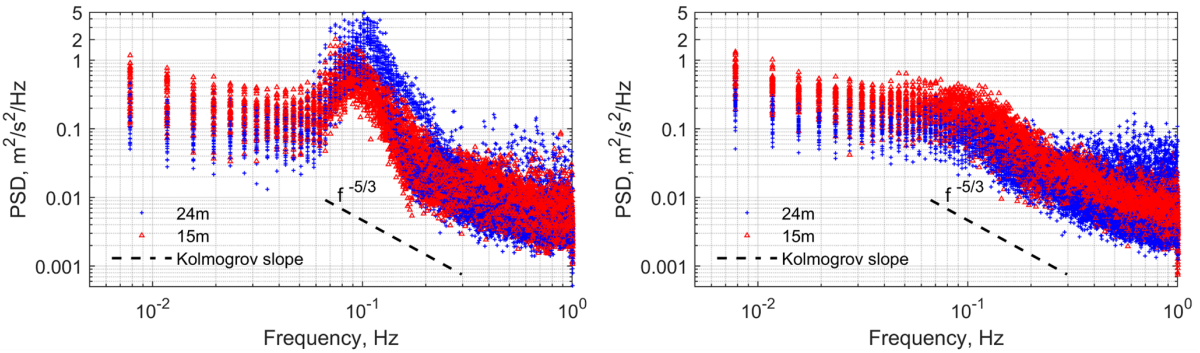

Figure 5.3 PSD of streamwise velocity measured by ADCP4

Blue represents recording at tidal tip-height (24 m above seabed); red represents tidal hub-height (15 m) with mean speeds of 2 m/s to 3 m/s. Left: waves over 2 m (43 series); right: waves under 0.3 m (45 series).

5.3 Wave-current decomposition method

5.3.1 Empirical Model Decomposition (EMD) method

The empirical mode decomposition method (EMD) is designed to decompose the target time series data $\mathrm{x}(t)$ to n numbers of normally distributed sub time series components $c_j(t)$ and a residual $r(t)$ of the same length as the original one,

$$\mathrm{x}(t) = \sum_{j=1}^{n} c_j(t) + r(t) \tag{5.1}$$

in which the subcomponents $c_j(t)$ all satisfy the rules of the intrinsic mode function (IMF): a) the number of extremes and the number of zero-crossings must either equal or differ at most by one, and b) the mean value of the envelope defined by the local maxima and the envelope defined by the local minima is near zero. To obtain these IMF components, the process involved within the EMD method is as follows:

1) identify all the local extrema in the test data $\mathrm{x}(t)$,

2) connect all the local maxima by a cubic spline line as the upper envelope,

3) repeat the procedure for the local minima to produce the lower envelope, and

4) the difference between the data covered by the upper and lower envelope to their mean values $m_{i(i=1,2,3\ldots)}$ is $h_i = \mathrm{x}(t) - m_i$.

If h_i satisfy the IMF definition or meet the stopping criteria of the algorithm then it becomes the first IMF component IMF1, and the remaining part of the test data, which is the $\mathrm{x}(t) -$ IMF1, will become the new test data to repeat the above process until the next IMF is generated. While if h_i is not an IMF time series, then h_i will becomes the new test data ($i = i + 1$) to repeat the above process until the first IMF is generated.

Notably the EMD method that was used in this research is the standard 'emd' function provided by the MATLAB signal processing toolbox [122]. In this function, a variety of parameters can be adjusted, but the most important parameter used in this work is the Cauchy-type convergence criterion 'SiftRelativeTolerance'. When the Relative Tolerance RT, defined by

$$RT \triangleq \frac{\|h_i - h_{i+1}\|_2^2}{\|h_i\|_2^2} \tag{5.2}$$

is smaller than a given value of 'SiftRelativeTolerance', the EMD process will stop. In this study, a default value of this parameter 0.2 is adopted. The sensitivity analysis of this parameter and the guidance for tuning is described in the Section 5.4.2. Another important parameter to control the termination of the EMD process is the maximum number of the IMF, and a value of 15 is used. Other parameters are left at their default setting.

5.3.2 Side information assisted decomposition

The flow velocity U consists of the mean velocity $\overline{U}$ and the instantaneous velocity fluctuation ${U_i}'$,

$$U = \overline{U} + {U_i}' \tag{5.3}$$

In the marine environment, the mean velocity $\overline{U}$ is the tidal harmonic component, while the instantaneous velocity fluctuation ${U_i}'$ is the combination of the current turbulence velocity U' and the wave orbital velocity $\widetilde{U}$, which is formulated as

$${U_i}' = U' + \widetilde{U} \tag{5.4}$$

Notably, this relationship also extends to its three-dimensional components, including streamwise velocity u, transverse velocity v, and vertical velocity w.

The objective of the decomposition in this study is to separate the current turbulence velocity U' and wave orbital velocity $\widetilde{U}$ from the target instantaneous fluctuation ${U_i}'$. To achieve this, this study proposed a side information assisted EMD method by incorporating a 'wave-clean' turbulence series U'_{clean} into the target data before the wave-current turbulence decomposition. This pure turbulence series is derived from the same ADCP measurement dataset but is strictly selected from periods when wave heights are very small (e.g., $< 0.2\ m$) and wave orbital velocities can be considered negligible. The series U'_{clean} is added to ${U_i}'$ to create a temporary dataset ${U_i}'_{temp}$. Then, the EMD method is applied to this temporary dataset, extracting various IMF components and a residual. For those IMF components within the wave frequency ranges are aggregated, then a band-pass filter is applied across the wave frequency (0.04 Hz to 0.25 Hz), and a temporary time series containing the wave information $\widetilde{U}_{temp}$ is generated. This series is subtracted from the initial target data ${U_i}'$ to derive the temporary turbulence

series U'_{temp}, whose PSD mirrors that of turbulence velocity spectra during small wave conditions.

To rebuild the final turbulence velocity U', an inverse Fast Fourier Transformation (iFFT) using the Fourier frequencies of U'_{temp} and the Fourier frequency phase angle of the original wave-current combined instantaneous velocity ${U_i}'$ is applied. The resulting U' is then subtracted from the target ${U_i}'$ to obtain the final wave orbital velocity $\widetilde{U}$. This strategy of using the inverse Fourier Transform to rebuild the signal references the partial idea of the Phase method technique [102,103,108]. The detailed process of this side information assisted wave-turbulence decomposition is illustrated by the flow chart in the red colour-shaded area of Figure 5.4.

In this study, the dataset is framed by a 30-minute-long window, and the decomposition method is applied to this window. It is assumed that the wave is stationary within 30 minutes. Another assumption is that there are no wave-current interactions for those frequencies out of the wave frequency range, that is smaller than 0.04 Hz or higher than 0.25 Hz in this study.

5.3.3 Validation methods

The method introduced in this study does not compare with other wave-turbulence decomposition methods outlined in the Introduction, as different methods require specific tuning (guidance for tuning this method is described in Section 5.4.2) to optimize their performance, which demands considerable attention and effort. Moreover, the primary aim of this research is to develop an effective approach for wave–current separation, for which direct comparison with alternative methods is not essential. To establish the reliability of this method, as illustrated in the blue colour-shaded area of Figure 5.4, a range of self-validation criteria is presented: (1) a comparison of energy spectra with those from current-alone flow or, more simply, with the Kolmogorov -5/3 slope that current-alone flow adheres to, and (2) a comparison of wave heights between results derived from the reconstructed wave orbital velocity and measurements or other reliable datasets. Additional evidence is provided in subsequent turbulence analysis in Section 5.5 and 5.6, where the turbulence profile of the separated current-only velocity should remain consistent under different wave conditions, indicating that waves have been effectively removed from the series.

The comparison of energy spectra is straightforward, with further details available in section 3. Regarding the wave heights comparison, the method to convert the wave orbital velocity into the wave heights utilizes Borgman's method [43,123] which is limited to linear wave theory.

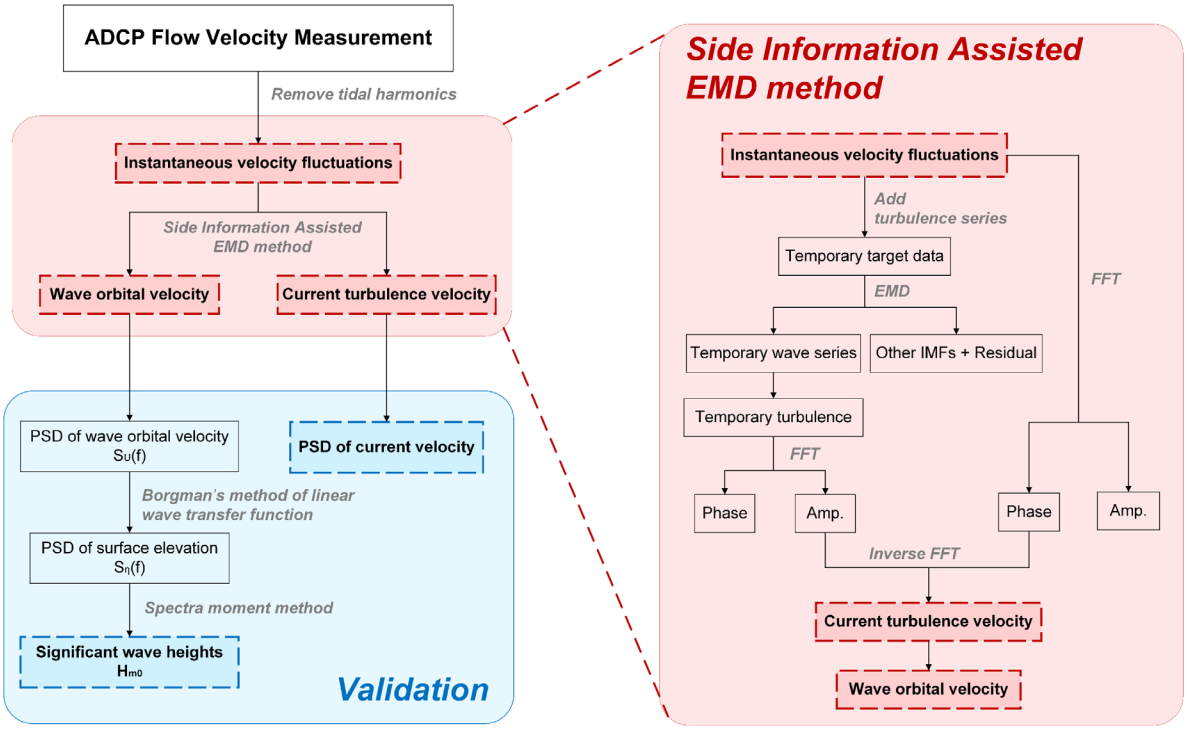

Figure 5.4 Flowchart of the side information assisted EMD wave-current decomposition process

According to it, the PSD of the velocity $S_U(f)$ can be transformed to the wave elevation spectra $S_\eta(f)$ through,

$$S_U(f) = (2\pi f)^2 \cdot \frac{\cosh^2\big(k(h+z)\big)}{\sinh^2(kh)} \cdot S_\eta(f) \tag{5.5}$$

where h is the mean water depth, z is the vertical coordinate with reference to the water surface, and the dispersion relation is applied to the wave number k and the intrinsic wave frequency f by Equation (3.3.

The significant wave heights H_{m0} for the 30-minute-long time series can be calculated using the spectral moment of the wave spectra S_η. This is accomplished by Equation (2.7. The wave heights H_{m0} can then be compared with the numerical simulation results for ADCP2 and ADCP3 locations and with the field measurements from ADCP4 for validation. The wave height validation method offers more focused information compared to the spectra method, as it consolidates the decomposition performance of thousands of cases into a single time series result.

5.4 Method validation

5.4.1 Case study of an individual decomposition process

As outlined in the methodology, the side information added to the original signal consists of a pure turbulence time series, whose spectra align with the Kolmogorov slope. In practice, due to significant variations in turbulence levels across different velocity groups, it is crucial to match the energy of the turbulence to that of the target data. Specifically, pure turbulence series for each depth under different speed ranges—below 0.5 m/s, from 0.5 to 1 m/s, from 1 to 2 m/s, from 2 to 3 m/s, and above 3 m/s—are added to the target data in the same speed category. These turbulence series are extracted from the raw ADCP measurements using a simple speed filter. Identification of these 'wave clean' turbulence series can be accomplished in two ways: 1) using available wave height data as a reference to select series when wave heights are below 0.2 m, or 2) examining the spectra to identify series with PSD that show no energy peaks at wave frequency ranges.

Taking a 30-minute streamwise velocity series of the ADCP4 starting at 09:58:42 on 9th November 2024, as an example, and after subjecting it to the spectral analysis, the green line in the right side of Figure 5.5 represents the PSD of the original measured signal (i.e., wave-current combined) after removing tidal harmonics. During this period, the mean speed is 2 m/s and there are waves present, prompting the selection of pure turbulence from the same speed group to be added to the target data. The PSD of this added turbulence is depicted by the black dash-dot line in the right side of Figure 5.5.

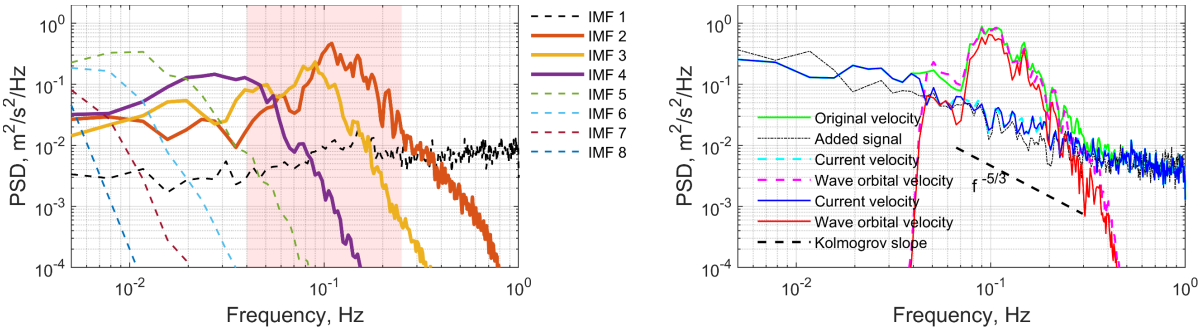

Figure 5.5 PSD for a 30-min time series using default EMD setting

'SiftRelativeTolerance' is 0.2 and mean speed of the added turbulence being 1 m/s. Right: PSD of the IMF components. Left: PSD of the velocity.

As it was mentioned before, using the 'emd' function from the MATLAB toolbox, a simple EMD process to the temporary target data (i.e., original signal + added turbulence) yields 8 IMF components as shown in Figure 5.5. By examining the PSDs of IMF components shown to

the left side of Figure 5.5, IMF2, IMF3, and IMF4 are identified as containing significant energy within the wave frequency range (shaded in light red rectangle). These three PSD components are combined and further subjected to a frequency band-pass filter from 0.04 Hz to 0.25 Hz, thus deriving the PSD for the temporary wave orbital velocity, represented by the magenta dotted line in Figure 5.5 (right). As a secondary outcome, the temporary current series is obtained by subtracting the temporary wave series from the original target data, indicated by the aqua-dotted line in Figure 5.5 (right). This procedure successfully removes the wave energy, exhibiting a pattern akin to the Kolmogorov slope. However, the energy in the temporary wave series exceeds that of the original data due to the added energy from the pure turbulence, which is deemed unacceptable and needs correction.

To address this, as described in the methodology, the FFT amplitudes of the temporary current turbulence and the FFT phase angles of the original target data are utilized to perform an inverse FFT. This process reconstructs the final current turbulence series, shown as the solid blue line in Figure 5.5 (right), which still aligns with the expected Kolmogorov pattern. Subtracting this from the original target data yields the final wave orbital velocity, with its PSD depicted by the red line in Figure 5.5 (right). This approach ensures that all energy levels are maintained below those of the original data, effectively resolving the issue of excess energy.

5.4.2 Sensitivity analysis

The effectiveness of the decomposition is primarily determined by the added signal (pure turbulence) rather than solely relying on the EMD method itself. This is evident by comparing Figure 5.5 and Figure 5.6 (a), where the same signal is decomposed under identical EMD parameters (‘SiftRelativeTolerance’ is 0.2) but different levels of added turbulence. Figure 5.5 represents turbulence with a mean speed of around 1 m/s, and Figure 6.a corresponds to a flow with a mean speed of around 0.5 m/s. Figure 5.6 (a) clearly overestimates the wave velocity, causing the current velocity spectra to deviate from the Kolmogorov slope. The way to choose the proper added signal has been described in Section 5.4.1.

Regarding the EMD method, the requirements for parameter setting are less stringent. An important parameter is the ‘SiftRelativeTolerance’, as described in Section 5.3.1. In general, a higher value of it leads to a less accurate and less refined IMF results, with an increased risk of mode mixing. To explore the sensitivity, three different values of ‘SiftRelativeTolerance’ were tested in addition to the default setting of 0.2 (shown in Figure 5.5) and the results are shown in Figure 5.6 (b) to (d).

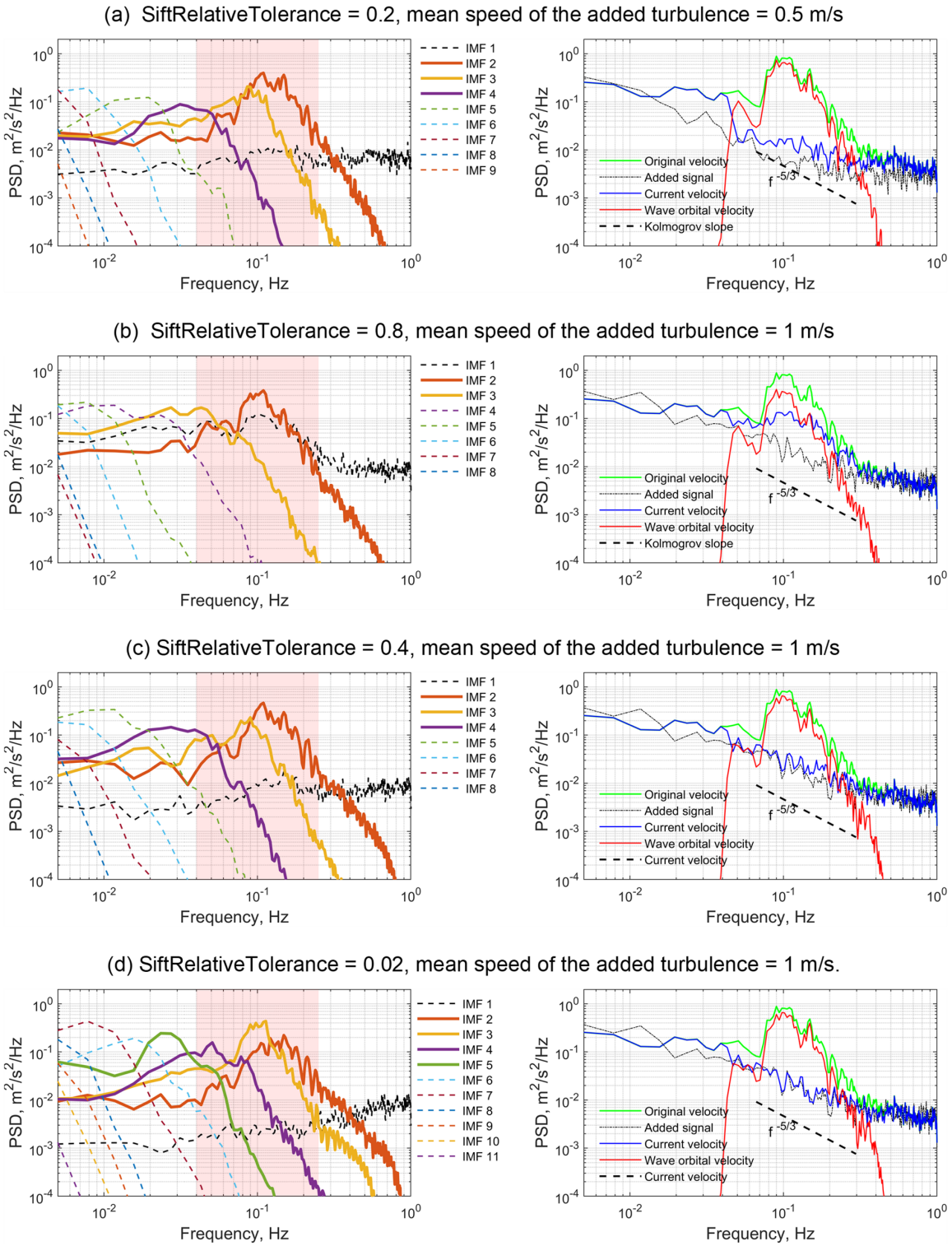

Figure 5.6 Sensitive analysis of the side information assisted EMD method

Right: PSD of the IMF components. Left: PSD of the velocity.

For a 'SiftRelativeTolerance' of 0.8 (Figure 5.6 (b)), IMFs 2 and 3 fall within the wave frequency range and are believed to represent wave components. However, the wave energy is under-estimated, and a part of the information remains in the current velocity. This occurs due to

mode mixing, where IMF 1 (typically considered pure noise, marked by the black dashed line) also contains wave information.

With a 'SiftRelativeTolerance' of 0.4 (Figure 5.6 (c)), three IMFs are located in the wave frequency range, as in the default setting. The final decomposition result (right-hand side) is nearly identical to Figure 5.5, demonstrating minimal difference between 0.2 and 0.4, confirming the robustness of the parameter setting.

For a smaller 'SiftRelativeTolerance' 0.002 (Figure 5.6 (d)), more IMFs are produced, with four components (IMFs 2 to 5) located in the wave frequency range. Although the final decomposition (right-hand side) shows little difference from the default setting, the current velocity energy spectra align more closely with the added signal. While this alignment is correct in this case, however, if the added signal has lower energy, the small 'SiftRelativeTolerance' could introduce larger errors.

In addition, to ensure the wave components are represented by IMF2, IMF3, and IMF4 across all time frames, a mean frequency $\bar{f}$ on the number of IMFs is calculated as below,

$$\bar{f} = \frac{\int f \cdot F_n^2(f) df}{\int F_n^2(f) df} \tag{5.6}$$

where $F_n(f)$ is the Fourier spectrum of the IMF number n, and f is the frequency component. This method is demonstrated to be effective by Singh et al. (2020). In the present study, the IMFs resulted from 2792 sets of 30-minute data segments of ADCP4 measurements are used for the calculation and the results are plotted by boxplot (see Figure 5.7), which allows for the visualization of variation and the identification of the median values for each IMF. These median values are then used to generate a logarithmic fitting curve.

The plot reveals that IMFs 1 through 8 generally follow a simple logarithmic trend, whereas IMFs 9 and 10 deviate from this pattern. This deviation is due to the EMD settings, specifically the 'SiftRelativeTolerance' at 0.2. These settings occasionally result in missing IMF9 and IMF10 components, producing NaN values in some data sets, which may finally lead to larger errors.

From the boxplot, it can be observed that IMF2, IMF3, and IMF4 display small variance and are tightly concentrated around their median values. This concentration supports the conclusion that IMF2 and IMF3 consistently lie within the wave frequency range (0.04 Hz to 0.25 Hz). IMF4, while positioned near the lower boundary of this range (approximately 0.04 Hz), likely expects to capture low-frequency wave components. Thus, IMF4 is also included as a

candidate for representing wave signals. As a result, the analysis demonstrates that IMF2, IMF3, and IMF4 are robust candidates for wave signal decomposition, with a clear distinction from the other IMFs.

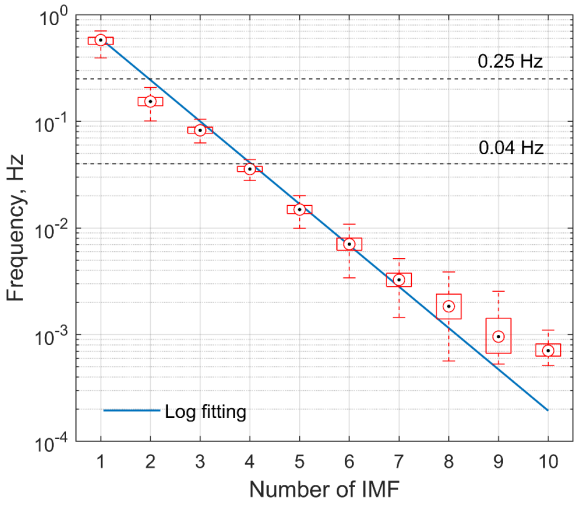

Figure 5.7 Dependency of mean frequency on the number of IMF

The boxplot made from 2792 sets of 30-minute data segments of ADCP4 recordings.

Based on the above investigation, the default setting of 'SiftRelativeTolerance' offers a good balance between avoiding mode mixing (which occurs with higher values) and minimizing over-reliance on the added signal (associated with smaller values). It also demonstrates robustness to small changes in the tolerance value, suggesting its applicability across various studies. With the default setting, it is also proved that IMF2, IMF3, and IMF4 is consistently distributed in the wave frequency range across thousands of data frames. However, specific tuning of the method may be necessary depending on the sampling frequency of the record, as the mean frequency of each IMF may differ from the one used in this study. A simple criterion for determining a proper 'SiftRelativeTolerance', beyond directly evaluating the decomposition results, could involve assessing the number of IMF components within the wave frequency range. In the example presented here, three IMFs provide reliable results, indicating that this could serve as a useful guideline.

5.4.3 Method validation of ADCP4

5.4.3.1 Validation on three-dimensional velocity

This section aims to demonstrate the effectiveness of this decomposition method with default settings across three velocity directions—streamwise, transverse, and vertical—for both Ebb and Flood flow. Figure 5.8 presents two 30-minute example periods from ADCP4, showcasing

the PSD of the turbulence velocity after wave removal (red line), compared to the initial velocity (blue line) and the added clean turbulence signal (thin black dash-dot line) at the tip-height. The left side subplots (Figure 5.8 (a)) correspond to a wave height of 0.92 m and a mean speed of 2.09 m/s during the Ebb phase, while the right side (Figure 5.8 (b)) shows a wave height of 3.57 m and a mean speed of 2.63 m/s on the Flood phase.

In both cases, the presence of waves is evident, indicated by peaks in the spectra. The results show the successful removal of the wave energy peak from the original wave-current combined signal, resulting in current-only spectra that align well with the Kolmogorov slope. This alignment is observed in both the high-energy density case of streamwise velocity and the low-energy density case of velocity. These findings indicate the method's efficacy across different wave height periods and velocity ranges.

5.4.3.2 Validation on the whole 58-days dataset

The complete ADCP4 dataset starts from 08:28:42, 15 October to 12:28:41, 12 December 2017, covering 58 days. Notably, upon examining the velocity PSD for the depth 8 m above the seabed during high waves ($H_{m0} > 2\ m$), it was found that the peak of wave energy is relatively low. To avoid overestimating wave components, target depths for ADCP4 analysis were kept starting from 10 m above the seabed and extended to the surface up to 36 m. This approach is necessary due to the inherent limitations of the EMD method, which lacks a physical basis [114]. Theoretically, the method can form upper and lower envelopes and produce multiple IMFs for any data type, even if it is purely turbulence with insufficient wave information. Consequently, some overestimation may occur under conditions with minimal wave effects.

Furthermore, to validate the method's effectiveness across different depths and additional series, Figure 5.9 displays the streamwise velocity PSD of Ebb flow before (blue dots) and after (red dots) wave removal, from the shallow depth at 32 m above the seabed down to 12 m, with a 4 m decrement between depths. Each set in the figure consists of 440 30-minute-long data segments. It is evident that wave energy significantly affects the tip-height depth (24 m) and is still present at 16 m which is near the turbine hub, underscoring the need to accurately characterize turbulence levels due to waves for the safe operation of tidal turbines. Generally, as water gets deeper, wave energy diminishes due to dissipation. Figure 5.9 clearly shows that wave energy peaks are effectively removed from the original wave-current combined velocity. It is important to note that the wave conditions are not filtered, meaning that the 440-time steps presented include various types of waves, further demonstrating the method's effectiveness and robustness.

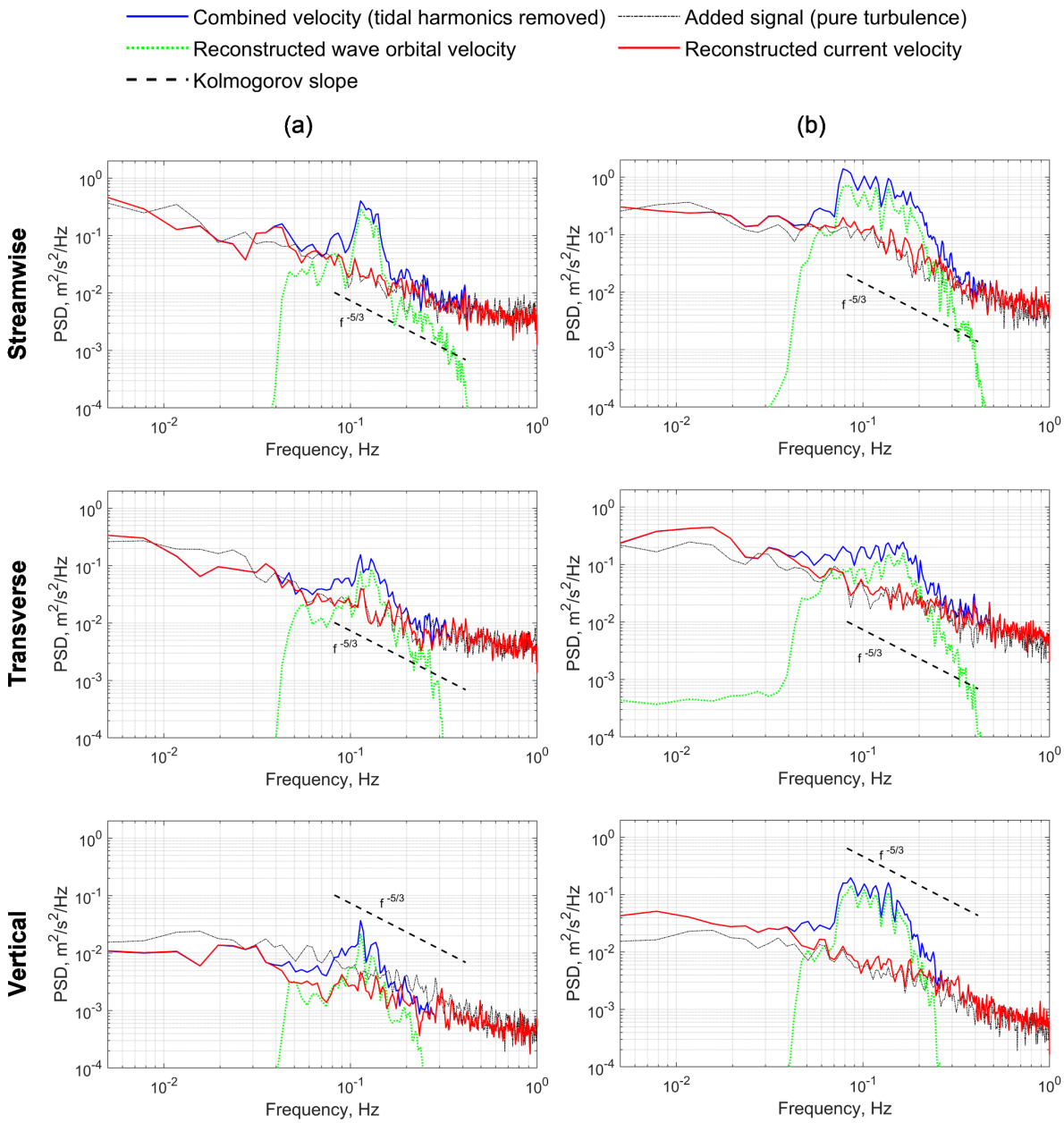

Figure 5.8 Three-dimensional velocity case study using side information assisted EMD decomposition
Left (a): mean wave height 0.92 m, mean speed 2.09 m/s, Ebb flow. Right (b): mean wave height 3.57 m, mean speed 2.63 m/s, Flood flow.

Figure 5.10 shows the comparison of significant wave heights between the measurements and EMD-derived values at various depths. It is observed that the blade tip-height (24 m) exhibits the highest correlation (R=0.86) with ADCP-measured wave heights. In the surrounding depths, from 20 m to 28 m, the derived wave heights still show a strong correlation (R > 0.8, RMSE < 0.4 m). However, at the top layer of depth 32 m, where turbulence intensity is expected to be highest (will be detailed in Figure 5.13 and Figure 5.14 in Section 5.5.1), the correlation drops to 0.68, though the trend generally aligns with the actual measurements. During periods of low wave heights, such as from November 1-5 and December 1-5, when

spring tidal currents are strong, but wave heights are minimal, errors primarily manifest as overestimations.

In the lower depths at 16 m and 12 m, this overestimation is even more pronounced during low wave height periods due to the minimal wave information embedded in the current velocity. This sensitivity is compounded by the amplification effect of the linear wave theory, specifically the water depth term $\cosh^2(k(h+z)) \,/\, \sinh^2(kh)$ in the Equation (5.5. As a result, turbulence and environmental noise are amplified in the results, making the converted wave heights at lower depths follow the tidal cycle, as the energy level is mainly dependent on the current velocity when wave effects are small. Despite this, the decomposition method should still be reliable as seen in the spectra comparison in Figure 5.9.

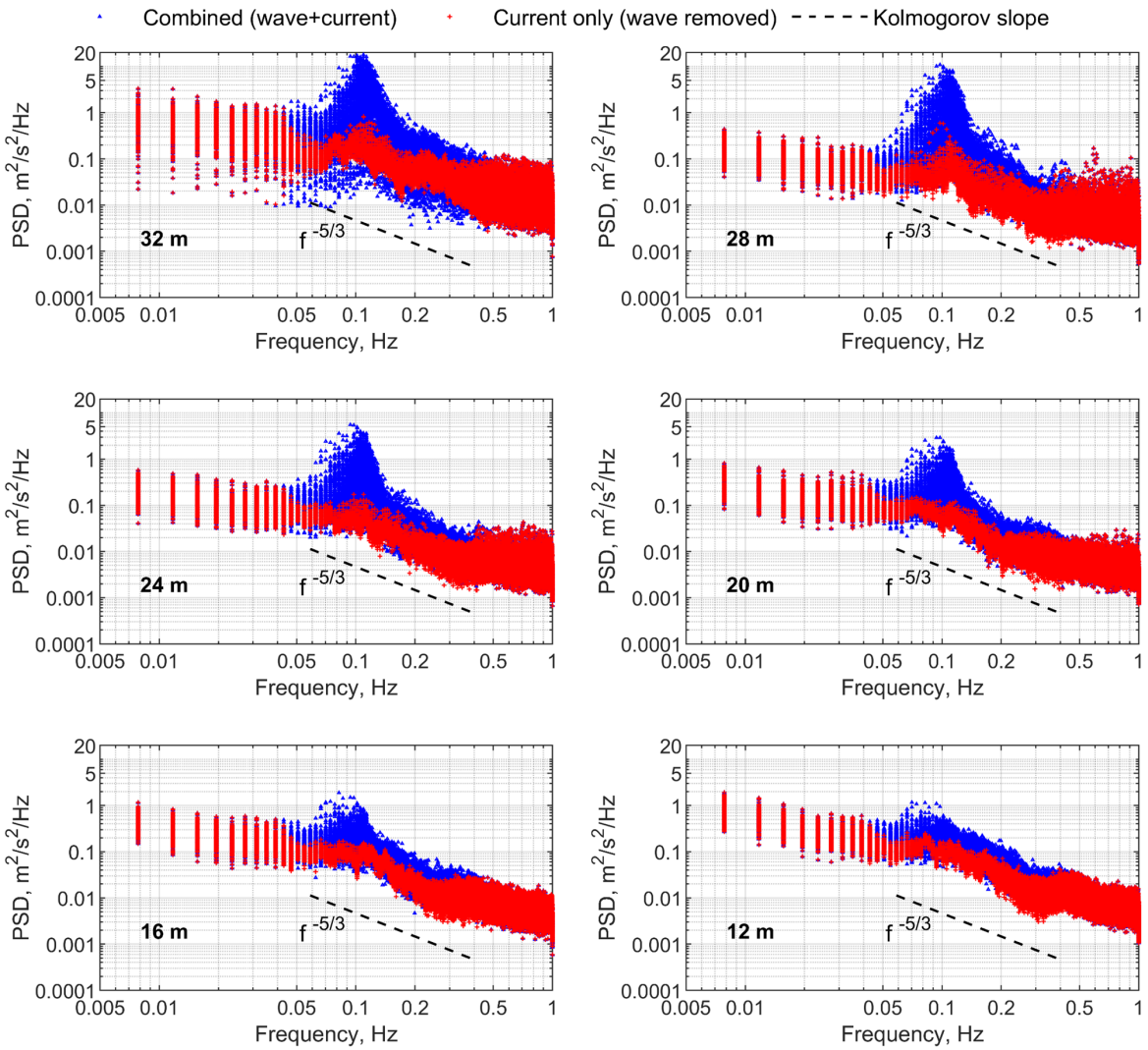

Figure 5.9 PSD comparison between wave-current velocity and separated current velocity at ADCP4 site
Six depths are shown here, from 12 m to 32 m above the seabed, with the interval of 4 m. Each plot contains 440 30-min time series of Ebb flows with speed range (2.5, 3) m/s.

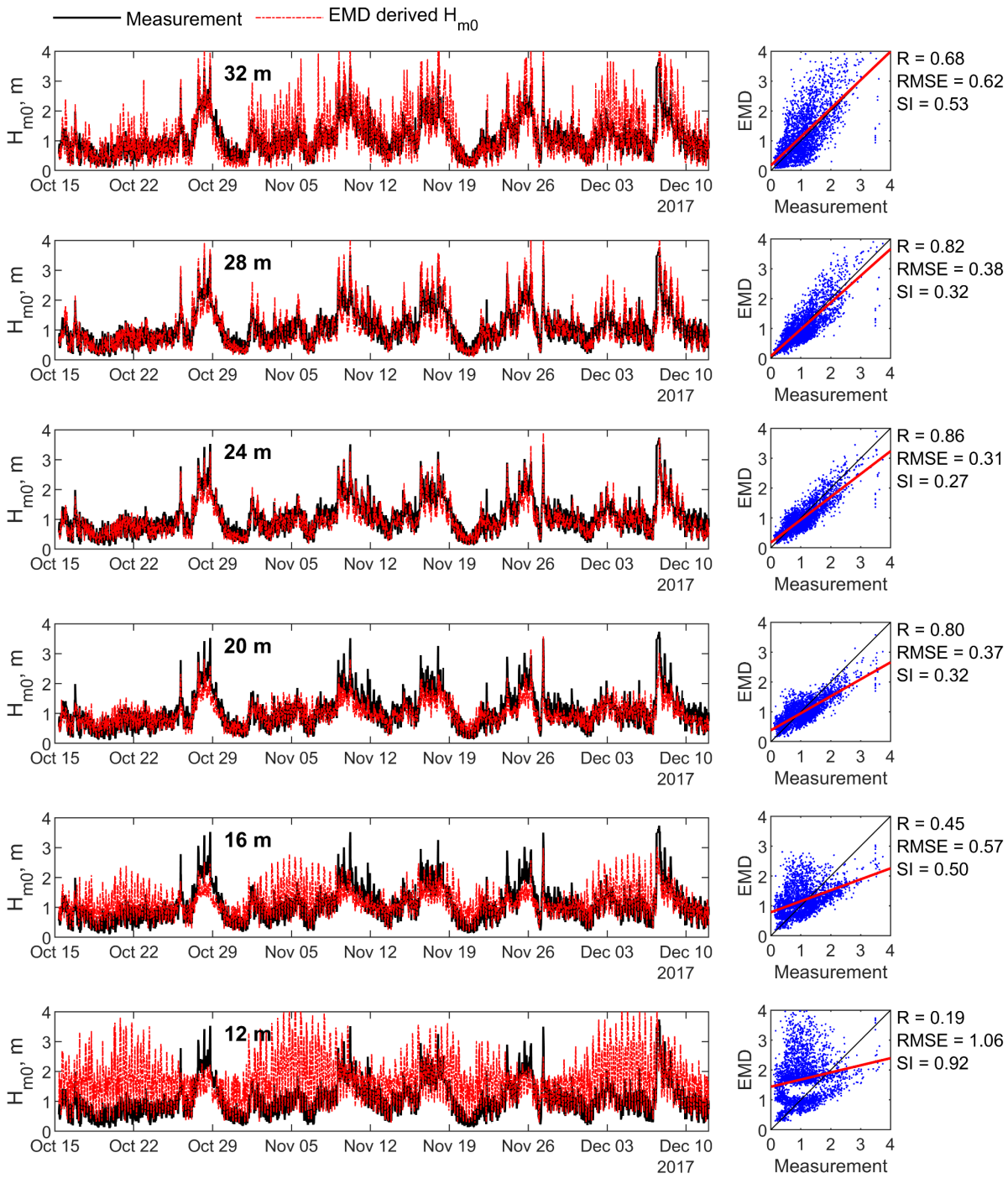

Figure 5.10 H_{m0} comparison of between field measurements and EMD-derived results at ADCP4 site
Six depths are shown here, from 12 m to 32 m above the seabed, with the interval of 4 m.

5.4.4 Method validation of ADCP2 and ADCP3

As the validation using ADCP4 measurements demonstrated the effectiveness of the wave-turbulence decomposition method during both active and low wave periods, this section examines its application to ADCP2 and ADCP3 measurements. As shown in Figure 5.11, the

decomposition method worked well for both measurements and effectively removed the waves. When compared to ADCP4 results at the same water depth, it is evident that the wave energy has significantly reduced (PSD wave peak drops from 5 in Figure 5.9 to about 1 here), indicating fewer active waves for these periods.

Additionally, as illustrated in Figure 5.12, the wave heights for ADCP2, derived from the separated wave orbital velocity at the depth of 24 m, closely matched the numerical modelling results (generated by TOMAWAC-TELEMAC 3D) with an R value of 0.79. For ADCP3, shown in Figure 5.12, the R value is 0.67, which, despite low amplitudes making correlation challenging and potentially causing significant variance for minor errors, is still considered acceptable.

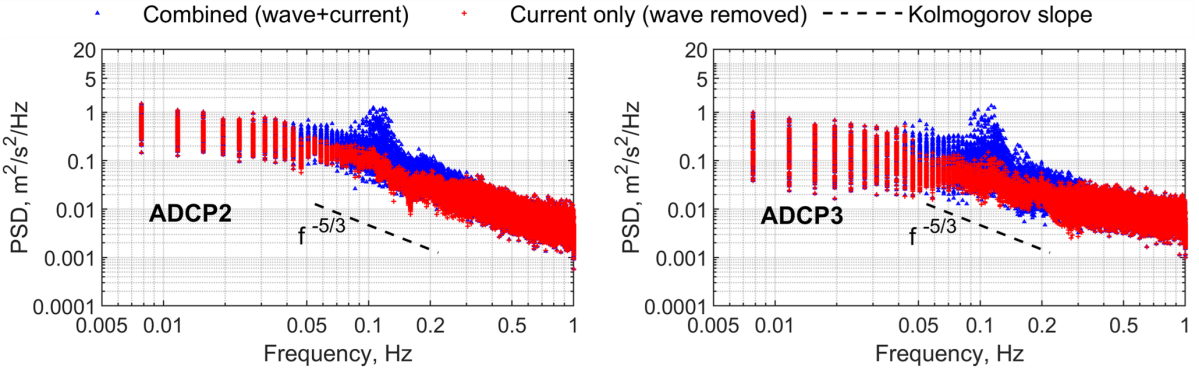

Figure 5.11 PSD comparison between wave-current velocity and separated current velocity at turbine tip-height for ADCP2 and ADCP3 sites

Only the depth of 24 m above the seabed is shown. Left: ADCP2, containing 97 30-min timeseries of Ebb flows with speed range (2.5, 3) m/s. Right: ADCP3, containing 110 series.

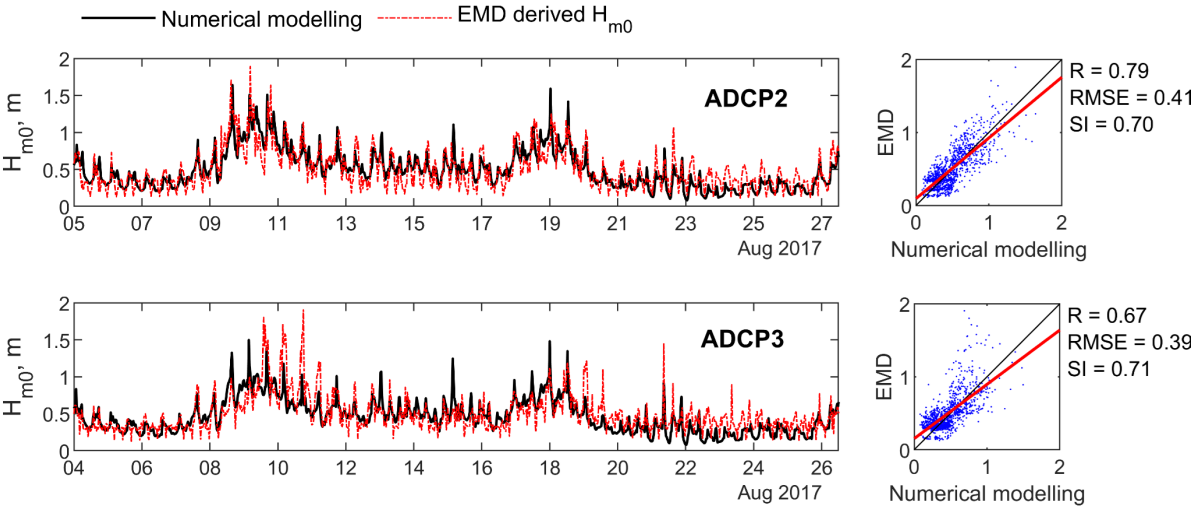

Figure 5.12 H_{m0} comparison of between numerical simulation results and EMD-derived results at ADCP2 and ADCP3 sites

Only the depth of 24 m above the seabed is shown. Upper: ADCP2. Lower: ADCP3.

5.5 Turbulence intensity (TI) characterisation for ADCP4

The turbulence intensity TI is the key parameter to represent the turbulence quantification. By using the decomposition method and having obtained the wave orbital velocity and current velocities in streamwise u, transverse v, and vertical w directions, it is possible to evaluate their corresponding TI values. For each direction, the TI is defined as the standard deviation of the velocity components over the mean streamwise velocity [124]:

$$TI = \frac{\sigma}{\bar{u}} \tag{5.7}$$

where σ represent the standard deviation velocity fluctuations. For the streamwise direction, the standard deviation velocity fluctuations of the original combined velocity u_i', current velocity u', and wave orbital velocity $\tilde{u}$ are given by

$$\sigma_{combined} = \sqrt{\overline{u_i'^2}} \tag{5.8}$$

$$\sigma_{current} = \sqrt{\overline{u'^2}} \tag{5.9}$$

$$\sigma_{wave} = \sqrt{\overline{\tilde{u}^2}} \tag{5.10}$$

The turbulence intensities of each velocity component are then expressed by

$$TI_{combined} = \frac{\sigma_{combined}}{\bar{u}} \tag{5.11}$$

$$TI_{current} = \frac{\sigma_{current}}{\bar{u}} \tag{5.12}$$

$$TI_{wave} = \frac{\sigma_{wave}}{\bar{u}} \tag{5.13}$$

This work has calculated these terms for all three directions (i.e., u, v, w), which will be grouped by the flow speeds at turbine hub-height (i.e., 15 m from the seabed) and wave heights, respectively.

5.5.1 Vertical profile of TI for varying speed range

To quantify the changes in TI caused by waves, the entire dataset is first divided into low and high wave height groups, using the median wave height of 1.02 m for ADCP4 recordings as the boundary. Within each dataset, TI is analysed for the original wave-current combined velocity (without tidal harmonics or trends), separated current velocity, and wave orbital velocity across three directions, grouped by different speed ranges. The hub-height speed is used for speed categories, which start from the turbine's cut-off speed (1 m/s) [121] and increase in intervals of 0.5 m/s up to the turbine's rated speed (3 m/s), with the last group for speeds over the rated speed. For each group, outliers were removed, and the median value was used to

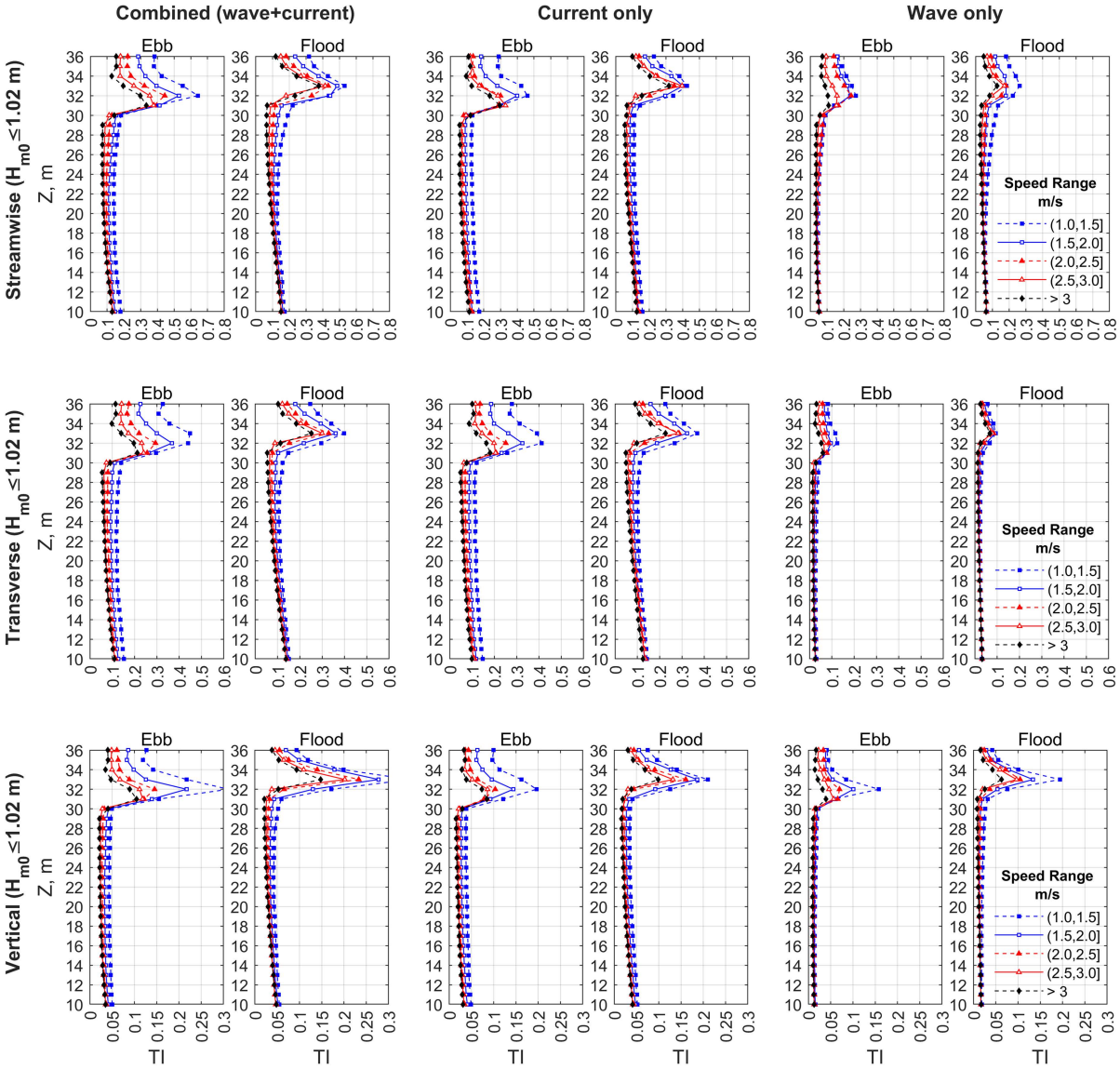

Figure 5.13 TI vertical profiles for streamwise, transverse, and vertical velocity grouped by hub-height flow speed for ADCP4 under low wave conditions (H_{m0} ≤ 1.02 m)

Z is the water depth above the seabed.

represent the TI level for that category. Median values at various depths created vertical profiles, displayed in Figure 5.13 for the low wave height dataset ($H_{m0} \leq 1.02\ m$) and Figure 5.14 for the high wave height dataset ($H_{m0} > 1.02\ m$).

Generally, for all depths, the TI in higher speed groups always have smaller values. Regarding the features of the vertical profiles, the flow above 30 m is more turbulent than at deeper depths due to proximity to the sea surface and strong vertical mixing. The maximum TI is seen at 32 m for the Ebb phase and 33 m for the Flood phase, where the TI for the original streamwise velocity exceeded 0.5. Below 30 m, the TI profile appears to stabilize, and changes became more monotonic.

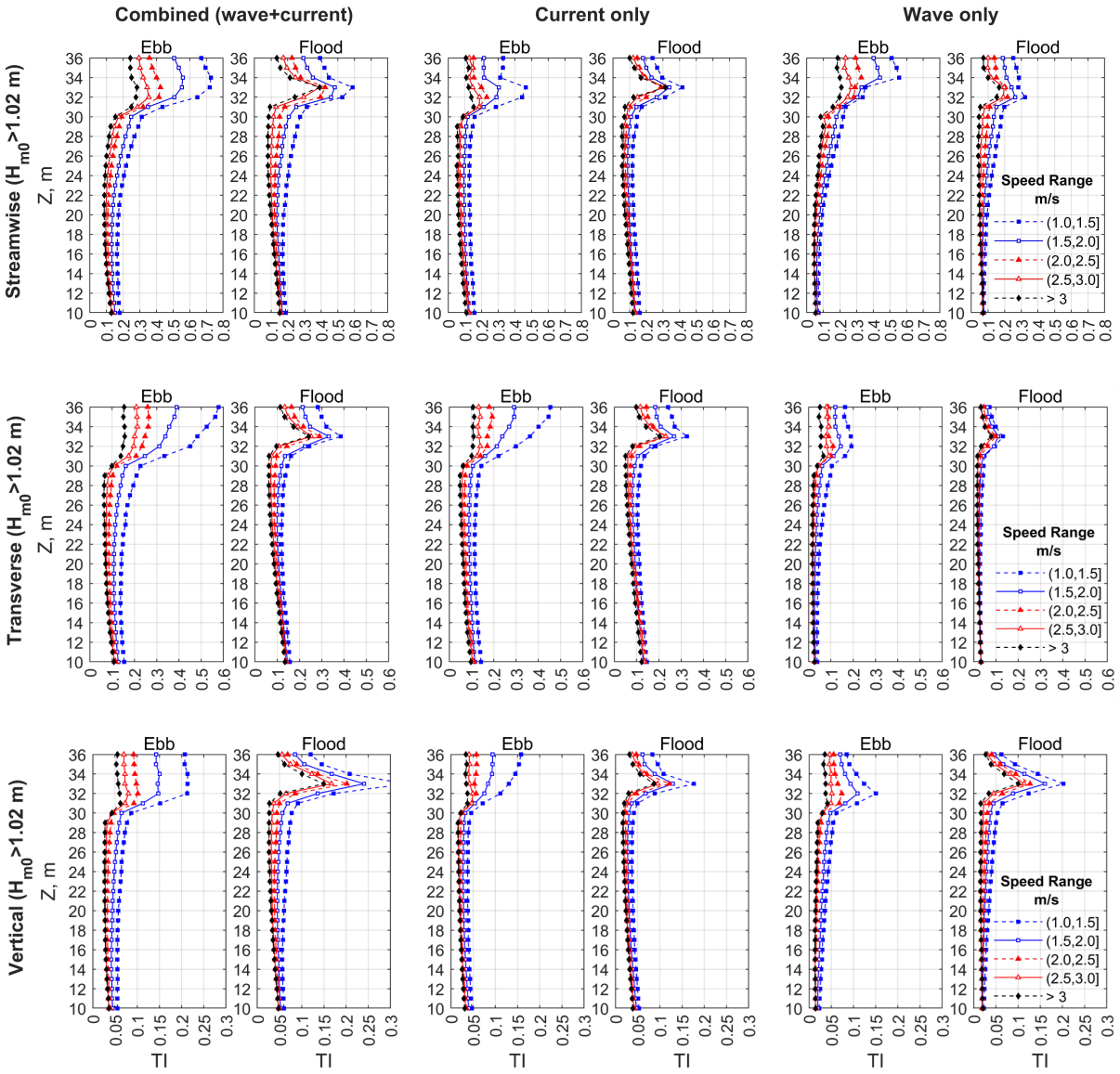

Figure 5.14 TI vertical profiles for streamwise, transverse, and vertical velocity grouped by hub-height flow speed for ADCP4 under low wave conditions (H_{m0} > 1.02 m)

Z is the water depth above the seabed.

Detailed analysis began with the streamwise velocity of the Ebb flow. Under small wave height conditions (Figure 5.13), at the blade tip-height (24 m), the wave-current combined TI ranged from 0.07 at speeds over 3 m/s to 0.14 at speeds from 1 to 1.5 m/s. The TI for current alone ranged from 0.06 to 0.13, while the wave-induced TI is between 0.03 and 0.05, indicating that turbulence by current alone dominated the flow and wave contributions were minimal. Under high wave height conditions (Figure 5.14), combined TI significantly increased to 0.09 for the speed group of over 3 m/s (by around 28.6% increase) to 0.21 for the speed between 1 and 1.5 m/s (by around 50% increase). This may be attributed to the increase of waves TI to 0.07 – 0.14, while the current contribution remains stable. It is noticeable that, at the tip-height, TI from waves is even higher than that from the current, highlighting the dominant role of wave-induced turbulence under high wave conditions.

Wave impacts are also observed at the hub-height (15 m). For small wave heights, the combined TI for Ebb flow ranged from 0.1 to 0.15, closely matching the current TI, with negligible wave TI at 0.04. Under high wave conditions, results for high-speed flow (> 3 m/s) remained consistent, while for lower speeds (1 to 1.5 m/s), the combined TI increased to 0.17 (by around 13% increase) due to a rise in wave TI to 0.07. Nevertheless, this increase seems small compared to the tip-height layer. Flood flow exhibited a similar increase in extent to Ebb flow. Further details can be found in Table 5.2, which summarises the streamwise turbulence intensity ranges at tip- and hub-height under both low and high wave conditions.

Table 5.2 Streamwise TI ranges by flow speed at tip- and hub-height under low (H_{m0} ≤ 1.02 m) and high wave conditions (H_{m0} > 1.02 m) for ADCP4

H_{m0} (m)	Position	Original		Current only		Wave only	
		Ebb	Flood	Ebb	Flood	Ebb	Flood
≤ 1.02	Tip	0.07 – 0.14	0.08 – 0.13	0.06 – 0.13	0.06 – 0.11	0.03 – 0.05	0.03 – 0.07
	Hub	0.10 – 0.15	0.12 – 0.15	0.08 – 0.15	0.10 – 0.14	0.04	0.06
> 1.02	Tip	0.09 – 0.21	0.08 – 0.20	0.05 – 0.13	0.06 – 0.12	0.07 – 0.14	0.05 – 0.12
	Hub	0.10 – 0.17	0.12 – 0.17	0.08 – 0.14	0.10 – 0.14	0.05 – 0.07	0.06 – 0.08

5.5.2 Temporal variation of current speed and TI related parameters

As the vertical profiles formed by median TI values may miss the temporal features of the velocity time series, Figure 5.15 presents two examples of a two-day time series for the streamwise TI at the 15 m depth to closely examine the wave impacts on the hub-height. These examples compare low wave cases with a mean H_{m0} of 0.9 m (Figure 5.15 (a)) and high wave cases with a mean H_{m0} of 1.9 m (Figure 5.15 (b)). Generally, the amplitudes of

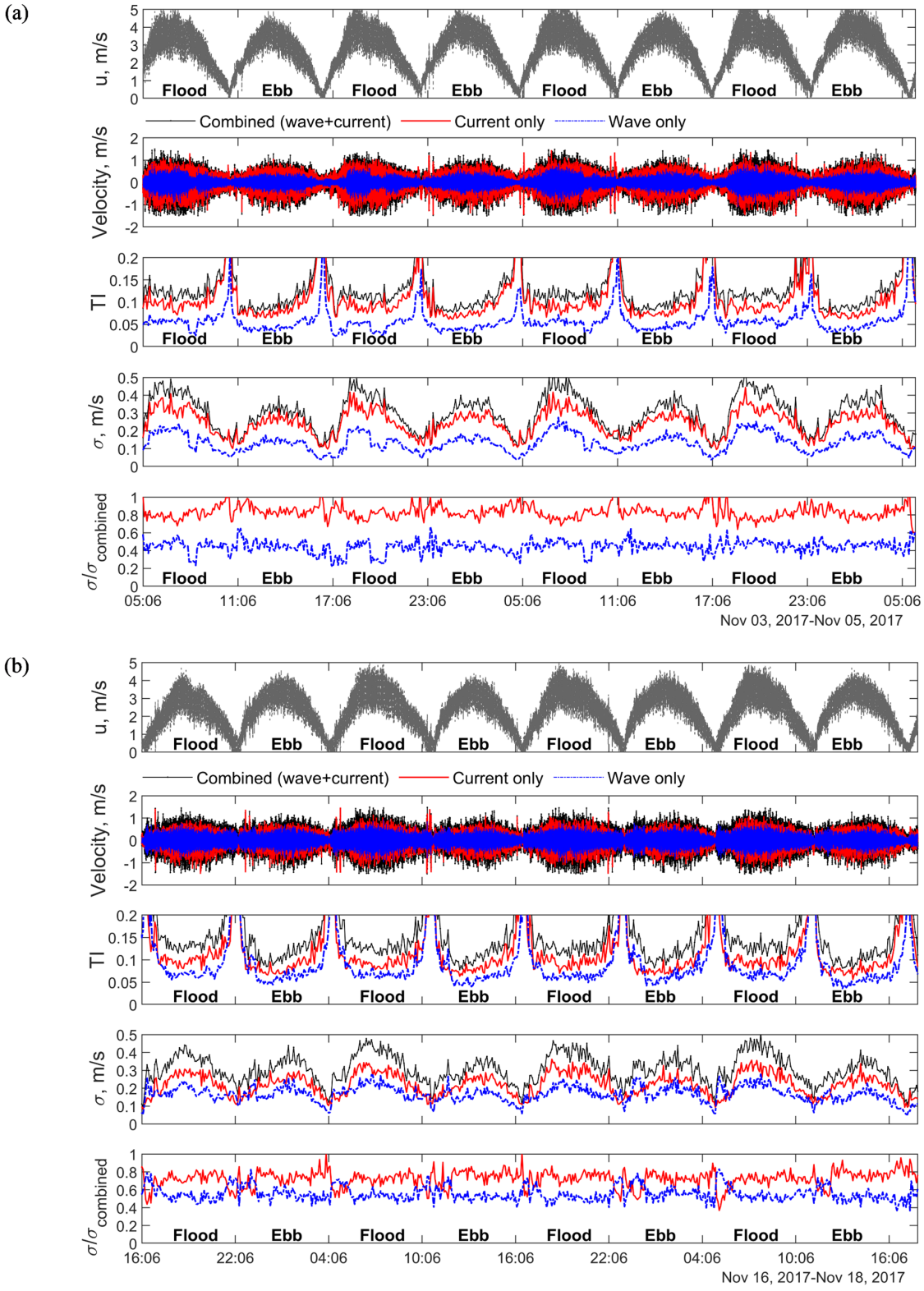

Figure 5.15 Analysis of two continuous two-day timeseries at hub-height of ADCP4

Upper figure (a): a low wave case (min: 0.38 m, max: 1.58 m, mean: 0.90 m). Bottom (b): a high wave case (min: 1.28 m, max: 3.26 m, mean: 1.90 m). The subplots from top to bottom are the initial streamwise velocity ($\boldsymbol{u}$), the velocity with tidal harmonics or trend removed, the turbulence intensity (TI), the standard deviation of the velocity ($\boldsymbol{\sigma}$), and the ratio of the standard deviation of wave or current velocity to that of the combined velocity ($\boldsymbol{\sigma/\sigma_{combined}}$).

streamwise velocity u in the low wave height case are observed to be higher than those in the high wave case, while the combined velocity amplitudes remain at a similar level of 1 m/s after removing tidal harmonics or trends. Regarding the TI series, for both cases, the Ebb flows generally exhibit a larger variance in TI values than the Flood flow, as the Ebb has a higher temporal slope than the Flood flow.

In the low wave height scenario (Figure 5.15 (a)), the amplitude of current-only velocity is just slightly lower than the combined velocity, while the wave orbital velocity is about half of it. This is also reflected in the velocity standard deviation σ and the ratio $\sigma/\sigma_{combined}$, where the former shows closer values between the combined and the current-only case, while the latter shows that the current accounts for over 80% of the total TI and the wave contribution remains below 50% most of the time. However, in cases with higher waves (Figure 5.15 (b)), the amplitudes of wave orbital velocity increase significantly, as indicated by the enlarged blue area in the velocity series plot and the reduced red area, as well as the increased amplitudes of σ_{wave} in the velocity standard deviation σ plot. The ratio of standard deviations $\sigma/\sigma_{combined}$ further reveals that the contributions of current and wave are converging, with the current ratio dropping to around 70% and the wave ratio rising to generally above 50%. Without the normalization of the streamwise velocity, the increase in σ_{wave} and $\sigma/\sigma_{combined}$ for the high wave cases more accurately highlight the impacts of waves on the turbine hub than just the TI analysis.

5.5.3 Histograms of TI related parameters

Further evidence of wave effects is visible in the histograms of occurrences probability (see Figure 5.16) of TI and the standard deviation ratio of currents or waves to the combined velocity $\sigma/\sigma_{combined}$. Figure 5.16 (a) and (b) display histograms for the tip and hub-height under low wave conditions ($H_{m0} \leq 1.02\,m$), while Figure 5.16 (c) and (d) show the same for high wave conditions ($H_{m0} > 1.02\,m$). A comparison at tip-height depth of 24 m reveals that for both Ebb and Flood flow, wave TI occupies a smaller range of values in low wave conditions but increases significantly to mirror the distribution profile of current in high wave scenarios. This is further evidenced by the wave ratio $\sigma_{\mathrm{wave}}/\sigma_{combined}$ shifting from a smaller value zone (median value of 49% for Ebb and 46% for Flood) to larger values (59% for Ebb and 68% for Flood), with its distribution overlapping that of the current-only case.

At the hub-height depth of 15 m (Figure 5.16 (b) and (d)), while the increase in wave contribution is less pronounced than at the tip-height depth, there is still a 15% increase for both Ebb and Flood flow in the median value of the $\sigma_{\mathrm{wave}}/\sigma_{combined}$ from low to high wave conditions.

The median value gap between waves and currents narrows from 51% to 39% for Ebb flow and from 45% to 33% for Flood flow. The histograms also reveal that the TI level gaps between the tip-height and hub-height depths become larger from low to high waves, suggesting that unequal turbulence level distribution is exacerbated during higher wave events, increasing the

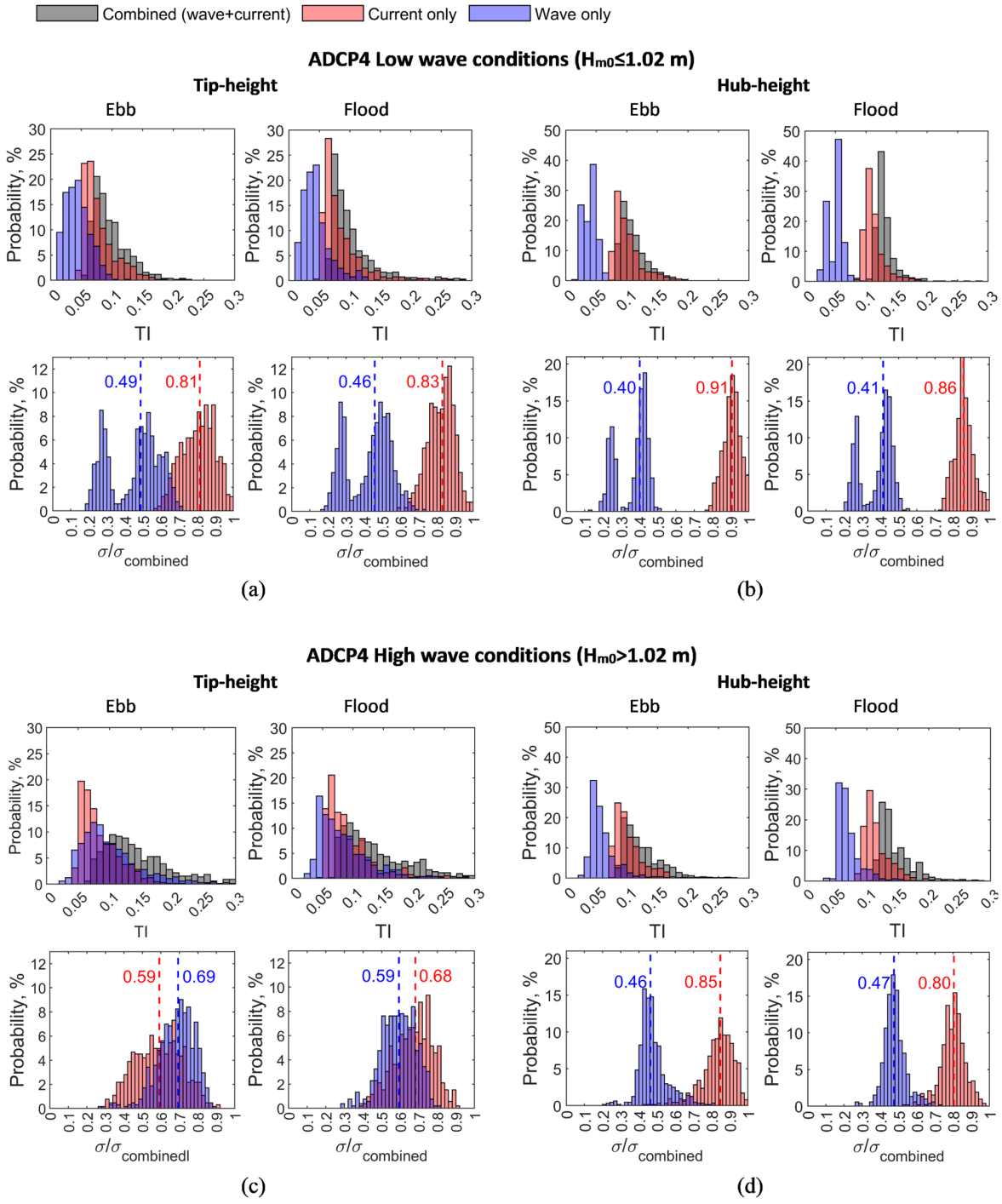

Figure 5.16 Probability histograms of occurrences for TI and $\sigma/\sigma_{combined}$ for ADCP4

$\sigma/\sigma_{combined}$ represents the standard deviation ratio of current or wave against the combined velocity. (a) tip-height depth at low wave heights, (b) hub-height depth at low wave heights, (c) tip-height depth at high wave heights, and (d) hub-height depth at high wave heights. Median value of the σ/σ_combined plot is marked by the dot line.

risk of unbalanced pressure around the turbine blade. Additionally, Ebb and Flood flow show slight differences in the shape of TI distribution, with Ebb flow consistently having larger variances, consistent with the slope observations of the TI time series shown in Figure 5.15.

When comparing the current histograms during low and high waves, their shape and probability of occurrences remain almost unchanged, aligning with expectations that once waves are effectively removed from the series, the remaining turbulence velocity distribution should follow a similar pattern. This further confirms the accurate decomposition between wave orbital velocity and current turbulence.

In addition to analysing streamwise velocity, this study examines transverse and vertical velocities to better understand wave effects on three-dimensional velocity. While some research has described the characteristics of three-dimensional flows for tidal site studies [124,125], this is the first comprehensive investigation applying wave-turbulence decomposition to them, revealing the effects of waves on three-dimensional flows. Referring back to Figure 5.13 and Figure 5.14, for transverse velocity during the Ebb phase at slow flows (1 to 1.5 m/s), the combined TI at the tip-height increases from 0.12 at low waves to 0.16 at high waves (33.3% increase) due to the significant increase of wave-only TI from 0.03 to 0.06; whereas, at hub-height, the increase in combined TI is relatively small being 7.6% (from 0.13 to 0.14), as the wave-only TI is almost unchanged. For vertical velocity, there is a 50% increase in combined TI at tip-height (0.04 to 0.06) and a 20% increase at hub-height (0.05 to 0.06) from low waves to high waves. Further details of the transverse and vertical TI ranges can be found in Table 5.3 and Table 5.4.

Table 5.3 Transverse TI ranges by flow speed at tip- and hub-height under low (H_{m0} ≤ 1.02 m) and high wave conditions (H_{m0} > 1.02 m) for ADCP4

H_{m0} (m)	Position	Original		Current only		Wave only	
		Ebb	Flood	Ebb	Flood	Ebb	Flood
≤ 1.02	Tip	0.06 – 0.12	0.07 – 0.11	0.06 – 0.12	0.06 – 0.10	0.01 – 0.03	0.02 – 0.02
	Hub	0.08 – 0.13	0.11 – 0.13	0.08 – 0.13	0.10 – 0.12	0.02 – 0.03	0.03
> 1.02	Tip	0.07 – 0.16	0.07 – 0.12	0.05 – 0.12	0.06 – 0.11	0.02 – 0.06	0.02 – 0.03
	Hub	0.08 – 0.14	0.11 – 0.14	0.07 – 0.12	0.10 – 0.13	0.02 – 0.04	0.03

Table 5.4 Vertical TI ranges by flow speed at tip- and hub-height under low (H_{m0} ≤ 1.02 m) and high wave conditions (H_{m0} > 1.02 m) for ADCP4

H_{m0} (m)	Position	Original		Current only		Wave only	
		Ebb	Flood	Ebb	Flood	Ebb	Flood
≤ 1.02	Tip	0.02 – 0.04	0.03 – 0.04	0.02 – 0.04	0.02 – 0.04	0.01 – 0.02	0.01 – 0.02
	Hub	0.03 – 0.05	0.04 – 0.05	0.02 – 0.04	0.03 – 0.04	0.01	0.02
> 1.02	Tip	0.03 – 0.06	0.03 – 0.06	0.02 – 0.04	0.02 – 0.04	0.02 – 0.04	0.02 – 0.04
	Hub	0.03 – 0.06	0.04 – 0.06	0.02 – 0.04	0.03 -0.04	0.01 – 0.03	0.02 – 0.03

5.5.4 Empirical relationship among wave, current, wave-current velocities

An empirical mathematical relationship among the turbulence intensity of the original velocity, current turbulence, and wave orbital velocity, which is simply as the original turbulence velocity equal to the 0.8 times the sum of the wave and current turbulence intensity:

$$TI \approx 0.8 \times (TI_{current} + TI_{wave}) \quad (5.14)$$

Figure 5.17 and Figure 5.18 display the streamwise approximation across various speed ranges during low and high wave events. The results indicate that the approximation (light green) closely matches the original results (black), providing engineers with useful insights for estimating wave effects under specific speed conditions. It is important to note that this relationship is an empirical result derived from observation. This research does not delve into the physical meaning behind this relationship.

Additionally, Figure 5.17 and Figure 5.18 offer a clearer comparison of turbulence intensity between current turbulence and wave orbital velocity. In low wave scenarios, whether for Ebb or Flood flows, the current generally exhibits higher values than the wave. However, in high wave cases, wave intensities exceed those of the current from layer 24m to 30m above the seabed during slower Flood flows (≤ 2m/s). For Ebb flows, this phenomenon extends to layers above 24m across all speed categories, indicating a significantly more turbulent environment at shallower depths.

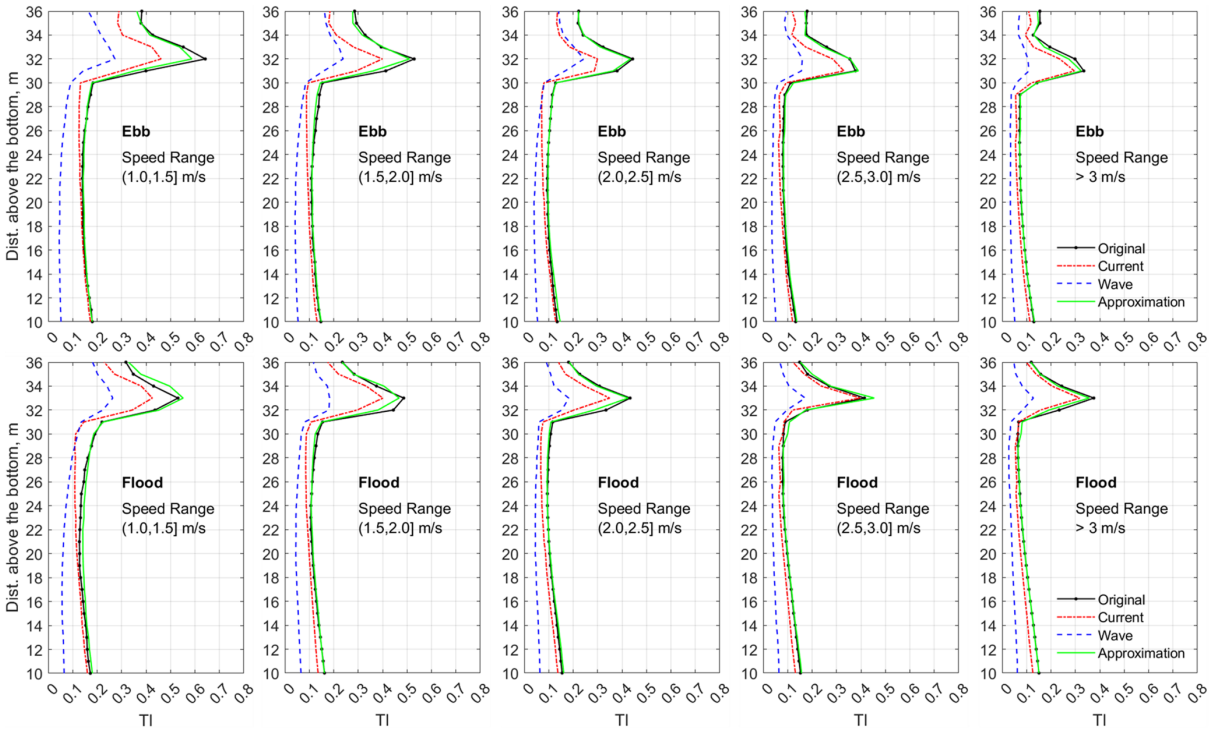

Figure 5.17 Approximation relationship among TI of wave, current, wave-current velocities for ADCP4 under low wave height conditions ($H_{m0} \leq 1.02$ m)

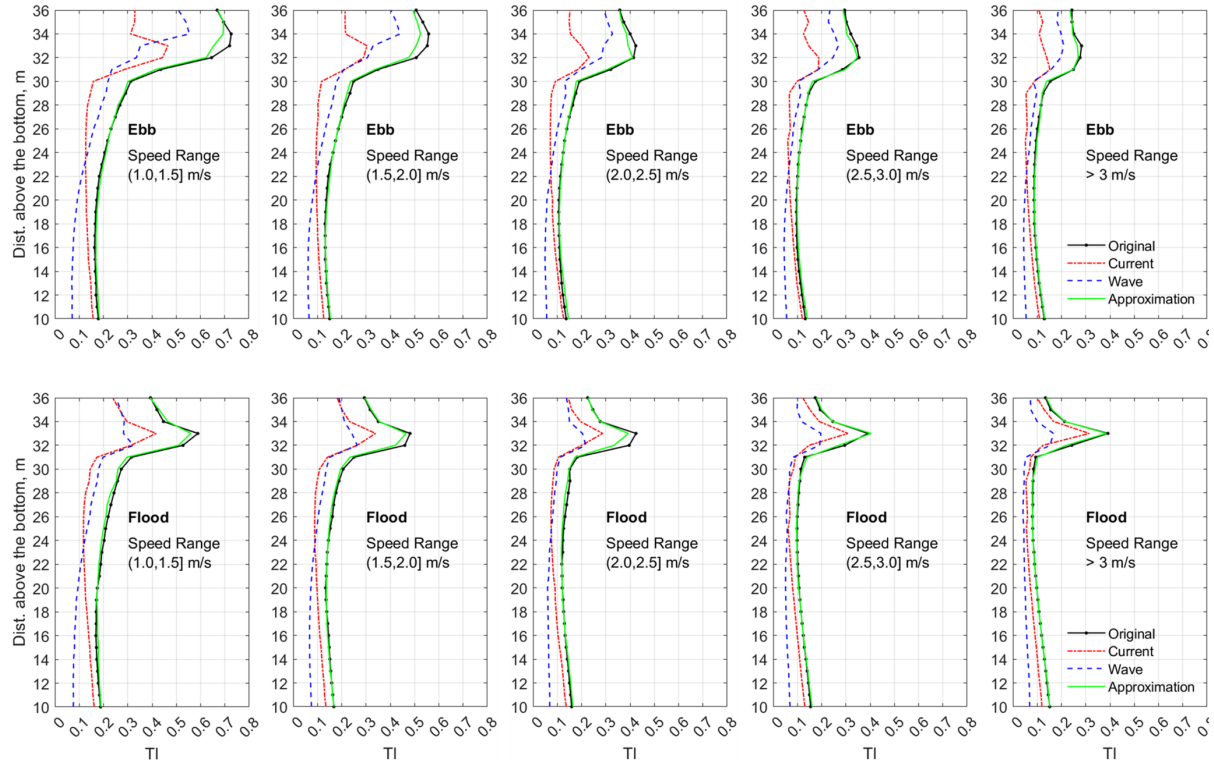

Figure 5.18 Approximation relationship among TI of wave, current, wave-current velocities for ADCP4 under high wave height conditions ($H_{m0} > 1.02$ m)

5.5.5 Vertical profile of TI for varying wave heights

To refine the discussion on wave influence beyond general categories of low and high waves, this study furtherly examines TI of wave-current combined velocity, current velocity and wave orbital velocity under finer wave ranges for flows whose speeds exceed the cut-off speed of the tidal turbine (i.e., 1 m/s). In order to guarantee adequate samples and representative wave categories, the data is segmented based on wave height levels of less than 1m, between 1 m and 1.5 m, 1.5 m to 2 m, and above 2 m. Figure 5.19 presents the three-dimensional vertical profiles of these groups, represented by median values.

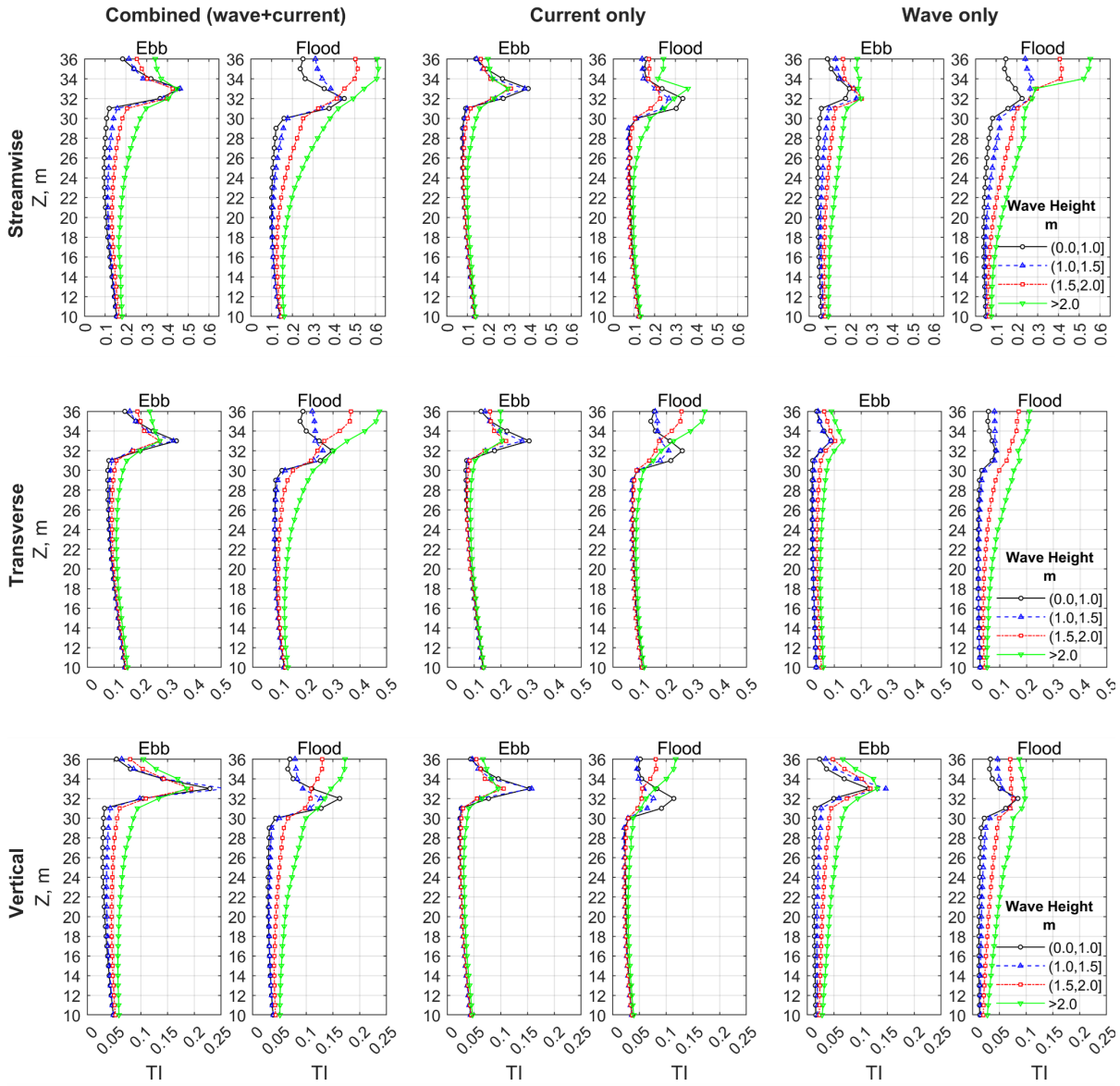

Figure 5.19 TI vertical profiles streamwise, transverse, and vertical velocity at speeds over 1 m/s, grouped by wave heights for ADCP4

Generally, TI increases with larger wave heights. At the tip-height, the original combined TI for the Ebb flow starts at 0.1 for small waves and reaches 0.2 for waves higher than 2 m with a double increase, while for the Flood flow it starts at 0.1 and increases to 0.23 with a 150% increase. This indicates that streamwise Flood flow at top layers is more susceptible to wave impact than Ebb flow. The contribution to TI at this water depth is primarily from the waves, which align closely with the combined TI and significantly exceed that from current turbulence. Notably, there is still a marked difference in combined TI at the hub-height, where the value for Ebb flow is 0.13 for low waves (< 1 m) and 0.17 for high waves (> 2 m).

Ideally, current TI should remain constant across all wave height groups if waves are effectively isolated from the measurements. While the profiles for wave heights smaller than 2 m nearly overlap for the depths below 30 m, indicating successful isolation, the profile for waves at 2 m shows slight deviations. This discrepancy could be due to an insufficient sample size for high wave conditions compared to other groups, leading to minor variations in the median values.

5.6 TI characterisation for ADCP2 and ADCP3

For ADCP2 and ADCP3, surface waves remained under 1 m for most of the recording period, resulting in insufficient samples to analyse more wave conditions. Consequently, only wave heights below 1.02 m were selected for speed range categorization and comparison with ADCP4's low wave analysis. The results for three-dimensional velocity are presented in Figure 5.20 and Figure 5.21. Similar to ADCP4, ADCP2 and ADCP3 exhibit strong vertical mixing for being turbulent in the surface layers, while the depths below 28 m show greater stability.

According to paper [79], the mean streamwise TI at ADCP2 and ADCP3 at the hub-height (15 m) is approximately 0.12 during the Ebb phase and 0.10 during the Flood phase, consistent with the results presented in Figure 5.20 and Figure 5.21 for speeds over 3 m/s, further validating this turbulence analysis method and affirming the accuracy of velocity analyses in the other two directions. The ebb flow of ADCP2 and ADCP3 also exhibits a larger variance in TI levels than the Flood flow across high and low-speed conditions. However, given the minimal wave heights, the wave TI remains at levels around 0.05, indicating relatively calm and safe periods for tidal turbine operation.

To further demonstrate wave effects on the turbine, Figure 5.22 and Figure 5.23 show histograms of the probability of occurrences of TI and the ratio of the standard deviation of current

turbulence or wave orbital velocity against the combined $\sigma/\sigma_{combined}$ for the tip-height and hub-height depths at ADCP2 and ADCP3, respectively. At both locations, the 15 m generally exhibits lower wave effects than the 24 m, as indicated distinctly by smaller values and a narrower concentration range for both TI and $\sigma/\sigma_{combined}$. The overlap with the current-only case is also smaller at this depth.

ADCP2 and ADCP3 display similar distribution profiles due to their proximity and identical recording periods, leading to comparable patterns. When compared to the low wave height results of ADCP4 in Figure 5.16, the distributions for both the 24 m and 15 m depths show similar profiles, confirming that the distribution primarily depends on wave height conditions, even though the data were recorded in different seasons.

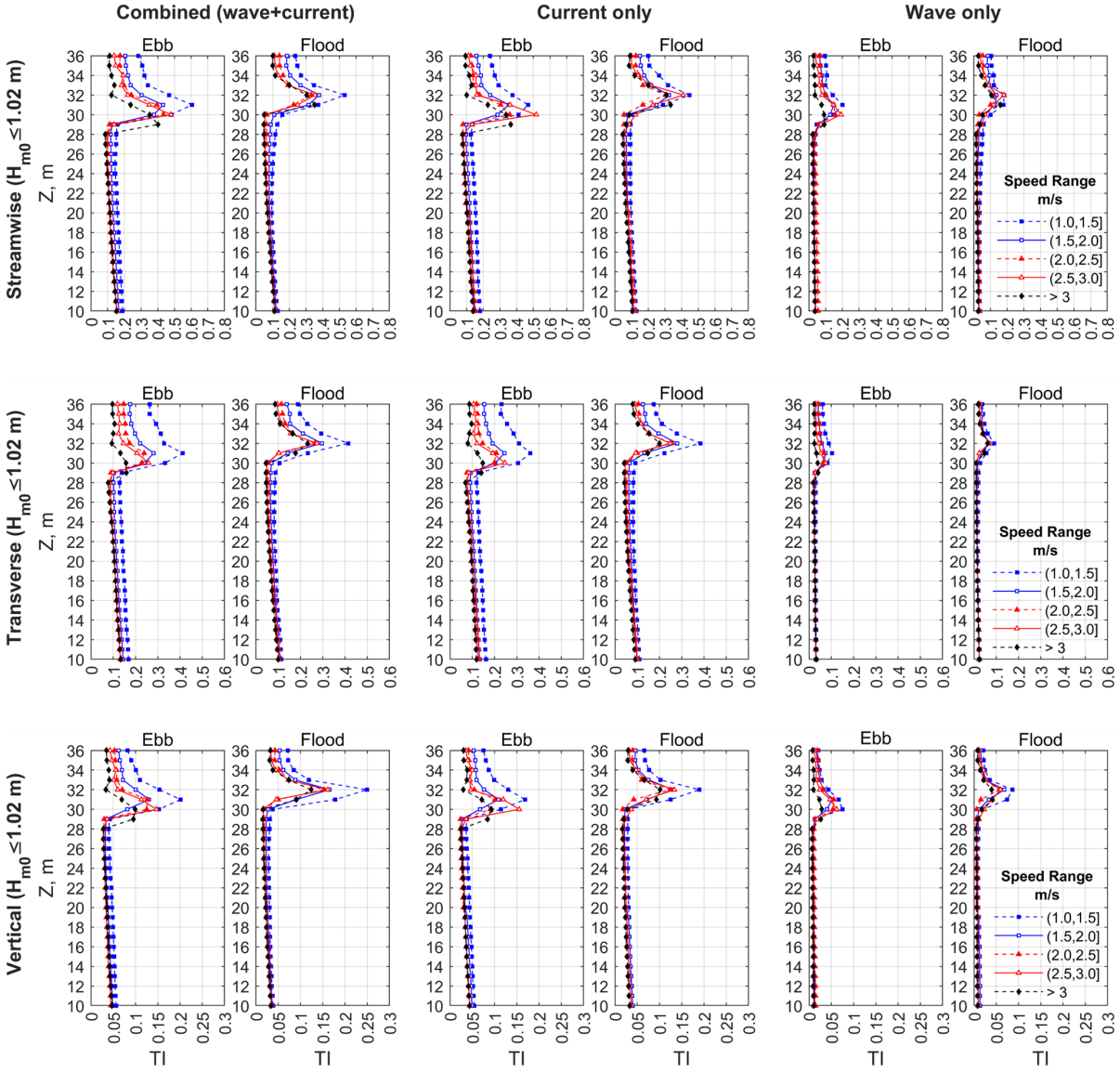

Figure 5.20 TI vertical profiles for streamwise, transverse, and vertical velocity grouped by hub-height flow speed for ADCP2 under low wave conditions (H_{m0} ≤ 1.02 m)

Z is the water depth above the seabed.

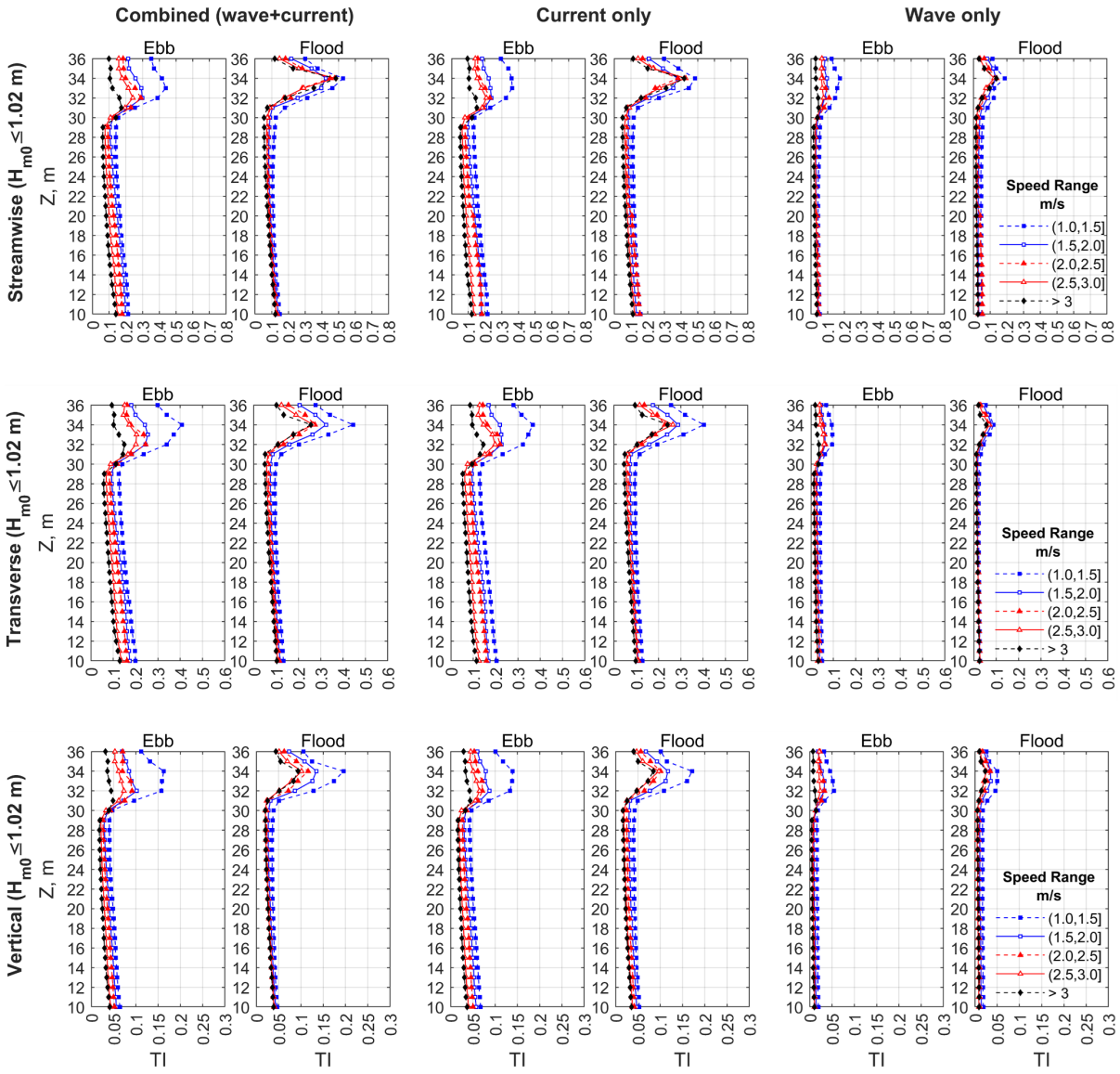

Figure 5.21 TI vertical profiles for streamwise, transverse, and vertical velocity grouped by hub-height flow speed for ADCP3 under low wave conditions (H_{m0} ≤ 1.02 m)

Z is the water depth above the seabed.

5.7 Turbulence kinetic energy (TKE) characterisation for ADCP4

TKE is a commonly used parameter to quantify the energy contained in turbulent fluctuations. Unlike turbulence intensity, which requires analysis in specific directions, TKE represents the combined effects of turbulence across all three dimensions. For the combine wave-current velocity, it is defined as:

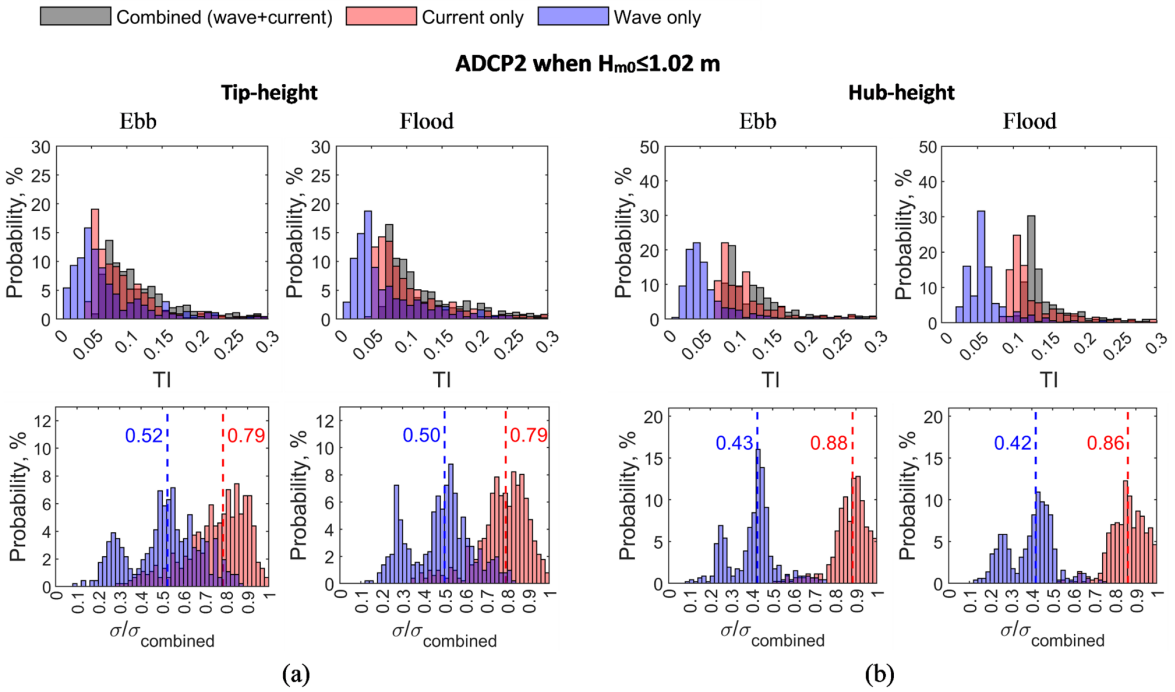

Figure 5.22 Probability histograms of occurrences for TI and $\sigma/\sigma_{combined}$ for ADCP2

$\sigma/\sigma_{combined}$ represents the standard deviation ratio of current or wave against the combined velocity. (a) tip-height depth when $H_{m0} \leq 1.02\ m$, (b) hub-height depth when $H_{m0} \leq 1.02\ m$. Median value of the $\sigma/\sigma_{combined}$ plot is marked by the dot line.

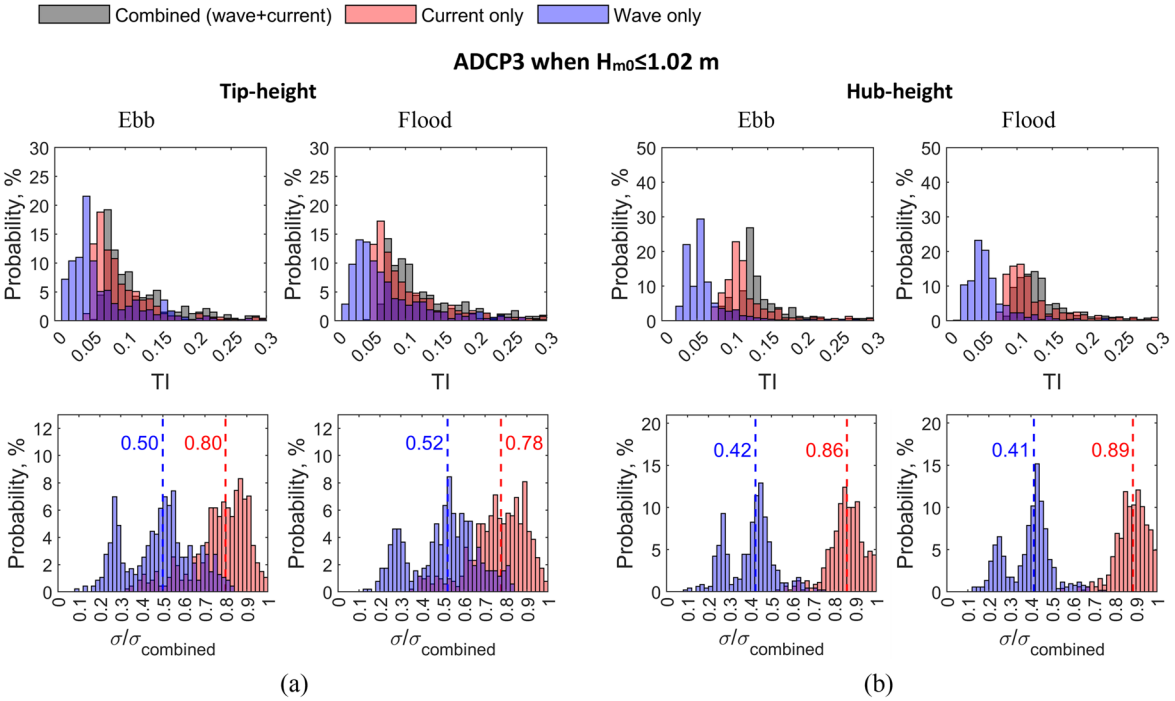

Figure 5.23 Probability histograms of occurrences for TI and $\sigma/\sigma_{combined}$ for ADCP3

$\sigma/\sigma_{combined}$ represents the standard deviation ratio of current or wave against the combined velocity. (a) tip-height depth when $H_{m0} \leq 1.02\ m$, (b) hub-height depth when $H_{m0} \leq 1.02\ m$. Median value of the $\sigma/\sigma_{combined}$ plot is marked by the dot line.

$$\mathrm{TKE}_{combined} = \frac{1}{2}\left(\overline{(u_i')^2} + \overline{(v_i')^2} + \overline{(w_i')^2}\right) \tag{5.15}$$

For the TKE contributed from the current turbulence velocity and wave orbital velocity, they are defined by

$$\mathrm{TKE}_{current} = \frac{1}{2}\left(\overline{(u')^2} + \overline{(v')^2} + \overline{(w')^2}\right) \tag{5.16}$$

$$\mathrm{TKE}_{wave} = \frac{1}{2}\left(\overline{(\tilde{u})^2} + \overline{(\tilde{v})^2} + \overline{(\tilde{w})^2}\right) \tag{5.17}$$

This section investigates the TKE vertical profiles categorized by tidal current speed and wave height for analysis.

Figure 5.24 shows the vertical profile of TKE for combined wave-current, current-only, and wave-only velocities, grouped by the hub-height flow speed at ADCP4. For the original velocity TKE, it can be observed that in the depth range of 26–29 m above the seabed, TKE values under different tidal flow speeds are similar, with their curves converging. This depth range serves as a boundary point. Above this region (i.e., z > 29 m, approximately within 7 m of the water surface), TKE values are significantly higher. This is likely due to the influence of wind stress, wave breaking, and shear at the air-water interface, which inject more energy into the water column compared to the calmer, more damped conditions in deeper waters. A similar phenomenon of a sudden increase in TKE near the upper meters of water column has also observed and attributed to surface waves in [40]. These observations are consistent with the changes in wave orbital velocity-associated TKE, which increases near the surface due to stronger wave activity. Below this boundary, TKE increases as the seabed is approached, driven by enhanced shear stresses, aligning with findings from previous studies.

For wave heights less than 1.02 m (upper panel of Figure 5.24), the TKE associated with wave orbital velocity is negligible, nearly zero. Consequently, the profiles of original TKE and current-only TKE are nearly identical, with minor differences. For example, during the Ebb phase, the maximum original TKE is 0.3 m²/s² at a depth of 33 m in high-speed flows exceeding 3 m/s, whereas the corresponding current-only TKE is reduced to 0.15 m²/s². Similarly, during the Flood phase, the original TKE reaches 0.23 m²/s² at a depth of 32 m, which drops to 0.15 m²/s² for current-only TKE. These differences reflect the influence of wave activity, which becomes more pronounced for wave heights exceeding 1.02 m (lower panel of Figure 5.24). For instance, during the Ebb phase with high wave heights, the original TKE in surface waters exceeds 0.5 m²/s², while the current-only TKE drops to 0.25 m²/s², a reduction of 50%. At the turbine tip height (24 m above the seabed), the original TKE during the Ebb phase is

approximately 0.1 m²/s², while the current-only TKE decreases to 0.03 m²/s², emphasizing the continued influence of surface wave activity at this depth.

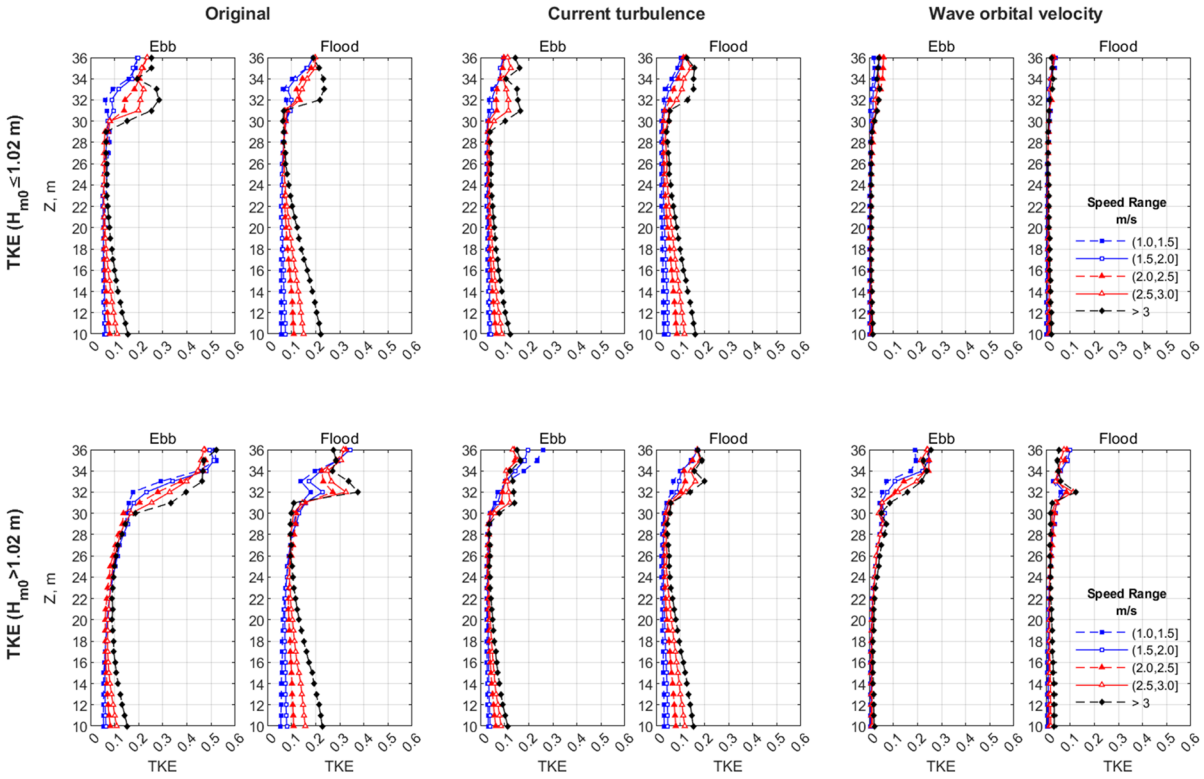

Figure 5.24 TKE vertical profiles grouped by hub-height flow speed for ADCP4 under both high (H_{m0} ≤ 1.02 m) and low (H_{m0} > 1.02 m) wave conditions

TKE unit is m²/s². Z is the water depth above the seabed.

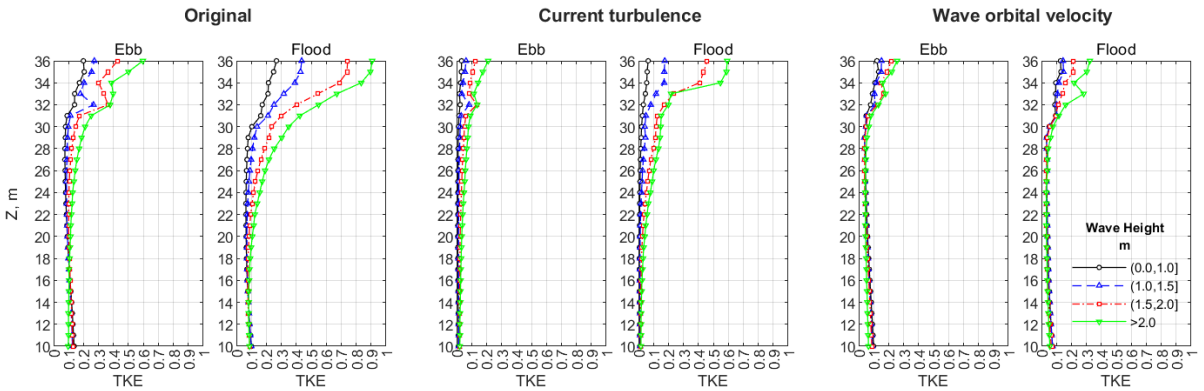

Figure 5.25 TKE vertical profiles at speeds over 1 m/s, grouped by wave heights for ADCP4

TKE unit is m²/s². Z is the water depth above the seabed.

To better illustrate the effect of waves, TKE grouped by wave height is shown in Figure 5.25. Distinct differences in TKE values are evident across four wave height categories. When wave heights exceed 2 m, the original TKE at the sea surface during the Flood phase exceeds 0.9

m^2/s^2, with wave-associated TKE surpassing 0.3 m^2/s^2. In contrast, for a wave height of 1 m, the original TKE is 0.25 m^2/s^2.

Theoretically, with sufficient data, the tidal current flow distributions across different wave height categories should be consistent. However, this study reveals that current-only TKE profiles do not overlap across wave height categories, suggesting that the dataset for high-wave conditions may be insufficient, potentially introducing representational bias. This limitation highlights an area for improvement in future research, emphasizing the need for larger datasets to enhance accuracy and reliability.

5.8 Limitation of the wave-current decomposition method

This study assumes that the phase of the reconstructed current velocity, obtained through inverse Fourier transform, is the same as the phase of the original wave-current combined velocity. While this assumption provides practical results, it is somewhat empirical and lacks a rigorous physical basis. This limitation, coupled with the EMD method—also not directly tied to physical mechanisms—makes the resulting decomposition less suitable for detailed physical analysis of wave-current interactions at small time scales. However, on a larger scale, this approach does not significantly impact statistical turbulence intensity values obtained over intervals of 10 or 20 minutes.

Given the large volume of data processed in this study, even using a 30-minute window, the decomposition spans thousands of time frames. It is impractical to manually verify each frame to ensure that the reconstructed velocities produce either an overestimation or underestimation on wave information. Moreover, it is difficult to guarantee that the energy peaks of each wave are confined to the expected frequency range of 0.04-0.25 Hz. Instances of higher or lower frequencies were indeed observed, meaning that some errors in the final separation results are unavoidable. Nevertheless, the use of median statistical methods to derive turbulence intensity profiles reduces the potential impact of such errors, ensuring that the overall results remain robust and reliable.

The ADCP data analysed in this study were collected from the Pentland Firth, where the maximum current velocity can reach up to 5 m/s. Such strong currents can lead to increased wave steepness and significant wave-breaking events, resulting in unusually strong turbulences. The method presented in this study encounters limitations in accurately separating wave and

current components within 5 meters of the water surface due to these effects. Consequently, the effectiveness of this approach in shallow water environments, where wave breaking is highly pronounced, has not yet been thoroughly validated. Further analysis using data from regions with less extreme wave-current interactions would be required to test the broader applicability of the method.

Additionally, the turbulence profile obtained from the Pentland Firth data differs from that observed in other regions where waves and currents coexist without significant wave breaking. This highlights the potential for geographical limitations in the results, underscoring the need for further studies using data from a variety of locations to ensure the findings are more universally applicable.

5.9 Summary

This study introduces a side information assisted Empirical Mode Decomposition (EMD) method to decompose wave and current velocity components from a wave-current combined time series measured at a tidal energy site by using ADCPs with the intention of quantifying the turbulence levels enhanced by wave activities. The key conclusions from this study are:

1. The decomposition method developed in this study to separate wave and current components velocities works well across various conditions: low and high wave scenarios, different depths, and three-dimensional velocities. With this technique, the depth-wise TI levels for waves alone, currents alone and wave-current combined scenarios for all three ADCP locations were successfully evaluated.

2. The gradient of the velocity spectra obtained for the current alone cases is found to agree well with the standard Kolmogorov spectral slope.

3. The Borgman's method [123] applied to compute wave spectra from the corresponding velocity spectra (obtained from the decomposition method) is found to reproduce significant wave heights reasonably well with ADCP4 measurements, specifically for depths between 20 to 28 m from the seabed. For the other two ADCPs, the wave height obtained through the numerical model simulations (conducted by using the TOMAWAC-TELEMAC 3D wave-current coupled model) produces a good comparison. To be specific, the wave heights derived from the decomposition method at the turbine tip-height match very well with the measurements of ADCP4 resulting in a high value of correlation coefficient (i.e.,

R=0.86). At ADCP2 and ADCP3 locations, a slightly lower R values above 0.67 were obtained.

4. For ADCP4 during the Ebb phase, at the tip-height, when combined TI values are grouped by current speeds, they range from 0.07 to 0.14 for low wave heights (below 1.02 m) and from 0.09 to 0.21 for high wave heights (above 1.02 m). For current-only TI under the same conditions, the ranges are 0.06 – 0.13 for low waves and 0.05 – 0.13 for high waves. For wave-only TI, the ranges are 0.03 – 0.05 for low waves and 0.07 – 0.14 for high waves.

5. For ADCP4 during the Ebb phase, at the hub-height, when combined TI values are grouped by current speeds, they range from 0.1 to 0.15 for low wave heights (below 1.02 m) and from 0.1 to 0.17 for high wave heights (above 1.02 m). For current-only TI under the same conditions, the ranges are 0.08 – 0.15 for low waves and 0.08 – 0.14 for high waves. For wave-only TI, the ranges are around 0.04 for low waves and 0.05 – 0.07 for high waves.

6. For ADCP4 during the Ebb phase, at the tip-height, when TI values are grouped by wave heights, they range from 0.1 to 0.2 for low (i.e., below 1 m) and high wave heights (above 2 m) respectively. During the Flood phase, the range is 0.1 (for wave height below 1m) to 0.23 (for wave height above 2 m).

7. For ADCP4, at the hub-height, when TI values are grouped by wave heights from low (i.e., below 1 m) to high values (above 2 m), the range is from 0.13 to 0.17 during the Ebb phase, and 0.11 to 0.15 during Flood phase.

8. The decomposition technique developed in this study is unique and will find use in analysing complex time series data. The streamwise, transverse and vertical TI values obtained by this method and presented in this study should be of interest to industry practitioners.

Chapter 6
Wave Predictions Using Machine Learning Methods

To effectively predict the real spatiotemporal complex wave conditions using machine learning, it is essential to adopt a step-by-step approach, beginning with simpler cases and progressively addressing more complex scenarios. This research follows such a methodology, initiating with wave predictions in open-sea, deep-water regions where wave conditions predominantly depend on wind, isolated from the intricate influences of tidal currents, geography, and bathymetry. Once the predictive framework demonstrates success in these relatively simpler conditions, the study advances to predict wave dynamics in shallower, strait regions—a significantly more challenging environment due to the pronounced effects of wave-current interactions.

6.1 Introduction

6.1.1 Machine learning for wave prediction

Wave prediction plays a crucial role in ocean engineering and climate change studies. The ocean, being an immense and constantly evolving system, presents significant challenges in accurate prediction. Traditionally, wave prediction has relied heavily on numerical modelling, such as SWAN [52], WAVEWATCH III [50], and TOMAWAC [67,93] as mentioned in Section 2.1, which are based on the laws of physics. These numerical models, while robust in simulating spatiotemporal wave variations, often require extensive geographic coverage and a dense mesh, even for short-term, location-specific forecasts. This approach not only demands considerable time for parameter adjustments and running simulations but also entails high computational resources and complexity, which may not always align with the scale of the problem at hand. Additionally, the reliance on high-performance, often commercially licensed hydrodynamic software, adds to the research costs. In contrast, the recent advancements in

artificial intelligence have opened new avenues in environmental data prediction. Machine learning and deep learning models have started to show promising results in meteorological forecasting, suggesting a potential shift away from traditional simulation methods in certain applications. This emergence of AI-driven methods offers a faster, more precise, and cost-effective alternative for wave prediction, marking a significant shift in the approach to understanding ocean dynamics.

Over the past decade, machine learning (ML) models have increasingly been applied to environmental and climate tasks, including wave prediction. James et al. [126] used wave measurements, tidal current velocities, wind velocities as inputs of a multi-layer perceptron (MLP) to create a surrogate for the SWAN spectral wave model. This approach demonstrated significantly faster computation compared to traditional numerical modelling. Shamshirband et. al. [127] used the artificial neural network (ANN), extreme learning machine (ELM), and support vector regression (SVR) to regress significant wave heights from wind velocities at two locations. While their ML methods matched the accuracy of SWAN's numerical results, both ML and SWAN underestimated extreme conditions. Domala [128] used wave speed, wind gusts, dominant wave period, average wave period, and wave direction to predict significant wave heights using FBProphet and ensemble ML methods (random forest, gradient boosting, and XGBoost). They found that ensemble methods, particularly XGBoost, yielded superior results with the fastest training speeds.

However, the aforementioned methods did not consider temporal dependencies in their inputs and, therefore, cannot capture time-related patterns in wave parameters. Waves are strongly influenced by preceding conditions, making it essential for models to learn from past data. Some approaches manually feed temporal information to ML models using features from different time frames, such as the sliding window method employed in XGBoost [129,130]. Alternatively, models designed to learn temporal patterns, like Recurrent Neural Networks (RNNs), can be used. Among RNNs, Long Short-Term Memory (LSTM) networks are the most popular choice for predicting wave parameter time series due to their ability to learn over long time horizons. Hu et al. [129] used wind velocities as inputs to an LSTM model to predict significant wave heights at two locations, showing improved performance during storm conditions compared to XGBoost and the WAVEWATCH III spectral wave model. Hao et al. [131] enhanced LSTM's performance on non-stationary data by integrating the Empirical Mode Decomposition (EMD) algorithm, improving short-term prediction capabilities. Ti et al. [132] introduced a three-layer LSTM model using NOAA's wind field data to predict significant wave heights in the Western Pacific. Their model effectively simulated diverse oceanic scenarios, including tropical cyclones, demonstrating its robust spatiotemporal capabilities.

6.1.2 Method selection

Wave parameters are influenced not only by simultaneous physical drivers such as wind, but also by their preceding conditions. Therefore, machine learning models selected for surface wave prediction must be capable of capturing both complex input relationships and temporal dependencies.

Neural networks have long been recognised as effective solutions for such tasks. Beyond the widely used LSTMs, more recent advances have introduced models based on attention mechanisms. The Transformer architecture [133], initially developed for natural language processing tasks, has demonstrated excellent performance in time-series forecasting due to its ability to capture long-range temporal dependencies and utilise historical sequences to forecast future data. Building on this foundation, the Informer model [134] has been proposed to address the computational limitations of Transformers when applied to long-sequence forecasting tasks. Despite its promising potential, the Informer and similar attention-based models had not yet been widely applied in the field of wave prediction at the outset of this research in 2022. To address this gap, the present study is among the first to apply the Informer deep learning model to wind wave prediction, intending to advance machine learning approaches in ocean forecasting and offer new methodological insights.

In parallel, gradient boosting algorithms such as XGBoost [135] have also shown strong performance in environmental modelling. XGBoost is well known for its computational efficiency and accuracy in handling nonlinear relationships, making it suitable for modelling interactions between variables such as wind and waves. It has been previously applied to wave prediction tasks [129,136] and, in this study, is employed as a baseline model to assess the necessity and added value of adopting more complex deep learning architectures like the Informer. Additionally, this work explores the potential of hybrid approaches that combine the strengths of both XGBoost and Informer to improve prediction accuracy in dynamic marine conditions [130].

6.1.3 Research focus

As outlined at the beginning of this chapter, the study first focuses on a simplified scenario of wave prediction in open-sea, deep-water regions, where wave conditions are primarily driven by wind. In this phase, the Informer and XGBoost models are applied, using wind and wave data sourced from publicly available datasets for training.

Beyond wind-only wave prediction, this research also investigates wave behaviour in more complex environments, particularly in regions with significant WCI. Despite rapid progress in

machine learning for wave prediction, the inclusion of tidal effects and wave–current coupling remains largely unexplored. This is primarily due to two challenges: (1) the novelty of relevant machine learning techniques, and (2) the scarcity of reliable, long-term datasets that capture wave–current interaction effects. Most field data are collected using wave buoys or acoustic Doppler instruments. While buoys can record over extended periods, they typically do not capture tidal current effects. Acoustic Doppler instruments can measure both waves and currents but are often deployed only temporarily, limiting their usefulness for long-term modelling.

Numerical models are capable of simulating WCIs; however, long-term datasets from such simulations are rarely available. This study overcomes that barrier by utilising a long-term wave–current coupled simulation (described in Chapter 4), enabling the application of machine learning models in regions such as straits where tidal influences are significant.

Following the demonstration of the Informer's capability in wind wave prediction, it is further applied to wave prediction under tidal current influence. By addressing the real-world complexity of ocean environments, this study contributes to the development of more accurate and practical machine learning-assisted wave forecasting tools, suitable for applications in marine operations, renewable energy, and coastal risk management.

6.2 Machine learning methods

This section presents the theoretical background of the Informer model and the XGBoost algorithm, along with the fusion model that integrates XGBoost prediction results into the training process of the Informer model. Loss function and metrics are also introduced.

6.2.1 Informer deep learning method

6.2.1.1 Transformer structure and multi-head attention mechanism

The Informer model, employed in this research, builds upon the Transformer architecture, which is widely used for sequence-to-sequence (seq2seq) tasks where both input and output are sequences. The Transformer employs an encoder-decoder structure: the encoder compresses the input sequence into a representation, while the decoder generates the target sequence from this representation. Unlike traditional temporal models like RNNs, the Transformer relies on the attention mechanism, which enables it to focus on relevant parts of the input sequence, making it both more efficient and effective.

The attention mechanism enables the model to focus on the relevant parts of the input data. It maps input sequences into three components: queries (Q), keys (K), and values (V), through

$$Attention\ (Q, K, V) = softmax(\frac{QK^T}{\sqrt{d_k}})V \tag{6.1}$$

where the Q represents the current element, the model is focusing on, K represents all elements in the input sequence, V contains the information associated with the keys, and d_k is the dimensionality of the keys, used to scale the dot-product. This attention is called scaled dot-product attention, as shown on the left side of Figure 6.1.

A key innovation in the Transformer is multi-head attention, which performs multiple attention operations in parallel, as shown on the right side of Figure 6.1. The h in the figure means the number of the heads. This enriches the representations and optimizes computational resource usage. Unlike RNNs, which rely on final sequence states and risk losing early information, Transformers can effectively retain and process contextual data from the entire sequence, making them well-suited for tasks like time-series prediction.

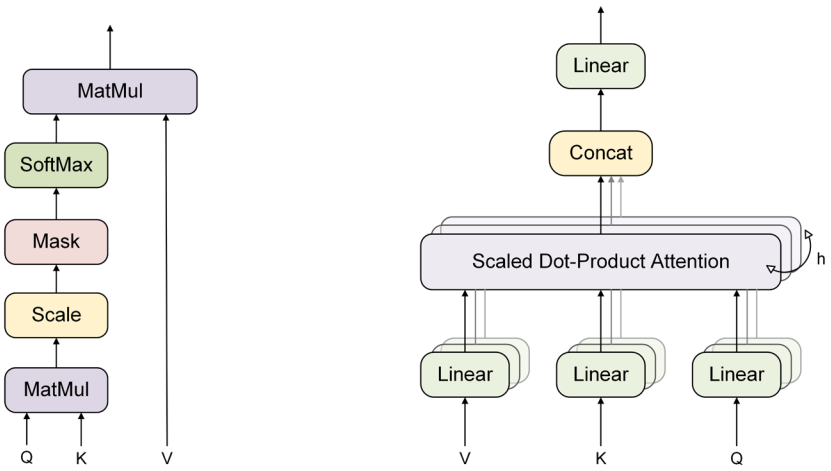

Figure 6.1 Attention mechanism [133]

Left: Scaled dot-product attention. Right: Multi-head attention. Q, K, V are query, key, and value. h is the number of the heads.

Notably, the self-attention mechanism is a specific type of attention which calculate the Q, K, and V from the same sequence, allowing the model to capture relationships between all elements regardless of their distance. While the cross-attention mechanism used Q from one sequence, but K and V from another sequence, facilitating inter-sequence focus.

6.2.1.2 Informer

Direct application of the Transformer model to time-series forecasting is computationally expensive for long sequences due to its complexity. To address this, Zhou et al. [134] developed the Informer model (Figure 6.2), which incorporates two key innovations: the "ProbSparse" attention mechanism and sequence distillation.

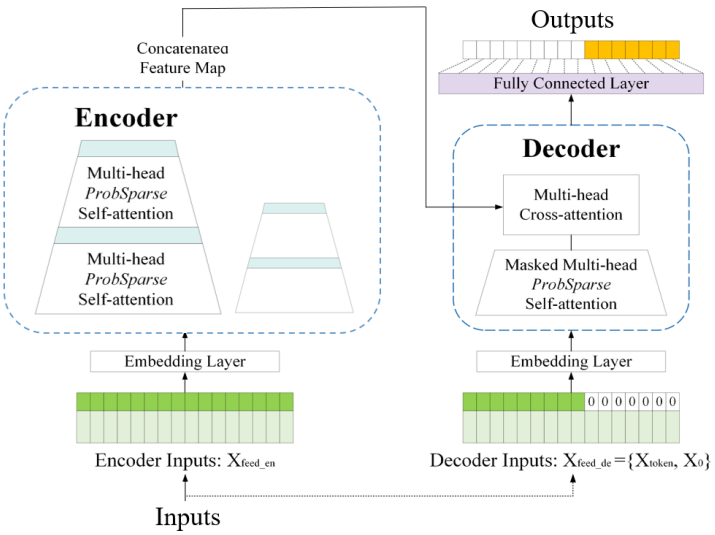

Figure 6.2 Informer [134]

The 'ProbSparse' attention mechanism, instead of computing attention scores for all elements in a sequence, it selects the most significant ones based on sparsity assumptions. This strategy reduced the computation complexity reduced from the $O(L^2)$ in the Transformer to of the $O(L\log L)$ in the Informer, making it feasible for long-sequence time-series forecasting (LSTF). Additionally, the distillation layer compresses input sequences by retaining only the most informative components, reducing memory and computation costs. These efficiencies are represented by the trapezoidal structure in Figure 6.4 (a), representing distilled information which is passed to the latter network.

The Informer introduces the concepts of fixed sequence length, label length, and prediction length, differing from the standard Transformer design. Sequence length represents the length of the input time-series data to the encoder for learning patterns, which is the length of $\mathrm{X}_{\mathrm{feed\_on}}$ in Figure 6.4 (a). The label length refers to the portion of the input sequence treated as context during decoding, serving as a bridge between the input data and the prediction horizon, as shown by the length of the $\mathrm{X}_{\mathrm{token}}$ in the input to the decoder. The prediction length indicates the number of future timesteps forecasted, as shown by the length of the X_0 in Figure 6.4 (a). For instance, using the past 24 hours of data (sampled every 30 minutes) to predict the next 12 hours implies a sequence length of 48 (24 hours × 2 samples/hour) and a prediction length

of 24 (12 hours × 2 samples/hour). During training, a subset of input data is treated as virtual output (label length) to assist the model in predicting the actual output.

6.2.2 XGBoost machine learning algorithm

6.2.2.1 Gradient Boosting Decision Trees

The XGBoost builds on the framework of the Gradient Boosting Decision Trees (GBDT), a machine learning library designed for supervised learning tasks, excelling in regression, classification, and ranking problems. GBDT combines the power of decision trees with boosting, an ensemble learning method.

Ensemble learning is a general term that refers to techniques that combine multiple base learners to make decisions. Each base learner is an algorithm that takes a set of labelled examples as input and produces a model that generalizes these examples [137]. By aggregating predictions from a set of base learners, ensemble methods reduce errors and variability, often achieving superior performance compared to individual models. Boosting is a specific ensemble learning technique where base learners are trained sequentially, with each learner correcting the errors of its predecessors.

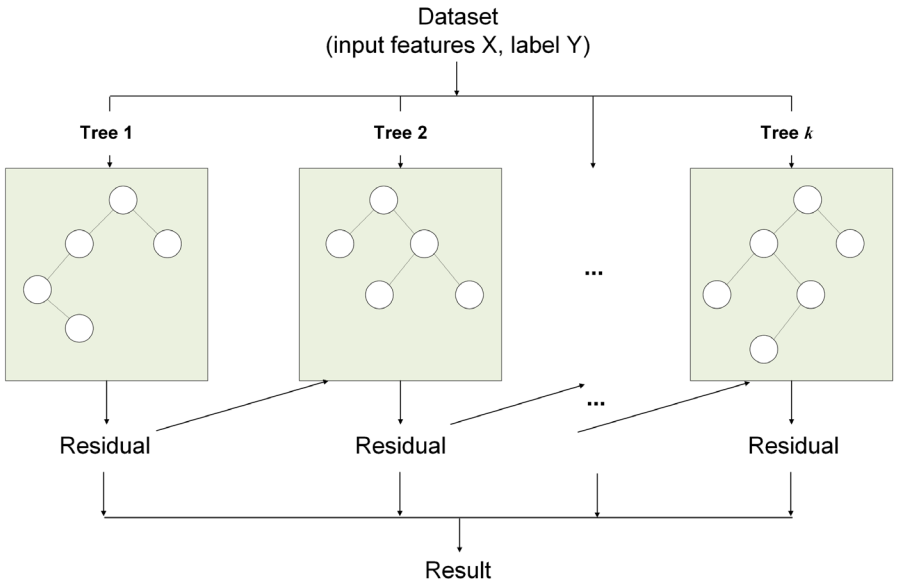

Figure 6.3 Schematic diagram of gredien boosting decision trees (GBDT)

GBDT is a boosting-based ensemble learning method that builds an ensemble of decision trees. As the base learner in GBDT, decision trees split the data into subsets based on feature values and optimize splits to minimize a specified loss function. The ‘Tree’ in the Figure 6.3 is

the base learner of the GBDT. Shallow trees are typically used to ensure simplicity and avoid overfitting. The training process starts with an initial prediction, often the mean of the target variable for regression. At each iteration, a new decision tree is trained on the residual errors from the current model, and its predictions are added to the existing model's outputs, scaled by a learning rate to control their influence. This iterative approach ensures that the ensemble captures both simple and complex patterns while remaining flexible across various loss functions, which is the mean squared error (MSE) in this study as mentioned in Section 6.2.4.

6.2.2.2 XGBoost

Building upon GBDT, XGBoost introduced the improvement in speed and performance [135]. A key advancement in XGBoost is its regularized loss optimization, which combines the training loss and a regularization term to prevent overfitting. The objective function $\mathcal{L}(t)$ in XGBoost is given by:

$$\mathcal{L}(t) = \sum_{i}^{n} l\left(y_i, \hat{y}_i^{(t)}\right) + \sum_{j=1}^{T} \Omega(f_j) \tag{6.2}$$

Here, n is the number of observations, y_i is the ground truth, $\hat{y}_i$ is the prediction, $l\left(y_i, \hat{y}_i^{(t)}\right)$ represents the loss function for the i-th data point at iteration t, and $\Omega(f_j)$ is the regularization term for the j-th tree,

$$\Omega(f_j) = \gamma T + \frac{1}{2}\lambda \|\omega\|^2 \tag{6.3}$$

where T is the number of leaves, ω is the leaf weights, γ penalizes complex trees, and λ controls the regularization of leaf weights. This regularization not only ensures that the ensemble generalizes well to unseen data but also enhances interpretability by discouraging overly complex trees.

XGBoost further optimizes the tree-building process through its greedy split finding algorithm, supported by a weighted quantile sketch for efficient split point determination. This ensures that XGBoost handles large datasets and high-dimensional feature spaces effectively. Moreover, XGBoost incorporates mechanisms for handling missing data by learning the optimal split directions for incomplete inputs, ensuring robust performance in real-world scenarios.

Additionally, XGBoost introduces parallelized tree construction, which accelerates training by enabling multiple data splits to be processed simultaneously. It also employs shrinkage (learning rate) and column sampling [135], further reducing overfitting and improving generalization.

The updated predictions at each step are scaled by the learning rate, ensuring smooth convergence and avoiding over-adjustment to the training data.

6.2.3 Informer-XGBoost fusion model

As subplots b-d of Figure 6.4 shows, this study introduces three methods for combining the strengths of the XGBoost and Informer models: (1) extra features - this is the simplest of the three, involving adding the prediction results from XGBoost as a new feature column to the original data table input to the Informer; (2) coupling XGBoost with Informer Encoder output - the enhanced XGBoost features are merged into the Encoder output of the Informer through a cross-attention mechanism. This approach allows the Informer to process the XGBoost predictions in conjunction with its own encoding process, potentially leading to a more nuanced understanding of the data; (3) coupling XGBoost with Informer Decoder output - the extracted features of XGBoost are used in a cross-attention mechanism with the Informer Decoder output, directly influencing the final predictive output. This direct integration into the Decoder harnesses the detailed context provided by the Informer's processing, aiming to further refine the accuracy of the predictions. In the latter two methods, the steps of data

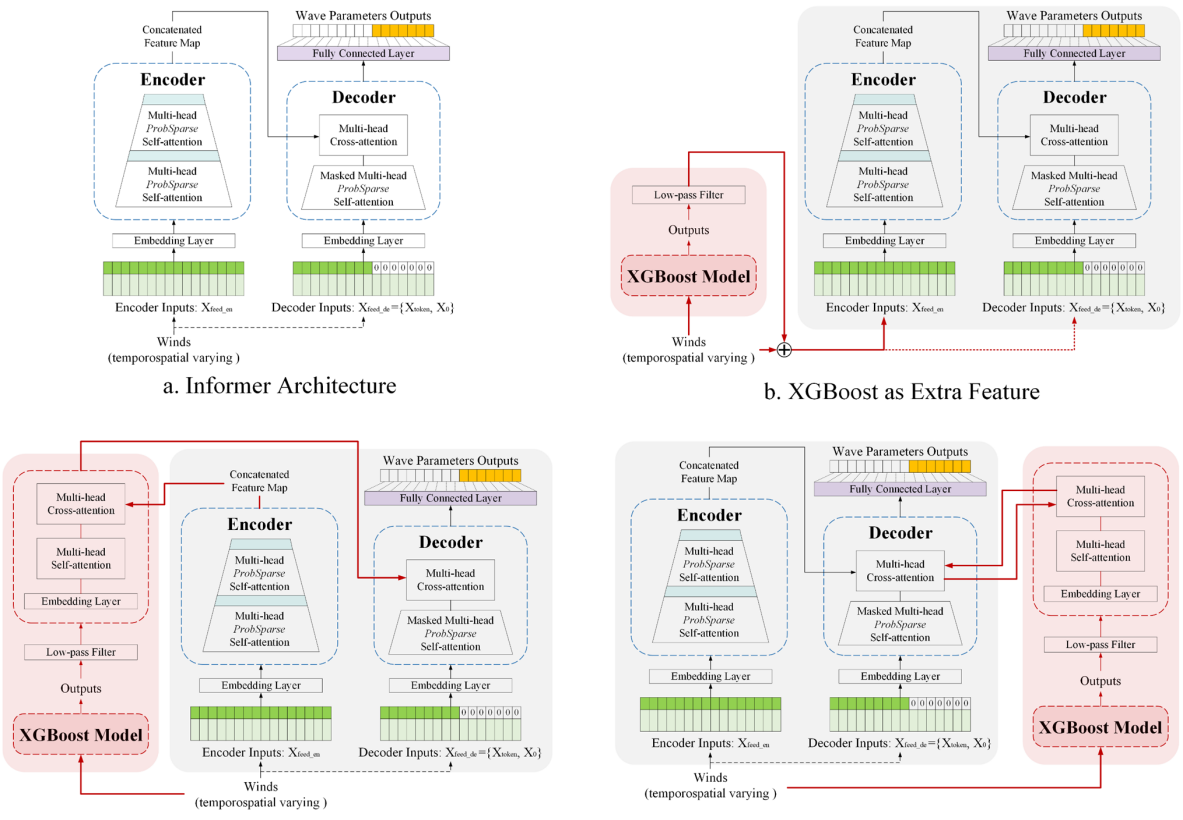

Figure 6.4 Intergrations between Informer and XGBoost

embedding and then performing self-attention feature extraction on XGBoost's outputs before integration allows for a more sophisticated fusion with the Informer model. These fusion models are applied to the wave predictions in the open-sea region.

6.2.4 Loss function and metrics

In machine learning training, the loss function quantifies the difference between the model's predicted output and the true target values. The objective of training is to minimize this loss. For regression tasks involving multiple features and a single target, common loss functions include mean squared error (MSE) and mean absolute error (MAE), defined by

$$\mathrm{MSE} = \frac{1}{n}\sum_{i=1}^{n}(x_{0_i} - x_{m_i})^2 \tag{6.4}$$

$$\mathrm{MAE} = \frac{1}{n}\sum_{i=1}^{n}\left|x_{0_i} - x_{m_i}\right| \tag{6.5}$$

in which x_{0_i} is the number ith of the ground truth, x_{m_i} is the number ith of the prediction results, n is the sample size.

In this study, MSE outperformed MAE for both the Informer and XGBoost models and was therefore selected as the loss function. The quality of wave prediction results is assessed using multiple metrics, including MAE, MSE, and others commonly used in numerical modelling, such as the R, RMSE, and SI (introduced in Section 2.2.3). Notably, RMSE is simply the square root of the MSE, providing an interpretable measure of prediction accuracy in the same units as the target variable.

6.3 Wave prediction for open-sea region

This study focuses on the open-sea waters around Scotland, bordered by the Atlantic Ocean to the west and the North Sea to the east. The tidal currents are ignorable at these sites.

Utilizing wind field data from the ECMWF [120] public climate dataset and Cefas WaveNet [77] public wave buoy measurements, the study initially employs the Informer and XGBoost models independently to predict wave height and period based on wind data, validating their performance across various locations and scenarios. Subsequently, the study explores an

innovative coupling of these two models, integrating XGBoost's predictions into the Informer framework. The research ambitiously targets both short-term forecasts spanning several days and long-term forecasts covering seasons or years, adaptable to a wide range of scenarios.

6.3.1 Dataset

In the realm of wave prediction, buoy-based sea surface observations are often considered the most direct source of training data. This research utilizes the significant wave heights (H_s) and zero-crossing mean wave periods (T_m) telemetry data collected by four buoys from Cefas WaveNet [77], West of Hebrides, Blackstone, Moray Firth, and Firth of Forth. Notably, these sites are also used for the validation of the North Atlantic wave-only model, with the detailed information can be found in Section 2.3.1.

The wind data are derived from the ERA5 by the ECMWF [120], which is also the wind input source for the previously mentioned numerical modelling, as described in Section 2.4.1.2. The specific subsets selected for analysis are the eastward U and northward V components of the wind. Sourced from an open-access database, this data encompasses the entire global geographical extent. For enhanced precision and analysis, the data is structured into a regular grid based on latitude and longitude, with the resolution of 0.25 degrees, as shown in Figure 6.5. The study uses wind data from four grid points around the wave observation sites, shown as green circles in Figure 6.5. The relative positions of these wind points and the wave observation stations vary, indicating a flexible approach in choosing wave prediction locations.

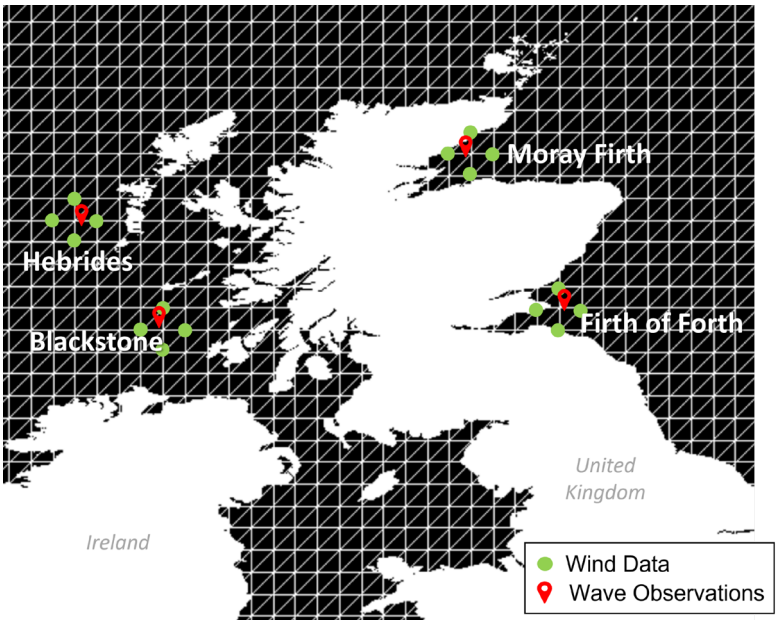

Figure 6.5 Positions of the wave sites and the ERA5 wind field

6.3.2 Wave prediction by Informer model

6.3.2.1 Input features and hyperparameters

This study delineates two distinct prediction problems using the Informer model. The first method involves incorporating target features (wave parameters, in this case) as part of the training input, which also follows the original logic of the Informer model. The second method, conversely, excludes target features from training, relying solely on wind data for predicting wave parameters.

The first method is well-suited for scenarios where historical wave data is available, such as in real-time short-term predictions. In this case, the input features of Informer include time, wind data (i.e., the hourly UV wind from four grid points around the wave observation site), and wave data (H_s or T_m), resulting in a total of 10 features. The second scenarios are more flexible, ideal for situations where historical wave data is unavailable, such as generating quarterly or annual long-term hindcast data. The input features are only the time and wind data, totalling 9 features.

Regarding the hyperparameter settings applied in the training, the MSE was selected as the loss function for its superior performance in regression tasks compared to MAE. Model optimization used the Adam optimizer with a learning rate starting at 0.0001, decaying by 0.5 per epoch. Training involved a total of 15 epochs with a patience value of 5. The number of head is 8. The encoder and decoder consisted of 2 and 1 layers, respectively, with a model dimensionality of 512 and a batch size of 32. Training and testing were conducted on a single NVIDIA 3070 GPU using the CUDA toolkit.

6.3.2.2 Results

In this study, the standard Informer model is employed for short-term wave prediction tests at four locations. The tested combinations of sequence length, label length, and prediction length in hours are (24, 12, 6), (24, 12, 12), (48, 24, 24), (96, 48, 48), (168, 96, 96), and (168, 168, 168). These configurations represent the input and output time lengths for features and targets, respectively. For example, (24, 12, 6) denotes using 24 hours of past data to predict the next 6 hours, with the last 12 hours of the past data serving as guidance in the prediction. The 2022 forecast results, compiled from these short-term predictions, are then compared with actual wave observations. Table 6.1 and Table 6.2 summarize the performance for predicting H_s and T_m with respect to R, MAE, and MSE, respectively.

The data indicates that prediction accuracy declines as the prediction length increases. However, the model still maintains a R value above 0.87 for wave heights and above 0.86 for wave periods prediction, with the MAE controlled within around 0.5 m for H_s and 0.5 s for T_m. This demonstrates the standard Informer model's effectiveness, even when the prediction time

Table 6.1 2022 yearly H_s predictions at four locations using standard Informer model

MAE unit is in s, MSE is in s^2.

Time (h)	Metric	West of Hebrides	Blackstone	Moray Firth	Forth Firth
6	R	**0.99**	**0.99**	0.98	0.98
	MAE	0.18	0.16	0.09	**0.08**
	MSE	0.08	0.06	0.02	**0.01**
12	R	0.99	0.99	0.97	0.98
	MAE	0.20	0.18	0.12	0.08
	MSE	0.09	0.07	0.02	0.01
24	R	0.98	0.97	0.96	0.96
	MAE	0.27	0.29	0.16	0.13
	MSE	0.17	0.11	0.04	0.03
48	R	0.97	0.96	0.95	0.96
	MAE	0.35	0.35	0.13	0.12
	MSE	0.28	0.23	0.04	0.03
96	R	0.94	0.95	0.93	0.93
	MAE	0.46	0.39	0.14	0.17
	MSE	0.42	0.30	0.06	0.06
168	R	0.93	0.94	**0.87**	0.91
	MAE	**0.50**	0.42	0.19	0.20
	MSE	**0.51**	0.34	0.09	0.09

Table 6.2 2022 yearly T_m predictions at four locations using standard Informer model

MAE unit is in s, MSE is in s^2.

Time (h)	Metric	West of Hebrides	Blackstone	Moray Firth	Forth Firth
6	R	**0.98**	**0.98**	0.96	0.96
	MAE	0.25	0.25	**0.18**	0.20
	MSE	0.11	0.11	**0.08**	**0.08**
12	R	0.98	0.98	0.96	0.96
	MAE	0.28	0.26	0.21	0.22
	MSE	0.14	0.12	0.10	0.09
24	R	0.97	0.97	0.95	0.95
	MAE	0.42	0.33	0.31	0.25
	MSE	0.28	0.20	0.18	0.11
48	R	0.95	0.96	0.93	0.92
	MAE	0.40	0.36	0.33	0.34
	MSE	0.30	0.22	0.19	0.18
96	R	0.95	0.95	0.92	0.89
	MAE	0.41	0.40	0.30	0.37
	MSE	0.29	0.27	0.18	0.24
168	R	0.91	0.92	0.91	**0.86**
	MAE	**0.55**	0.50	0.33	0.40
	MSE	**0.51**	0.42	0.23	0.29

matches the input length. The increased error with longer predictions is likely due to the model's underestimation of waves during extreme weather. For instance, as depicted in Figure 6.6 and Figure 6.7, the 168-hour forecasts (marked by the red curve) underestimate peak wave heights at Hebrides and Firth of Forth. This underestimation is evident in the right-hand scatter plots, where the curve flattens in high wave conditions, while the 24-hour predictions align more closely with the peaks.

As previously discussed, the approach of including the target parameter in training aligns with short-term prediction methodologies but is incompatible with long-term forecasting. In scenarios where predictions extend over months or years, prior wave parameter values are unknown, presenting a challenge. Addressing this, this study modifies the Informer model's by excluding

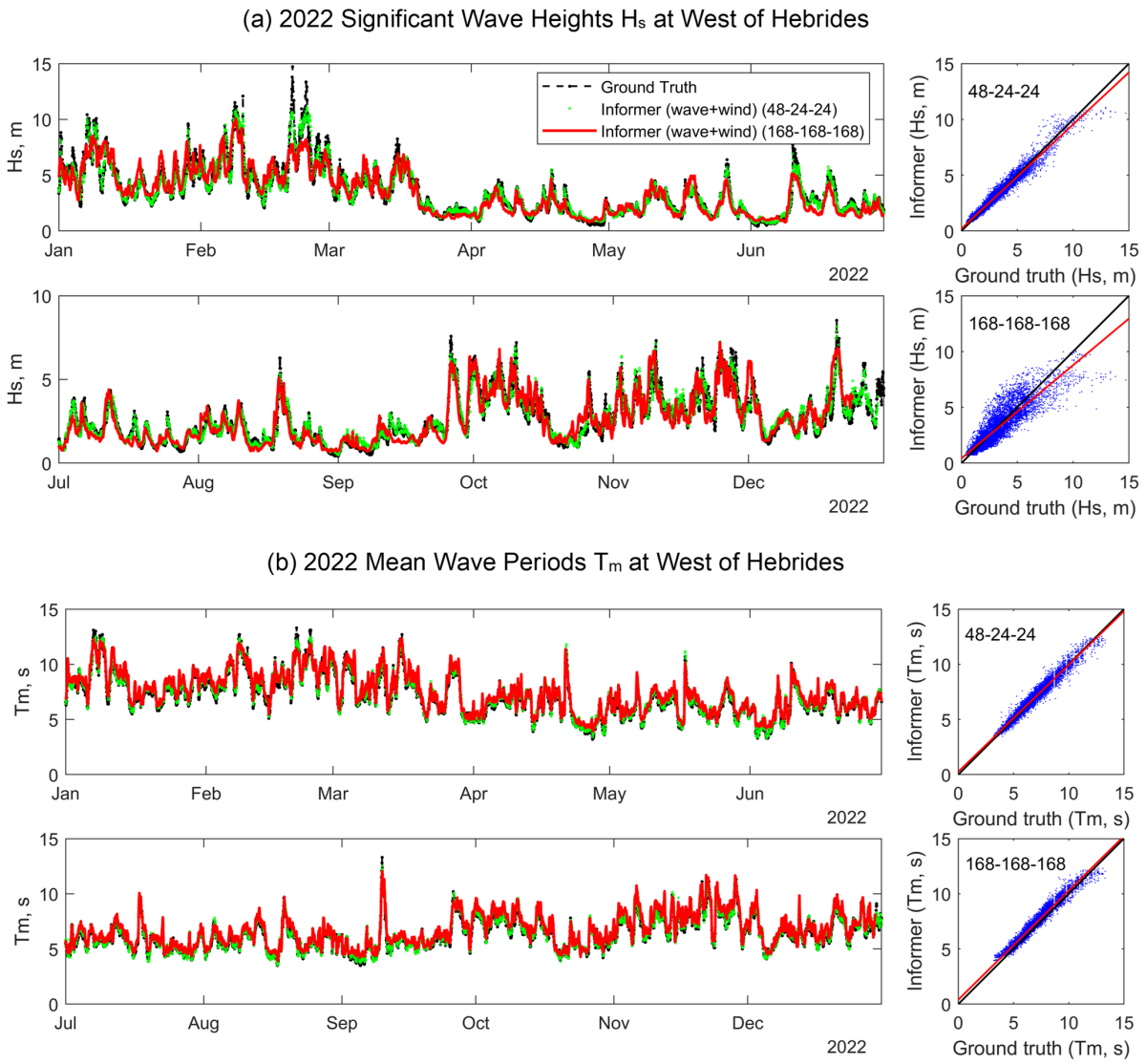

Figure 6.6 2022 Yearly H_{m0} and T_m prediction at West of Hebrides using standard Informer model
Standard Informer model use wave and wind as input. Two examples are shown here: prediction length of 24 hours (48, 24, 24) and 168 hours (168, 168, 168).

the target value from the training process and using it solely for loss function computation. Consequently, only wind data is utilized for making predictions. Here, the modified model is named Informer*. This change resulted in a significant decrease in the R value for the yearly significant wave heights at Hebrides in 2022, as it is shown in subplots (a) and (c) of Figure 6.8, dropping from 0.99 to 0.90 (6-hour prediction), and from 0.98 to 0.87 (24-hour prediction), respectively. The absence of historical wave data as a reference led to a reduction in the Informer's prediction accuracy. However, this limitation also sparked the idea of exploring alternative wave data sources to guide the Informer* model. This is where the integration of XGBoost becomes instrumental.

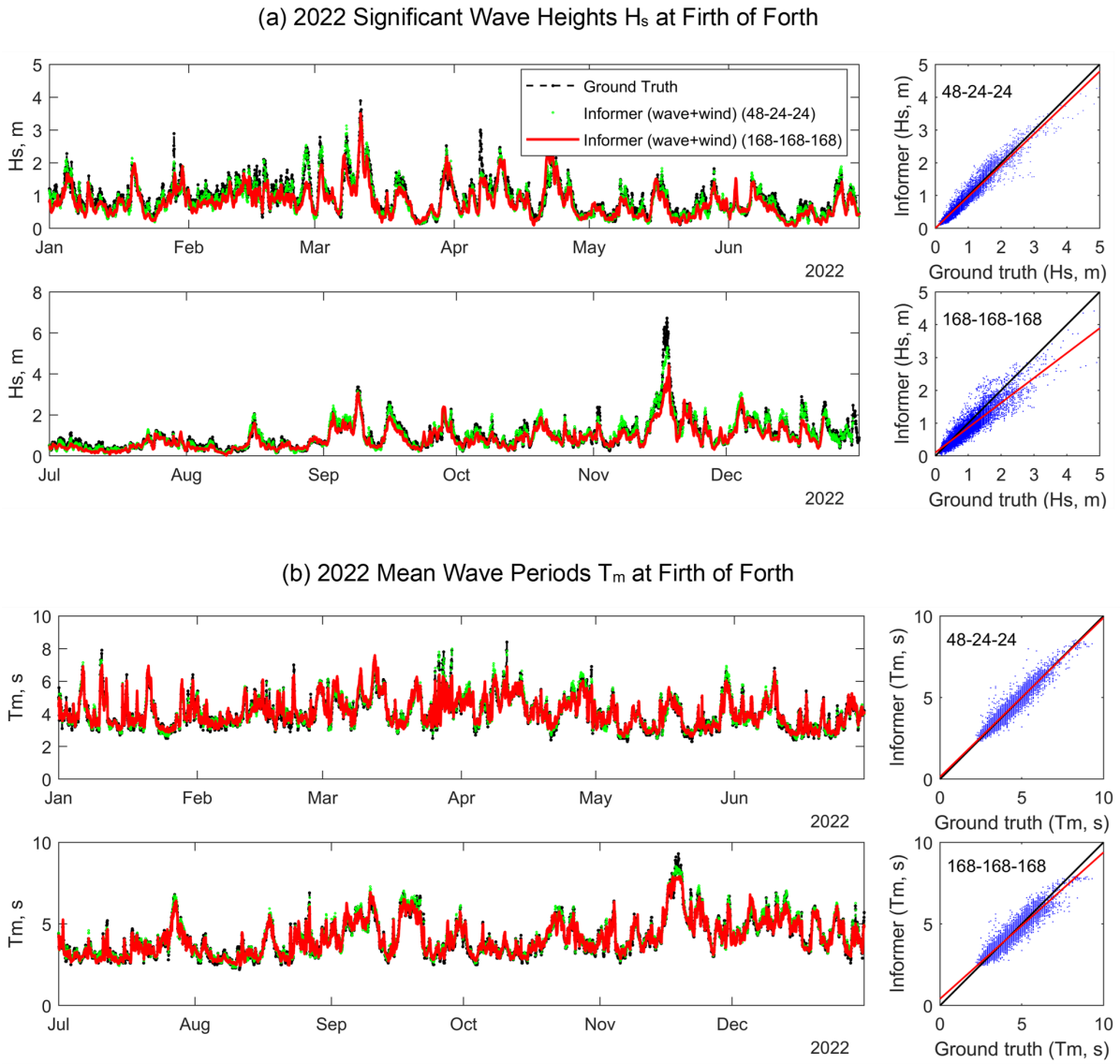

Figure 6.7 2022 Yearly Hm0 and Tm prediction at West of Hebrides using standard Informer model
Standard Informer model use wave and wind as input. Two examples are shown here: prediction length of 24 hours (48, 24, 24) and 168 hours (168, 168, 168).

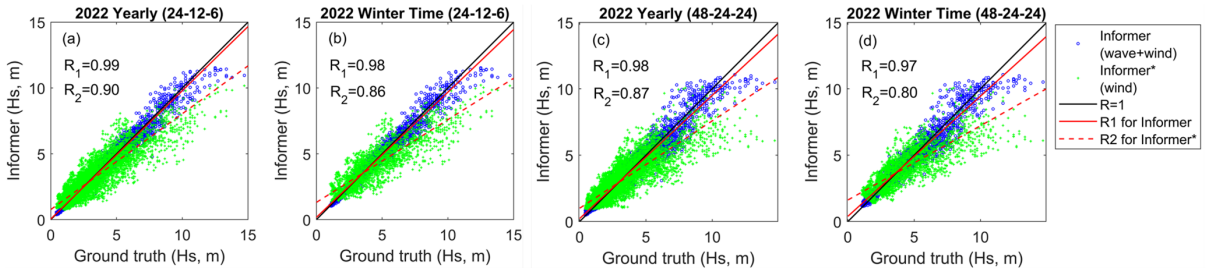

Figure 6.8 Scatter plot comparison of H_s between standard Informer and Informer*

Data at at West of Hebrides are used for comparison.

6.3.3 Wave prediction by XGBoost algorithm

6.3.3.1 Input features and hyperparameters

XGBoost's strength lies in its ability to discern complex nonlinear relationships between input features such as various wind parameters, and the target output like wave heights or periods. It achieves this through an ensemble of decision trees, enabling it to detect patterns and interactions in wind data that correlate with wave conditions. However, XGBoost's architecture is not inherently designed for time series analysis. To mitigate this, a sliding window method is employed, feeding the model with the same type of features but from different time frames to incorporate temporal information. This method, while effective for short-term time analysis, is limited in handling longer-term data.

In this research, XGBoost is provided with 40 input features: hourly UV wind data from four grid nodes surrounding the target location, along with total wind data from these nodes at the current time and at three-hour intervals over the preceding twelve hours (= 8 × 5). The output targets are H_s or T_m. For the model configuration, the number of estimators is 400, learning rate of XGBoost is 0.05, and the maximum depth is 30.

6.3.3.2 Results

The training of the XGBoost model uses hourly data collected over ten years, from January 1, 2012, to December 31, 2021. This trained model is then applied to predict wave parameters for the year 2022 (timeseries examples are shown in Figure 6.9 and the metrics are summarized in Table 6.3). Due to XGBoost's limitation in processing sequential data, its predictions often contained high-frequency noise, leading to the need for low-pass filtering. The model demonstrated good performance in predicting wave height, with R values exceeding 0.8 when compared to actual observations at the four locations. However, its effectiveness in predicting

wave period was less accurate, with R values all equal or below 0.7. This discrepancy suggests that XGBoost more effectively captures the nonlinear relationship between wind and wave height, whereas wave period predictions might depend more on temporal factors and less on wind conditions.

The combined XGBoost-Informer model requires XGBoost's forecasts, leading to separate training phases for each. XGBoost was first trained with 2012-2016 data to make predictions for 2017-2021, which then informed the Informer's training. Testing the 2012-2016 trained XGBoost on 2022, as shown in Table 6.3, revealed that five years of data can achieve similar accuracy to ten years, indicating sufficiency for Informer training. This suggests that for XGBoost, increasing data volume doesn't necessarily improve performance, which could be due to factors like overfitting with larger datasets or the model's ability to effectively capture essential patterns from a more concise dataset.

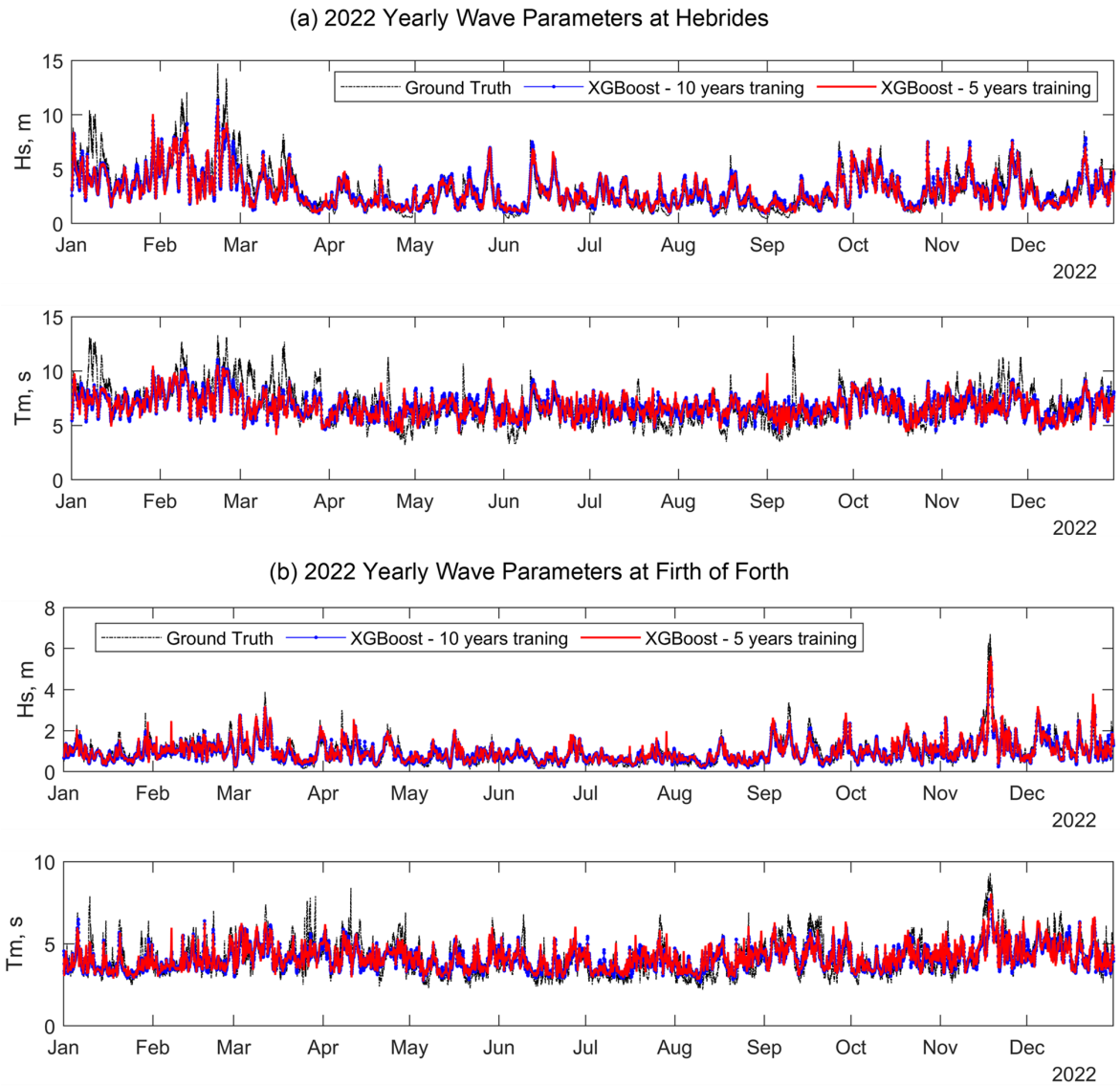

Figure 6.9 2022 yearly H_s and T_m prediction using XGBoost

Table 6.3 2022 yearly Hs and Tm predictions at four locations using XGBoost

Comparison between using 10 years data of training and 5 years of training. MAE unit is in s, MSE is in s^2.

Wave Para.	Metric	Hebrides	Blackstone	Moray Firth	Forth Firth
		10-year / 5-year	10-year / 5-year	10-year / 5-year	10-year / 5-year
H_s	R	0.86 / 0.86	**0.83**/ 0.83	0.81 / 0.81	**0.86** / 0.85
	MAE	**0.70** / 0.71	**0.63** / 0.69	0.25 / 0.25	0.11 / 0.11
	MSE	**0.94** / 0.97	**0.71** / 0.93	**0.13** / 0.14	**0.20** / 0.24
T_m	R	**0.64** / 0.62	**0.64** / 0.62	**0.60** / 0.58	0.70 / 0.70
	MAE	**0.97** / 1.00	**0.97** / 0.99	**0.74** / 0.77	**0.56** / 0.57
	MSE	**1.65** / 1.73	**1.63** / 1.70	**0.60** / 0.61	0.56 / 0.56

6.3.4 Model integration and storm conditions

Although the Informer model demonstrated commendable predictive ability in 2022, even after excluding the target parameter from its input features, it notably underestimated peak wave heights. An analysis focusing on winter data (defined as January to March and December) is shown in subplots (b) and (d) of Figure 6.8. When the Informer* model uses only wind data for input, the correlation coefficients R for 6-hour and 24-hour prediction drop from yearly values of 0.9 and 0.87 to 0.86 and 0.8, respectively, during the winter period. In contrast, XGBoost maintained a robust performance in winter peaks as it shows in Figure 6.9. For instance, XGBoost's prediction for Hebrides on February 20, 2022, was 10.88 m against an actual peak of 14.72 m, outperforming the Informer*'s 24-hour and 168-hour prediction of 10.66 m and 7.78 m, respectively. Similarly, at Firth of Forth on November 18, 2022, XGBoost predicted 5.63 m, while the Informer* produced 5.29 m (24-hour) and 4.42 m (168-hour) against the actual 6.72 m. Consequently, this study employs XGBoost's predictions to inform the Informer* model specifically for the winter season, selecting winter data from 2017 to 2021 to train the model and predict the wave heights in the winter time of 2022.

The Table 6.4 compiled with the winter data results of Hebrides in 2022 shows that the XGBoost-Informer hybrid model generally outperforms individual Informer* models for 6, 24-, 48-, 96-, and 168-hours predictions. For the prediction length over 24 hours, incorporating XGBoost predictions directly into the Informer* encoder inputs results in slightly inferior outcomes compared to adding them to the encoder or decoder outputs. This finding aligns with the intrinsic design logic of these models: introducing XGBoost predictions as an encoder feature may not fully leverage their potential, leading to greater information loss during the Informer's 'ProbSparse' and 'Self-Attention Distillation' processes. The results also show that the advantages of coupling XGBoost with Informer* is more significant as the prediction length

gets larger. Conversely for the 6-hour forecast, while the combined model still performs better than the Informer alone, the marginal difference suggests that the Informer's robust analytical capability for short-term forecasts, particularly with comprehensive winter training data, might diminish the need for XGBoost assistance.

Additionally, given XGBoost's relatively poor performance in predicting wave periods, this aspect has not been incorporated into the Informer training. The wave periods prediction results from XGBoost do not justify its use in guiding the Informer.

Table 6.4 2022 wintertime H_s prediction at West of Hebrides by Informer* and fusion models
Informer* uses only winds as input. MAE unit is in s, MSE is in s^2.

Time (h)	Metric	Informer*	Extra Feature	Encoder Output	Decoder Output
6	R	0.86	**0.88**	**0.88**	0.87
	MAE	0.82	**0.78**	0.79	0.79
	MSE	1.29	**1.15**	1.19	1.29
24	R	0.82	0.83	**0.87**	**0.87**
	MAE	0.93	0.90	0.84	**0.81**
	MSE	1.64	1.52	1.30	**1.20**
48	R	0.68	0.70	0.70	**0.75**
	MAE	1.20	1.14	1.13	**1.04**
	MSE	2.70	2.56	2.62	**2.33**
96	R	0.44	0.48	0.57	**0.66**
	MAE	1.47	1.42	1.31	**1.20**
	MSE	3.87	3.87	3.31	**2.79**
168	R	0.44	0.51	**0.53**	0.52
	MAE	1.50	1.44	1.43	**1.41**
	MSE	3.96	3.86	3.57	**3.58**

6.3.5 Summary

This study employed the Informer deep learning model and the XGBoost machine learning model to predict significant wave height H_s and mean wave period T_m at four observation sites in Scottish waters, exploring the integration of these two models. The models are trained on data sourced from public databases.

The research initially applied the standard Informer model for short-term predictions (6 to 168 hours) at these locations, demonstrating its effectiveness in processing wave height and period data. The study then modified the Informer model to exclude historical target wave data,

relying solely on wind data for predictions. This changed results in a marked decrease in the Informer's predictive accuracy, particularly for high waves in winter. To address this, the study integrated XGBoost's wave prediction output with the Informer's training process, focusing on improving simulations of high-wave conditions in winter. The results confirmed that this hybrid XGBoost-Informer approach enhanced prediction accuracy. The coupling strategy proposed here is among several potential methods for combining XGBoost and Informer. Future research may uncover more effective approaches to synergistically leverage the strengths of both models.

In this research, hardware comprising an AMD7950X 32-thread CPU and an NVIDIA 3070 GPU was utilized. On this setup, training the Informer model with 5 years' worth of data required up to 10 minutes, while the XGBoost model completed its training on a decade length in 3 minutes. For both models, conducting a continuous forecast spanning an entire year took within seconds. This efficiency markedly contrasts with traditional numerical modelling, highlighting the significant speed advantage offered by machine learning techniques.

6.4 Wave prediction in strait area

Unlike previous predictions in open-sea waters, this section focuses on waves in the strait region around the Pentland Firth and Orkney Waters, where strong wave and tidal current interactions coexist. Utilizing numerical modelling results from earlier chapters (Chapter 2 and Chapter 4), the study applies the Informer model to predict wave parameters under the influence of wave-current interactions. As the first research to integrate machine learning methods for wave prediction in regions with significant WCI effects, this work establishes a foundation for accurate wave forecasting in strait environments.

In this section, the original Informer model is modified by removing the target features from the feed of the inputs as introduced in Section 6.3.2, to enable regression predictions from the inputs to the target. This modified version of the model is referred to as Informer*. Aside from adjustments related to the time and input features, such as the number of inputs and variable names, all other hyper-parameter settings remain consistent with those described in Section 6.3.2.

6.4.1 Dataset

The selection of the 10 input features was determined based on a physical understanding of the wave-current interactions process [34]. These features include time, wave parameters without tidal effects, tidal current parameters, and time-varying water depth. Specifically, the 4 input wave parameters are obtained from the TOMAWAC wave-only model and include factors related to the wave heights ($H_{s,0}$), an approximation of the wave steepness ($H_{s,0}/T_{m,0}$), and terms reflecting wave directions ($\sin\theta_0$, $\cos\theta_0$, where θ is the 'travel toward' direction of waves and the denote 0 of the terms represent the absence of the ambient tidal current). The remaining 5 inputs are obtained from the TOMAWAC-TELEMAC wave-current coupled model, including water depths, tidal current directions (i.e., $\sin\alpha$, $\cos\alpha$ where α is the traveling direction of tides), depth-averaged tidal speed U, relative currents speed U_c which is defined by

$$U_c = U \cdot \cos(\alpha - \theta) \tag{6.6}$$

Notably, no data cleansing was conducted in this research. This is because noise from unimportant sources (e.g., instrument or environmental noise) that affects the quality of field data is largely absent in numerical simulations. It is assumed that all variations in the data result from reasonable physical mechanisms related to waves, and any instability during computational simulations is negligible.

Although a 10-year dataset is available, this study uses only a portion of the data to evaluate the feasibility of the Informer model for time-series forecasting. Specifically, the dataset spans July 2015 to December 2016 and is split into three subsets: training set, validation set, and test set, with a ratio of 7:1:2.

During the training process, the data is not shuffled, as preserving the temporal order is crucial for time-series forecasting. The training set, covering the first 70% of the dataset (July 2015 to July 2016), was carefully selected to include all four seasons, ensuring the model could capture strong inter-seasonal wave patterns. The remaining data, from August 2016 to December 2016, was used for validation and testing. After training, the model was tested by predicting wave patterns for the entire year of 2017, allowing an assessment of its ability to accurately capture seasonal patterns.

6.4.2 Prediction at the training site

6.4.2.1 Model settings

This study utilized numerical simulation data from Westray Firth to train the Informer model, examining three sampling intervals: 10 minutes (the original temporal resolution of the numerical model), 30 minutes, and 60 minutes. For each sampling interval, six input-output time combinations were tested, including: using the past 2 hours to predict the next 1 hour, past 6 hours to predict the next 3 hours, past 12 hours to predict the next 6 hours, and so on, up to using the past 48 hours to predict the next 48 hours. The specific sequence, label, and prediction lengths for each interval are:

- 10 min interval: (12, 6, 6), (36, 18, 18), (72, 36, 36), (144, 72, 72), (288, 144, 144), (288, 288, 288)

- 30 min interval: (4, 2, 2), (12, 6, 6), (24, 12, 12), (48, 24, 24), (96, 48, 48), (96, 96, 96)

- 60 min interval: (3, 1, 1)*, (6, 3, 3), (12, 6, 6), (24, 12, 12), (48, 24, 24), (48, 48, 48)

For each configuration, predictions were accumulated to produce results for the entirety of 2017. Notably, for the 60 min interval, the minimum sequence length (marked by *) required by the Informer design necessitated testing with 3-hour input.

The performance of these configurations for 2017 is summarized by the metrics shown in Table 6.5, with R, MSE, and the SI also displayed in Figure 6.10. To visually assess whether the Informer model captures tidal modulation effects, time-series analyses focused on specific months: March, July, and December, reflecting high wave activity in spring and winter, and low activity in summer.

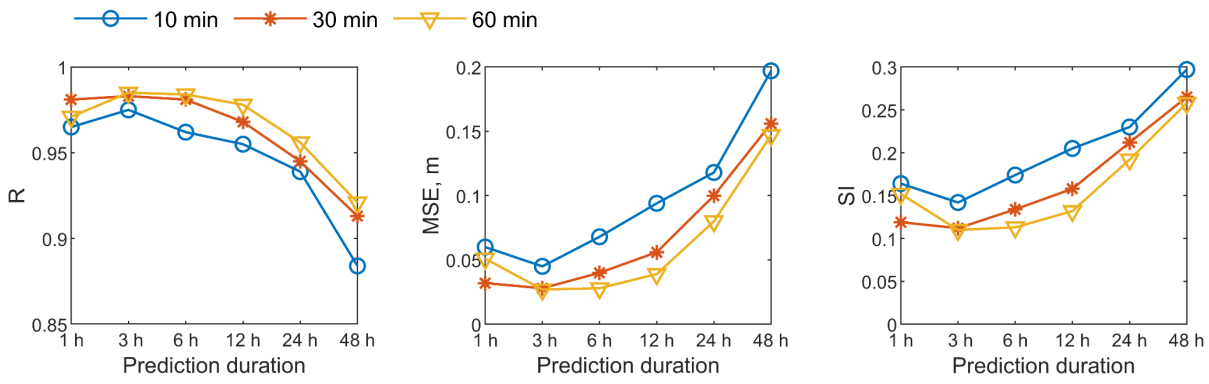

Figure 6.10 Metrics comparison among different samping intervals of 10 min, 30 min, and 60 min

Table 6.5 2017 yearly Hs predictions at Westray Firth by Informer* model

MAE and RMSE units are in s, MSE is in s^2.

Time Interval	Prediction Hours	Prediction Length	Metrics				
			R	MSE	MAE	RMSE	SI
10 min	1	6	0.965	0.060	0.168	0.245	0.164
	3	18	**0.975**	**0.045**	**0.157**	**0.211**	**0.142**
	6	36	0.962	0.068	0.196	0.260	0.174
	12	72	0.955	0.094	0.225	0.306	0.205
	24	144	0.939	0.118	0.252	0.344	0.230
	48	288	0.884	0.197	0.308	0.444	0.297
30 min	1	2	0.981	0.032	0.129	0.178	0.119
	3	6	**0.983**	**0.028**	**0.124**	**0.167**	**0.112**
	6	12	0.981	0.040	0.146	0.200	0.134
	12	24	0.968	0.056	0.170	0.236	0.158
	24	48	0.945	0.100	0.218	0.316	0.212
	48	96	0.913	0.156	0.284	0.395	0.265
60 min	1	1	0.971	0.051	0.174	0.226	0.152
	3	3	**0.985**	**0.027**	0.124	**0.164**	**0.110**
	6	6	0.984	0.028	**0.122**	0.167	0.113
	12	12	0.978	0.039	0.142	0.197	0.132
	24	24	0.956	0.080	0.207	0.285	0.192
	48	48	0.921	0.147	0.260	0.384	0.258

6.4.2.2 Analysis of Input-Output Time Lengths

The configuration using the past 6 hours to predict the next 3 hours consistently delivered the best performance across all three sampling intervals, as indicated by bolded font in Table 6.5 and the highest R values and lowest MSE and SI shown in Figure 6.10. Specifically, Figure 6.11 (a), Figure 6.12 (a), and Figure 6.13 (a) show timeseries results for this configuration in March, July, and December using the 30 min interval data. The model accurately captured tidal modulation during both high and low wave periods, achieving R values above 0.97 in the selected three months and SI values below 0.1 in March and December. Even during periods with wave heights approaching 5 m (e.g., March 15 and December 8), predictions were highly accurate. These results confirm that a 6-hour input sufficiently captures the information needed for wave-current interaction predictions.

Table 6.5, Figure 6.11, Figure 6.12, and Figure 6.13 also reveal that when the input and prediction durations exceed 6 hours and 3 hours, respectively, prediction accuracy decreases with increasing sequence and prediction lengths. This can be explained by: (1) longer inputs may include redundant or less relevant data which can dilute the important patterns, and 2) longer prediction horizons may amplify small errors in the model's predictions over time. The

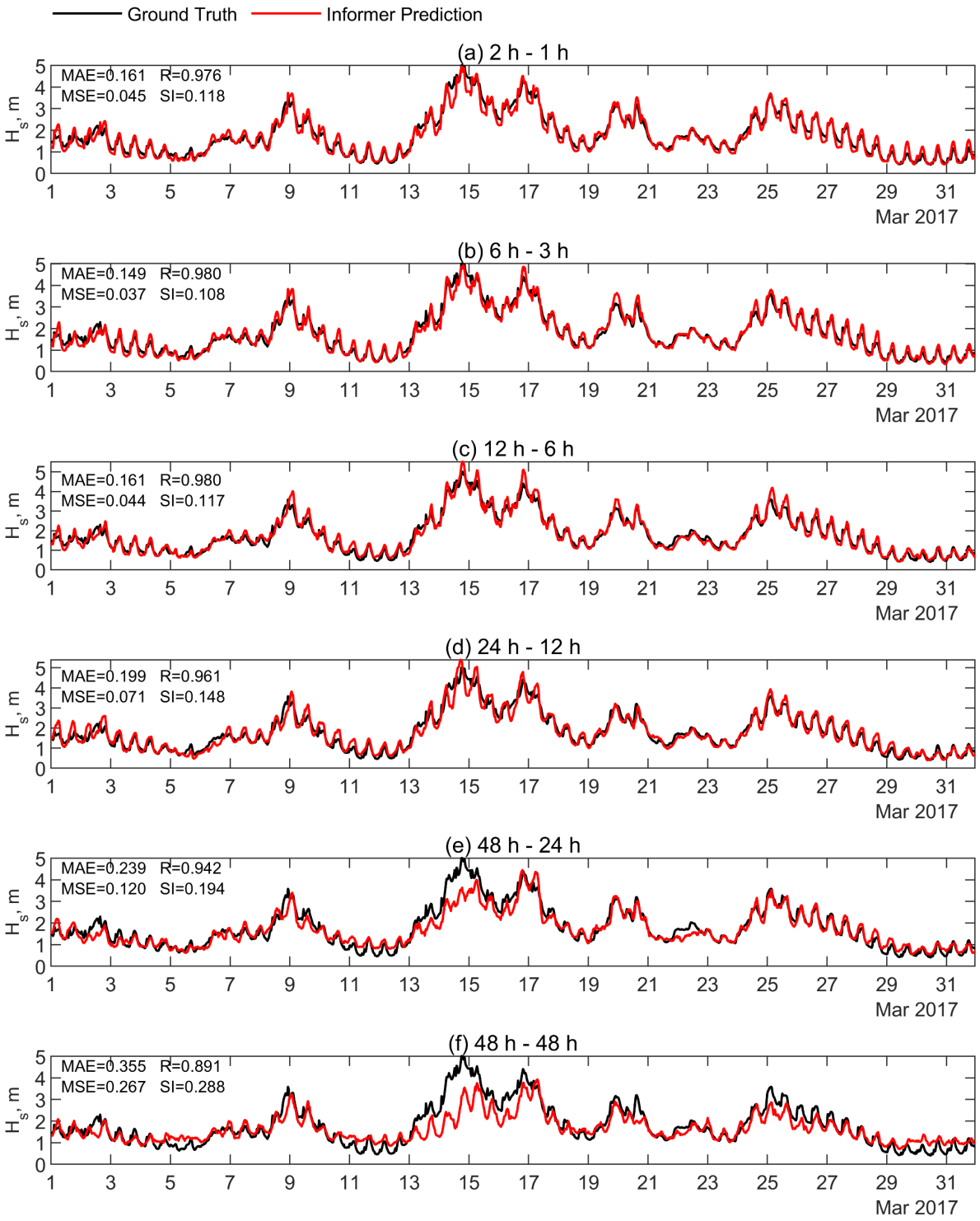

Figure 6.11 H_s at Westray Firth in March 2017 predicted by the Informer* model

The samping time interval is 30 min. From top (a) to bottom (f): 2 hours predict 1 hour (4,2,2), 6 hours predict 3 hours (12,6,6), 12 hours predict 6 hours (24,12,12), 24 hours predict 12 hours (48,24,24), 48 hours predic 24 hours (96,48,48), and 48 hours predict 48 hours (96,96,96).

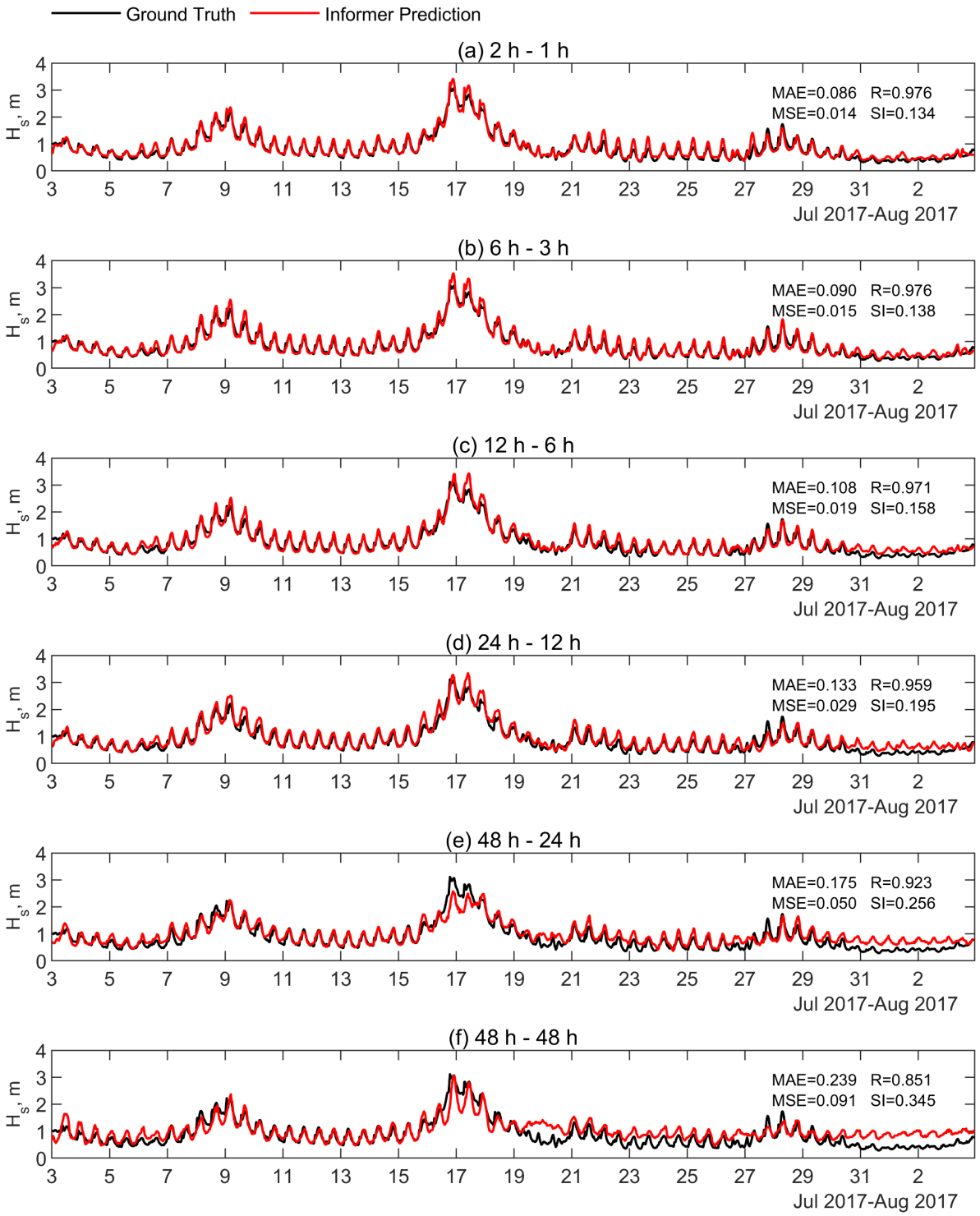

Figure 6.12 H_s at Westray Firth from July 3 to Aug 3, 2017 predicted by the Informer* model

The samping time interval is 30 min. From top (a) to bottom (f): 2 hours predict 1 hour (4,2,2), 6 hours predict 3 hours (12,6,6), 12 hours predict 6 hours (24,12,12), 24 hours predict 12 hours (48,24,24), 48 hours predic 24 hours (96,48,48), and 48 hours predict 48 hours (96,96,96).

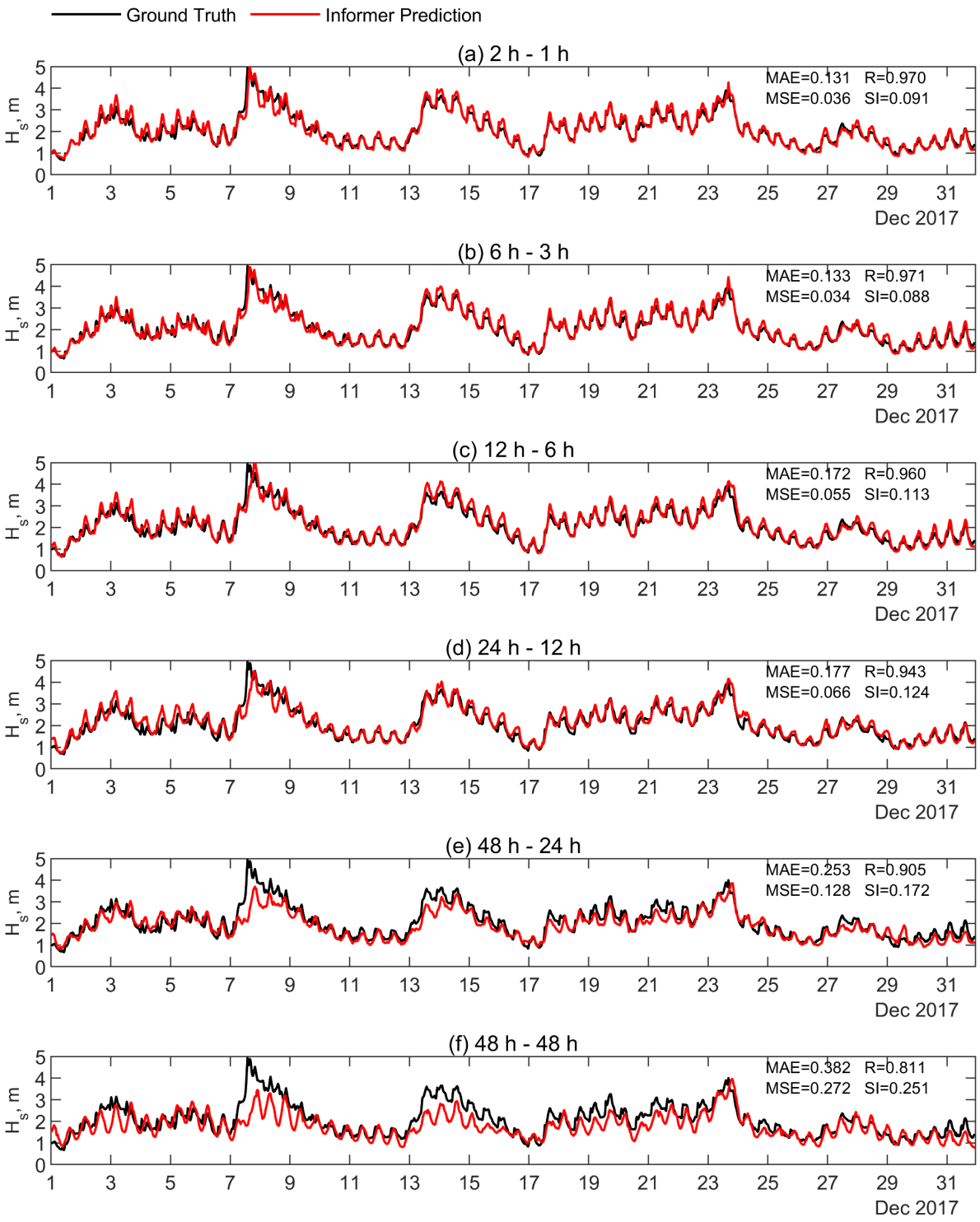

Figure 6.13 H_s at Westray Firth in Dec. 2017 predicted by the Informer* model

The samping time interval is 30 min. From top (a) to bottom (f): 2 hours predict 1 hour (4,2,2), 6 hours predict 3 hours (12,6,6), 12 hours predict 6 hours (24,12,12), 24 hours predict 12 hours (48,24,24), 48 hours predic 24 hours (96,48,48), and 48 hours predict 48 hours (96,96,96).

most pronounced issue with longer prediction length is the underestimation of peak waves. For example, the configuration using the past 48 hours to predict the next 24 hours (green curve) still performed fairly well during low wave periods but significantly underestimated wave heights by over 1 m during high wave events (e.g., around March 15, July 17, and December 8). Nevertheless, the shortest configuration (2-hour or 3-hour input to predict 1-hour) performed worse than the 6-hour input predicting 3-hour setup, indicating that shorter inputs lack sufficient representative information. Possible reasons include:

1. Tidal Periodicity: The studied region experiences semi-diurnal tides with a roughly 12-hour cycle. Every 6 hours the ebb and flood phase would change, meaning shorter inputs (less than 6 hours) might miss crucial tidal information.

2. Phase Misalignment: Tidal phases often do not synchronize with wave modulation phases, meaning insufficient input duration could overlook critical phase relationships, resulting in inaccurate predictions.

These findings highlight the importance of past information in predicting current and future wave-current coupling processes, emphasizing the necessity of employing machine learning models capable of temporal data mining.

6.4.2.3 Impact of Sampling Intervals

For the same input-output durations, larger sampling intervals often yielded higher prediction accuracy and faster training speeds. Figure 6.10 shows that the 60 min interval data consistently outperformed the 30 min and the 10 min intervals, with higher R values and lower MSE and SI curves. The improved performance is likely due to shorter sequence lengths required in the 60 min data, which reduced overfitting compared to the longer sequences required for 30 min and 10 min intervals. These results suggest that the loss of data resolution from larger intervals may have a smaller impact than the overfitting risk associated with longer sequences, underscoring the trade-off between data resolution and model complexity.

6.4.2.4 Application in data generation

The Informer model can be applied in two typical scenarios: (1) hindcast data generation and (2) forecast the near unknown future. Hindcast data generation is suitable for producing extensive historical data over long timescales (e.g., wave resource assessments). Since the final results are continuously generated by the model, the length of individual prediction windows is not critical, and thereby shorter prediction windows are often preferable for accuracy. In this

study, using 6 hours to predict the next 3 hours through 60 min interval data (6,3,3) provided excellent hindcast data for 2017 at Westray Firth. Figure 6.14 (a) shows the boxplot of the results against numerical modelling and demonstrates that this configuration can effectively replicate maximum, minimum, and median values across all months.

On the other hand, forecasting emphasizes longer single prediction windows. While longer prediction durations inevitably reduce accuracy, a suitable compromise is using 24 hours to predict the next 12 hours. For 60 min interval data, this configuration provided good metrics and closely matched data variability with ground truth, as shown in Figure 6.14 (b). However, configurations predicting beyond 24 hours (e.g., 48 hours to predict 24 or 48 hours) showed significant accuracy drops, with R values below 0.95 and SI exceeding 0.15.

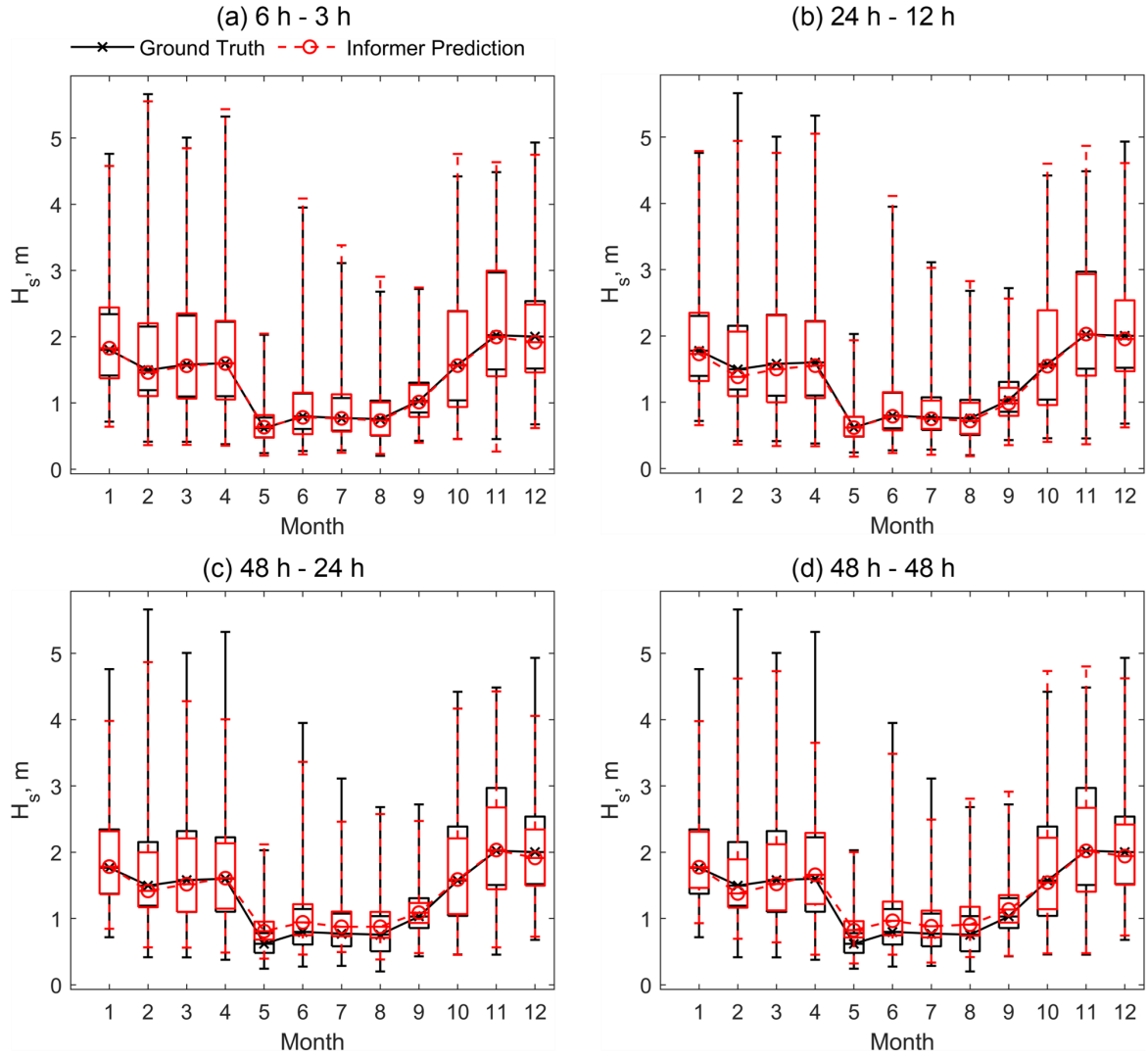

Figure 6.14 Boxplots of the Informer prediction results in 2017

The samping time interval is 60 min. From(a) to (d): 6 hours predict 3 hours (6,3,3), 24 hours predict 12 hours (24,12,12), 48 hours predict 24 hours (48,24,24), 48 hours predict 48 hours (48,48,48).

Table 6.6 2016 and 2017 yearly H_s hindcast prediction at Fall of Warness and Pentland Firth by Informer*
MAE and RMSE units are in s, MSE is in s^2.

Location	Year	Pred. Hours	Prediction Length	Metrics				
				R	MSE	MAE	RMSE	SI
Fall of Warness	2016	3	18	0.890	0.038	0.146	0.195	0.265
		6	36	0.880	0.040	0.148	0.200	0.272
		12	72	0.878	0.039	0.150	0.196	0.267
	2017	3	18	0.874	0.040	0.152	0.201	0.259
		6	36	0.861	0.043	0.155	0.207	0.267
		12	72	0.864	0.040	0.153	0.200	0.258
Pentland Firth	2016	3	18	0.892	0.068	0.189	0.261	0.305
		6	36	0.892	0.066	0.191	0.257	0.300
		12	72	0.898	0.058	0.179	0.240	0.283
	2017	3	18	0.898	0.080	0.199	0.283	0.314
		6	36	0.896	0.079	0.207	0.280	0.311
		12	72	0.897	0.068	0.191	0.261	0.289

6.4.3 Prediction at other sites

The tests used the model trained by 10-minute interval dataset of Westray Firth with three prediction configurations: 6-hour input predicting 3 hours (36, 18, 18), 12-hour input predicting 6 hours (72, 36, 36), and 24-hour input predicting 12 hours (144, 72, 72). The model generated time-series predictions for Fall of Warness and Pentland Firth for 2016 and 2017. The metrics are summarized in Table 6.6.

6.4.3.1 Fall of Warness

Fall of Warness is characterized by generally low wave heights, rarely exceeding 2 m even during winter peaks, with most of the year below 1 m. However, the site experiences strong tidal currents with maximum speeds reaching 3.5 m/s, inducing significant wave-current interactions and leading to pronounced tidal modulation. Due to the low wave heights, modulated waves were less likely to break, resulting in large fluctuations compare to Westray Firth and posing challenges in prediction. As shown in Figure 6.15, the model underestimated tidal modulation amplitudes compared to the target, specifically in July. For example, around July 10, 2017, real modulated wave peaks and troughs were 1 m and 0.25 m, respectively, with a modulation amplitude of 0.75 m. The model predicted peaks and troughs of 0.8 m and 0.37 m, yielding a modulation amplitude of 0.43 m, underestimating by 43%. Nevertheless, R values across three seasonal wave conditions remained above 0.81, and SI values stayed below 0.3, indicating strong correlation and reasonable relative accuracy despite the underestimation.

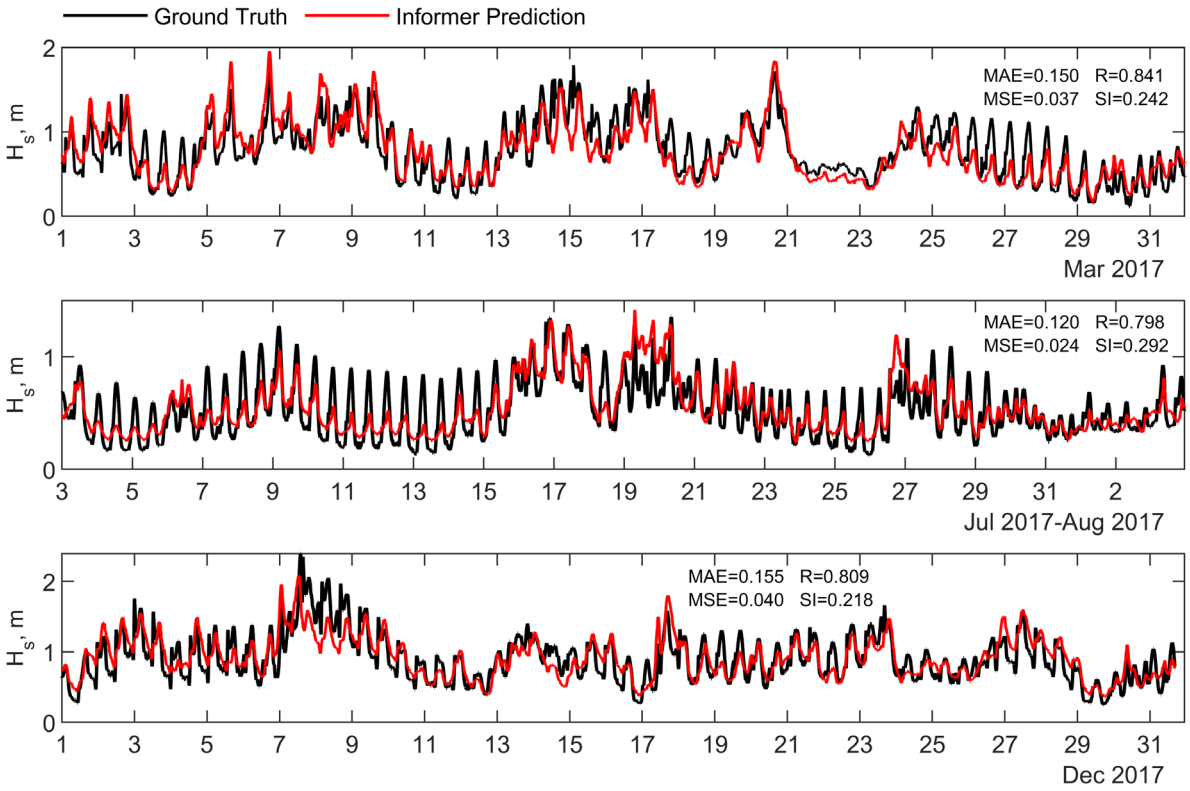

Figure 6.15 H_s prediction at Fall of Warness in March, July, and December, 2017 by the Informer*
The samping time interval is 10 min.

6.4.3.2 Pentland Firth

Pentland Firth exhibits smaller tidal modulation amplitudes due to high wave levels combined with extremely fast tidal currents (>5 m/s). These conditions often lead to wave steepening and extensive wave breaking. This is evident in the high-frequency components of the wave parameters time series and the overall reduction in wave heights compared to non-tidal conditions. For instance, as shown in Figure 2.8 (Section 2.5.2), the wave heights under tidal influence (red curve) were consistently lower than those without tidal influence (green curve). Remarkably, the Informer model accurately reproduced the modulation amplitudes and overall wave levels under tidal effects, as evidenced by high R values (over 0.89) in Table 6.6 and closely match fluctuations in Figure 6.16. This suggests the model can replicate complex phenomena like wave breaking, which typically requires extensive tuning in numerical modelling. However, MAE and MSE remained relatively high, likely due to underestimation of high wave events. For example, in March and December 2017, the model failed to predict waves above 3 m, underestimating by 1 m across all sequence configurations.

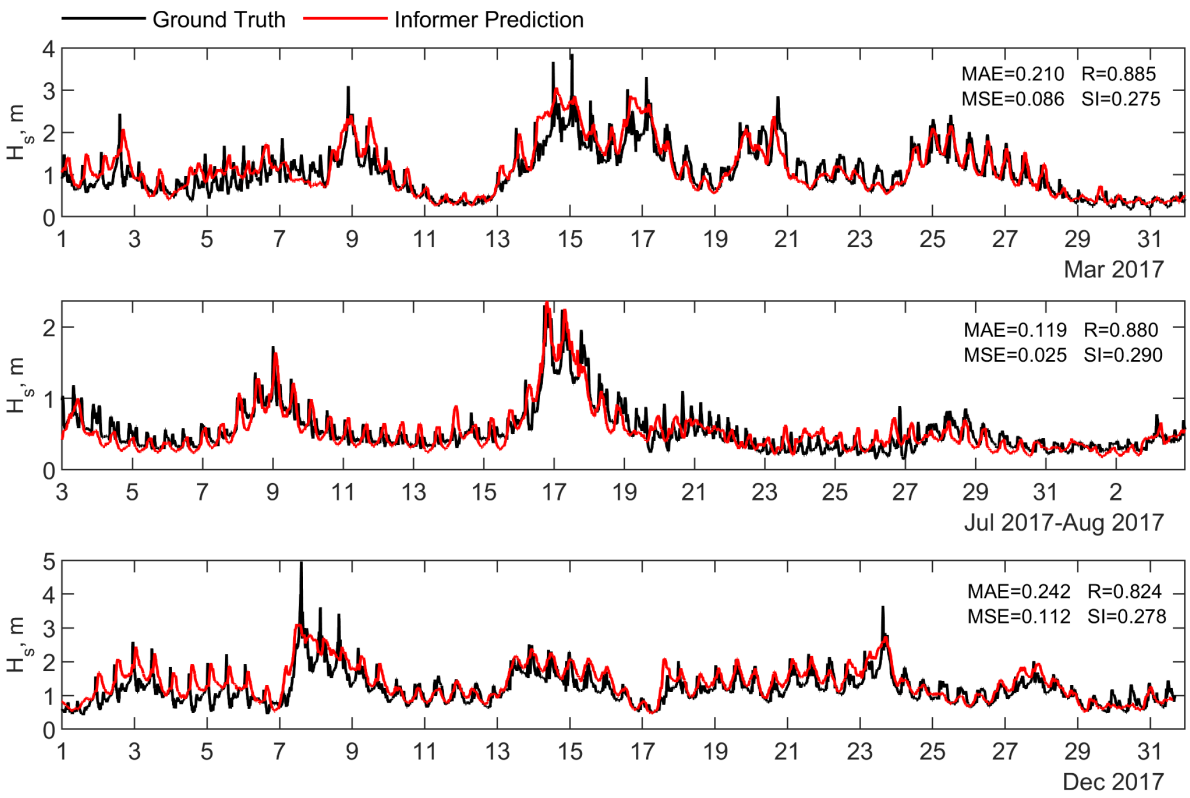

Figure 6.16 H_s prediction at Pentland Firth in March, July, and December, 2017 by the Informer*

The samping time interval is 10 min.

The predictions at Pentland Firth exhibited a 2-hour phase lead compared to observations. This phase difference was manually corrected in the results presented. The discrepancy likely arises from the model's training on Westray Firth data, where the phase relationship between wave modulation and tidal currents differs naturally from Pentland Firth. While the phase correction ensures accurate comparisons here, it highlights the model's limitations in directly generalizing to new locations. Future work should incorporate additional parameters, such as geographic coordinates, and expand training sites to account for phase-related variations, enhancing the model's adaptability across regions.

Notably, predictions for 2017 did not show significant degradation compared to 2016 at both locations, indicating the model's robustness to temporal proximity of training data. Additionally, the 6-hour input predicting 3-hour configuration (36, 18, 18), which performed best at Westray Firth, did not outperform other configurations at Fall of Warness and Pentland Firth. Instead, all three configurations delivered comparable performance, suggesting that sensitivity to input-output sequence lengths is location-dependent and less critical at sites with differing wave-current conditions.

This study used a simple model architecture with only 2 encoder layers and 1 decoder layer. Despite this simplicity, the model delivered outstanding results, demonstrating its general applicability for predicting wave-current coupling effects using deep learning. Future improvements could include integrating geographic information, enhanced tuning methods, or spatio-temporal deep learning models to improve predictions across broader regions or spatial domains. Additionally, incorporating wind data alongside tidal data could further refine wave height predictions and better address engineering applications.

6.4.4 Summary

The data for this research were derived from numerical simulations using the TOMAWAC wave model (Section 2.4) and the TOMAWAC-TELEMAC coupled wave-current model (Section 2.5). Training data from Westray Firth, northern Scotland, spanned July 2015 to December 2016, with one year of effective training data. Predictions were conducted on data from January to December 2017. The Informer model accurately captured tidal modulation effects on wave parameters.

This study evaluated the model's performance across six input-output time combinations. Results showed that longer input and output times reduced prediction accuracy. Using the past 6 hours to predict the next 3 hours yielded the best performance, even outperforming the past 2 hours predicting the next 1 hour. Shorter intervals likely failed to adequately represent tidal information and phase differences, highlighting the importance of machine learning models capable of processing temporal information.

The effect of data sampling intervals was also examined. Among 10-minute, 30-minute, and 60-minute intervals, the 60-minute interval performed best for equivalent input-output durations. Shorter sequences facilitated faster training and reduced overfitting, demonstrating an effective trade-off between data resolution and model complexity.

The model's generalization capability was tested at two additional locations: Fall of Warness and Pentland Firth. While performance at these sites was slightly lower than at the training location, the model achieved R values above 0.85 at both sites and above 0.89 at Pentland Firth. SI values remained below 0.3, demonstrating reliable predictions. Notably, the model successfully captured wave breaking phenomena at Pentland Firth, where tidal influences reduce wave amplitudes.

Chapter 7

Concluding Remarks and Future Work

The Pentland Firth and Orkney Waters region is a global leader in ocean energy development, characterized by the coexistence of strong waves and tidal currents and abundant resources for both wave and tidal energy. However, the significant wave-current interactions in this area must be carefully understood to fully harness its ocean energy potential while managing associated risks.

To address this, this PhD work comprehensively quantifies wave-current interactions through three distinct yet interconnected approaches:

1. Numerical Modelling: Investigates the effects of tidal currents on waves to quantify their interactions.
2. Wave-Current Decomposition: Examines the enhanced turbulence levels in tidal current flows caused by wave influences.
3. Machine Learning: Predicts wave parameters under the influence of tidal currents using advanced machine learning techniques.

While these approaches differ in methodology, they are firmly interconnected through shared data and outputs, ensuring consistency and robustness:

- The Cefas WaveNet wave buoy data used to validate the wave-only numerical model in Task 1 forms the training dataset for machine learning-based wave prediction at open-sea region in Task 3.
- The ADCP data (collected at Pentland Firth) used to validate the wave-current numerical model in Task 1 also serves as the data source for wave-current decomposition in Task 2.
- The numerical modelling results from Task 1 are used as validation data for Task 2 and as training data for the wave prediction at strait area Task 3.

Below is a detailed summary of each task and its contributions to understanding wave-current interactions in PFOW.

7.1 Numerical modelling

This part provides a complete summary of the construction of numerical models and their application to wave resource assessment by combining Chapter 2, 3, and 4.

7.1.1 Conclusion

Waves can be significantly influenced by strong tidal currents, which can lead to substantial inaccuracies in wave resource estimation. Such inaccuracies may result in risky site selection for wave energy development. To mitigate this risk, it is essential to understand the effects of wave-current interactions and to conduct wave resource assessments that account for these interactions. Numerical modelling is the most appropriate approach for achieving this goal.

This study developed two numerical models: (1) A North Atlantic scale wave-only model by the spectral wave model TOMAWAC, providing wave boundary conditions for smaller regional scale modelling, and simulating wave parameters without tidal current influence; and (2) A regional scale two-way coupled wave-current model combining TOMAWAC with the TELEMAC flow model, generating wave parameters that incorporate tidal effects. The feasibility of this research relies on that both TOMAWAC and TELEMAC are sub-modules of the open-source Telemac system, which enable an easy constructed and straightforward two-way coupling process between waves and tidal currents.

Both models were validated with reliable site measurements. The North Atlantic wave model is validated with wave buoy measurements at four locations at 10 years scale, which also confirms the interannual reliability of the model. The effectiveness of the wave-current coupled model, including both tidal currents and wave simulation results, was demonstrated by a total of 135-day comparison with AWAC and ADCP data, both deployed in environments with strongly coexisting waves and currents (i.e., sites at Westray Firth and Pentland Firth, respectively).

With these models, this study analysed the effects of wave-current interactions on wave parameters (i.e., H_{m0}, T_m, T_p, and mean wave directions) across different times, from Neap Tide to Spring Tide, Ebb phase to Flood phase, with specific focus on eight locations around the PFOW which were under different tide and wave conditions. Comparing to the wave-only model results, the strong current induced wave breakings are frequently observed in the wave-current model during the timeseries analysis and are also highlighted by the difference in unidirectional and directional wave spectrum between both models.

Furthermore, the wave-only model and the coupled wave-current model were continuedly running to cover 10 years (2014–2023) period, providing accurate interannual, seasonal, and monthly wave data under the effects of tidal currents for PFOW. The comparison (regarding the numerical difference and the ratio difference) of the simulation results between the wave-current and wave-only models reveals the long-term influence of wave-current interactions and the spatial distribution features around this region.

Specifically, including tidal currents, substantial decreases in wave height and power were observed at the northern and southern edges of the Orkney Islands and Stroma Island in Pentland Firth, with reductions around Stroma Island up to 0.5 m (25%) in wave height and 6 kW/m (over 50%) in wave power. Conversely, wave power increases at the tidal inlets of straits (Pentland Firth, Hoy Mouth, and Westray Firth), with a 10-year rise of up to 7.7 kW/m (22%) for a site at the Westray Firth. Extreme wave conditions are also amplified by tidal currents, particularly at the tidal inlets. The maximum increases exceed 2 m in wave height and being over 227 kW/m increase in wave power for the Westray Firth, indicating an elevated risk of extreme weather.

7.1.2 Future work

7.1.2.1 Three-dimensional wave-current coupling

The numerical modelling in this study focused on the effects of tidal currents on wave parameters, utilizing a simplified tidal flow model with only two vertical layers (bottom and surface). This approach limited the ability to simulate complex three-dimensional flows. Future work could extend the wave-current coupled model by increasing the number of intermediate vertical layers and incorporating an advanced vertical turbulence model in TELEMAC-3D. Such enhancements would allow for a more detailed analysis of surface wave effects on tidal current flows. These results could be compared with findings from Chapter 5, which applied wave-current decomposition to real field measurements, providing deeper insights into how wave-current interactions enhance ocean turbulence.

7.1.2.2 Application to wave energy convertor design

The numerical wave and tidal current models developed in this research can also support the optimization of wave energy converter (WEC) designs. Future studies could integrate WEC arrays into the wave models to quantify the differences in wave energy extraction under scenarios with and without tidal currents. While similar work has been conducted in wave-only

scenarios [57], it has yet to be explored using wave-current coupled models. Addressing this gap could provide critical insights for improving the design and efficiency of WECs in regions with significant wave-current interactions.

7.1.2.3 Impact of WCI on tidal turbines

If successful coupling between the wave model and a 3D flow model with enhanced vertical resolution is achieved, these models could be applied to study tidal energy converter arrays. This would enable the quantification of wave-induced turbulence effects on tidal turbine operations, highlighting potential challenges and guiding the development of strategies to mitigate these effects. Understanding the impact of wave-induced turbulence is essential for improving turbine performance and reliability in energetic marine environments.

7.2 Wave-current decomposition

7.2.1 Conclusion

In regions with fast-flowing currents, any presence of waves may significantly increase turbulence levels due to wave-current interactions, heightening the design and safety risks for ocean engineering operations, particularly for tidal energy converters. Understanding and characterising the turbulence levels for conditions where both waves and currents co-exist is crucial for mitigating any potential risks.

Chapter 5 introduces a side information assisted EMD method to decompose wave and current velocity components from a wave-current combined time series measured at tidal energy sites by using ADCPs with the intention of quantifying the turbulence levels enhanced by wave activities. The effectiveness of this technique is confirmed through two methods: (1) the spectra of the wave-removed velocity align with the Kolmogorov -5/3 power law, and (2) the extracted wave orbital velocities were used to derive significant wave heights through Borgman's method [123], which were validated against wave heights measured by the same ADCPs and through numerical modelling carried out with the coupled wave-current tool derived in Chapter 2.5.

With validation methods, the decomposed wave and current components velocities are proved to be reliable across various conditions: low and high wave scenarios, different depths, and three-dimensional velocities (i.e., velocities along streamwise, transverse, and vertical

directions). With this technique, the vertical profiles of the turbulence intensities (TI) and turbulence kinetic energy (TKE) for waves alone, currents alone, and wave-current combined scenarios for Ebb and Flood phases, different flow speed categories, and different wave height conditions were successfully evaluated. With these results, an empirical approximation that the combined TI equals to 0.8 times the sum of the wave and current TI was also proposed.

This work provides valuable insights into the dynamics of areas where waves and currents coexist. The decomposition technique developed in this study is unique and will find use in analysing complex time series data. The vertical profiles of TI and TKE obtained in this study should be of interest to industry practitioners.

7.2.2 Future work

As the three investigation sites in this study are geographically close, the relationships between wave-only, current-only, and wave-current turbulence levels might be site-specific and not universally representative. Future work could apply this wave-current decomposition technique to other sea regions to evaluate its performance and generalizability. Such studies might reveal different insights into how waves enhance turbulence levels in diverse real-world marine environments, broadening the applicability of the technique.

The decomposition technique in this research has been validated using real-world site measurements, where tidal flow strength and direction vary dynamically. However, it has not yet been tested against experimental data generated in controlled laboratory settings. Future validation in such environments could directly assess the effectiveness of the separation method by comparing results with predefined experimental wave and tidal conditions. Laboratory experiments would provide a controlled framework to evaluate the method's accuracy and identify potential limitations.

Additionally, applying this decomposition technique to laboratory-generated data could serve broader purposes in studying wave dynamics under homogeneous and inhomogeneous conditions. Controlled experiments would allow for systematic investigations of wave-current interactions and turbulence, offering new perspectives on wave-enhanced turbulence in settings where environmental variables are precisely managed. These insights could further refine the technique and expand its utility in both academic research and practical applications.

7.3 Machine learning based wave prediction

7.3.1 Conclusion

Traditional wave prediction methods, which rely heavily on extensive numerical modelling, raise the question: Can wave prediction be achieved faster? This study explores advanced machine learning techniques to address this challenge, focusing on two scenarios: (1) wave prediction in open-sea regions and (2) wave prediction in strait regions.

In the open-sea scenario, tidal current influences are negligible, and waves are predominantly driven by winds. Focusing on the waters around northern Scotland, the spatiotemporal relationship between wind and wave parameters, such as significant wave heights and mean wave periods, was modelled using Informer deep neural networks and XGBoost machine learning. Ten years (2012–2021) of wind and wave data from ECMWF ERA5 and Cefas WaveNet were used for training and testing. Both the standard Informer model and a modified version (excluding target features from inputs) were employed, alongside the XGBoost model, to predict wave conditions for 2022. These models also facilitated the development of versatile and specialized frameworks for typical and extreme weather conditions, enabling precise wave predictions based solely on wind data.

In the strait scenario, where tidal currents significantly impact wave behaviour, the focus shifted to the Pentland Firth and Orkney Waters. Training data were derived from high-precision, long-term simulations generated by wave-only and wave-current coupled models (introduced in Chapter 4). Data from July 2015 to December 2016 were used for training, with evaluations conducted over prediction windows ranging from 1 to 48 hours. The model was then looped to produce year-long predictions for 2017. The Informer model effectively captured tidal modulations on waves, achieving optimal performance when using past 6-hour data to predict the next 3 hours. Tests with different temporal resolutions (10, 30, and 60 minutes) showed the best results with 60-minute intervals for matching prediction windows. Predictions at two distinct locations demonstrated the model's robustness, even without incorporating geographic features, highlighting its potential for future spatially varying applications.

The data-driven approach significantly outperformed traditional numerical models in efficiency. While numerical simulations require over 24 hours to process a year’s data, machine learning methods can achieve the same result within seconds. This breakthrough in efficiency marks a pivotal step forward in wave prediction research, demonstrating the potential of AI in revolutionizing oceanographic modelling.

7.3.2 Future work

7.3.2.1 Addressing site-specific limitations

The wave prediction models in this research remain site-specific, limiting their application to real-world practices. To enhance generalizability, future work will aim to incorporate geographically relevant features and develop spatially varying models for spatiotemporal predictions. Potential approaches include: (1) Adding geographic related features as input variables to the model; (2) Introducing position embedding processes for input features before feeding them into the encoder; (3) Using a spatial model, such as a Convolutional Neural Network (CNN), to process spatial relationships within the data before utilizing advanced models like Informer for temporal predictions.

The expected outcomes of this spatiotemporal modelling: for open-sea regions, using wind grid data to predict wave conditions across a broader area. For strait regions, combining wave-only maps and tidal current maps to predict wave conditions influenced by wave-current interactions.

7.3.2.2 Towards replacing numerical modelling

Another important direction for future work is to integrate wind data-based wave predictions with methods that incorporate tidal currents. This progression could culminate in a framework where wind data and tidal current data are used to predict waves with tidal effects, creating a realistic and computationally efficient alternative to traditional numerical modelling.

By addressing these aspects, the future research aims to advance AI-driven wave prediction from site-specific applications to comprehensive, scalable solutions for real-world oceanographic challenges.

7.3.2.3 Exploring different methods

Using AI methods in wave prediction is becoming an inevitable trend in the field. While the best solution is yet to be identified, exploring a wide variety of methods is crucial. The increasing popularity of attention mechanisms in temporal predictions has led to a trend of combining LSTM (Long Short-Term Memory) networks with attention mechanisms. Future work can leverage advanced approaches such as integrating LSTM with Transformer (or Informer) or LSTM with attention mechanisms to improve wave prediction performance in both open-sea and complex strait regions.

Appendix A
Numerical Model Construction

This study involves the development of two numerical models: (1) the North Atlantic scale TOMAWAC wave model and (2) the PFOW regional scale TOMAWAC-TELEMAC wave-current coupled model. Both models are implemented within the Telemac system, utilizing either the TOMAWAC wave model or the TELEMAC 2D/3D flow models. Due to their shared foundation in the Telemac system, the models follow a similar logic in their construction and configuration processes. A graphical summary of the inputs and outputs of the numerical modelling is given in Figure A.1.

This chapter provides a comprehensive introduction to the input and output files required for these models, along with detailed steps for file pre-processing. Additionally, the chapter concludes with practical lessons and tips, learned by the author, for successfully implementing simulations within the Telemac framework.

A.1 Inputs

A.1.1 General inputs: mesh, boundary condition file, steering file

The simulation for either waves or tidal currents using the Telemac system simply requires three basic files: the geometry file (i.e., mesh), the boundary condition file, and the steering file.

The geometry file is normally the SELAFIN-formatted binary file (*.slf), which include the complete information about the horizontal mesh as well as the bathymetry information of each mesh node. The software used for the mesh creation the SELAFIN format file exportation is the BlueKenue, developed by the Canadian Hydraulics Centre (https://nrc.canada.ca/en/research-development/products-services/software-applications/blue-kenuetm-software-tool-hydraulic-modellers).

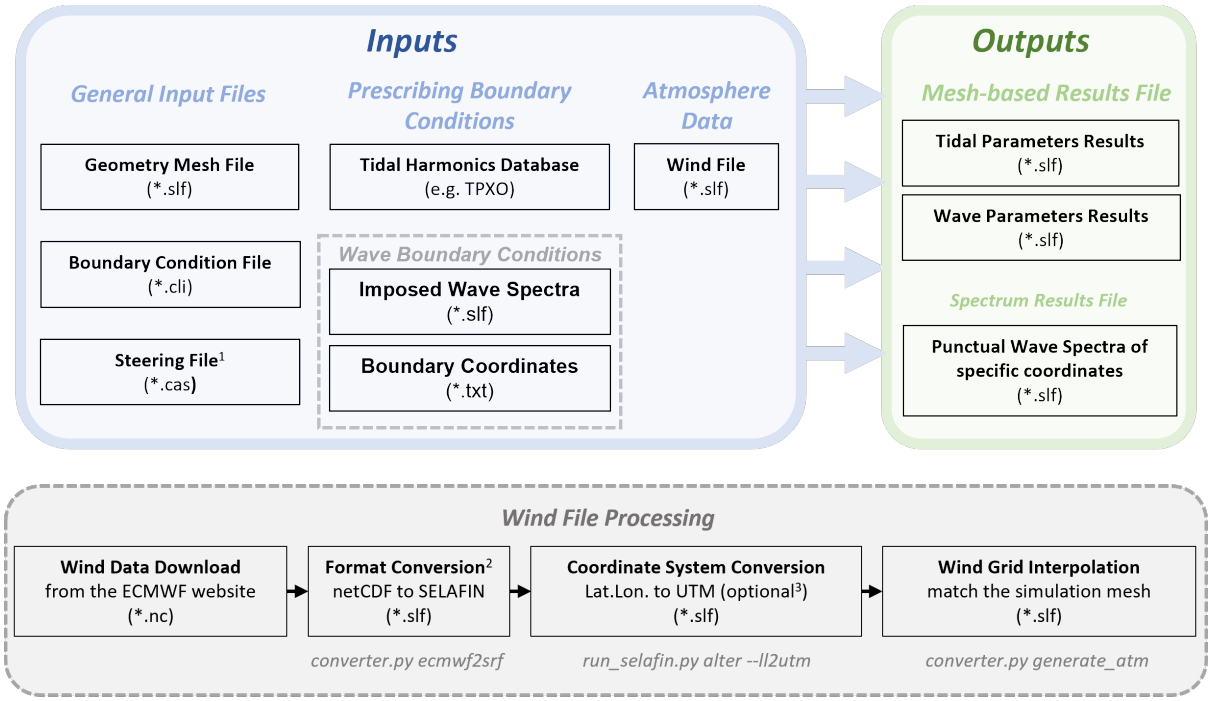

Note

1. For the wave-current coupled model, both TOMAWAC steering file and TELEMAC steering file are required
2. The initial python code is modified by the author: changed the naming logic of wind variables to 'Wind Alone X/Y' instead of 'Wind Velocity U/V'
3. Only required when simulating in a Cartesian coordinate system (or UTM system)

Figure A.1 Input and output file for Telemac system simulation

A.1.1.1 Coastlines/shorelines preparation

For either the North Atlantic-scale model, or the regional-scale model, the shape information of the coastline/shorelines are sourced from the GSHHS [138], which is then visualized and extracted by the GEODAS Coastline Extractor (https://www.ngdc.noaa.gov/mgg/gdas/). After that, the desired coastline/shorelines by shape format file (*.shp) are imported to the BlueKenue to serve as the possible solid boundary of the geometry mesh. The pre-processing of these coastlines/shorelines including the resample with different resolution scale as desire.

The general principal of mesh generation is that the area of interest requires finer mesh to capture the spatial difference. Therefore, the strategy of nesting several sub-mesh with finer spatial resolution is applied. The mesh is created by using the function of 'T3 Mesh Generator' and filled the content of 'Outline' (i.e., mesh boundary), 'Hardlines' (i.e., closed boundary of islands, derived from the coastlines/shorelines introduced before), 'SubMeshes' (if have) with the corresponding information. Geometry mesh details (e.g., size, resolution of sub-meshes) of this North Atlantic-scale model is given in the Section 2.4 and of the regional-scale model will be given in the Section 2.5.

When the horizontal mesh is generated and the SELAFIN object is created, then the nodes of the mesh are ready to be assigned with the bathymetry information using the '2D Interpolator' of the BlueKenue, which the bathymetry dataset is obtained from the GEBCO [118] with the spatial resolution of 15 arc-second (around 1 km). For those nodes within the minimum resolution of the bathymetry data, interpolation will be made. Therefore, it may always cause the inaccuracy by using GEBCO if the simulation domain is very small, and the purpose of task requires very high resolution. Considering the simulation domain of this study, GEBCO should be sufficient.

It is noticeable that either the GSHHS or GEBCO dataset are under the sphere (latitude/longitude) system refers to the WGS84. For the large-scale model, such as the North Atlantic model, the simulation is usually conducted under the same coordinate system and the dataset can be directly used without any coordinate transfer. However, for the regional scale simulation, such as the PFOW scale model in this study which is simulated under the UTM system of zone 30, it is necessary to transfer all the dataset to the UTM coordinate system first before use. This can be easily realized by BlueKenue or other available MATLAB code.

A.1.1.2 Boundary condition file generation

The mesh boundary conditions can also be defined and outputted by the BlueKenue once the geometry mesh is ready. The conditions of the liquid boundary at the mesh outline of both the North Atlantic model and the regional scale model in this study are set to be 'open boundary with prescribed H' (H is the water depth). The boundary conditions object is consisted of two objects: 1) 'bc2 mesh' for the boundary segment definitions and provide geometry for visualization and editing, and 2) the table object '*.cli' for use with Telemac system.

A.1.1.3 Steering file preparation

The steering file '*.cas' is a text file and can be accessed by means of a text editor. It serves as the computation control panel, which includes a set of key words to which values are assigned. For example, besides defining the name of the input and output files, parameters for the wave spectrum and whitecapping in the wave simulation, bottom friction and turbulence model in the flow simulation are all defined in the steering file. The details of the specific parameters are given in Section 2.4.1.3 for the wave model, and Section 2.5.1.2 for the current flow model and wave-current coupled model.

A.1.2 Other inputs: wind file, tidal harmonic database, and wave boundary conditions

Besides the three basic files, additional input file may also be required depends on the purpose of modelling, such as the atmosphere data (i.e., wind), prescribing boundary conditions, and other Fortran subroutines to modify the default simulation routine.

In the wave simulation, reliable wind data are necessary to accurately simulate the real-world wind-driven waves. In this study, the ECMWF ERA5 hourly 10-m UV wind, with the wind grid resolution being 0.25×0.25 degrees, are adopted and defined in the TOMAWAC steering file for both the North Atlantic wave model and the regional-scale wave-current coupled model. The data is in the netCDF format.

The use of the ECMWF wind file requires several steps of pre-process due to the reasons: 1) in the Telemac system, the wind input should be in the ASCII format or SELAFIN format; 2) the simulation coordinate system may be different from the wind dataset, and 3) the wind grid should be interpolated to match with the geometry mesh before simulation, as the interpolation between two different meshes during the simulation is computationally very expensive. The pre-process can be achieved by the python tool provided the Telemac system at '[installation path]\v8p1r0\scripts\python3\'. To be clarity, file conversion can be realized by the 'converter.py ecmwf2srf' with the information of the time period and geographical area of the wind region. It is notably that the initial code of the ecmwf2srf is modified: the initial name of the wind variables 'Wind Alone X' and ''Wind Alone Y'' to 'Wind Velocity U' and 'Wind Velocity V' respectively, as the former name is only supported by the TELEMAC flow model while the TOMAWAC wave model only support the latter names. The length of the variable name is 16 alphabet spaces, which means if the name length is less than it should be filled with blank space.

The prescribing boundary conditions of coastal boundary subject to tidal evolution are generally characterized by the tidal harmonic constants. In this study, the global TPXO9 database (version 9 with the resolution of 1/6 degrees) is utilized in the TELEMAC 2D/3D flow model to provide the tidal harmonics. Specifically, the 'h_tpxo9.v4a' is served as water level database and the 'u_tpxo9.v4a' is served as the velocity database.

The prescribing wave spectrum of the boundary nodes are necessarily required for the wave simulation in a small geometry area, such as the Orkney Waters regional-scale model. With this as the prescribed wave boundary conditions, the wave travel from far away locations where the model doesn't cover also able to transport the energy into the model. In this study,

the way to input the wave boundary conditions is by imposing the wave spectra along the nodes of open boundary with two input files: 1) imposed spectra file, and 2) file with coordinate of spectra to impose. The former wave spectra file is generated by a large-scale wave model, which is the North Atlantic scale in this study. The latter coordinates file contains the coordinates as well as the bathymetry information of the nodes.

The Telemac system provide a variety of the Fortran subroutine templates which is ready to be modified for the specific purpose at '[installation path]\v8p1r0\sources\'. In this study, the 'condim.f' and 'user_mesh_transf.f' are used to define the mesh transformation methods of the TELEMAC 3D model.

A.1.3 Inputs for this study

With the knowledge of the inputs and outputs, it can be summarized that the inputs for the North Atlantic-scale TOMAWAC model are: (1) geometry file, (2) the boundary condition file, (3) the TOMAWAC steering file, (4) the atmosphere data, and (5) coordinates information to write the wave spectra.

The inputs for the Pentland Firth and Orkney Waters regional-scale TOMAWAC-TELEMAC wave-current coupled model are: (1) geometry file, (2) the boundary condition file, (3) the TOMAWAC steering file, (4) the TELEMAC steering file, (5) the atmosphere data (SELAFIN format wind file), (6) the prescribed tidal boundary conditions of water level, (7) the prescribed tidal boundary conditions of velocity, (8) prescribed wave boundary conditions, (9) coordinates information to impose the wave spectra, (10) coordinates information to write the wave spectra, and (11) Fortran subroutine to define the vertical layer of the TELEMAC 3D flow model.

A.2 Outputs

Both the TOMAWAC results file and TELEMAC results file are in SELAFIN format. The results files contain the information on the mesh geometry, the names of the stored variables, and the values of the different variables for each time step as well as all mesh points. The output variables of the TOMAWAC wave model at the North Atlantic-scale (i.e., 'L' in the table) and at regional-scale (i.e., 'S') are listed in the Table A.1.

Table A.1 Output variables and definition equations of the TOMAWAC model

Symbol* are the variable names used in the Fortran code of TOMAWAC.

Variable Name	Symbol	Unit	Equation/Description	Scale	
				L	S
Significant Wave Height	HM0	m	$H_{m0} = 4 \cdot \sqrt{\int_0^\infty S(f)\, df}$	✓	✓
Mean Wave Direction	DMOY	deg.	Mean wave direction θ_m with respect to the north $a = \frac{\int_0^\infty \int_0^{2\pi} \cos(\theta)\, F(f,\theta)\, df d\theta}{\int_0^\infty S(f)\, df}$ $b = \frac{\int_0^\infty \int_0^{2\pi} \sin(\theta)\, F(f,\theta)\, df d\theta}{\int_0^\infty S(f)\, df}$ $\theta_m = \tan^{-1}\left(\frac{b}{a}\right) \cdot \frac{180}{\pi}$	✓	✓
Wave Spread	SPD	deg.	Mean angular spreading σ of the directional wave spectrum $\sigma = \sqrt{2\left(1 - \sqrt{a^2 + b^2}\right)} \cdot \frac{180}{\pi}$	✓	
Energy Wave Period	TMOY	s	$T_{moy} = \frac{m_{-1}}{m_0} = \frac{\int_0^\infty S(f) \cdot f^{-1}\, df}{\int_0^\infty S(f)\, df}$	✓	✓
Mean Wave Period	TM01	s	$T_{01} = \frac{m_0}{m_1} = \frac{\int_0^\infty S(f)\, df}{\int_0^\infty S(f) \cdot f\, df}$	✓	✓
Peak Wave Period (Order 5)	TPR5	s	$T_{pR5} = \frac{m_0}{m_1} = \frac{\int_0^\infty S^5(f)\, df}{\int_0^\infty S^5(f) \cdot f\, df}$	✓	✓
Wave Power	POW	kW/m	Unit wave power rate (per meter of crest length) Equation (2.5)	✓	✓
Force FX	FX	m/s^2	Component along X axis of the radiation force due to waves		✓
Force FY	FY	m/s^2	Component along Y axis of the radiation force due to waves		✓

Regarding the flow model, the TELEMAC 2D output variables of this study is U (velocity along x axis, m/s), V (velocity along y axis, m/s), H (water depth, m), S (free surface elevation, m). The TELEMAC 3D output variables of this study are three-dimensional Z (elevation, m), U (velocity along x axis, m/s), V (velocity along y axis, m/s), W (velocity along z axis, m/s), which

is composed of the multiple layers of 2D results. Notably, the simulation results of the TELEMAC 3D model consists of both TELEMAC 2D results which represent the depth-averaged values and TELEMAC 3D results. In this study, the tidal flow is simulated under the code of TELEMAC 3D, even though the number if horizontal levels is set to 2 (bottom and free surface) which basically is recognized as a 2D model. This is because the primary focus of this study is on the mean flow speed and surface waves, which means the number of vertical layers in this case need be simplified to optimize simulation efficiency. However, with the truth that the source code of the TELEMAC 2D and 3D are different, the author expects to use the 3D model developed in this study to do the complex 3D research in the future.

It is notably that the time series results of each variable (including the punctual wave spectra result file) may not have the same time interval as the simulation time steps. This depends on the parameter 'Period for Graphic Printouts' if the number is an integral larger than 1. The time interval of the final results will be 'Time Step × Period for Graphic Printouts' to reduce the storage space. For example, in this study, the flow model is simulated every 5 seconds, and the graphic printout period is 120, then the time interval of the final results is 600 s or 10 min. Similar in the wave-current model, the time step of the wave simulation is 300 seconds while the printout period is twice of it to be 10 min.

The SELAFIN format simulation results can be access by the BlueKenue. There is also a variety of the MATLAB toolbox available for the visualization, get the temporal maximum/minimum/mean values of the results domain: https://www.mathworks.com/matlabcentral/fileexchange/25021-telemac-tools

A.3 Steering/CAS files

For the parameters not listed in the CAS files, default values are applied. Lines beginning with '/' are comment lines used for explanation and are not executed in the simulation. This section provides the contents of three CAS files: 1) the wave simulation CAS file for the North Atlantic scale wave model, 2) the wave simulation CAS file for the regional scale wave-current model, and 3) the tidal current simulation CAS file for the regional scale wave-current model.

Notably, the definitions and codes used for these parameters are explained in the TOMAWAC and TELEMAC manuals [73,76]; therefore, no further introduction is provided here.

1. The wave simulation CAS file for the North Atlantic scale wave model

```
/----------------------------------------------------------------------
/ BOTTOM FRICTION
/----------------------------------------------------------------------
BOTTOM FRICTION DISSIPATION =1
BOTTOM FRICTION COEFFICIENT =0.038

/----------------------------------------------------------------------
/ BREAKING
/----------------------------------------------------------------------
DEPTH-INDUCED BREAKING DISSIPATION =2
NUMBER OF BREAKING TIME STEPS      =3

/----------------------------------------------------------------------
/ CURRENT
/----------------------------------------------------------------------
CONSIDERATION OF A STATIONARY CURRENT =NO

/----------------------------------------------------------------------
/ INPUT DATA FILE
/----------------------------------------------------------------------
STEERING FILE           ='TOM_2021_2.cas'
BINARY WINDS FILE       ='wind2021_2.slf'
SPHERICAL COORDINATES       =true
GEOMETRY FILE           ='Atlantic.slf'
BOUNDARY CONDITIONS FILE ='Atlantic.cli'

/----------------------------------------------------------------------
/ INITIAL CONDITION
/----------------------------------------------------------------------
INITIAL PEAK FREQUENCY         =0.3
INITIAL PHILLIPS CONSTANT      =0.024
INITIAL PEAK FACTOR            =1.0
INITIAL SIGNIFICANT WAVE HEIGHT =5.
INITIAL DIRECTIONAL SPREAD 1    =1.
INITIAL MAIN DIRECTION 1       =270.

/----------------------------------------------------------------------
/ SPECTRE INITIAL
/----------------------------------------------------------------------
TYPE OF INITIAL DIRECTIONAL SPECTRUM =4

/----------------------------------------------------------------------
/ RESULTS
/----------------------------------------------------------------------
NUMBER OF TIME STEP =26490
TIME STEP          =600
PERIOD FOR LISTING PRINTOUTS       =2
VARIABLES FOR 2D GRAPHIC PRINTOUTS =HM0,DMOY,SPD,TMOY,TM01,TPR5,POW
2D RESULTS FILE                 ='TOM_2021_2.slf'
PUNCTUAL RESULTS FILE           =' Boundary_2021_2.slf'
FILE WITH COORDINATES OF SPECTRA TO WRITE = ‘CoorBoundary_LL.txt'
```

```
/-----------------------------------------------------------------
/ SPECTRUM
/-----------------------------------------------------------------
NUMBER OF DIRECTIONS  =36
MINIMAL FREQUENCY     =0.040539
FREQUENTIAL RATIO     =1.08
NUMBER OF FREQUENCIES =36

/-----------------------------------------------------------------
/ TRANSFERS
/-----------------------------------------------------------------
NON-LINEAR TRANSFERS BETWEEN FREQUENCIES =1

/-----------------------------------------------------------------
/ WHITE CAPPING
/-----------------------------------------------------------------
WESTHUYSEN DISSIPATION COEFFICIENT       =0.00002
SATURATION THRESHOLD FOR THE DISSIPATION =0.00175
WHITE CAPPING DISSIPATION                =2
WESTHUYSEN WHITE CAPPING DISSIPATION     =1.5

/-----------------------------------------------------------------
/ TERMES SOURCES
/-----------------------------------------------------------------
CONSIDERATION OF SOURCE TERMS =YES
WINDS FILE FORMAT       =3
WIND GENERATION         =3
CONSIDERATION OF A WIND =YES
STATIONARY WIND         =NO
WATER DENSITY           =1025.
```

2. The wave simulation CAS file for the regional scale wave-current model

```
/-----------------------------------------------------------------
/ BOTTOM FRICTION
/-----------------------------------------------------------------
BOTTOM FRICTION DISSIPATION =1
BOTTOM FRICTION COEFFICIENT =0.038

/-----------------------------------------------------------------
/ BREAKING
/-----------------------------------------------------------------
DEPTH-INDUCED BREAKING DISSIPATION =2
NUMBER OF BREAKING TIME STEPS      =3

/-----------------------------------------------------------------
/ INPUT DATA FILE
/-----------------------------------------------------------------
STEERING FILE           ='Year2021_2_wave_regionalScale.cas'
BINARY WINDS FILE       =wind2021_2_regional.slf'
SPHERICAL COORDINATES         =NO
```

```
GEOMETRY FILE           ='Regional_PFOW.slf'
BOUNDARY CONDITIONS FILE ='Regional_PFOW.cli'
IMPOSED SPECTRA FILE = 'Boundary_2021_2.slf'
FILE WITH COORDINATES OF SPECTRA TO IMPOSE = 'CoorBoundary_UTM.txt'

/----------------------------------------------------------------------
/ TIDAL CURRENT SETTINGS
/----------------------------------------------------------------------
CONSIDERATION OF A STATIONARY CURRENT =NO
DISSIPATION BY STRONG CURRENT = 2
DISSIPATION COEFFICIENT FOR STRONG CURRENT = 5.2

/----------------------------------------------------------------------
/ INITIAL CONDITION
/----------------------------------------------------------------------
INITIAL PEAK FREQUENCY         =0.3
INITIAL PHILLIPS CONSTANT      =0.024
INITIAL PEAK FACTOR            =1.0
INITIAL SIGNIFICANT WAVE HEIGHT =5.
INITIAL DIRECTIONAL SPREAD 1    =1.
INITIAL MAIN DIRECTION 1       =270.

/----------------------------------------------------------------------
/ SPECTRE INITIAL
/----------------------------------------------------------------------
TYPE OF INITIAL DIRECTIONAL SPECTRUM =4

/----------------------------------------------------------------------
/ RESULTS
/----------------------------------------------------------------------
NUMBER OF TIME STEP =52980
TIME STEP          =300
PERIOD FOR LISTING PRINTOUTS      =2
PERIOD FOR GRAPHIC PRINTOUTS = 2
VARIABLES FOR 2D GRAPHIC PRINTOUTS =HM0,DMOY,TMOY,TM01,TPR5,FX,FY,POW
2D RESULTS FILE                 ='Year2021_regionalWave.slf'
PUNCTUAL RESULTS FILE           ='Y2021_2_SpecAtCoor.slf'
FILE WITH COORDINATES OF SPECTRA TO WRITE = 'CoorWaveSpectra.txt'

/----------------------------------------------------------------------
/ SPECTRUM
/----------------------------------------------------------------------
NUMBER OF DIRECTIONS  =36
MINIMAL FREQUENCY     =0.040539
FREQUENTIAL RATIO     =1.08
NUMBER OF FREQUENCIES =36

/----------------------------------------------------------------------
/ TRANSFERS
/----------------------------------------------------------------------
NON-LINEAR TRANSFERS BETWEEN FREQUENCIES =1
NUMBER OF ITERATIONS FOR THE SOURCE TERMS = 1

/----------------------------------------------------------------------
/ WHITE CAPPING
```

```
/-----------------------------------------------------------------
WESTHUYSEN DISSIPATION COEFFICIENT       =0.00002
SATURATION THRESHOLD FOR THE DISSIPATION =0.00175
WHITE CAPPING DISSIPATION                =2
WESTHUYSEN WHITE CAPPING DISSIPATION     =1.5

/-----------------------------------------------------------------
/ TERMES SOURCES
/-----------------------------------------------------------------
CONSIDERATION OF SOURCE TERMS =YES
WINDS FILE FORMAT       =3
WIND GENERATION         =3
CONSIDERATION OF A WIND =YES
STATIONARY WIND         =NO
WATER DENSITY           =1025.
```

3. The tidal current simulation CAS file for the regional scale wave-current model

```
/-----------------------------------------------------------------/
/     PROPAGATION                                                 /
/-----------------------------------------------------------------/
SOLVER FOR PROPAGATION                    =2
ACCURACY FOR PPE                          =1.E-2
VERTICAL TURBULENCE MODEL                 =2
LAW OF BOTTOM FRICTION                    =2
ACCURACY FOR PROPAGATION                  =1.E-2
ACCURACY FOR DIFFUSION OF VELOCITIES      =1.E-2
FRICTION COEFFICIENT FOR THE BOTTOM       =66

/-------------------------------------------------
/          ADVECTION-DIFFUSION
/-------------------------------------------------
SCHEME FOR ADVECTION OF VELOCITIES =1
OPTION OF SOLVER FOR DIFFUSION OF VELOCITIES =5

/-----------------------------------------------------------------
/ EQUATIONS, BOUNDARY CONDITIONS
/-----------------------------------------------------------------
OPTION FOR LIQUID BOUNDARIES =2
INITIAL CONDITIONS           ='TPXO SATELLITE ALTIMETRY'
OPTION FOR THE TREATMENT OF TIDAL FLATS =1

/-----------------------------------------------------------------
/ EQUATIONS, DIFFUSION
/-----------------------------------------------------------------
PRECONDITIONING FOR DIFFUSION OF VELOCITIES      =2
MAXIMUM NUMBER OF ITERATIONS FOR PPE             =500
MAXIMUM NUMBER OF ITERATIONS FOR DIFFUSION OF VELOCITIES =500

/-----------------------------------------------------------------
/ INPUT DATA FILES
/-----------------------------------------------------------------
```

```
STEERING FILE             ='Year2021_2_tides_regionalScale.cas'
GEOMETRY FILE              ='Regional_PFOW.slf'
BOUNDARY CONDITIONS FILE   ='Regional_PFOW.cli'
BINARY DATABASE 2 FOR TIDE ='u_tpxo9.v4a'
BINARY DATABASE 1 FOR TIDE ='h_tpxo9.v4a'
FORTRAN FILE              ='user_fortran'

/-----------------------------------------------------------------
/ WAVE COUPLING SETTINGS
/-----------------------------------------------------------------
COUPLING WITH             ='TOMAWAC'
TOMAWAC STEERING FILE     =''Year2021_2_wave_regionalScale.cas'
WAVE DRIVEN CURRENTS              =true
COUPLING PERIOD FOR TOMAWAC       =60

/-----------------------------------------------------------------
/ RESULTS
/-----------------------------------------------------------------
TIME STEP                         =5.
NUMBER OF TIME STEPS       =3178800
ORIGINAL DATE OF TIME             =2021;7;1
NUMBER OF HORIZONTAL LEVELS =2
MASS-BALANCE                      =YES
VARIABLES FOR 2D GRAPHIC PRINTOUTS =U,V,H,S
VARIABLES FOR 3D GRAPHIC PRINTOUTS =Z,U,V,W
GRAPHIC PRINTOUT PERIOD           =120
LISTING PRINTOUT PERIOD           =150
2D RESULT FILE            ='Year2021_regionalTides2D.slf'
3D RESULT FILE            ='Year2021_regionalTides3D.slf'

/-------------------------------------------------
/                   TIDE CONDITIONS
/-------------------------------------------------
OPTION FOR TIDAL BOUNDARY CONDITIONS =1
COEFFICIENT TO CALIBRATE TIDAL RANGE =1.33
COEFFICIENT TO CALIBRATE SEA LEVEL   =5.8
MASS-LUMPING FOR DIFFUSION          =1
TIDAL DATA BASE                   =2
GEOGRAPHIC SYSTEM                 =2
ZONE NUMBER IN GEOGRAPHIC SYSTEM     =30
FREE SURFACE GRADIENT COMPATIBILITY  =0.1
DYNAMIC PRESSURE IN WAVE EQUATION    =true
MESH TRANSFORMATION               =3

/-----------------------------------------------------------------
/ NUMERICAL PARAMETERS, VELOCITY-CELERITY-DEPTH
/-----------------------------------------------------------------
MASS-LUMPING FOR DEPTH  =1
IMPLICITATION FOR DEPTH =0.6
```

A.4 Lessons (tips) for successful model execution

After numerous trials and errors during model construction and simulation, I have summarized several important points to be mindful of when using the modules of the Telemac system:

1. **Managing Large File Sizes for Wave Spectra Boundary Conditions**:

   When the model requires wave spectra as boundary conditions, the Telemac system copies all the input spectra to match the number of CPU cores in parallel simulations, rather than splitting the data. This strategy can result in significant temporary storage demands.

   For instance, a six-month wave spectra file containing data for 295 coordinates is approximately 30 GB. Running this simulation on a 32-core CPU would require temporary storage exceeding 30×32=960 GB on the disk, creating substantial space requirements.

2. **Ensuring Sufficient Drive Space for Result Files**:

   In addition to the large temporary storage needs during simulation, extra disk space is required near the end of the process. This is because, as the simulation concludes, the system merges temporary results into a single output file. At this stage, both the temporary files and the final output file coexist briefly on the disk.

   Insufficient disk space at this critical moment can result in failed saves and permanent data loss in the final output. To avoid this, ensure that the available disk space exceeds the combined requirements of the temporary files during simulation and the space needed for the final output.

3. **Limitation on the Number of Output Variables**:

   The maximum number of output variables that the model can reliably handle is 9. If you attempt to output 9 or more variables, some of the data may be randomly lost, resulting in incomplete or erroneous results. Be cautious, run a test case to double check it.

4. **Output File Naming Convention**:

   The name of the output file must begin with an alphabetical character, not a number. Naming files starting with a number can led to partial data loss in the results. There should be no ‘space’ in the name. Adhering to these naming conventions ensures data integrity.

Appendix B

Figures and Tables

B.1 Ten years hindcast by wave-only model

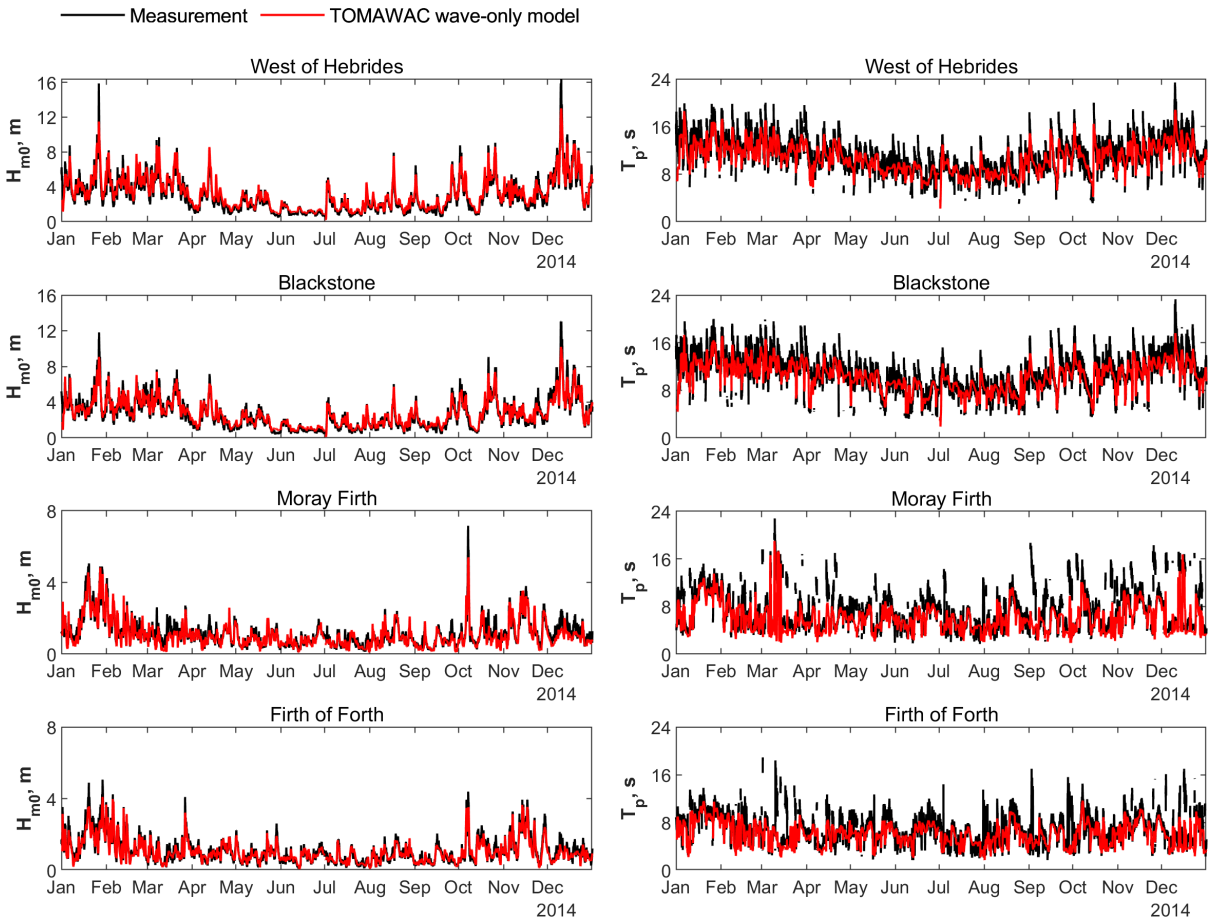

Figure B.1 Hindcast H_{m0} and T_p by wave-only model in 2014

Table B.1 Metrics of the North Atlantic scale wave model in 2014

Location	Parameter	Mean		Bias	Normalized Bias	RMSE	SI	R
		Model	Real					
West of Hebrides	H_{m0}, m	2.98	3.23	-0.25	-0.08	0.46	0.14	0.98
	T_p, s	11.17	10.70	0.48	0.04	1.39	0.13	0.89
Blackstone	H_{m0}, m	2.66	2.76	-0.09	-0.03	0.41	0.15	0.98
	T_p, s	10.85	10.41	0.44	0.04	1.54	0.15	0.88
Moray Firth	H_{m0}, m	1.14	1.08	0.07	0.06	0.26	0.24	0.94
	T_p, s	7.13	6.08	1.05	0.17	2.83	0.47	0.58
Forth of Firth	H_{m0}, m	1.07	1.05	0.03	0.03	0.20	0.19	0.96
	T_p, s	7.13	6.08	1.05	0.17	2.83	0.47	0.58

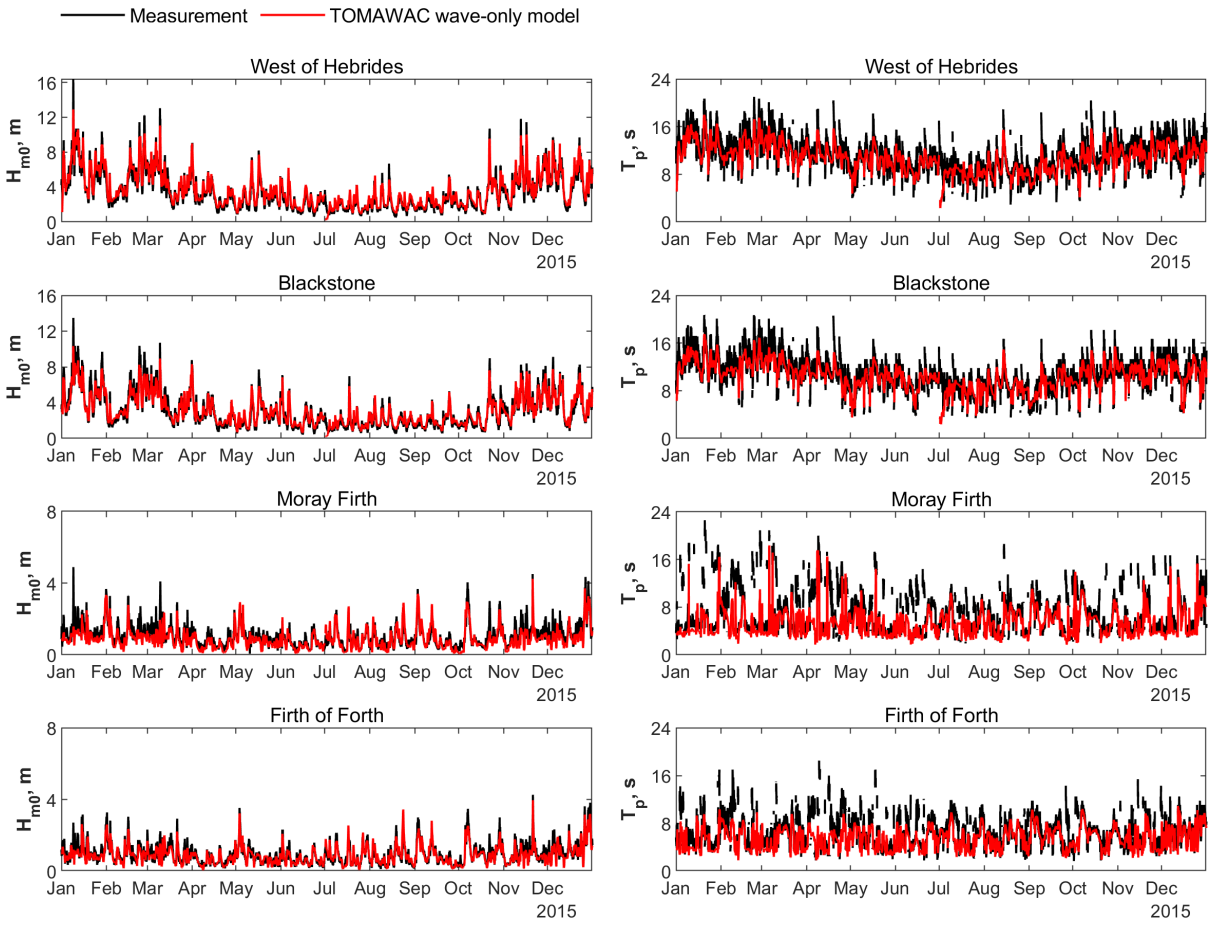

Figure B.2 Hindcast H_{m0} and T_p by wave-only model in 2015

Table B.2 Metrics of the North Atlantic scale wave model in 2015

Location	Parameter	Mean		Bias	Normalized Bias	RMSE	SI	R
		Model	Real					
West of Hebrides	H_{m0}, m	3.41	3.66	-0.25	-0.07	0.47	0.13	0.98
	T_p, s	11.26	10.77	0.49	0.05	1.45	0.14	0.87
Blackstone	H_{m0}, m	3.03	3.08	-0.05	-0.02	0.44	0.14	0.98
	T_p, s	10.93	10.50	0.43	0.04	1.51	0.14	0.87
Moray Firth	H_{m0}, m	1.04	0.91	0.13	0.14	0.31	0.34	0.89
	T_p, s	6.94	5.39	1.54	0.29	3.34	0.62	0.51
Forth of Firth	H_{m0}, m	0.94	0.90	0.04	0.05	0.21	0.23	0.93
	T_p, s	6.94	5.39	1.54	0.29	3.34	0.62	0.51

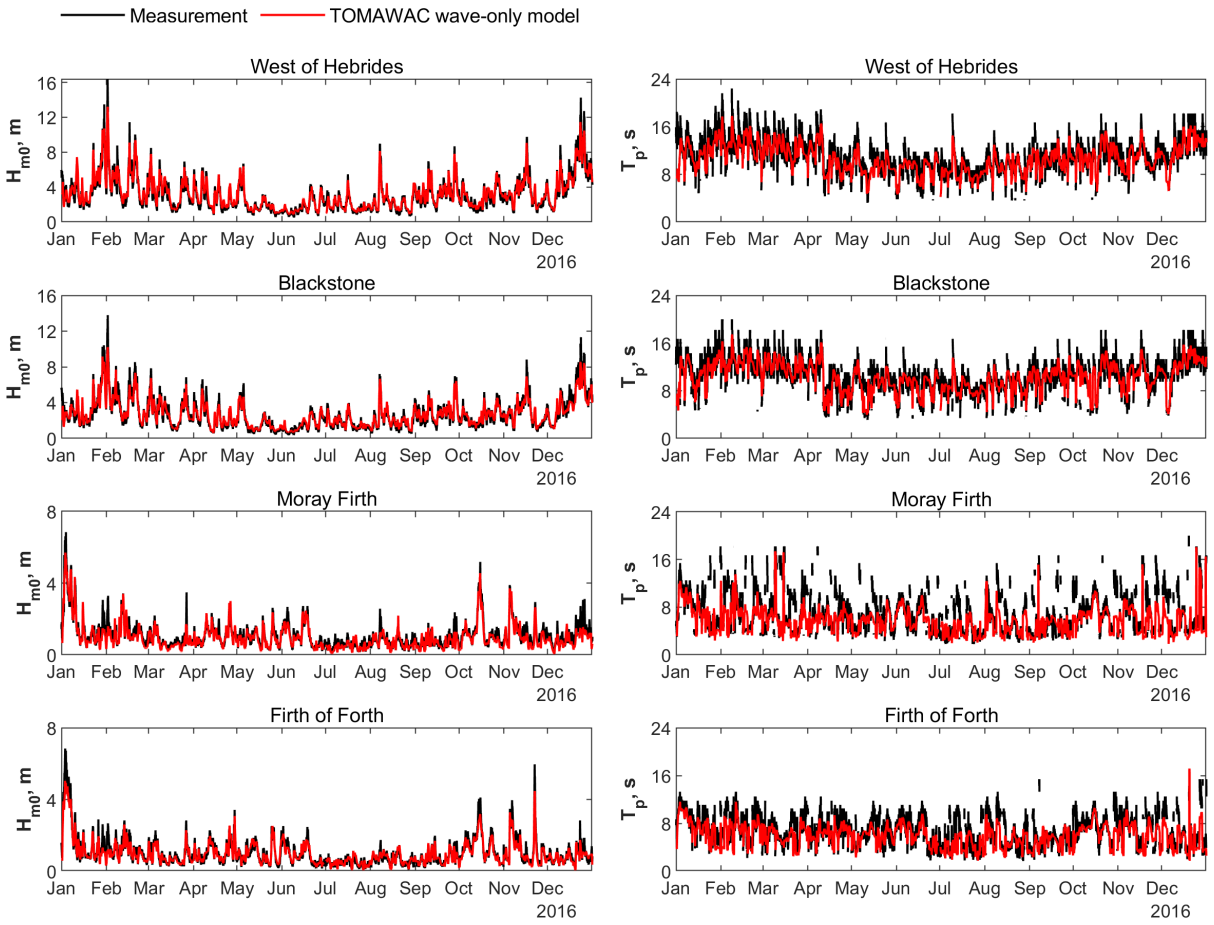

Figure B.3 Hindcast H_{m0} and T_p by wave-only model in 2016

Table B.3 Metrics of the North Atlantic scale wave model in 2016

Location	Parameter	Mean		Bias	Normalized Bias	RMSE	SI	R
		Model	Real					
West of Hebrides	H_{m0}, m	3.06	3.19	-0.14	-0.04	0.43	0.13	0.98
	T_p, s	11.09	10.64	0.46	0.04	1.35	0.13	0.88
Blackstone	H_{m0}, m	2.63	2.68	-0.05	-0.02	0.43	0.16	0.97
	T_p, s	10.67	10.36	0.31	0.03	1.43	0.14	0.86
Moray Firth	H_{m0}, m	1.07	0.96	0.10	0.11	0.26	0.27	0.95
	T_p, s	7.05	5.75	1.29	0.22	2.94	0.51	0.59
Forth of Firth	H_{m0}, m	1.01	0.98	0.04	0.04	0.23	0.24	0.96
	T_p, s	7.05	5.75	1.29	0.22	2.94	0.51	0.59

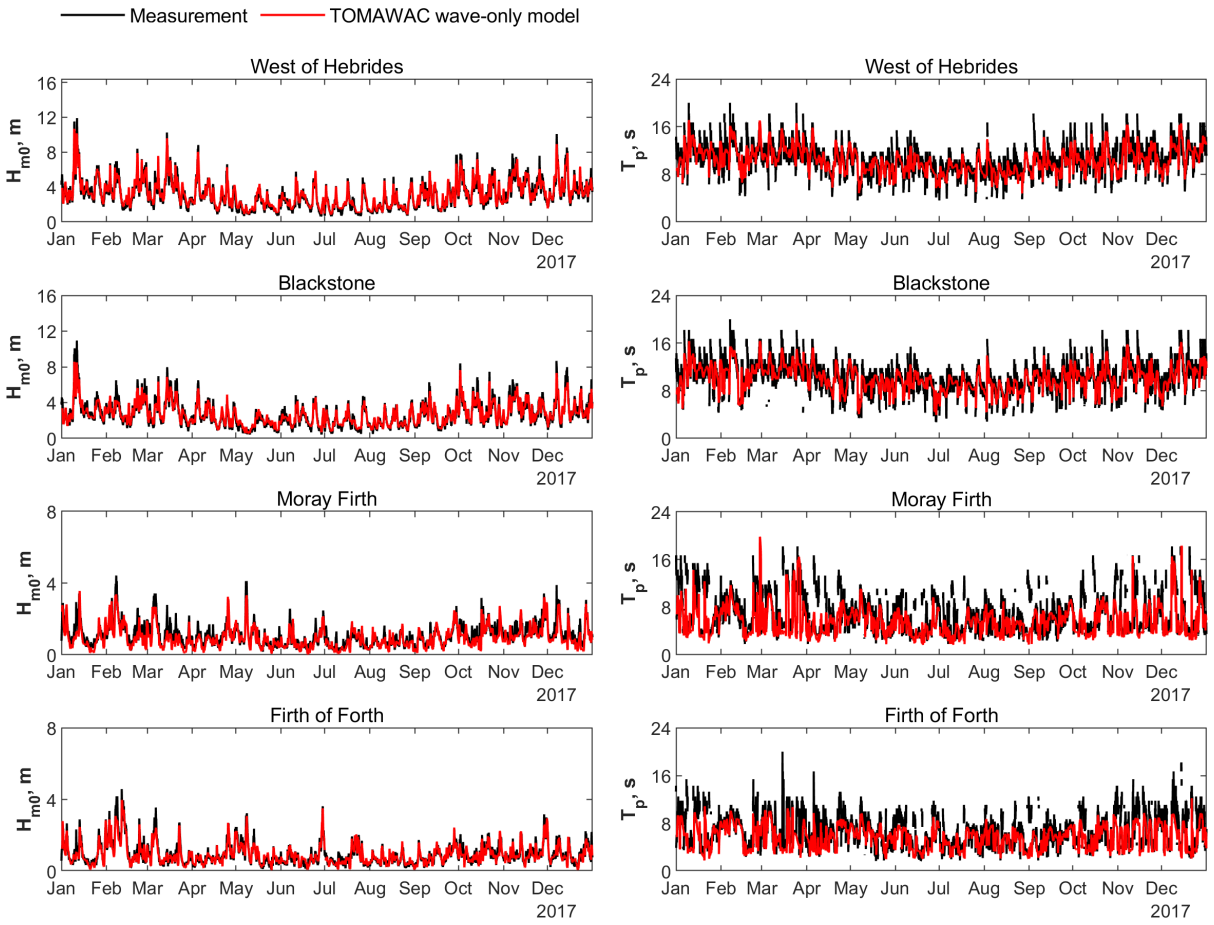

Figure B.4 Hindcast H_{m0} and T_p by wave-only model in 2017

Table B.4 Metrics of the North Atlantic scale wave model in 2017

Location	Parameter	Mean		Bias	Normalized Bias	RMSE	SI	R
		Model	Real					
West of Hebrides	H_{m0}, m	3.08	3.21	-0.13	-0.04	0.36	0.11	0.98
	T_p, s	10.67	10.38	0.30	0.03	1.28	0.12	0.85
Blackstone	H_{m0}, m	2.67	2.71	-0.04	-0.02	0.37	0.14	0.97
	T_p, s	10.37	10.14	0.23	0.02	1.31	0.13	0.87
Moray Firth	H_{m0}, m	1.07	0.96	0.11	0.12	0.28	0.29	0.91
	T_p, s	6.90	5.69	1.21	0.21	2.93	0.51	0.59
Forth of Firth	H_{m0}, m	0.94	0.93	0.01	0.01	0.18	0.20	0.95
	T_p, s	6.90	5.69	1.21	0.21	2.93	0.51	0.59

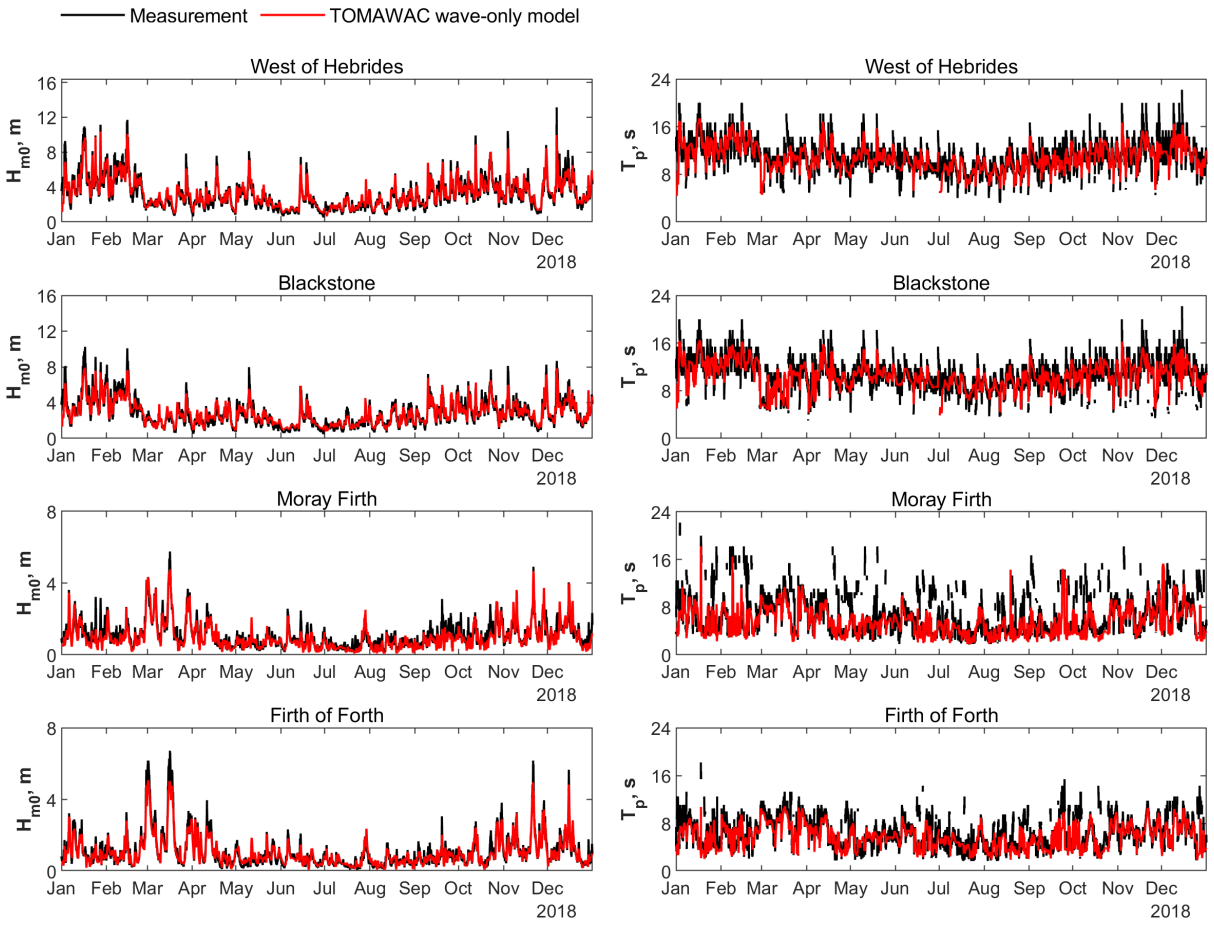

Figure B.5 Hindcast H_{m0} and T_p by wave-only model in 2018

Table B.5 Metrics of the North Atlantic scale wave model in 2018

Location	Parameter	Mean		Bias	Normalized Bias	RMSE	SI	R
		Model	Real					
West of Hebrides	H_{m0}, m	3.16	3.26	-0.10	-0.03	0.40	0.12	0.97
	T_p, s	11.12	10.83	0.30	0.03	1.30	0.12	0.86
Blackstone	H_{m0}, m	2.76	2.79	-0.03	-0.01	0.41	0.15	0.96
	T_p, s	10.83	10.56	0.27	0.03	1.44	0.14	0.84
Moray Firth	H_{m0}, m	1.08	0.99	0.09	0.09	0.26	0.27	0.94
	T_p, s	6.85	5.60	1.25	0.22	3.11	0.55	0.51
Forth of Firth	H_{m0}, m	1.08	1.05	0.03	0.03	0.23	0.22	0.97
	T_p, s	6.85	5.60	1.25	0.22	3.11	0.55	0.51

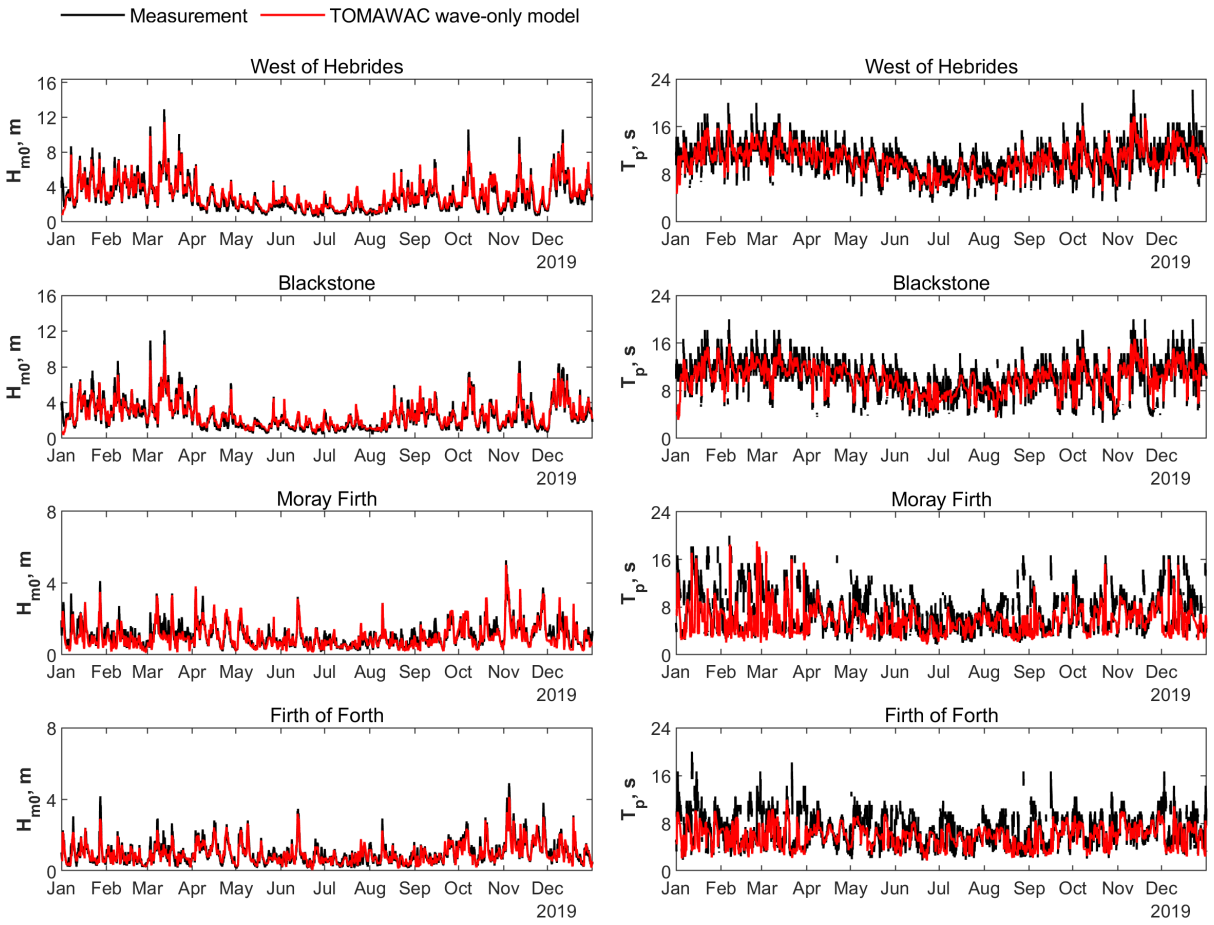

Figure B.6 Hindcast H_{m0} and T_p by wave-only model in 2019

Table B.6 Metrics of the North Atlantic scale wave model in 2019

Location	Parameter	Mean		Bias	Normalized Bias	RMSE	SI	R
		Model	Real					
West of Hebrides	H_{m0}, m	2.90	3.11	-0.21	-0.07	0.43	0.14	0.97
	T_p, s	10.81	10.51	0.29	0.03	1.29	0.12	0.87
Blackstone	H_{m0}, m	2.52	2.62	-0.10	-0.04	0.40	0.15	0.97
	T_p, s	10.44	10.21	0.24	0.02	1.51	0.15	0.85
Moray Firth	H_{m0}, m	1.08	1.01	0.07	0.07	0.26	0.25	0.93
	T_p, s	7.15	5.83	1.32	0.23	3.11	0.53	0.53
Forth of Firth	H_{m0}, m	0.99	0.98	0.01	0.01	0.19	0.19	0.95
	T_p, s	7.15	5.83	1.32	0.23	3.11	0.53	0.53

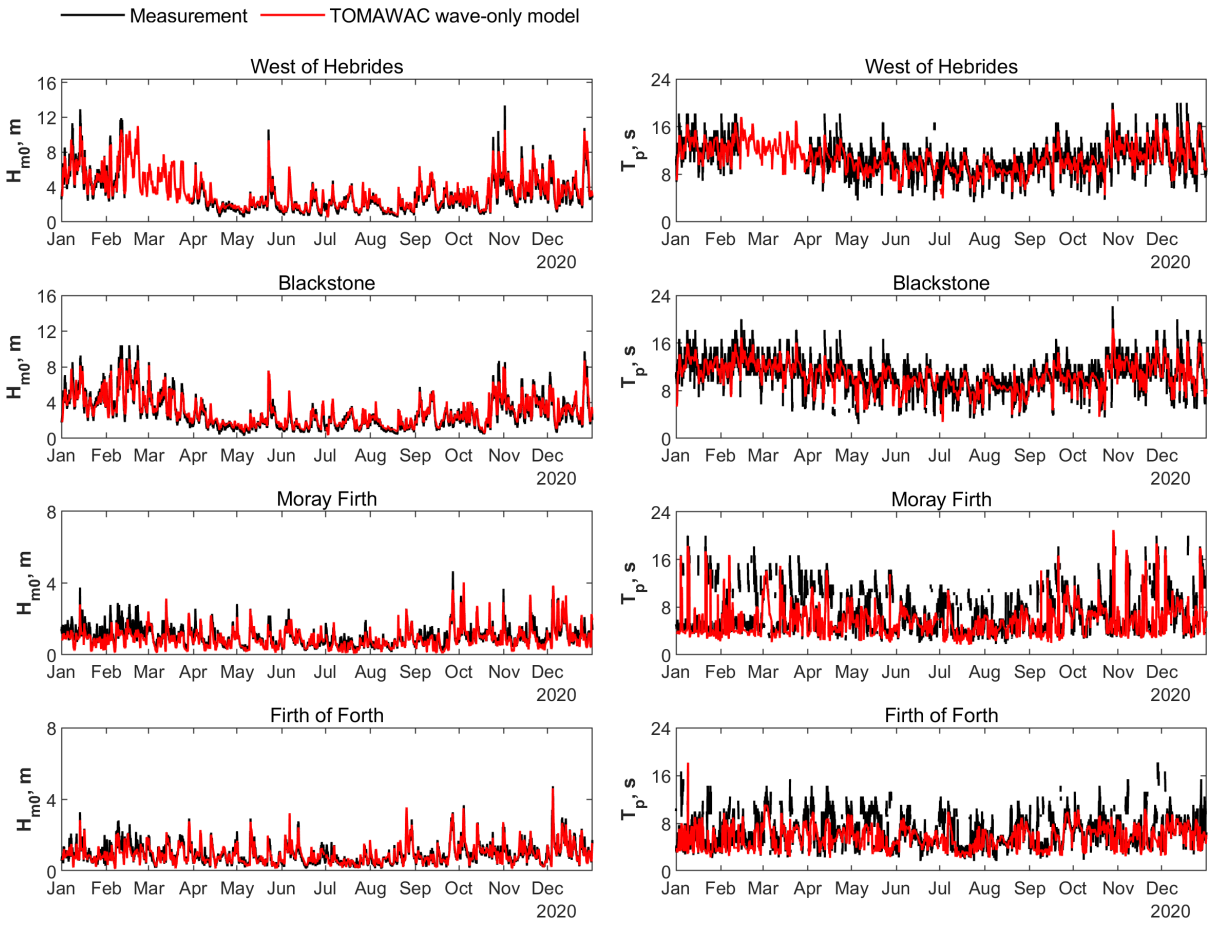

Figure B.7 Hindcast H_{m0} and T_p by wave-only model in 2020

Table B.7 Metrics of the North Atlantic scale wave model in 2020

Location	Parameter	Mean		Bias	Normalized Bias	RMSE	SI	R
		Model	Real					
West of Hebrides	H_{m0}, m	3.02	3.28	-0.26	-0.08	0.46	0.14	0.98
	T_p, s	10.80	10.52	0.28	0.03	1.36	0.13	0.85
Blackstone	H_{m0}, m	2.83	2.98	-0.15	-0.05	0.43	0.14	0.98
	T_p, s	10.79	10.53	0.26	0.03	1.38	0.13	0.86
Moray Firth	H_{m0}, m	1.02	0.91	0.11	0.12	0.28	0.31	0.89
	T_p, s	7.00	5.74	1.26	0.22	3.10	0.54	0.61
Forth of Firth	H_{m0}, m	0.96	0.96	0.00	0.00	0.20	0.21	0.93
	T_p, s	7.00	5.74	1.26	0.22	3.10	0.54	0.61

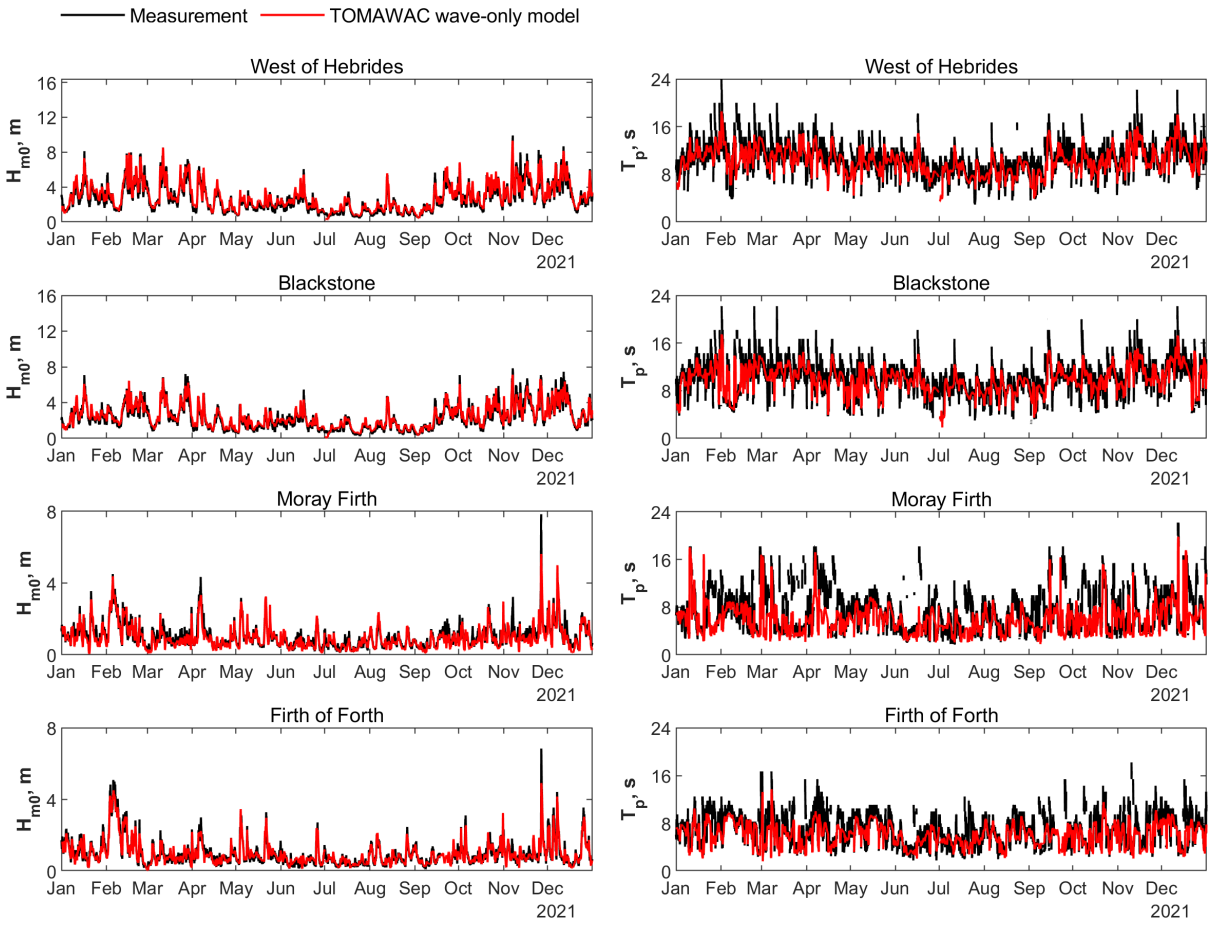

Figure B.8 Hindcast H_{m0} and T_p by wave-only model in 2021

Table B.8 Metrics of the North Atlantic scale wave model in 2021

Location	Parameter	Mean		Bias	Normalized Bias	RMSE	SI	R
		Model	Real					
West of Hebrides	H_{m0}, m	2.66	2.89	-0.23	-0.08	0.41	0.14	0.98
	T_p, s	10.82	10.32	0.50	0.05	1.68	0.16	0.79
Blackstone	H_{m0}, m	2.29	2.44	-0.14	-0.06	0.35	0.14	0.97
	T_p, s	10.35	9.96	0.39	0.04	1.69	0.17	0.79
Moray Firth	H_{m0}, m	1.03	0.96	0.07	0.07	0.24	0.25	0.94
	T_p, s	7.44	5.95	1.49	0.25	3.36	0.56	0.52
Forth of Firth	H_{m0}, m	0.99	0.99	0.00	0.00	0.19	0.19	0.97
	T_p, s	7.44	5.95	1.49	0.25	3.36	0.56	0.52

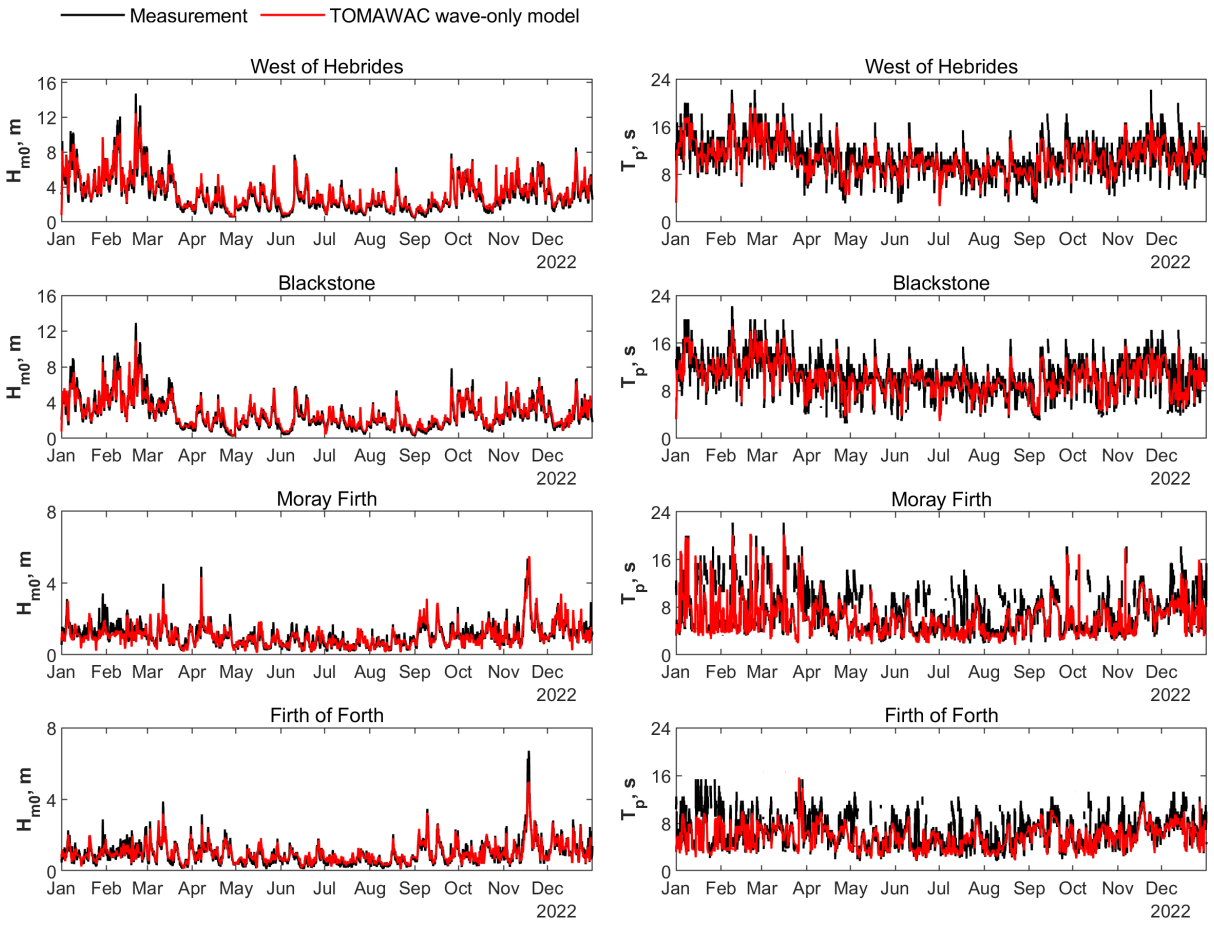

Figure B.9 Hindcast H_{m0} and T_p by wave-only model in 2022

Table B.9 Metrics of the North Atlantic scale wave model in 2022

Location	Parameter	Mean		Bias	Normalized Bias	RMSE	SI	R
		Model	Real					
West of Hebrides	H_{m0}, m	3.09	3.33	-0.24	-0.07	0.44	0.13	0.98
	T_p, s	10.97	10.65	0.33	0.03	1.39	0.13	0.87
Blackstone	H_{m0}, m	2.68	2.77	-0.09	-0.03	0.42	0.15	0.97
	T_p, s	10.56	10.30	0.25	0.02	1.52	0.15	0.86
Moray Firth	H_{m0}, m	1.08	0.99	0.09	0.09	0.25	0.25	0.93
	T_p, s	7.12	5.82	1.29	0.22	3.14	0.54	0.60
Forth of Firth	H_{m0}, m	0.98	0.98	0.00	0.00	0.19	0.19	0.96
	T_p, s	7.12	5.82	1.29	0.22	3.14	0.54	0.60

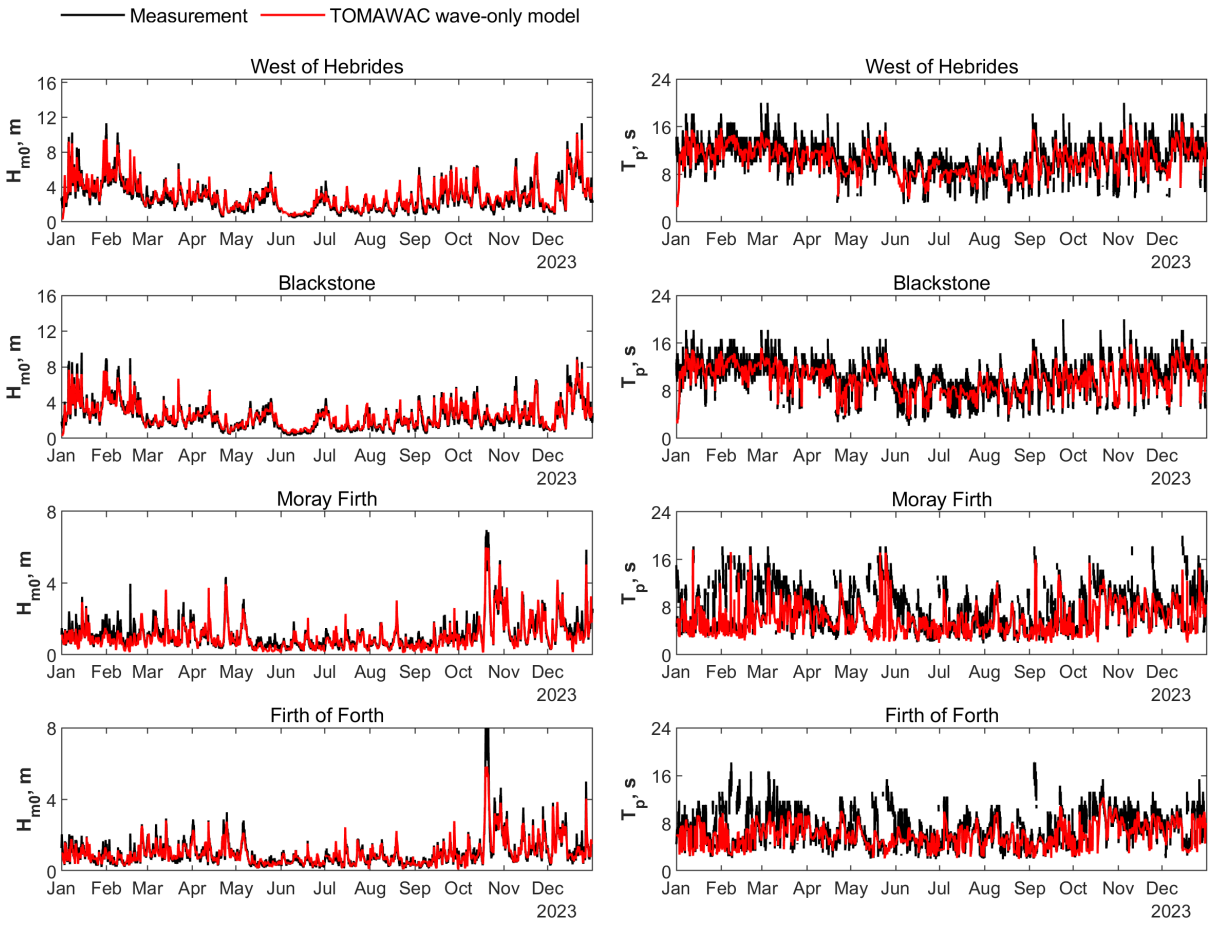

Figure B.10 Hindcast H_{m0} and T_p by wave-only model in 2023

Table B.10 Metrics of the North Atlantic scale wave model in 2023

Location	Parameter	Mean		Bias	Normalized Bias	RMSE	SI	R
		Model	Real					
West of Hebrides	H_{m0}, m	2.80	3.03	-0.23	-0.08	0.43	0.14	0.97
	T_p, s	11.31	10.95	0.36	0.03	1.34	0.12	0.84
Blackstone	H_{m0}, m	2.50	2.56	-0.06	-0.02	0.35	0.14	0.98
	T_p, s	10.87	10.60	0.27	0.03	1.40	0.13	0.86
Moray Firth	H_{m0}, m	0.99	0.89	0.10	0.11	0.27	0.30	0.91
	T_p, s	7.76	6.01	1.75	0.29	3.61	0.60	0.53
Forth of Firth	H_{m0}, m	0.88	0.88	0.00	0.00	0.18	0.20	0.94
	T_p, s	7.76	6.01	1.75	0.29	3.61	0.60	0.53

B.2 Ten years wave maps

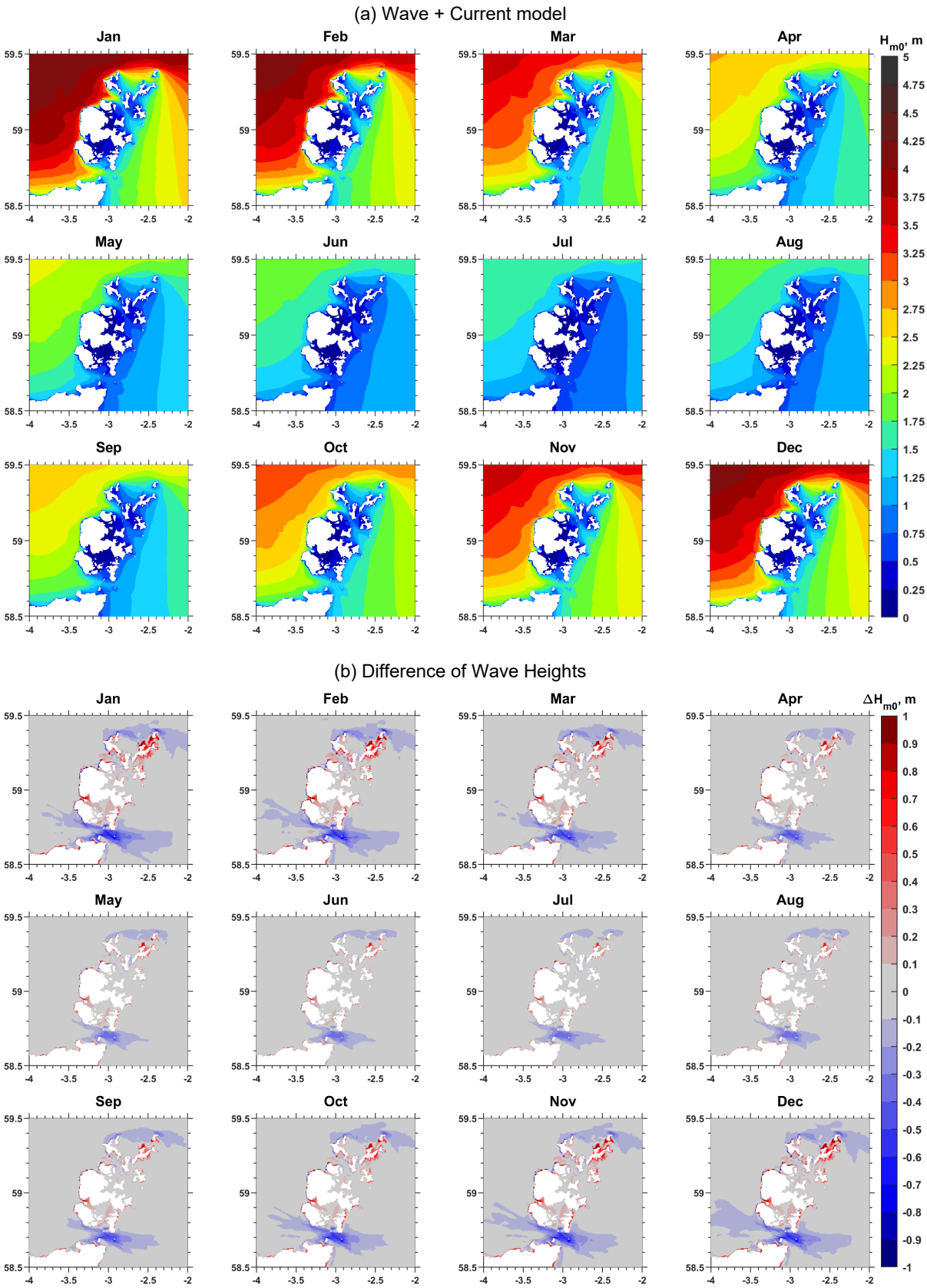

Figure B.11 Monthly mean wave power over 10 years

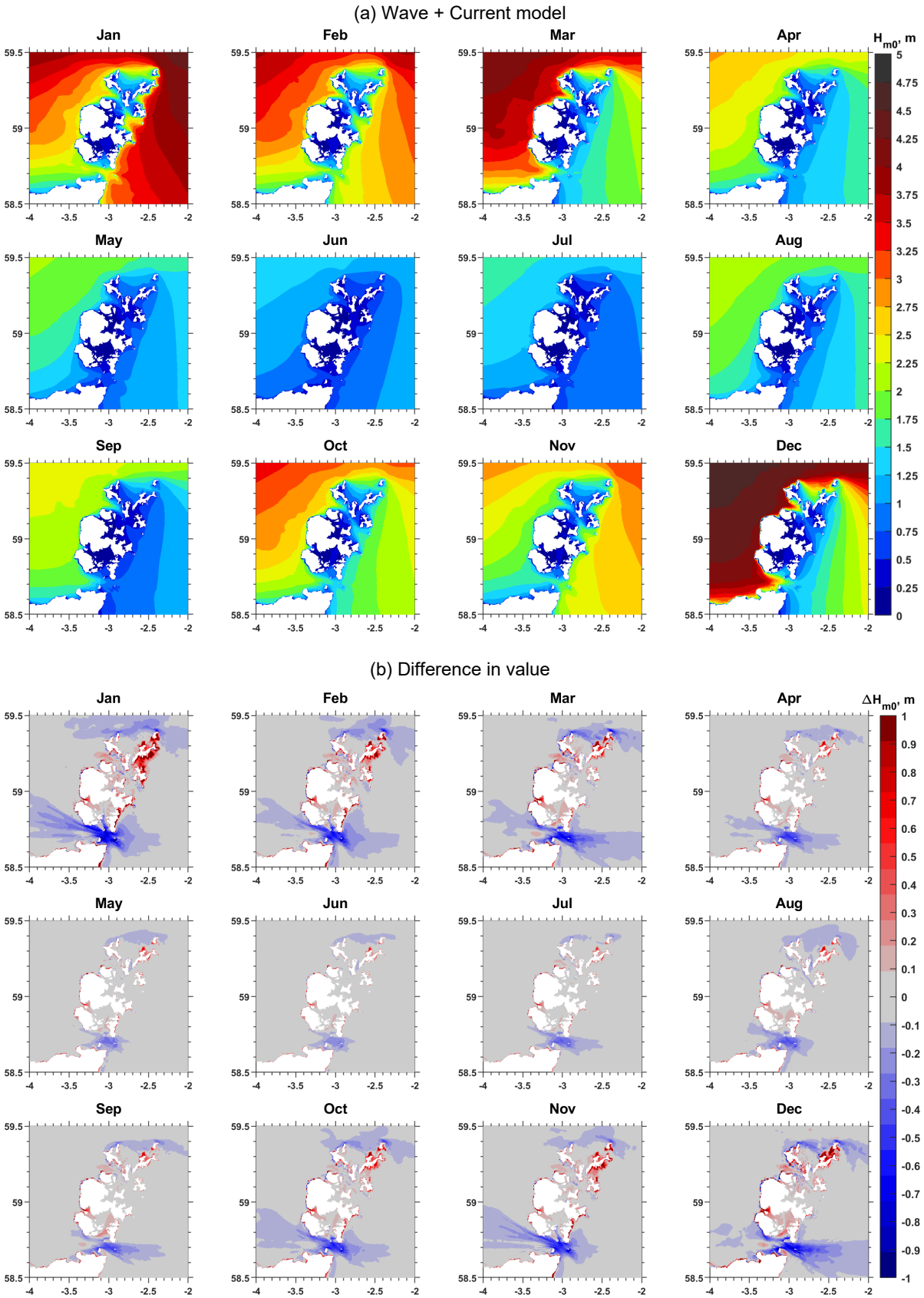

Figure B.12 H_{m0} monthly map in 2014

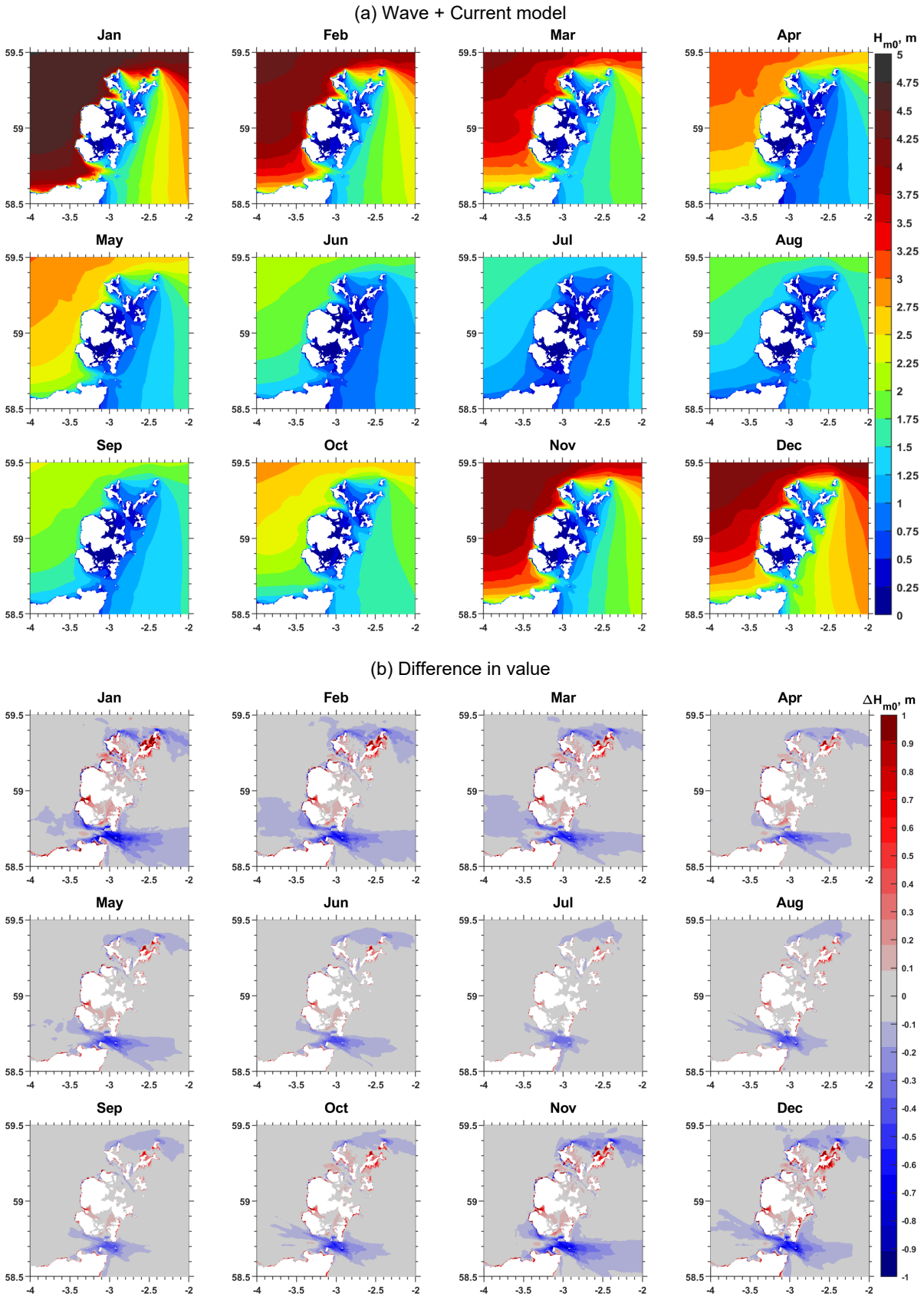

Figure B.13 H_{m0} monthly map in 2015

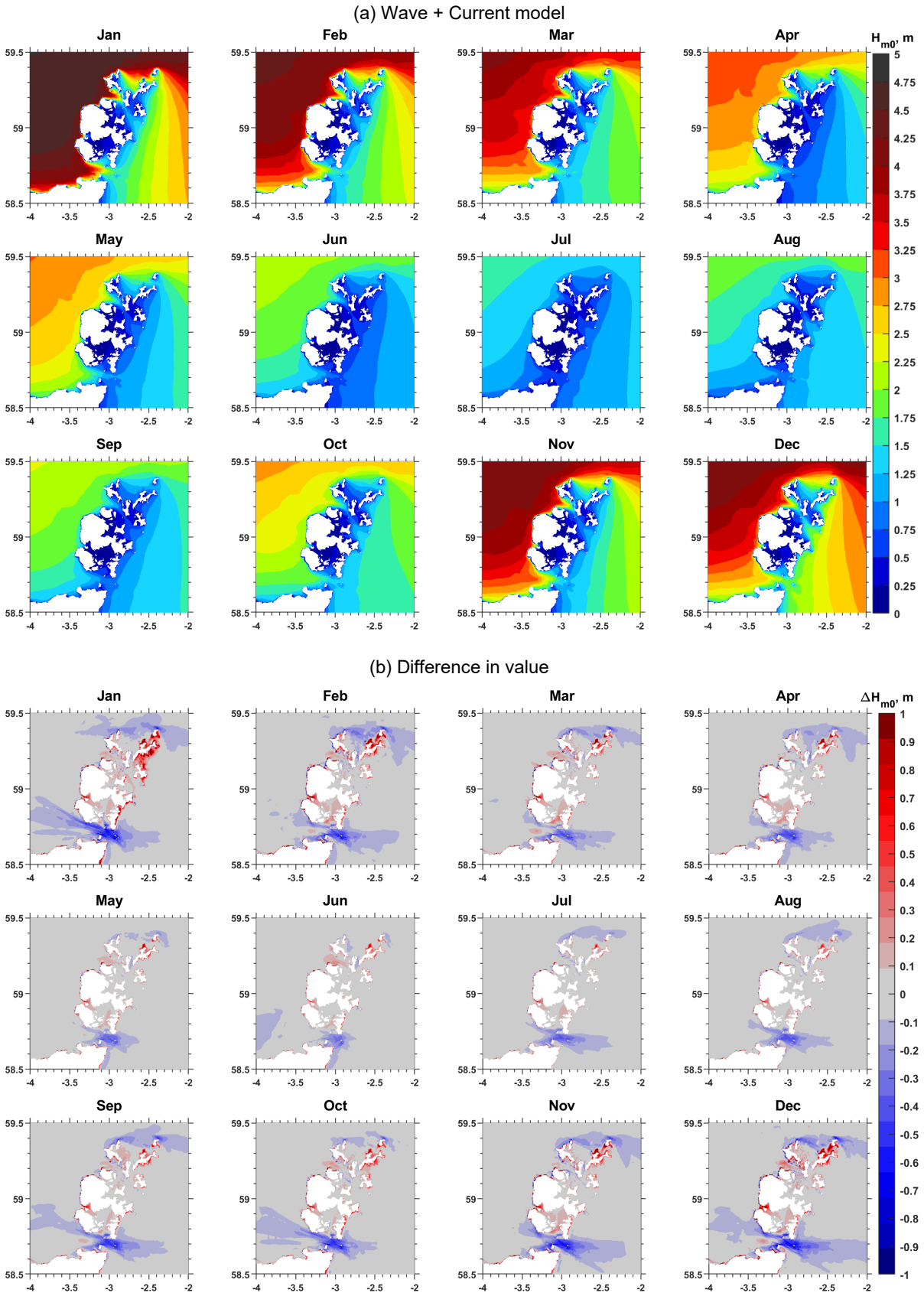

Figure B.14 H_{m0} monthly map in 2016

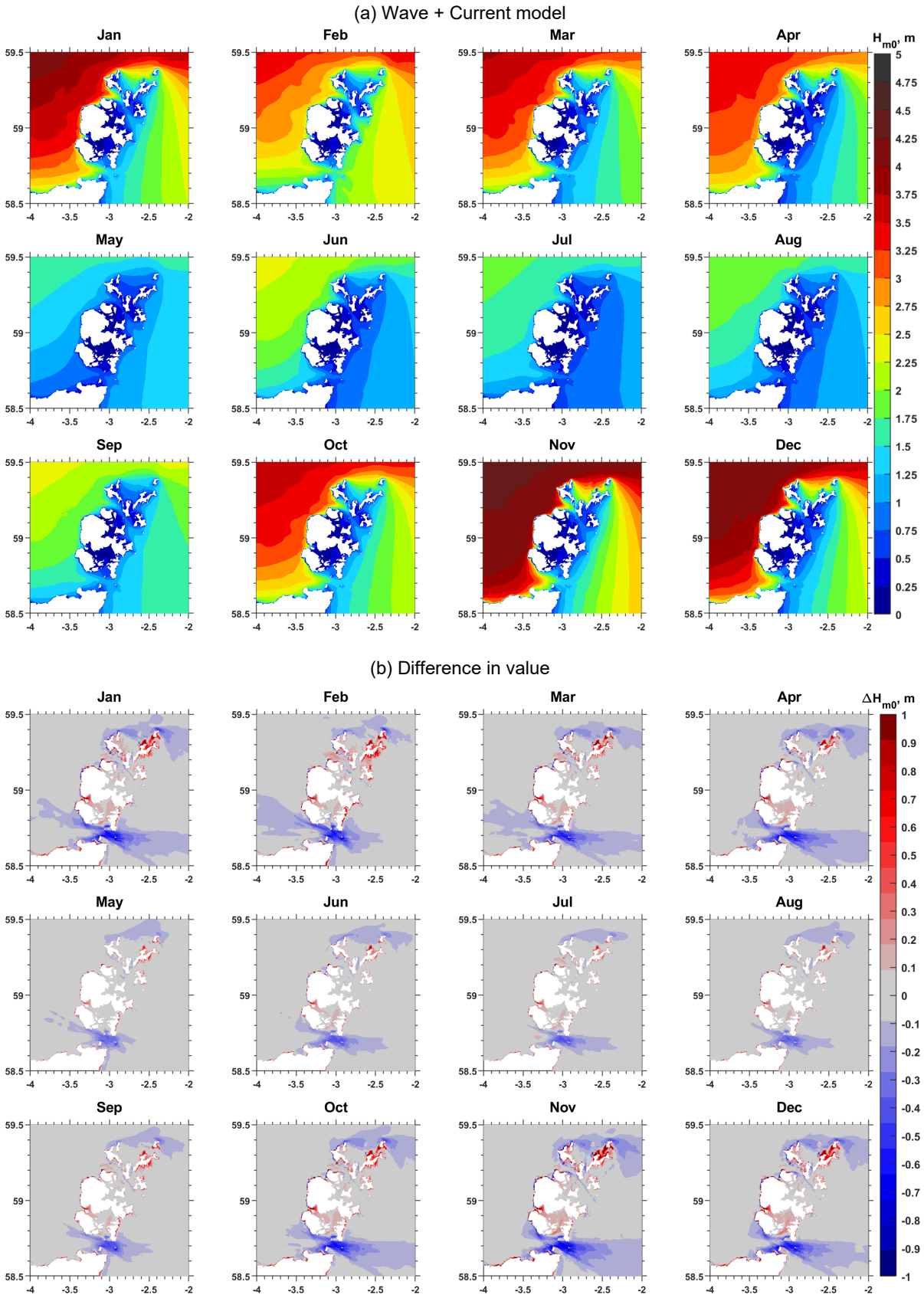

Figure B.15 H_{m0} monthly map in 2017

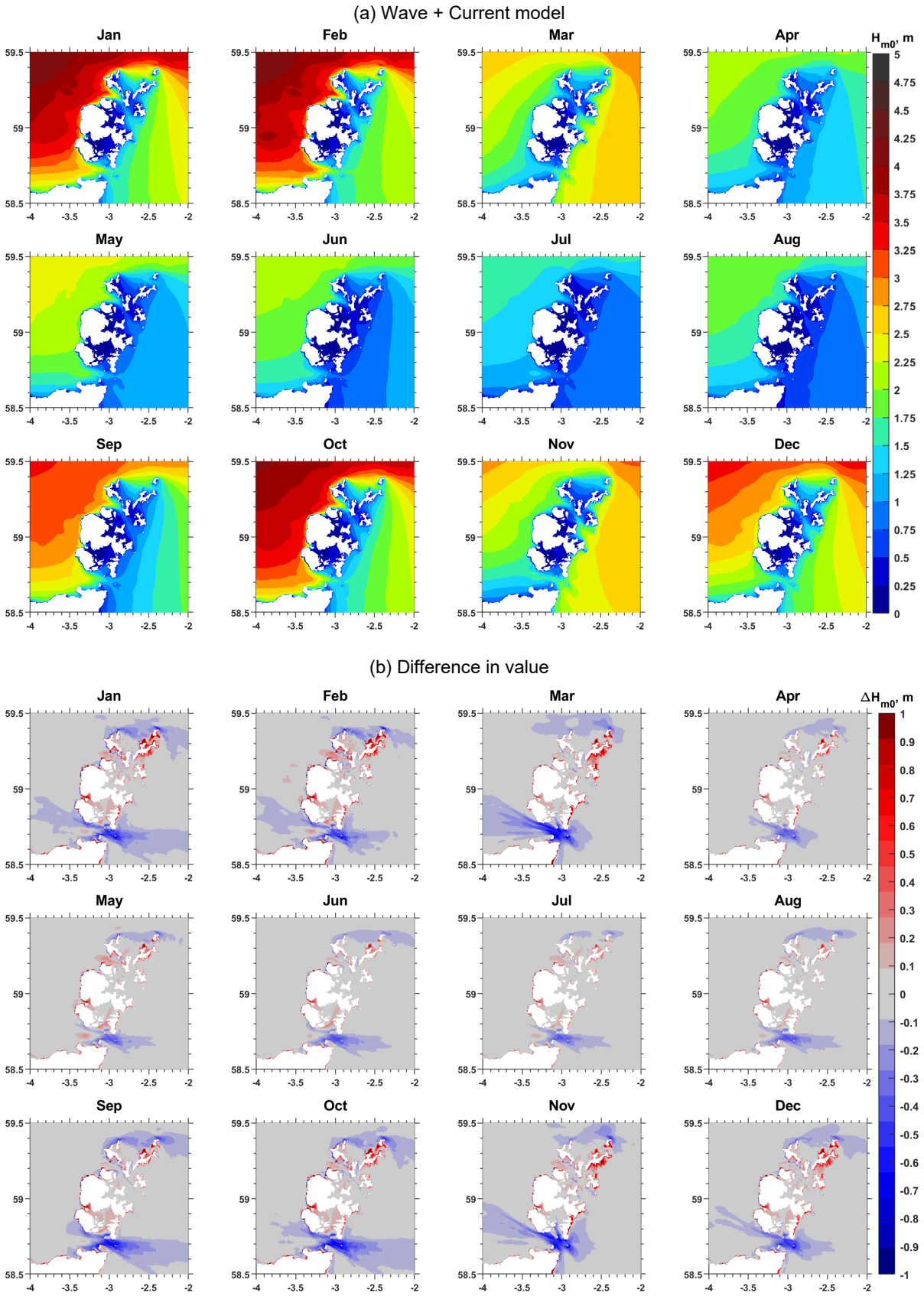

Figure B.16 H_{m0} monthly map in 2018

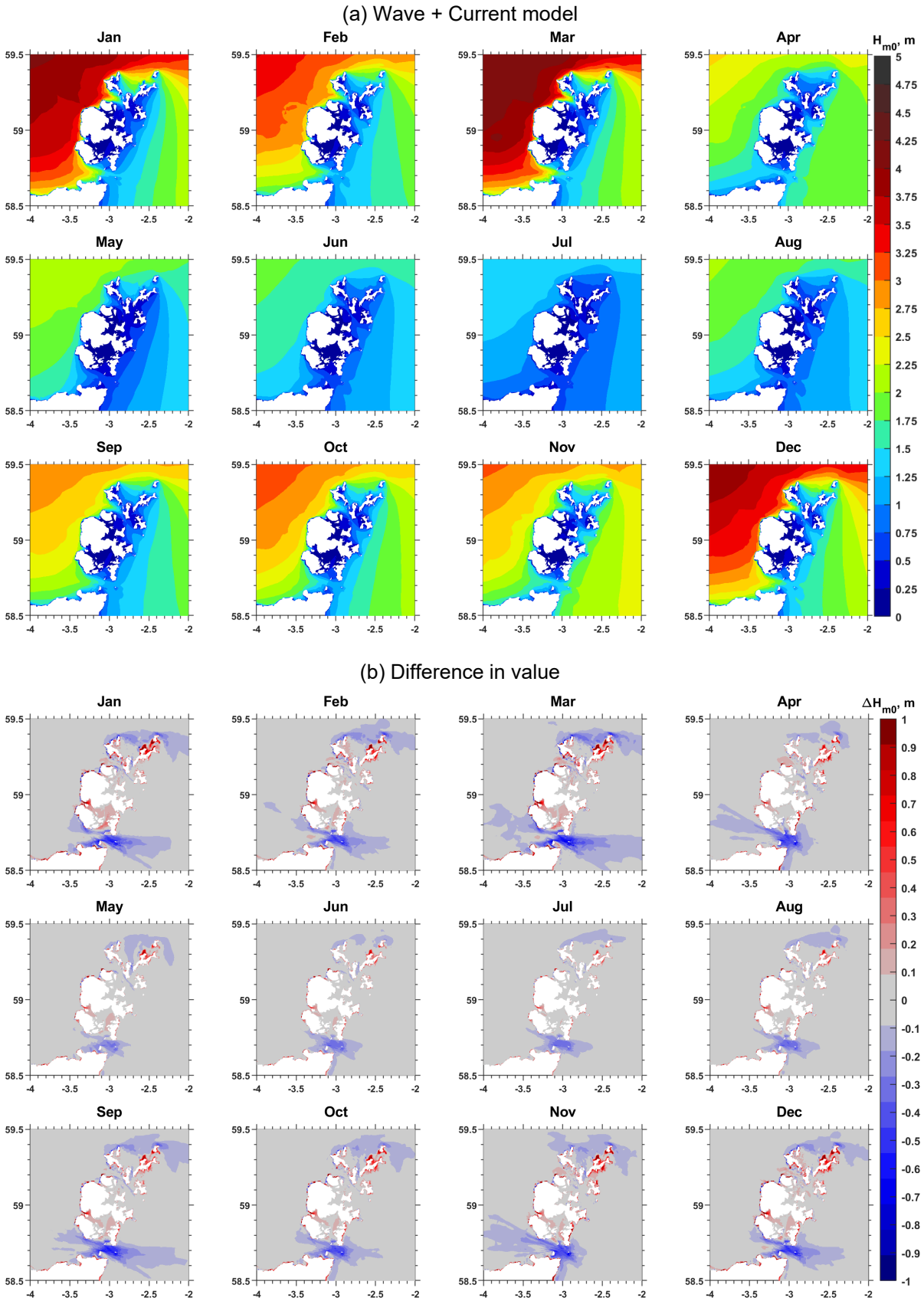

Figure B.17 H_{m0} monthly map in 2019

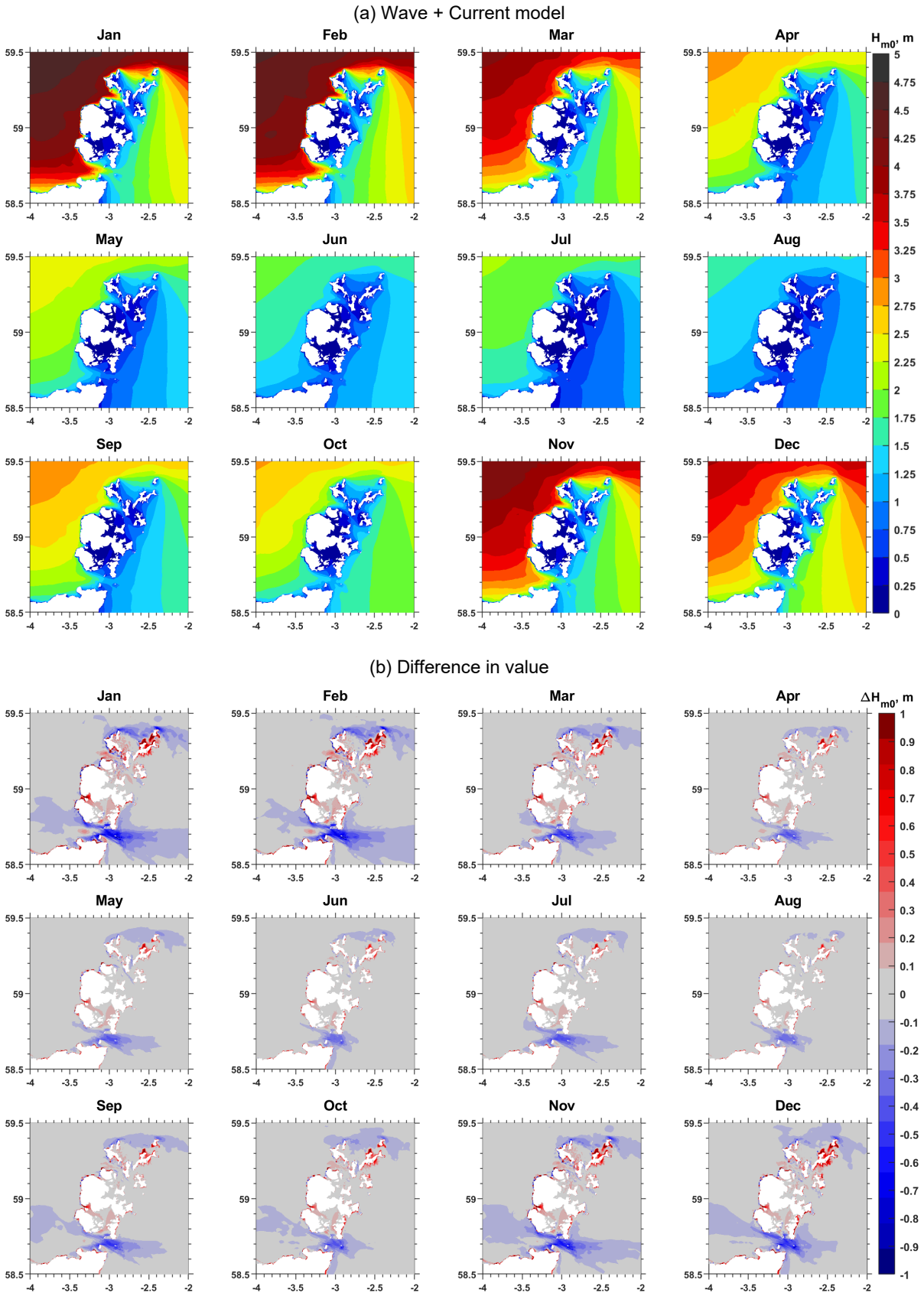

Figure B.18 H_{m0} monthly map in 2020

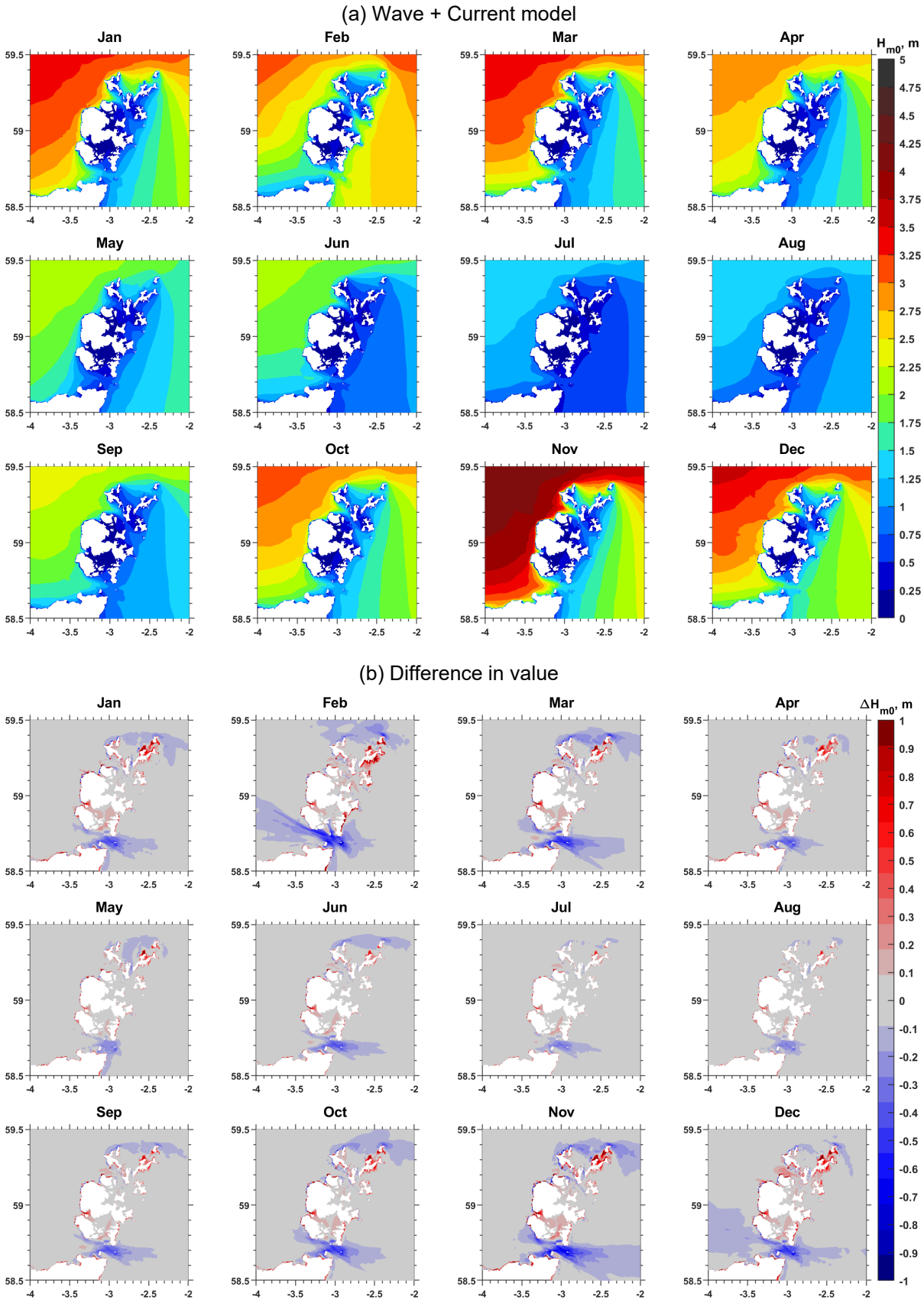

Figure B.19 H_{m0} monthly map in 2021

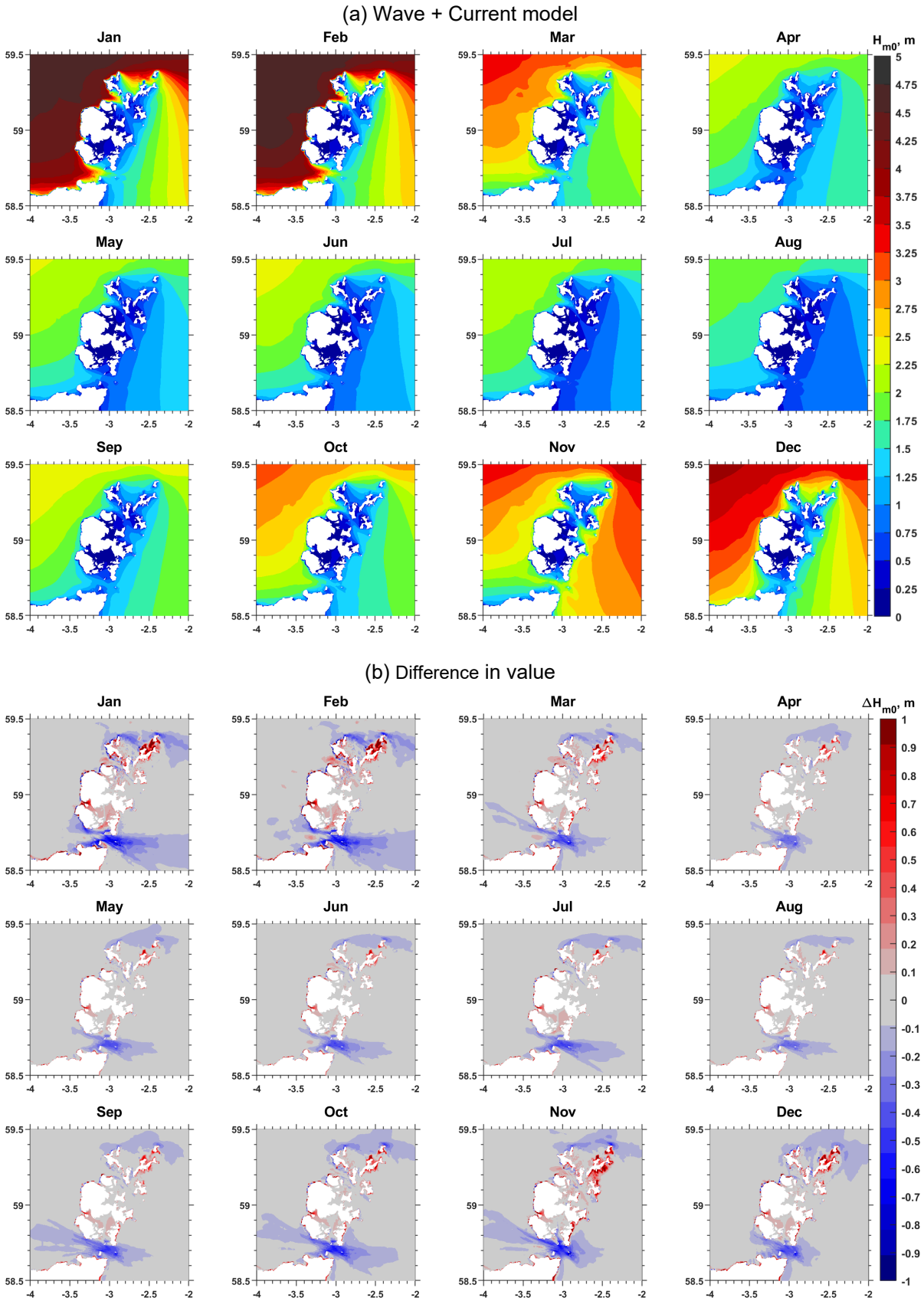

Figure B.20 H_{m0} monthly map in 2022

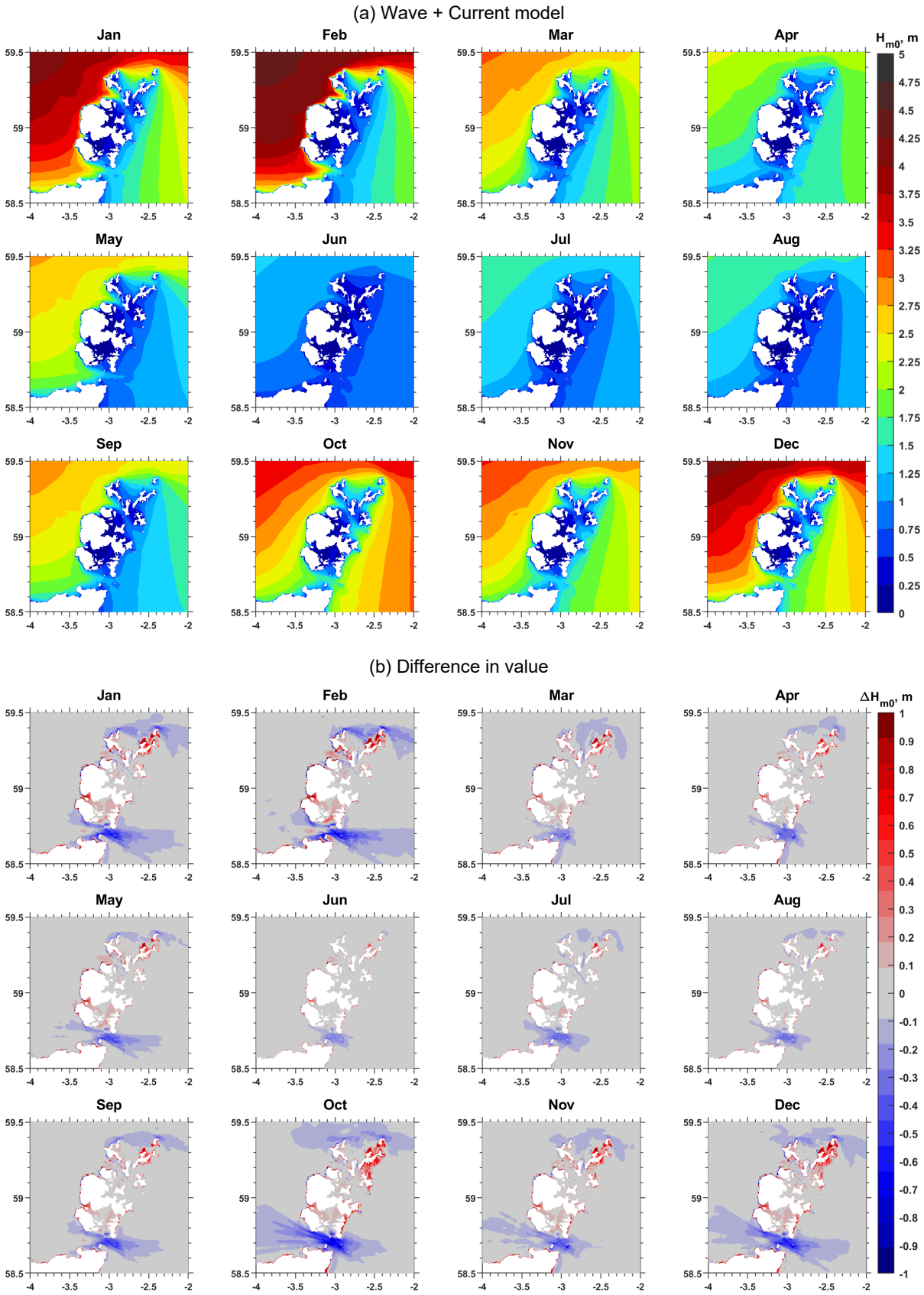

Figure B.21 H_{m0} monthly map in 2023

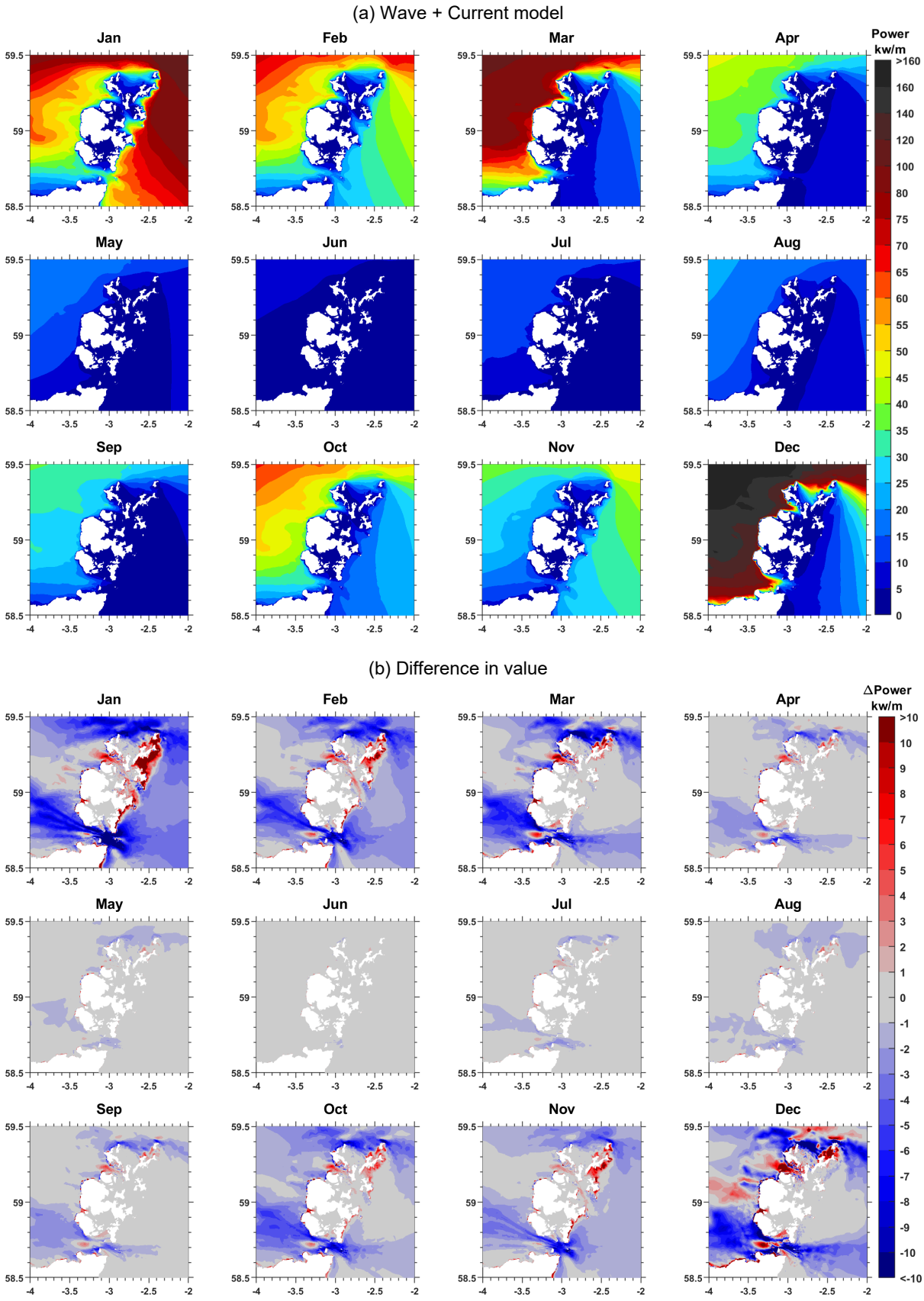

Figure B.22 Wave power monthly map in 2014

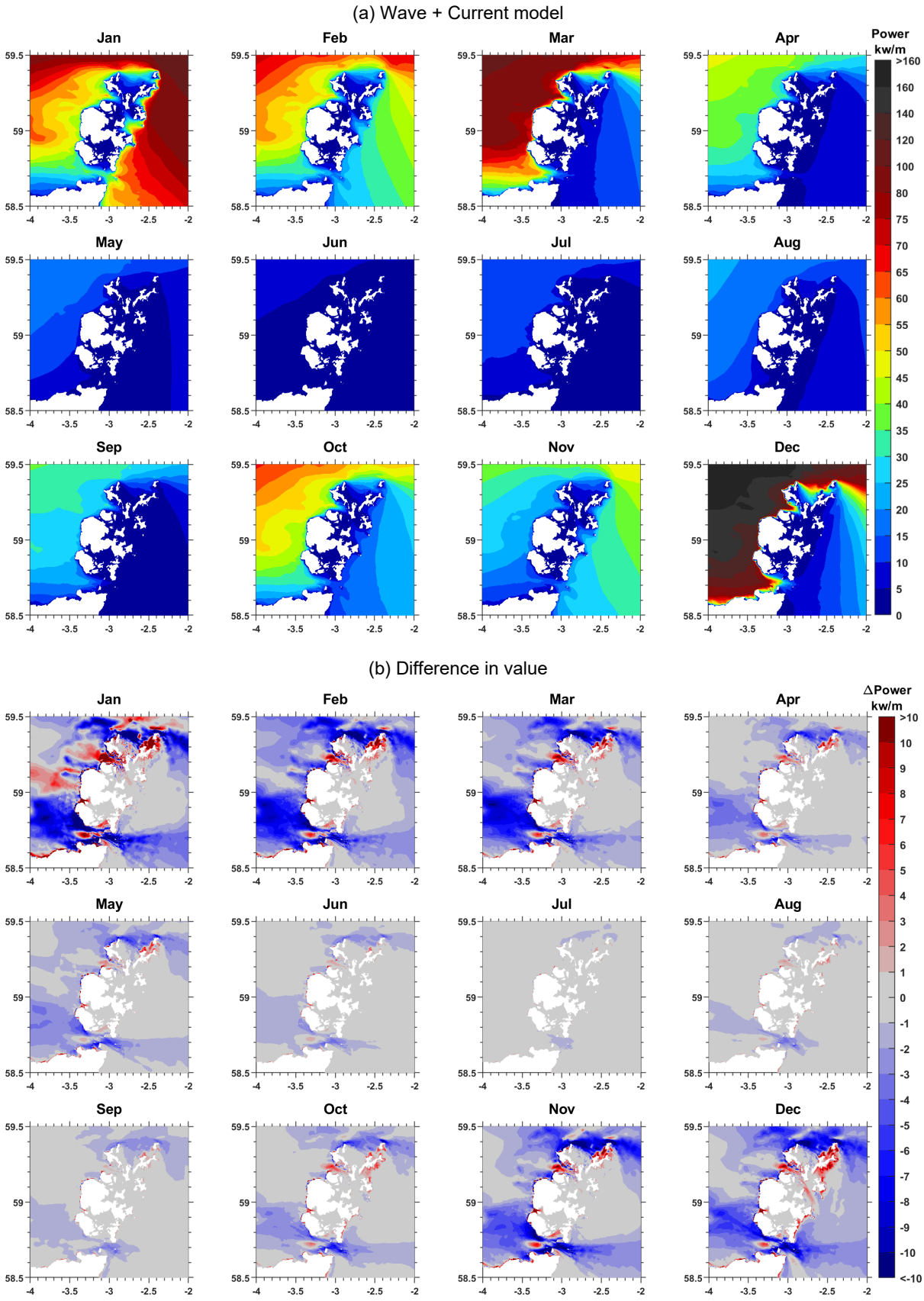

Figure B.23 Wave power monthly map in 2015

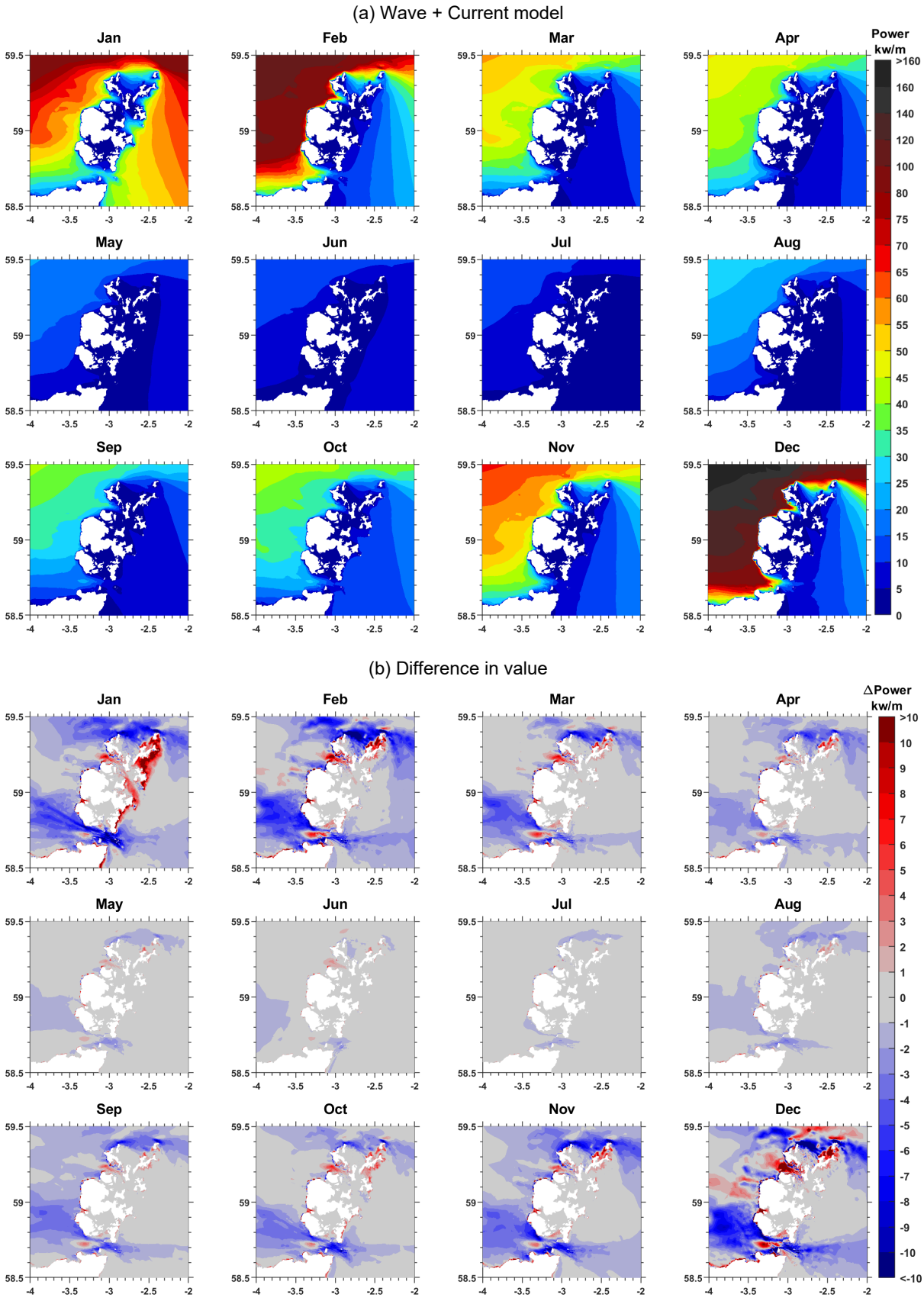

Figure B.24 Wave power monthly map in 2016

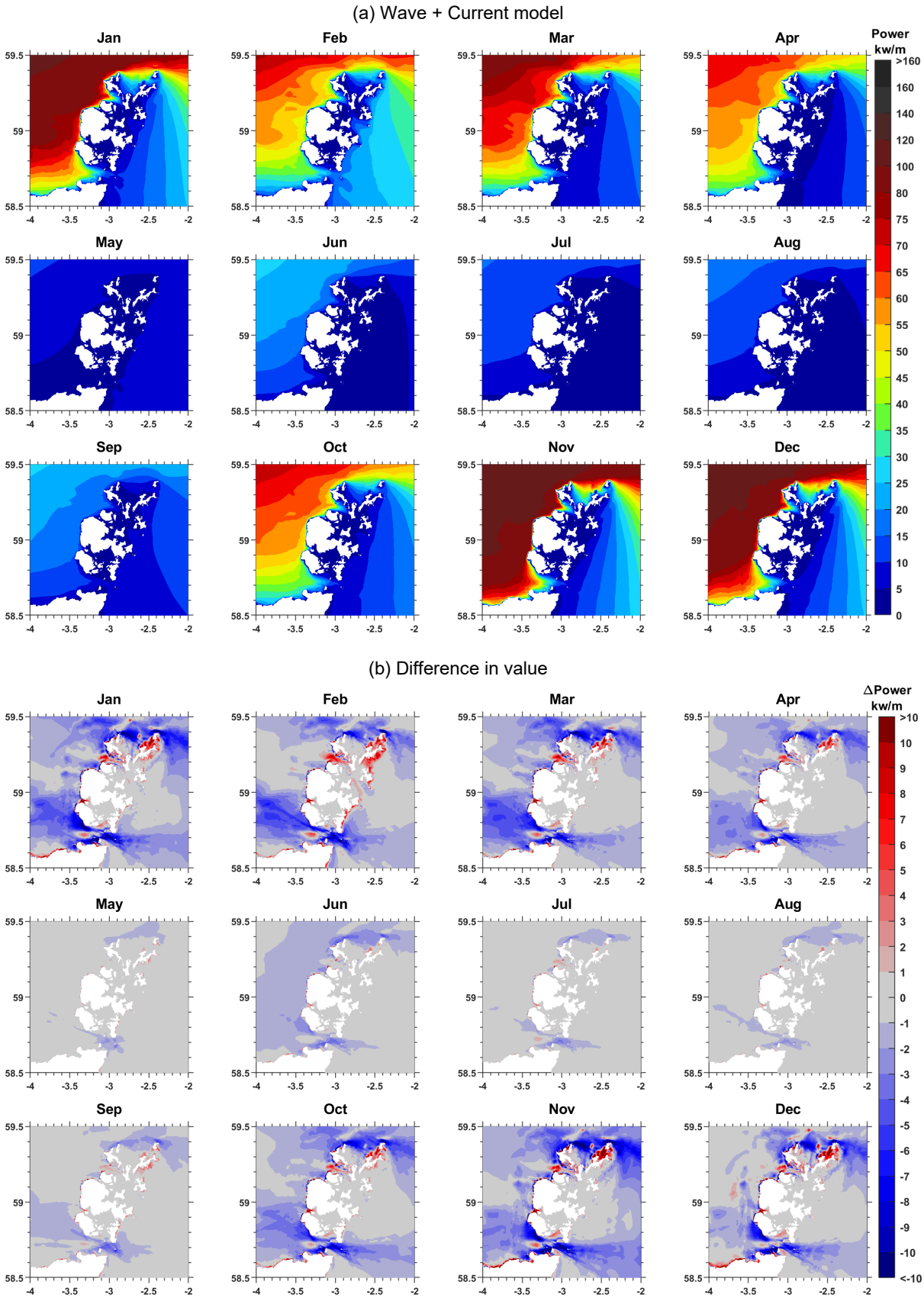

Figure B.25 Wave power monthly map in 2017

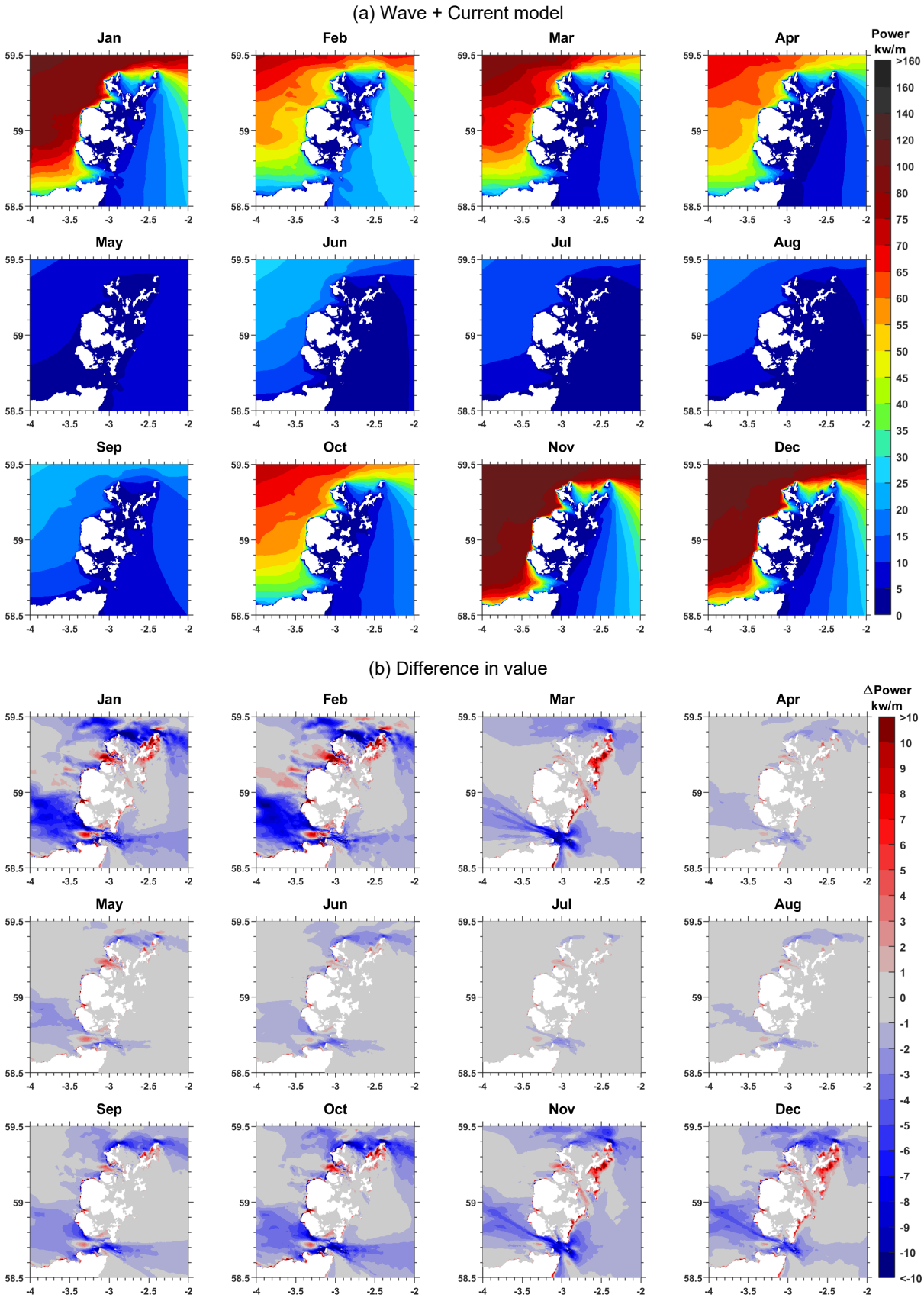

Figure B.26 Wave power monthly map in 2018

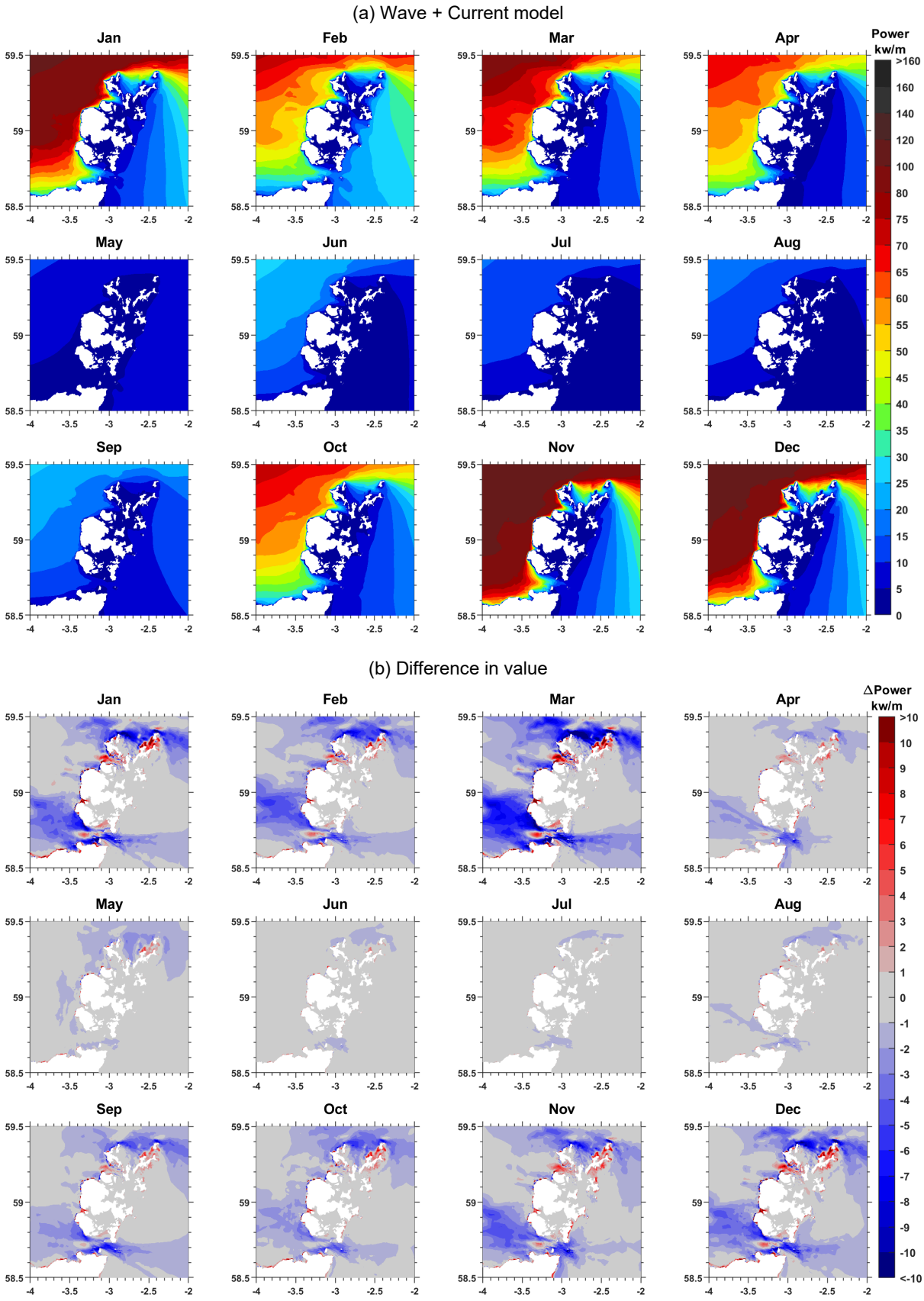

Figure B.27 Wave power monthly map in 2019

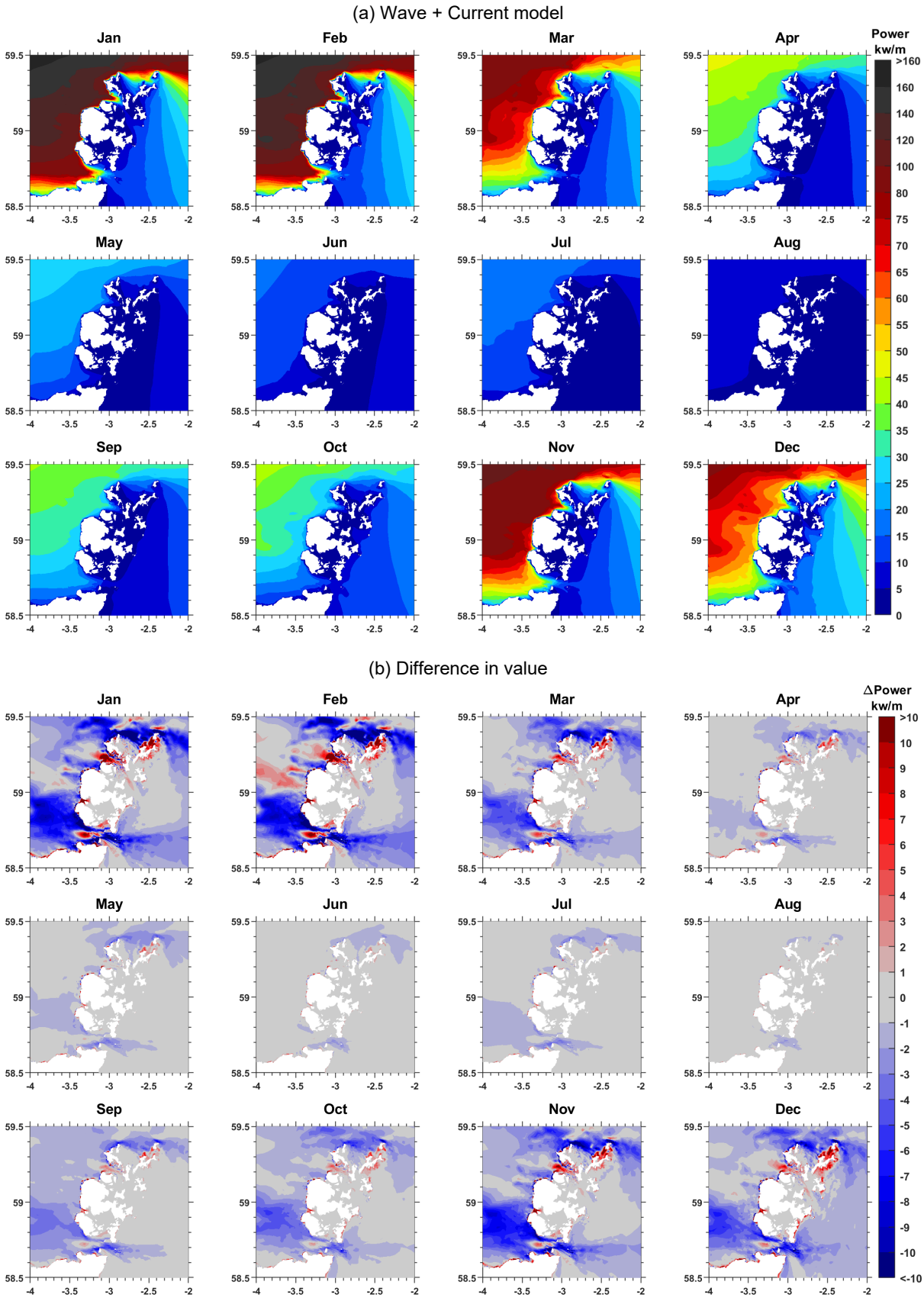

Figure B.28 Wave power monthly map in 2020

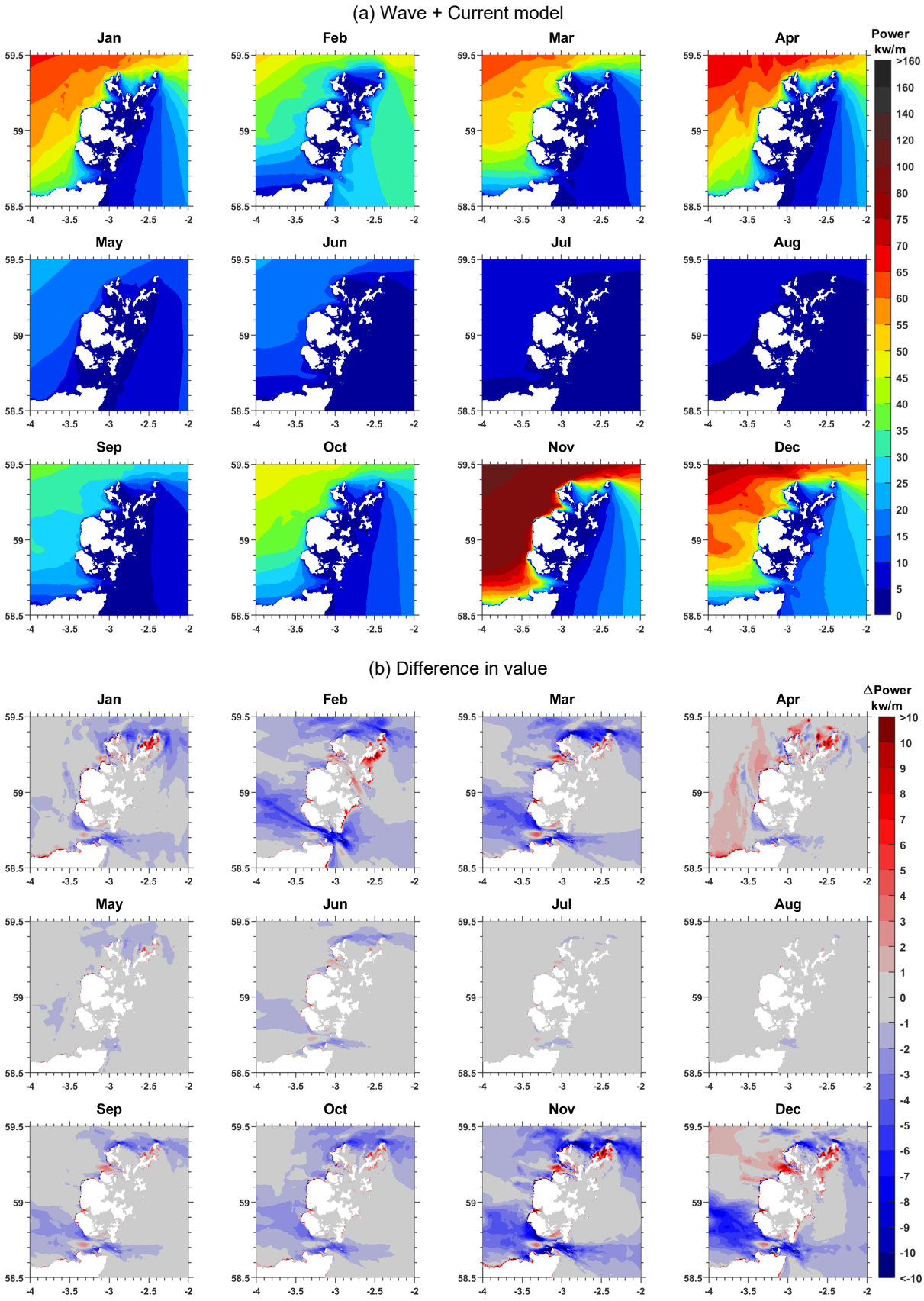

Figure B.29 Wave power monthly map in 2021

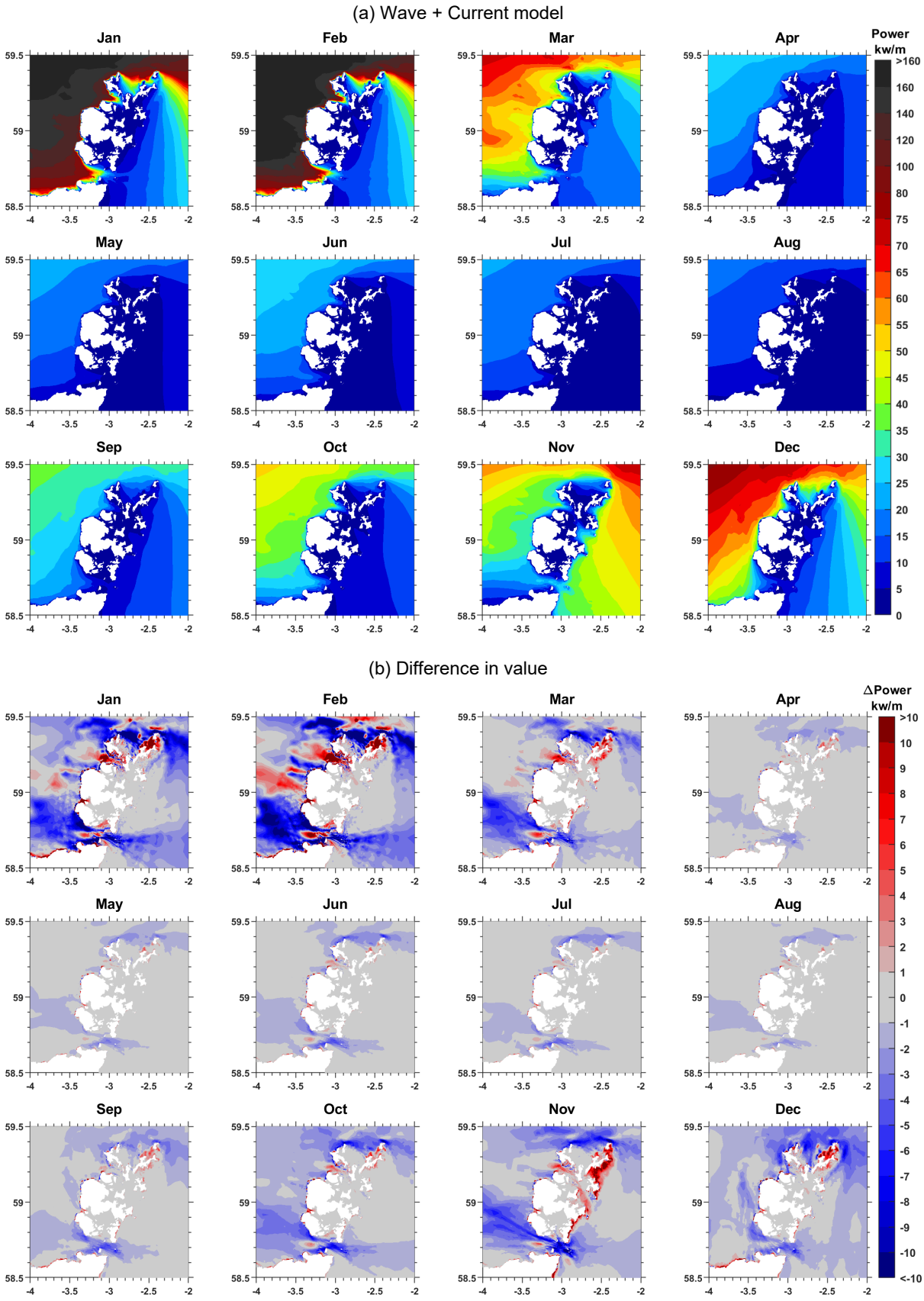

Figure B.30 Wave power monthly map in 2022

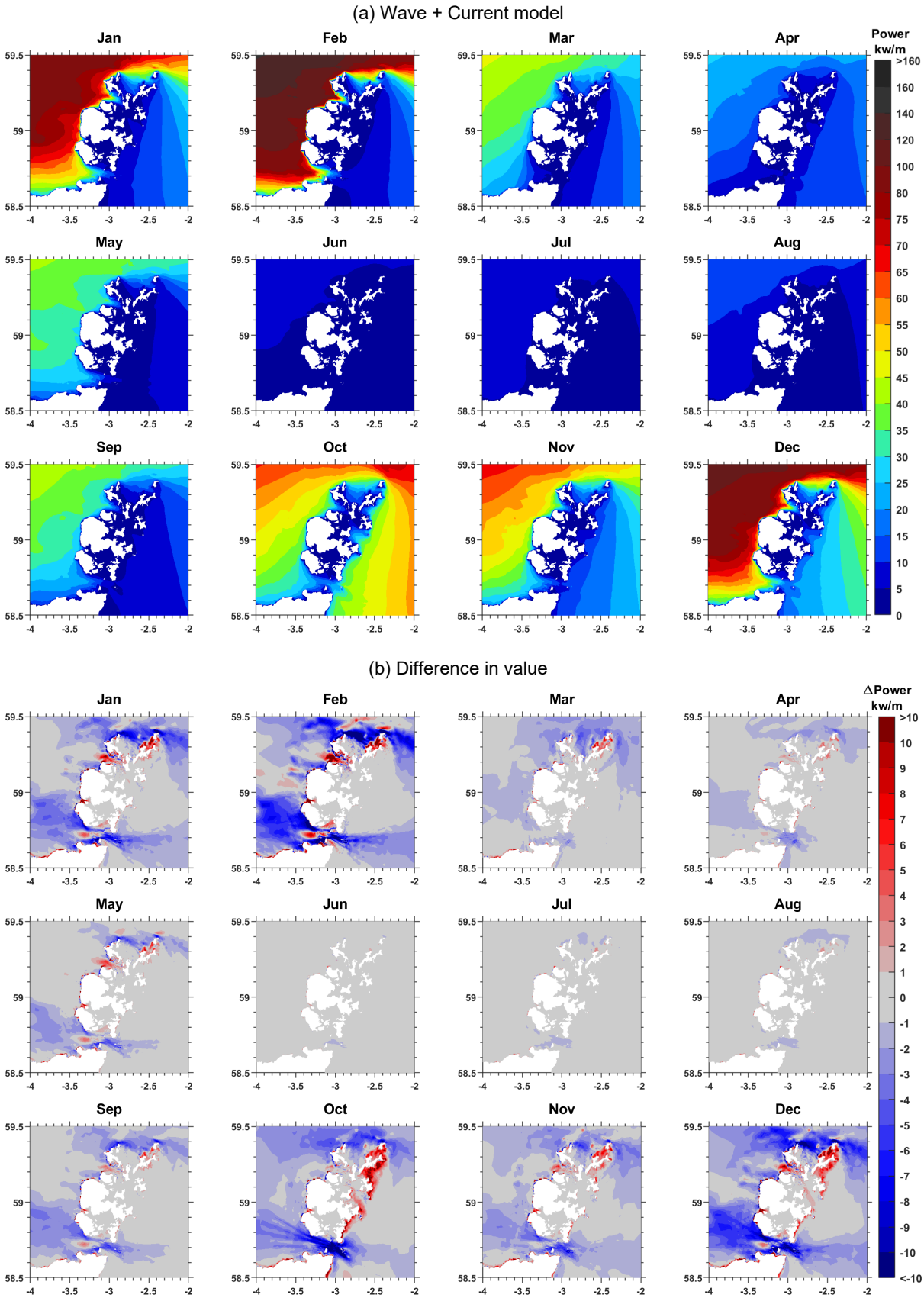

Figure B.31 Wave power monthly map in 2023

Appendix C
Publications

C.1 Conference papers

Peer-reviewed and published

1. **Tan T.**, Venugopal V.: Machine learning and deep learning for enhanced spatio-temporal wave parameters prediction, *Proceedings of the ASME 2024 43nd International Conference on Ocean, Offshore and Arctic Engineering (OMAE, Singapore, 2024)*. https://doi.org/10.1115/OMAE2024-127930

   Best Paper Award

2. Venugopal V., **Tan T.**: Hydrodynamic assessment of the CorPower C4 point absorber wave energy converter in extreme wave conditions, *Proceedings of the ASME 2024 43nd International Conference on Ocean, Offshore and Arctic Engineering (OMAE, Singapore, 2024)*.

   https://doi.org/10.1115/OMAE2024-127861

3. **Tan T.**, Venugopal V.: Numerical modelling of wave and tidal current interactions and their impact on wave parameters, *Proceedings of the 15th European Wave and Tidal Energy Conference (EWTEC, Bilbao, Spain, 2023)*.

   https://doi.org/10.36688/ewtec-2023-279

4. **Tan T.**, Venugopal V., Sellar B.: Analysis of turbulence parameters for a tidal energy site in a wave-current environment, *Proceedings of the ASME 2023 42nd International Conference on Ocean, Offshore and Arctic Engineering (OMAE, Melbourne, Australia, 2023)*.

   https://doi.org/10.1115/OMAE2023-104347

C.2 Journal papers

Peer-reviewed and published

5. **Tan T.**, Venugopal V. (2024): Characterisation of turbulence at sites with coexisting waves and currents: an analysis by Empirical Mode Decomposition, *Ocean Engineering.* https://doi.org/10.1016/j.oceaneng.2024.119616

Under review

6. **Tan T.**, Venugopal V. (2025): Enhancing wave resource assessment of high energy sites through wave-current interaction modelling, *Ocean Modelling.*
7. **Tan T.**, Venugopal V. (2025): A decade long high-resolution wave resource map for Pentland Firth and Orkney Waters - hindcast by two-way coupling of wave-current models, *Applied Ocean Research.*

Draft finished, ready to submit

8. **Tan T.**, Venugopal V. (2025): Prediction of Wave Parameters under Tidal Current Influence using Informer Deep Neural Network, *Environmental Modelling & Software.*

References

[1] Net-Zero Unveiled: UK's Ambitions Analysed, Carbon Free Europe (n.d.). https://www.carbonfreeeurope.org (accessed January 4, 2025).

[2] Wind and solar power could significantly exceed Britain's energy needs | University of Oxford, (2023). https://www.ox.ac.uk/news/2023-09-26-wind-and-solar-power-could-significantly-exceed-britain-s-energy-needs (accessed January 4, 2025).

[3] Wave Energy Scotland, Wave Energy Scotland (n.d.). https://www.waveenergyscotland.co.uk/ (accessed January 13, 2025).

[4] Marine Energy Wales, Marine Energy Wales (n.d.). https://www.marineenergywales.co.uk/ (accessed January 13, 2025).

[5] Renewable energy – Technology collaboration, IEA (n.d.). https://www.iea.org/about/technology-collaboration/renewable-energy (accessed January 4, 2025).

[6] A. Clément, P. McCullen, A. Falcão, A. Fiorentino, F. Gardner, K. Hammarlund, G. Lemonis, T. Lewis, K. Nielsen, S. Petroncini, M.-T. Pontes, P. Schild, B.-O. Sjöström, H.C. Sørensen, T. Thorpe, Wave energy in Europe: current status and perspectives, Renewable and Sustainable Energy Reviews 6 (2002) 405–431. https://doi.org/10.1016/S1364-0321(02)00009-6.

[7] M. Lehmann, F. Karimpour, C.A. Goudey, P.T. Jacobson, M.-R. Alam, Ocean wave energy in the United States: Current status and future perspectives, Renewable and Sustainable Energy Reviews 74 (2017) 1300–1313. https://doi.org/10.1016/j.rser.2016.11.101.

[8] S. Jin, D. Greaves, Wave energy in the UK: Status review and future perspectives, Renewable and Sustainable Energy Reviews 143 (2021) 110932. https://doi.org/10.1016/j.rser.2021.110932.

[9] A. Martinez, G. Iglesias, Wave exploitability index and wave resource classification, Renewable and Sustainable Energy Reviews 134 (2020) 110393. https://doi.org/10.1016/j.rser.2020.110393.

[10] The UK renewable energy strategy, GOV.UK (n.d.). https://www.gov.uk/government/publications/the-uk-renewable-energy-strategy (accessed January 13, 2025).

[11] Ocean Energy in Scotland, Ocean Energy Europe (n.d.). https://www.oceanenergy-europe.eu/annual/ocean-energy-scotland/ (accessed January 13, 2025).

[12] The Crown Estate, The Crown Estate (2025). https://www.thecrownestate.co.uk/ (accessed January 13, 2025).

[13] G. Lemonis, Wave and Tidal Energy Conversion, in: C.J. Cleveland (Ed.), Encyclopedia of Energy, Elsevier, New York, 2004: pp. 385–396. https://doi.org/10.1016/B0-12-176480-X/00344-2.

[14] M. Melikoglu, Current status and future of ocean energy sources: A global review, Ocean Engineering 148 (2018) 563–573. https://doi.org/10.1016/j.oceaneng.2017.11.045.

[15] Wave devices : EMEC: European Marine Energy Centre, (n.d.). https://www.emec.org.uk/marine-energy/wave-devices/ (accessed December 31, 2023).

[16] S.P. Neill, A. Vögler, A.J. Goward-Brown, S. Baston, M.J. Lewis, P.A. Gillibrand, S. Waldman, D.K. Woolf, The wave and tidal resource of Scotland, Renewable Energy 114 (2017) 3–17. https://doi.org/10.1016/j.renene.2017.03.027.

[17] Mocean Energy | Ocean energy technology developer | Scotland, Mocean Energy (n.d.). https://www.mocean.energy/ (accessed January 13, 2025).

[18] AWS Ocean Energy : EMEC: European Marine Energy Centre, (n.d.). https://www.emec.org.uk/about-us/wave-clients/aws-ocean-energy/ (accessed July 13, 2024).

[19] CorPower Ocean - Wave Power. To Power the Planet., (2021). https://corpowerocean.com/ (accessed December 31, 2023).

[20] CorPower Ocean announces wave energy breakthrough, (n.d.). https://corpowerocean.com/corpower-ocean-announces-wave-energy-breakthrough/ (accessed January 13, 2025).

[21] 100% Sustainable Electricity in the Faroe Islands: Expansion Planning Through Economic Optimization | IEEE Journals & Magazine | IEEE Xplore, (n.d.). https://ieeexplore.ieee.org/document/9323058 (accessed January 13, 2025).

[22] Case Study: Scotland's tidal stream resource, Marine.Gov.Scot (n.d.). https://marine.gov.scot/sma/assessment/case-study-scotlands-tidal-stream-resource.

[23] MeyGen, SAE Renewables (n.d.). https://saerenewables.com/tidal-stream/meygen/ (accessed May 28, 2024).

[24] Orbital O2, Orbital Marine (n.d.). https://www.orbitalmarine.com/o2/ (accessed January 13, 2025).

[25] 2030 Ocean Energy Vision, Ocean Energy Europe (n.d.). https://www.oceanenergy-europe.eu/wp-content/uploads/2020/10/OEE_2030_Ocean_Energy_Vision.pdf.

[26] RENEWABLE POWER GENERATION COSTS IN 2023, IRENA International Renewable Energy Agency (n.d.). https://www.irena.org/-/media/Files/IRENA/Agency/Publication/2024/Sep/IRENA_Renewable_power_generation_costs_in_2023.pdf.

[27] A. Vögler, V. Venugopal, Hebridean Marine Energy Resources: Wave-Power Characterisation Using a Buoy Network, in: American Society of Mechanical Engineers Digital Collection, 2013: pp. 477–488. https://doi.org/10.1115/OMAE2012-83658.

[28] Scale test sites : EMEC: European Marine Energy Centre, (n.d.). https://www.emec.org.uk/facilities/scale-test-sites/ (accessed July 13, 2024).

[29] Grid-connected wave test site : EMEC: European Marine Energy Centre, (n.d.). https://www.emec.org.uk/facilities/wave-test-site/ (accessed July 13, 2024).

[30] Laminaria : EMEC: European Marine Energy Centre, (n.d.). https://www.emec.org.uk/about-us/wave-clients/laminaria/ (accessed July 13, 2024).

[31] Mocean Energy : EMEC: European Marine Energy Centre, (n.d.). https://www.emec.org.uk/about-us/wave-clients/mocean-energy/ (accessed July 19, 2024).

[32] CorPower Ocean : EMEC: European Marine Energy Centre, (n.d.). https://www.emec.org.uk/about-us/wave-clients/corpower-ocean/ (accessed December 2, 2024).

[33] A. Saruwatari, D.M. Ingram, L. Cradden, Wave–current interaction effects on marine energy converters, Ocean Engineering 73 (2013) 106–118. https://doi.org/10.1016/j.oceaneng.2013.09.002.

[34] J. Wolf, D. Prandle, Some observations of wave–current interaction, Coastal Engineering 37 (1999) 471–485. https://doi.org/10.1016/S0378-3839(99)00039-3.

[35] The Treacherous and Productive Seas of Southern Africa, (2017). https://earthobservatory.nasa.gov/images/89535/the-treacherous-and-productive-seas-of-southern-africa (accessed July 13, 2024).

[36] G. Dodet, X. Bertin, N. Bruneau, A.B. Fortunato, A. Nahon, A. Roland, Wave-current interactions in a wave-dominated tidal inlet, Journal of Geophysical Research: Oceans 118 (2013) 1587–1605. https://doi.org/10.1002/jgrc.20146.

[37] T. Halsne, P. Bohlinger, K.H. Christensen, A. Carrasco, Ø. Breivik, Resolving regions known for intense wave–current interaction using spectral wave models: A case study in the energetic flow fields of Northern Norway, Ocean Modelling 176 (2022) 102071. https://doi.org/10.1016/j.ocemod.2022.102071.

[38] M.R. Hashemi, S.P. Neill, P.E. Robins, A.G. Davies, M.J. Lewis, Effect of waves on the tidal energy resource at a planned tidal stream array, Renewable Energy 75 (2015) 626–639. https://doi.org/10.1016/j.renene.2014.10.029.

[39] S.A. Thorpe, An Introduction to Ocean Turbulence, Cambridge University Press, Cambridge, 2007. https://doi.org/10.1017/CBO9780511801198.

[40] L. Perez, R. Cossu, A. Grinham, I. Penesis, Seasonality of turbulence characteristics and wave-current interaction in two prospective tidal energy sites, Renewable Energy 178 (2021) 1322–1336. https://doi.org/10.1016/j.renene.2021.06.116.

[41] M.J. Lewis, S.P. Neill, M.R. Hashemi, M. Reza, Realistic wave conditions and their influence on quantifying the tidal stream energy resource, Applied Energy 136 (2014) 495–508. https://doi.org/10.1016/j.apenergy.2014.09.061.

[42] A.V. Babanin, B.K. Haus, On the Existence of Water Turbulence Induced by Nonbreaking Surface Waves, (2009). https://doi.org/10.1175/2009JPO4202.1.

[43] B.M. Sumer, J. Fredsøe, Chapter 7: Forces on a cylinder in irregular waves, in: Hydrodynamics Around Cylindrical Strucures, World Scientific, 2006: pp. 325–328. https://doi.org/10.1142/9789812772770_0007.

[44] R.L. Soulsby, S. Clarke, Bed shear-stress under combined waves and currents on smooth and rough beds (TR 137), HR Wallingford, Wallingford, 2005. https://eprints.hrwallingford.com/558/ (accessed October 14, 2024).

[45] J. Wolf, Coastal flooding: impacts of coupled wave–surge–tide models, Nat Hazards 49 (2009) 241–260. https://doi.org/10.1007/s11069-008-9316-5.

[46] M.J. Lewis, T. Palmer, R. Hashemi, P. Robins, A. Saulter, J. Brown, H. Lewis, S. Neill, Wave-tide interaction modulates nearshore wave height, Ocean Dynamics 69 (2019) 367–384. https://doi.org/10.1007/s10236-018-01245-z.

[47] Climate model biases in the eastern tropical oceans: causes, impacts and ways forward - Richter - 2015 - WIREs Climate Change - Wiley Online Library, (n.d.). https://wires.onlinelibrary.wiley.com/doi/10.1002/wcc.338 (accessed May 21, 2025).

[48] M.A. Hemer, K.L. McInnes, R. Ranasinghe, Climate and variability bias adjustment of climate model-derived winds for a southeast Australian dynamical wave model, Ocean Dynamics 62 (2012) 87–104. https://doi.org/10.1007/s10236-011-0486-4.

[49] T.W. Group, The WAM Model—A Third Generation Ocean Wave Prediction Model, (1988). https://journals.ametsoc.org/view/journals/phoc/18/12/1520-0485_1988_018_1775_twmtgo_2_0_co_2.xml (accessed July 12, 2024).

[50] H.L. Tolman, User manual and system documentation of WAVEWATCH III TM version 3.14, (n.d.).

[51] DHI, MIKE 21/3 | 2D, 3D, Marine Water Modelling Software, DHI (2024). https://www.dhigroup.com/technologies/mikepoweredbydhi/mike-21-3 (accessed July 14, 2024).

[52] N. Booij, L.H. Holthuijsen, R.C. Ris, The “Swan” Wave Model for Shallow Water, (2015) 668–676. https://doi.org/10.1061/9780784402429.053.

[53] L. Bertotti, L. Cavaleri, Modelling waves at Orkney coastal locations, Journal of Marine Systems 96–97 (2012) 116–121. https://doi.org/10.1016/j.jmarsys.2012.02.012.

[54] P. Gleizon, D. Woolf, Wave Energy Assessment in Scottish Seas, in: Proceedings of the 10th European Wave and Tidal Energy Conference, Aalborg, Denmark, 2013.

[55] P. Gleizon, A. Murray, Modelling Wave Energy in Archipelagos - Case of Northern Scotland, 2014.

[56] V. Venugopal, R. Nemalidinne, Wave resource assessment for Scottish waters using a large scale North Atlantic spectral wave model, Renewable Energy 76 (2015) 503–525. https://doi.org/10.1016/j.renene.2014.11.056.

[57] V. Venugopal, R. Nemalidinne, A. Vögler, Numerical modelling of wave energy resources and assessment of wave energy extraction by large scale wave farms, Ocean & Coastal Management 147 (2017) 37–48. https://doi.org/10.1016/j.ocecoaman.2017.03.012.

[58] G. Lavidas, V. Venugopal, D. Friedrich, Wave energy extraction in Scotland through an improved nearshore wave atlas, International Journal of Marine Energy 17 (2017) 64–83. https://doi.org/10.1016/j.ijome.2017.01.008.

[59] A. Benetazzo, S. Carniel, M. Sclavo, A. Bergamasco, Wave–current interaction: Effect on the wave field in a semi-enclosed basin, Ocean Modelling 70 (2013) 152–165. https://doi.org/10.1016/j.ocemod.2012.12.009.

[60] F. Barbariol, A. Benetazzo, S. Carniel, M. Sclavo, Improving the assessment of wave energy resources by means of coupled wave-ocean numerical modeling, Renewable Energy 60 (2013) 462–471. https://doi.org/10.1016/j.renene.2013.05.043.

[61] V. Venugopal, R. Nemalidinne, Marine Energy Resource Assessment for Orkney and Pentland Waters With a Coupled Wave and Tidal Flow Model, in: Volume 9B: Ocean Renewable Energy, American Society of Mechanical Engineers, San Francisco, California, USA, 2014: p. V09BT09A010. https://doi.org/10.1115/OMAE2014-24027.

[62] V. Venugopal, A. Vögler, Modelling Wave-Current-Turbulence Interactions for Tidal Energy Applications, in: Volume 9: Ocean Renewable Energy, American Society of Mechanical Engineers, Virtual, Online, 2020: p. V009T09A009. https://doi.org/10.1115/OMAE2020-19298.

[63] V. Venugopal, A. Vögler, B. Sellar, Characterisation of Wave-Tidal Current-Turbulence Interactions at Tidal Energy Sites in the Orkney Islands, in: OnePetro, 2018. https://onepetro.org/ISOPEIOPEC/proceedings/ISOPE18/All-ISOPE18/ISOPE-I-18-240/20382 (accessed October 11, 2022).

[64] J. Hopkins, S. Elgar, B. Raubenheimer, Observations and model simulations of wave-current interaction on the inner shelf, Journal of Geophysical Research: Oceans 121 (2016) 198–208. https://doi.org/10.1002/2015JC010788.

[65] N. Guillou, Modelling effects of tidal currents on waves at a tidal stream energy site, Renewable Energy 114 (2017) 180–190. https://doi.org/10.1016/j.renene.2016.12.031.

[66] A. Webb, T. Waseda, K. Kiyomatsu, A high-resolution, long-term wave resource assessment of Japan with wave–current effects, Renewable Energy 161 (2020) 1341–1358. https://doi.org/10.1016/j.renene.2020.05.030.

[67] TOMAWAC - Wave propagation in coastal areas, (n.d.). http://www.opentelemac.org/index.php/presentation?id=20 (accessed August 17, 2022).

[68] N. Guillou, Evaluation of wave energy potential in the Sea of Iroise with two spectral models, Ocean Engineering 106 (2015) 141–151. https://doi.org/10.1016/j.oceaneng.2015.06.033.

[69] A. Abdul Rahman, V. Venugopal, Inter-Comparison of 3D Tidal Flow Models Applied To Orkney Islands and Pentland Firth, in: 2015.

[70] A. Perez Ortiz, A Systematic Approach to Undertake Tidal Energy Resource Assessment with Telemac-2D, 2013.

[71] S. Danilov, Ocean modeling on unstructured meshes, Ocean Modelling 69 (2013) 195–210. https://doi.org/10.1016/j.ocemod.2013.05.005.

[72] M. Zijlema, Computation of wind-wave spectra in coastal waters with SWAN on unstructured grids, Coastal Engineering 57 (2010) 267–277. https://doi.org/10.1016/j.coastaleng.2009.10.011.

[73] T. Awk, TOMAWAC user manual version 8.1, The TELEMAC-Mascaret Consortium 7 (2019).

[74] A.J. van der Westhuysen, Spectral modeling of wave dissipation on negative current gradients, Coastal Engineering 68 (2012) 17–30. https://doi.org/10.1016/j.coastaleng.2012.05.001.

[75] A.J. van der Westhuysen, M. Zijlema, J.A. Battjes, Nonlinear saturation-based whitecapping dissipation in SWAN for deep and shallow water, Coastal Engineering 54 (2007) 151–170. https://doi.org/10.1016/j.coastaleng.2006.08.006.

[76] T. Awk, TELEMAC 3D user manual version 8.1, The TELEMAC-Mascaret Consortium 7 (2019).

[77] Cefas - WaveNet interactive map, (n.d.). https://wavenet.cefas.co.uk/Map (accessed May 10, 2023).

[78] MeyGen, MeyGen, SIMEC ATLANTIS ENERGY (2018). https://simecatlantis.com/tidal-stream/meygen/ (accessed August 17, 2022).

[79] D. Coles, C. Greenwood, A. Vogler, T. Walsh, D. Taaffe, Assessment of the turbulent flow upstream of the Meygen Phase 1A tidal stream turbines, in: Proceedings of the Asian Wave and Tidal Energy Conference, Taipei, Taiwan., 2018: pp. 9–13.

[80] K. Hasselmann, D. Olbers, Measurements of wind-wave growth and swell decay during the Joint North Sea Wave Project (JONSWAP), Ergänzung Zur Deut. Hydrogr. Z., Reihe A (8) 12 (1973) 1–95.

[81] J.A. Battjes, J.P.F.M. Janssen, Energy Loss and Set-Up Due to Breaking of Random Waves, Coastal Engineering (1978) 569–587. https://doi.org/10.1061/9780872621909.034.

[82] G.D. Egbert, S.Y. Erofeeva, Efficient Inverse Modeling of Barotropic Ocean Tides, Journal of Atmospheric and Oceanic Technology 19 (2002) 183–204. https://doi.org/10.1175/1520-0426(2002)019<0183:EIMOBO>2.0.CO;2.

[83] M. Lewis, S.P. Neill, P. Robins, M.R. Hashemi, S. Ward, Characteristics of the velocity profile at tidal-stream energy sites, Renewable Energy 114 (2017) 258–272. https://doi.org/10.1016/j.renene.2017.03.096.

[84] S.P. Neill, M.R. Hashemi, M.J. Lewis, The role of tidal asymmetry in characterizing the tidal energy resource of Orkney, Renewable Energy 68 (2014) 337–350. https://doi.org/10.1016/j.renene.2014.01.052.

[85] O.M. Philips, The dynamics of the upper ocean, Cambridge University Press, 1977.

[86] I.G. Jonsson, Wave-current interactions, n.d.

[87] L. Holthuijsen, Appendix D Tides and currents, in: Waves in Oceanic and Coastal Waters, Cambridge University Press, 2007: pp. 335–341.

[88] L. Holthuijsen, Linear wave theory (coastal waters), in: Waves in Oceanic and Coastal Waters, Cambridge University Press, 2007: pp. 197–243.

[89] X. Shi, S. Li, B. Liang, J. Zhao, Y. Liu, Z. Wang, Numerical study on the impact of wave-current interaction on wave energy resource assessments in Zhoushan sea area, China, Renewable Energy 215 (2023) 119017. https://doi.org/10.1016/j.renene.2023.119017.

[90] M.R. Hashemi, S.T. Grilli, S.P. Neill, A simplified method to estimate tidal current effects on the ocean wave power resource, Renewable Energy 96 (2016) 257–269. https://doi.org/10.1016/j.renene.2016.04.073.

[91] S.P. Neill, M.J. Lewis, M.R. Hashemi, E. Slater, J. Lawrence, S.A. Spall, Inter-annual and inter-seasonal variability of the Orkney wave power resource, Applied Energy 132 (2014) 339–348. https://doi.org/10.1016/j.apenergy.2014.07.023.

[92] E.B.L. Mackay, A.S. Bahaj, P.G. Challenor, Uncertainty in wave energy resource assessment. Part 2: Variability and predictability, Renewable Energy 35 (2010) 1809–1819. https://doi.org/10.1016/j.renene.2009.10.027.

[93] T. Tan, V. Venugopal, Numerical modelling of wave and tidal current interactions and their impact on wave parameters, in: Proceedings of the European Wave and Tidal Energy Conference, 2023. https://doi.org/10.36688/ewtec-2023-279.

[94] K.-A. Chang, P.L.-F. Liu, Experimental investigation of turbulence generated by breaking waves in water of intermediate depth, Physics of Fluids 11 (1999) 3390–3400. https://doi.org/10.1063/1.870198.

[95] H. Ma, D. Dai, S. Jiang, C. Huang, J. Deng, F. Qiao, Quantitatively study on wave-turbulence interactions by laboratory experiments, Dynamics of Atmospheres and Oceans 99 (2022) 101302. https://doi.org/10.1016/j.dynatmoce.2022.101302.

[96] S.K. Singh, A. Khait, P.K. Raushan, K. Debnath, Localized and Distributed Energy in Wave–Current Flow, Journal of Offshore Mechanics and Arctic Engineering 143 (2020). https://doi.org/10.1115/1.4047521.

[97] S.K. Singh, K. Debnath, Combined effects of wave and current in free surface turbulent flow, Ocean Engineering 127 (2016) 170–189. https://doi.org/10.1016/j.oceaneng.2016.10.014.

[98] L. Perez, R. Cossu, C. Couzi, I. Penesis, Wave-Turbulence Decomposition Methods Applied to Tidal Energy Site Assessment, Energies 13 (2020) 1245. https://doi.org/10.3390/en13051245.

[99] L. Perez, R. Cossu, A. Grinham, I. Penesis, Evaluation of wave-turbulence decomposition methods applied to experimental wave and grid-generated turbulence data, Ocean Engineering 218 (2020) 108186. https://doi.org/10.1016/j.oceaneng.2020.108186.

[100] C. Bian, Z. Liu, Y. Huang, L. Zhao, W. Jiang, On Estimating Turbulent Reynolds Stress in Wavy Aquatic Environment, Journal of Geophysical Research: Oceans 123 (2018) 3060–3071. https://doi.org/10.1002/2017JC013230.

[101] C.J. Huang, F. Qiao, Simultaneous Observations of Turbulent Reynolds Stress in the Ocean Surface Boundary Layer and Wind Stress over the Sea Surface, Journal of Geophysical Research: Oceans 126 (2021) e2020JC016839. https://doi.org/10.1029/2020JC016839.

[102] J.D. Bricker, S.G. Monismith, Spectral Wave–Turbulence Decomposition, Journal of Atmospheric and Oceanic Technology 24 (2007) 1479–1487. https://doi.org/10.1175/JTECH2066.1.

[103] L.J. MacVean, J.R. Lacy, Interactions between waves, sediment, and turbulence on a shallow estuarine mudflat, Journal of Geophysical Research: Oceans 119 (2014) 1534–1553. https://doi.org/10.1002/2013JC009477.

[104] A.N. Kolmogorov, V. Levin, J.C.R. Hunt, O.M. Phillips, D. Williams, The local structure of turbulence in incompressible viscous fluid for very large Reynolds numbers, Proceedings of the Royal Society of London. Series A: Mathematical and Physical Sciences 434 (1997) 9–13. https://doi.org/10.1098/rspa.1991.0075.

[105] A.N. Kolmogorov, On degeneration (decay) of isotropic turbulence in an incompressible viscous liquid, Dokl. Akad. Nauk SSSR 31 (1941) 538--540.

[106] A.N. Kolmogorov, V. Levin, J.C.R. Hunt, O.M. Phillips, D. Williams, Dissipation of energy in the locally isotropic turbulence, Proceedings of the Royal Society of London. Series A: Mathematical and Physical Sciences 434 (1997) 15–17. https://doi.org/10.1098/rspa.1991.0076.

[107] S.B. Pope, Turbulent Flows, Meas. Sci. Technol. 12 (2001) 2020. https://doi.org/10.1088/0957-0233/12/11/705.

[108] B. Liu, Y. Chen, T. Cai, Y. Li, L. Sun, Estimating Waves and Currents at the Saltmarsh Edge Using Acoustic Doppler Velocimeter Data, Frontiers in Marine Science 8 (2021). https://www.frontiersin.org/article/10.3389/fmars.2021.708116 (accessed May 25, 2022).

[109] N.E. Huang, Z. Shen, S.R. Long, M.C. Wu, H.H. Shih, Q. Zheng, N.-C. Yen, C.C. Tung, H.H. Liu, The empirical mode decomposition and the Hilbert spectrum for nonlinear and non-stationary time series analysis, Proc. R. Soc. Lond. A 454 (1998) 903–995. https://doi.org/10.1098/rspa.1998.0193.

[110] F. Foucher, P. Ravier, Determination of turbulence properties by using empirical mode decomposition on periodic and random perturbed flows, Exp Fluids 49 (2010) 379–390. https://doi.org/10.1007/s00348-009-0804-5.

[111] X. Chen, X. Zhao, Y. Liang, X. Luan, Ocean Turbulence Denoising and Analysis Using a Novel EMD-Based Denoising Method, Journal of Marine Science and Engineering 10 (2022) 663. https://doi.org/10.3390/jmse10050663.

[112] F.G. Schmitt, Y. Huang, Z. Lu, Y. Liu, N. Fernandez, Analysis of velocity fluctuations and their intermittency properties in the surf zone using empirical mode decomposition, Journal of Marine Systems 77 (2009) 473–481. https://doi.org/10.1016/j.jmarsys.2008.11.012.

[113] F. Qiao, Y. Yuan, J. Deng, D. Dai, Z. Song, Wave–turbulence interaction-induced vertical mixing and its effects in ocean and climate models, Philosophical Transactions of the Royal Society A: Mathematical, Physical and Engineering Sciences 374 (2016) 20150201. https://doi.org/10.1098/rsta.2015.0201.

[114] N.E. Huang, Z. Shen, S.R. Long, A NEW VIEW OF NONLINEAR WATER WAVES: The Hilbert Spectrum1, Annual Review of Fluid Mechanics 31 (1999) 417–457. https://doi.org/10.1146/annurev.fluid.31.1.417.

[115] T. Tan, V. Venugopal, B. Sellar, Analysis of Turbulence Parameters for a Tidal Energy Site in a Wave-Current Environment, in: ASME 2023 42nd International Conference on Ocean, Offshore and Arctic Engineering, 2023: pp. OMAE2023-104347. https://doi.org/10.1115/OMAE2023-104347.

[116] Z. Wu, N.E. Huang, Ensemble empirical mode decomposition: a noise-assisted data analysis method, Adv. Adapt. Data Anal. 01 (2009) 1–41. https://doi.org/10.1142/S1793536909000047.

[117] J. Chávez-Dorado, I. Scherl, M. DiBenedetto, Wave and turbulence separation using dynamic mode decomposition, (2024). https://doi.org/10.48550/arXiv.2403.00223.

[118] GEBCO Bathymetric Compilation Group 2020, The GEBCO_2020 Grid - a continuous terrain model of the global oceans and land., (2020). https://doi.org/10.5285/a29c5465-b138-234d-e053-6c86abc040b9.

[119] TELEMAC-3D - 3D Hydrodynamics, (n.d.). https://www.opentelemac.org/index.php/presentation?id=18 (accessed July 15, 2024).

[120] Copernicus Climate Change Service (C3S), ERA5: Fifth Generation of ECMWF Atmospheric Reanalyses of the Global Climate . Copernicus Climate Change Service Climate Data Store (CDS) (2017). https://cds.climate.copernicus.eu/cdsapp#!/home (accessed August 17, 2022).

[121] Black & Veatch Corporation, Lessons Learnt from MeyGen Phase 1A Final Report, 2020. https://webassets.bv.com/2020-06/MeyGen%20Lessons%20Learnt%20Full%20Report.pdf (accessed August 17, 2022).

[122] MATLAB and Signal Processing Toolbox, (n.d.). https://uk.mathworks.com/products/signal.html.

[123] L.E. Borgman, Random Hydrodynamic Forces on Objects, The Annals of Mathematical Statistics 38 (1967) 37–51. https://doi.org/10.1214/aoms/1177699057.

[124] I.A. Milne, R.N. Sharma, R.G.J. Flay, S. Bickerton, Characteristics of the turbulence in the flow at a tidal stream power site, Philosophical Transactions of the Royal Society A: Mathematical, Physical and Engineering Sciences 371 (2013) 20120196. https://doi.org/10.1098/rsta.2012.0196.

[125] C. Greenwood, A. Vogler, V. Venugopal, On the Variation of Turbulence in a High-Velocity Tidal Channel, Energies 12 (2019). https://doi.org/10.3390/en12040672.

[126] S.C. James, Y. Zhang, F. O'Donncha, A machine learning framework to forecast wave conditions, Coastal Engineering 137 (2018) 1–10. https://doi.org/10.1016/j.coastaleng.2018.03.004.

[127] S. Shamshirband, A. Mosavi, T. Rabczuk, N. Nabipour, K. Chau, Prediction of significant wave height; comparison between nested grid numerical model, and machine learning models of artificial neural networks, extreme learning and support vector machines, Engineering Applications of Computational Fluid Mechanics 14 (2020) 805–817. https://doi.org/10.1080/19942060.2020.1773932.

[128] V. Domala, W. Lee, T. Kim, Wave data prediction with optimized machine learning and deep learning techniques, Journal of Computational Design and Engineering 9 (2022) 1107–1122. https://doi.org/10.1093/jcde/qwac048.

[129] H. Hu, A.J. van der Westhuysen, P. Chu, A. Fujisaki-Manome, Predicting Lake Erie wave heights and periods using XGBoost and LSTM, Ocean Modelling 164 (2021) 101832. https://doi.org/10.1016/j.ocemod.2021.101832.

[130] T. Tan, V. Venugopal, Machine Learning and Deep Learning for Enhanced Spatio-Temporal Wave Parameters Prediction, in: American Society of Mechanical Engineers Digital Collection, 2024. https://doi.org/10.1115/OMAE2024-127930.

[131] W. Hao, X. Sun, C. Wang, H. Chen, L. Huang, A hybrid EMD-LSTM model for non-stationary wave prediction in offshore China, Ocean Engineering 246 (2022) 110566. https://doi.org/10.1016/j.oceaneng.2022.110566.

[132] T. Zilong, S. Yubing, D. Xiaowei, Spatial-temporal wave height forecast using deep learning and public reanalysis dataset, Applied Energy 326 (2022) 120027. https://doi.org/10.1016/j.apenergy.2022.120027.

[133] A. Vaswani, N. Shazeer, N. Parmar, J. Uszkoreit, L. Jones, A.N. Gomez, Ł. Kaiser, I. Polosukhin, Attention is All you Need, in: Advances in Neural Information Processing Systems, Curran Associates, Inc., 2017. https://proceedings.neurips.cc/paper_files/paper/2017/hash/3f5ee243547dee91fbd053c1c4a845aa-Abstract.html (accessed January 9, 2024).

[134] H. Zhou, S. Zhang, J. Peng, S. Zhang, J. Li, H. Xiong, W. Zhang, Informer: Beyond Efficient Transformer for Long Sequence Time-Series Forecasting, Proceedings of the AAAI Conference on Artificial Intelligence 35 (2021) 11106–11115. https://doi.org/10.1609/aaai.v35i12.17325.

[135] T. Chen, C. Guestrin, XGBoost: A Scalable Tree Boosting System, in: Proceedings of the 22nd ACM SIGKDD International Conference on Knowledge Discovery and Data Mining, Association for Computing Machinery, New York, NY, USA, 2016: pp. 785–794. https://doi.org/10.1145/2939672.2939785.

[136] F. Anggraeni, D. Adytia, A.W. Ramadhan, Forecasting of Wave Height Time Series Using AdaBoost and XGBoost, Case Study in Pangandaran, Indonesia, in: 2021 International Conference on Data Science and Its Applications (ICoDSA), 2021: pp. 97–101. https://doi.org/10.1109/ICoDSA53588.2021.9617524.

[137] O. Sagi, L. Rokach, Ensemble learning: A survey, WIREs Data Mining and Knowledge Discovery 8 (2018) e1249. https://doi.org/10.1002/widm.1249.

[138] P. Wessel, W.H. Smith, A global, self-consistent, hierarchical, high-resolution shoreline database, Journal of Geophysical Research: Solid Earth 101 (1996) 8741–8743.